KAUNAS UNIVERSITY OF TECHNOLOGY

GALYNA SYCH

DESIGN AND CHARACTERIZATION OF NEW INTRA- AND INTER- MOLECULAR DONOR-ACCEPTOR SYSTEMS

DOCTORAL DISSERTATION
Technological Sciences, Materials Engineering (T 008)

2020, Kaunas

This doctoral dissertation was prepared at Kaunas University of Technology, Faculty of Chemical Technology, Department of Polymer Chemistry and Technology during the period of 2015–2019. The studies were supported by the Research Council of Lithuania.

Scientific Supervisor:
Prof. Habil. dr. Juozas Vidas GRAŽULEVIČIUS (Kaunas University of Technology, Technological sciences, Materials engineering T 008).

Scientific Advisor:
Dr. Jūratė SIMOKAITIENĖ (Kaunas University of Technology, Technological sciences, Materials engineering T 008).

Edited by: Armandas Rumšas (Publishing Office “Technologija”).

KAUNO TECHNOLOGIJOS UNIVERSITETAS

GALYNA SYCH

NAUJŲ INTRAMOLEKULINIŲ IR TARPMOLEKULINIŲ SISTEMŲ DONORAS-AKCEPTORIUS KŪRIMAS IR APIBŪDINIMAS

DAKTARO DISERTACIJA
Technologijos mokslai, Medžiagų inžinerija (T 008)

2020, Kaunas

Disertacija parengta 2015-2019 metais Kauno technologijos universiteto Cheminės technologijos fakulteto Polimerų chemijos ir technologijos katedroje. Mokslinius tyrimus rėmė Lietuvos mokslo taryba.

Mokslinis vadovas:

Habil. dr. Juozas Vidas GRAŽULEVIČIUS (Kauno technologijos universitetas, technologijos mokslai, Medžiagų inžinerija (T 008).

Mokslinis konsultantas :

Dr. Jūratė SIMOKAITIENĖ (Kauno technologijos universitetas, technologijos mokslai, Medžiagų inžinerija (T 008)

Redagavo: Armandas Rumšas (leidykla “Technologija”).

TABLE OF CONTENTS

LIST OF ABBREVIATIONS

^{1}CT	Charge transfer singlet state
3CzPFP	3-(3-(carbazole-9-yl)phenyl)pyrido[3′,2′:4,5]furo[2,3-b] pyridine
^{3}LE	Locally excited triplet state
3TPYMB	Tris-[3-(3-pyridyl)mesityl]borane
ACQ	Aggregation caused quenching
AIBN	Azobisisobutyronitrile
AIEE	Aggregation induced emission enhancement
BmPyPb	3,3″,5,5″-tetra(pyridine-3-yl)-1,1′:3′1″-terphenyl
CCT	Correlated color temperature
CE/PE	Current and power efficiencies
CELIV	Charge extraction by linearly increasing voltage technique
CIE	Commission Internationale de l’Eclairage
CRI	Color rendering index
CT	Charge-transfer
CV	Cyclic voltammetry
D*/A*	Excited donor/acceptor species
D-A	Donor-acceptor
DFT	Density functional method
DMAC	9,9-dimethyl-9,10-dihydroacridine
DPEPO	Bis[2-(diphenylphosphino)phenyl] ether oxide
DSC	Differential scanning calorimetry
DTAF	9,9-Di[4-(di-*p*-tolyl)aminophenyl]fluorine
D-π-A	Donor-π-acceptor
E	Orbital energy
$EA_{acceptor}$	Electron affinity of acceptor
EA_{donor}	Electron affinity of donor
$E^{elc}_{g,}$	Electrical energy band gap
EML	Electron-transporting layer
$E^{opt}_{g,film}$	Optical energy band gap
E_{ox}	Oxidation potential
EQE	External quantum efficiency
E_{red}	Reduction potential
ESIPT	Excited-state intramolecular proton transfer
E^{theor}_{g}	Theoretical energy band gap
$\hbar$	Planck constant
HLCT	Hybridized local charge transfer mechanism
HOMO	Highest occupied molecular orbital
HPS	Hexaphenylsilole
HTL	Hole-transporting layer
$IP_{acceptor}$	Ionization potential of acceptor
IP_{donor}	Ionization potential of donor
IQE	Internal quantum efficiency (IQE)

ISC	Intersystem crossing
J	Exchange energy
JAF	J-aggregate formation
K	Electron repulsion energy
k_B	Boltzmann constant
LCD	Liquid-crystal display
LE	Locally excited
LED	Light-emitting diodes
LUMO	Lowest unoccupied molecular orbital
MCL	Mechanochromic luminescent
mCP	1,3-bis(N -carbazolyl)benzene
mCPCN	9-(3-(9*H*-carbazol-9-yl)phenyl)-9*H* -carbazole-3-carbonitrile
m-MTDATA	4,4′,4″-Tris[3-methylphenyl(phenyl)amino]triphenylamine
M_w	Molecular weight
NPB	*N*,*N′*-Di(1-naphthyl)-*N*,*N′*-diphenyl-(1,1′-biphenyl)-4,4′-diamine
NPNPB	*N*,*N* 9-diphenyl-*N*,*N* 9-di-[4-(*N*,*N*diphenyl-amino)phenyl]benzidine
OLEDs	Organic light-emitting diodes
OXD-7	2-(4-*Tert*-butylphenyl)-5-(4-biphenylyl)-1,3,4-oxadiazole
$Pd(PPh_3)_4$	*Tetrakis*-triphenylphosphine palladium (0)
PL/PH	Photoluminescence/Phosphorescence
PLQY	Photoluminescence quantum yield
PO-T2T	2,4,6-Tris[3-(diphenylphosphinyl)phenyl]-1,3,5-triazine
RIM	Restriction of molecular motion
RIR	Restriction of intramolecular rotations
rISC	Reverse intersystem crossing
RIV	Restriction of intramolecular vibrations
S, T	Singlet, triplet state
TADF	Thermally activated delayed fluorescence
TAPC	1,1-Bis[(di-4-tolylamino)phenyl]cyclohexane
t-Bu-PBD	2-(Biphenyl-4-yl)-5-(4-*tert*-butylphenyl)-1,3,4-oxadiazole
TCTA	Tri(N-carbazolyl)triphenylamine
T_d	5% Weight loss temperatures
TDDFT	Time dependent density functional theory technique
T_g	Glass transition temperature
TGA	Thermogravimetric experiment
TICT	Twisted intramolecular charge transfer
T_m	Melting point
TOF	Time-of-flight technique
TPBi	2,2′,2"-(1,3,5-Benzinetriyl)-tris(1-phenyl-1-H-benzimidazole)
TPD	*N*,*N′*-Bis(3-methylphenyl)-*N*,*N′*-diphenylbenzidine
TPD	*N*,*N′*-Bis(3-methylphenyl)-*N*,*N′*-diphenylbenzidine
TSBPA	4,4′-(Diphenylsilanediyl)bis(*N*,*N* diphenylaniline)

TTA	Triplet-triplet annihilation
UV-vis	Ultraviolet-visible
WOLED	White organic light-emission diodes
XRD	X-ray diffraction
γ	Charge balance factor
ΔE_{S-T}	Singlet-triplet energy splitting
$-\Delta G$	Gibbs energy
η_{fr}	Singlet ratio
η_L	Current efficiency in cd A^{-1}
η_{out}	Optical out coupling efficiency
η_P	Luminous efficiency
λ_{EL}	Electroluminescence peak
λ_{PL}	Photoluminescence peak
τ	Excited-state lifetime
χ	Estimated error

1. INTRODUCTION

Light is essential for everybody from microorganisms to human beings. Light reaches the deepest parts of our planet. Even in absolute darkness, light can appear by energy metabolism of bioluminescent creatures themselves. Luminescence (lat. *lumen* – light and *essentia* – the substance of) is defined as light emission or electromagnetic waves caused by chemical reactions, electrical energy, subatomic motions, etc.[1]. Considering the nature of light as a particle or a wave, it has always been one of the greatest mysteries since the early times: starting from the corpuscular theory supported by Isaac Newton up to the original concept of light as a particle – photon – developed by Albert Einstein[2, 3]. Thus, the smallest unit of light named *photon* is the discrete amount of electromagnetic radiation.

Humanity in general and scientists in particular always seek new knowledge and improvement of life, starting from the first artificial light source – fire – and up to the present century of advanced sciences and technologies. We can note the step-by-step scientific progress and improvement along with the world market demands to develop new effective, reliable and sustainable solid-state lighting technologies. Thus, the breakthroughs in electronic and optoelectronic devices, such as organic thin film transistors, solar cells, organic light emitting diodes (OLEDs), etc. contributed to achieving remarkable device efficiencies[4, 5]. Particularly, the relatively new concept of OLED leading to consumption of less energy was developed in the late 1980s and became a major leap in display technology. This strategy is already commercially applied in smartphones and TV displays[8]. The usage of organic electroactive molecules as the main components of OLEDs made them an attractive alternative to devices containing toxic or rare metals (iridium, platinum, *etc*.). Third generation OLEDs exploiting highly luminescent organic materials exhibiting thermally activated delayed fluorescence (TADF) [6, 7] offers a combination of high efficiency and low cost. OLEDs based on organic TADF molecules allowed to activate triplet excitons by up-conversion to the singlet state. Nevertheless, OLEDs are still denoted by a variety of drawbacks, such as short lifetimes and lower stability of blue devices, susceptibility to water, and relatively high cost. Meanwhile, careful design of organic materials for OLEDs can highly improve the stability and efficiency of the devices. Therefore, the field of OLEDs is always in demand for new blue organic emitters with a cheap synthetic procedure, high luminescence quantum efficiency, and thermal stability.

The aim of this work is the design and investigation of the properties of new bipolar compounds for effective donor-acceptor systems with intramolecular and intermolecular charge-transfer for OLEDs. Comparative analysis of the properties of compounds supported by theoretical calculations is also an urgent task. To achieve the set goals of the thesis, the following objectives were defined:

- Design, synthesis, and comparative investigation of a new series of monomers and corresponding polymers containing an electron-deficient tetrafluorobenzene moiety.

- Synthesis and estimation of applicability in organic light-emitting diodes of new derivatives of tetrafluorophenylcarbazole and tri/tetraphenylethylene displaying aggregation-induced emission enhancement.
- Design and characterization of new isomeric bipolar compounds forming versatile exciplexes comprised of quinoline and phenylcarbazolyl moieties with *meta*- and *para*- linking topology.
- Synthesis and investigation of donor-acceptor and donor-π-acceptor compounds with mechanochromic and thermally activated delayed fluorescence properties.
- Design, synthesis and investigation of series of cyanocarbazolyl-based exciplex-forming materials.

Novelty of the work:

- A series of new donor-acceptor monomers and polymers were synthesized. The donor strength and polymerization of vinyl monomers highly affect the photophysical, electrochemical and thermal properties of tetrafluorobenzene-based monomers and the corresponding polymers.
- New highly luminescent and thermally stable AIEE-active derivatives of tetrafluorophenylcarbazole and tri/tetraphenylethylene were synthesized and investigated. Exciplex-host-based OLEDs containing one or two emitting layers of tetraphenylethenyl were fabricated and showed more than 50% higher external quantum efficiency as compared to that of the corresponding non-doped device.
- New bipolar thermally stable carbazolyl and quinoline-based compounds were synthesized and characterized. The compounds formed versatile exciplexes and were applied in white OLEDs.
- New mechanoresponsive quinoline and di-*tert*-butyl phenothiazine derivatives with D-A and D-π-A architecture were obtained and investigated. It was established that a D-A compound without a phenyl linker showed the TADF feature.
- Three new exciplex-forming cyano-carbazolyl-based compounds with high triplet state energies were synthesized and characterized. It was established that compounds form efficient TADF exciplex systems in pair with the acceptor. The influence of side-substituents on the properties of compounds and exciplexes was studied.

The contribution of the author:

The author has designed, synthesized, purified and characterized five new series of compounds. The author has also conducted the theoretical investigations of the compounds. The author has analyzed the results of differential scanning calorimetry, thermogravimetric analysis, single crystal XRD, powder XRD and infrared spectroscopy. Therefore, the author has performed cyclic voltammetry and photophysical measurement and analyzed the obtained results. Single crystal XRD measurement was done in collaboration with dr. Audrius Bucinskas (Kaunas University of Technology) and dr. Ramin Pashazadeh (Kaunas University of

Technology). Meanwhile, powder XRD measurements were performed with the help of dr. Algirdas Lazauskas (Kaunas University of Technology). The ionization potential of solid samples and charge-transporting measurements were performed by dr. Dmytro Volyniuk (Kaunas University of Technology), and the results were analyzed by the author. The OLEDs described in the Results and Discussions Chapter were fabricated in collaboration with dr. Dmytro Volyniuk (Kaunas University of Technology) and Oleksandr Bezvikonnyi (Kaunas University of Technology).

2. LITERATURE REVIEW

2.1. Why OLEDs? Structure of OLEDs

Organic light-emitting diodes (OLEDs) are optoelectronic devices based on electroluminescence, in which, light emission is generated by radiative recombination of hole-electron pairs injected from the electrodes under applied electric field. The field of OLEDs has been successfully gaining in popularity after the breakthrough discoveries made by Tang and VanSlyke in 1987[8] who presented a unique at that time electroluminescent device implementing small light-emitting molecules. While continuing the work of Tang, Friend *et al.* reported organic devices based on high molecular weight polymeric materials as the emitting layers[9]. With the technological progress, nowadays, the OLED technology represents one of the most successful areas of widely commercialized applications of organic semiconductors, such as emissive display technology and lightning sources. The key advantages of OLEDs over other types of displays (crystal LED or LCD) are that they are flat, thinner, lighter in weight, and more flexible. Moreover, OLEDs are characterized with low operative voltages, higher brightness, and a superior viewing angle (~170 °), which are essential parameters for the display technology. Despite all the advantages, OLEDs still meets a series of technical problems and challenges. Among the drawbacks are their shorter lifetimes, the expensive fabrication process, sensitivity to water, and the overall degradation of organic molecules. The continuous collaboration between chemists and physicists opens new opportunities to overcome the obstacles as new discoveries yield innovative molecules and modified device structures, and, subsequently, more efficient devices.

OLEDs are thin-film organic semiconductor light emitting devices comprised of organic layers sandwiched between two electrodes. The schematic multi-layer OLEDs structure is depicted in Fig. 2.1. The implementation of the multi-layer-type device can improve the carrier injection and boost the efficiency of OLEDs.

The layers of OLEDs are the following:

1. *Substrate* (plastic, glass, or metal foil);
2. *Anode* (transparent electrode for the injection of holes);
3. *The hole-injecting layer*;
4. *The hole-transporting layer* (HTL) (transport of holes and blocking of electrons);
5. *The light-emitting layer* (EML);
6. *The electron-transporting layer* (ETL) (transport of electrons and blocking of holes);
7. *Cathode* (metal alloys: Ag, Li, Al, Ca, thin insulator, LiF, MgO_x)

Looking deeper into the working principles of OLEDs, when the voltage is applied across the device holes, and electrons are injected into the emissive layer from the cathode and the anode, respectively. Thus, holes and electrons pass through hole-transporting (HTL) and electron-transporting (ETL) layers which are usually included to facilitate the carrier injection. The recombination of hole and electron pairs (excitons) formed in the emitting layer results in the formation of the light photon.

The color of electroluminescence mainly depends on the type of the organic light-emitting material and can be changed by the variation of emitters.

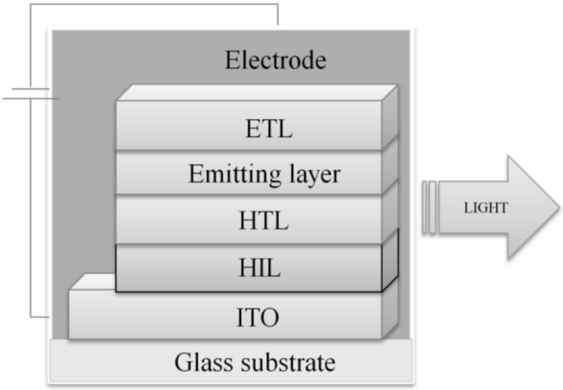

Fig. 2.1. Schematic structure of multi-layer OLEDs

Devices can be fabricated by two main approaches: the vacuum deposition technique, and the solution process (spin-coating, ink-jet printing, casting, etc.). Both methods are denoted by advantages and disadvantages. The choice of the fabrication method mainly depends on the size and nature of organic materials being used for the fabrication of OLEDs discussed below. Three main parameters are being used to evaluate the quality of light produced by OLEDs: *Commission Internationale de l'Eclairage* (CIE) coordinates, the color rendering index (CRI), and the correlated color temperature (CCT). Meanwhile, under electrical excitation, the efficiency of the device can be characterized with the external quantum efficiency (EQE), the current efficiency in cd A^{-1} (η_L), or the luminous efficiency (η_P) in lmW^{-1}. Quantum efficiency covers two parameters: *internal quantum efficiency* (IQE) and *external quantum efficiency* (EQE). EQE is the ratio between the numbers of the emitted photons from the surface of the device and the number of the injected charges:

$$EQE = \eta_{out} \cdot PLQY \cdot \gamma \cdot \eta_{fr}$$

where η_{out} – optical out-coupling efficiency, defined to be 20%[14]; $PLQY$ – luminescence quantum yield; γ – charge balance factor (assumed to be 1); η_{fr} – singlet ratio (considered to be 0.25 for fluorescent molecules due to the singlet- and triplet-yielding in 3:1 fractions). A lot of effort has been made to increase the total EQE value of the devices, such as the usage of heavy metal complexes and emitters possessing delayed fluorescence as emitting dopants.

2.2. Materials for optoelectronic devices: small molecules *versus* polymers

Devices can be fabricated from two types of materials: low molecular weight compounds, and high molecular weight polymers and dendrimers. Materials for optoelectronic application, small molecules and polymers should meet the following requirements: high solid state PLQY, good carrier mobility (holes and electrons), good thermal and oxidative stability, and high color purity (adequate CIE coordinates). The layers composed of small molecules or polymeric compounds have their advantages and disadvantages when compared to each other. The main merits of small molecules over high molecular weight materials are the easier synthesis and purification process as well as the capability of vacuum-processing, which enables easier fabrication of multilayer systems with higher purity (Table 2.1). Devices fabricated by vacuum deposition methods based on small molecules allow achieving significantly higher performances in terms of lifetime and efficiency than the solution-processed ones. Nevertheless, the vacuum deposition method is rather expensive and can be applied exclusively for the fabrication of smaller devices. Meanwhile, polymeric compounds are suitable for the large-area solution processable devices. Due to poor solid state morphology and, usually, fast crystallization upon spin-coating, small molecules are rarely suitable for the solution processable devices[10, 11]. Meanwhile, high molecular weight compounds are light-weight and flexible materials with supreme morphological stability. Therefore, polymers are easily soluble, so they can be adapted for solution-processing techniques such as spin-coating or inkjet printing, etc. at room temperature. Currently, the efficiency of solution processable devices is gradually rising and reaching the values similar to the vacuum deposited small molecules. Thus polymers are preferable for the manufacturing at low cost as well as large-area employment, while vacuum deposited small molecules are widely used in many mobile devices and TVs.

Table 2.1. Summarized advantages of low- and high- molecular weight materials.

Small molecules	***Polymers***
Easier synthesis	Improved solid state morphology
Higher purity	Solution processable
Possibility of vacuum deposition	Suitable for large-area devices
Better device performance	Less expensive

2.3. Delayed fluorescence mechanisms as a tool for efficiency enhancement

In pursuit of new, cheap and effective organic molecules for optoelectronic devices, several concepts have been applied to harvest 75% of ‘dark’ triplet excitons, such as phosphorescence, triplet-triplet annihilation (TTA), hybridized local charge transfer mechanism (HLCT), and thermally activated delayed fluorescence (TADF).

Phosphorescent OLEDs based on organic metal complexes can reach the internal quantum efficiency of 100% by harvesting both 25% of singlet and 75% of triplet excitons. It is well known that, in comparison to fluorescent compounds, triplet emitters are characterized with enhanced intersystem crossing (ISC) from S_1 to T_1 and next transition through the phosphorescent channel to the ground state S_0 (Fig. 2.2 (a)). Normally, efficient ISC can be achieved due to the spin-orbit coupling process caused by heavy metal atoms in metal complexes[12]. Nowadays, the EQE of devices utilizing triplet emitters exceeds 30%[13]. Nevertheless, noble metals which are used in organic metal complexes, such as iridium and platinum, are high-cost, rare and limited metals. Moreover, the efficiency and lifetime of particularly blue phosphorescent emitters is inefficient for commercial application.

A promising approach towards harvesting triplet excitons in organic molecules is the fusion of excited triplet states well-known as triplet-triplet annihilation (TTA)[14].

Firstly observed in the pyrene molecule[15], P-type delayed fluorescence appears via the interaction of two excited triplet states with the generation of one excited high-energy singlet state (Fig. 2.2 (b). The next transition of the formed excited singlet state to the ground state gives rise to delayed fluorescence with a long luminescence lifetime. Triplet fusion enables to increase the device efficiency, however, the successful realization of the TTA mechanism in organic molecules requires accurate alignment of the energies of the singlet and triplet excited states. In the best way of the proper arrangement of excited state energies, the possible maximum IQE that can be reached is 62.5%. The utilization of the triplet fusion mechanism in organic semiconductors allows to achieve low excitation power, delayed fluorescence, and deep-blue electroluminescence. Nevertheless, to achieve an efficient TTA process, concentrated triplet excitons in a device are essential, which leads to inevitable device efficiency roll-off.

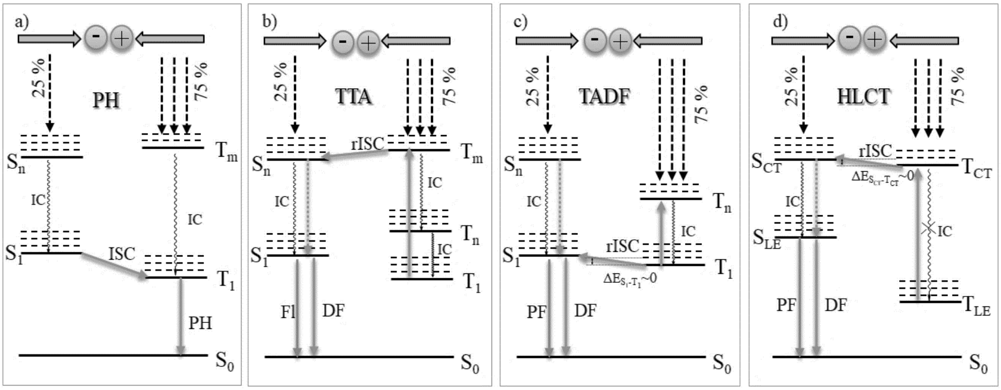

Fig. 2.2. Schematic representation of mechanisms of triplet harvesting (PH-phosphorescence, TTA-triplet-triplet annihilation, TADF-thermally activated delayed fluorescence, HLCT-hybridized local and charge transfer mechanism) (adapted from literature [7])

Another attempt to utilize triplet emission is based on the harvesting of the so-called hot excitons which are located higher than the excited S_1 and T_1 energy levels. In this way, the rISC process is occurring between the upper $T_n \rightarrow S_n$ levels of the charge-transfer character with the next transition to the lower energy singlet state (S_1) of the local character from where the emission occurs (Fig. 2.2 (c)). Ideally, hot exciton rISC process realizes the 75% of triplets and has a potential to achieve 100% IQE. The difficulty with the hot exciton mechanism is that the internal conversion process from hot excitons to the T_1 state is very efficient and can hardly be blocked. Thus the ideal HLCT material should exhibit close-lying LE and CT states and negligible internal conversion to the S_1 and T_1 states.

In contrast to the above mentioned mechanisms, the TADF technique, or E-type delayed fluorescence, was found to be the most effective approach towards harvesting both singlet and triplet excitons. TADF was first observed in early 1961 by Parker and Hatchar[16] in the molecule of eosin which could emit delayed fluorescence in ethanol at 70 °C (Fig. 2.2 (c)). This approach enables the achievement of 100% IQE via endothermic up-conversion of triplet excitons to S_1 via the rISC process with thermal energy. The small singlet-triplet energy splitting ($\Delta E_{S\text{-}T}$) between S_1 and T_1 is essential to ensure rISC and thus the efficient TADF process. rISC is a temperature-dependent endothermic process which is facilitated in high temperatures (> 100 K) and commonly suppressed in low temperatures (< 100 K). The rISC constant is closely related to the energy splitting ($\Delta E_{S\text{-}T}$) and temperature (T)

$$k_{RISC} \propto exp\left(\frac{\Delta E_{S-T}}{k_B T}\right) \tag{1}$$

where k_B is the Boltzmann constant.

The energy of the lowest singlet and triplet excited states can be explained by the relation of orbital energy (E), electron repulsion energy (K), and exchange energy (J) of two unpaired electrons at the excited state (Equations 2, 3).

$$E_S = E + K + J \tag{2}$$

$$E_T = E + K - J \tag{3}$$

$$\Delta E_{S-T} = E_S - E_T = 2J \tag{4}$$

Due to the same singlet and triplet electron arrangements in the molecule, *E, K* and *J* at the two excited states are equal with each other. Nevertheless, due to the same triplet spin states of the unpaired electrons, E_T is reduced (Equation 3). Thus, the $\Delta E_{S\text{-}T}$ value is defined as approximately the double value of exchange energy J. The approach to decrease the J value is the effective separation between the highest occupied molecular orbital (HOMO) and the lowest unoccupied molecular orbital (LUMO). From the molecular aspects, a negligible $\Delta E_{S\text{-}T}$ value can be realized by the accurate molecular design of materials with a twisted structure and a small HOMO-LUMO overlap. Therefore, the introduction of fragments causing a large steric hindrance/twisted or a spiro donor-acceptor (D-A) system can reduce the HOMO-LUMO overlap as well. The D-A type systems can be realized via the intra- or intermolecular charge transfer where electron-donor and electron-acceptor are covalently linked or are two separate molecules, respectively.

2.3.1. Design principles of thermally activated delayed fluorescence donor-acceptor materials.

Efficient TADF intramolecular D-A molecules require a careful combination of donor and acceptor moieties. Therefore, the modulation of the HOMO-LUMO gap of compounds is an essential factor for achieving the desirable emission color. Thus, for a blue TADF emitter, the combination of a weaker donor and a stronger acceptor is preferable. Nitrogen-containing donors, such as carbazole, diphenylamine, acridan, and their derivatives, are widely used for the design of blue emitters (Fig. 2.3). Meanwhile, phenoxazine, phenothiazine and dihydrophenazine donors are used for green and orange emitting materials.

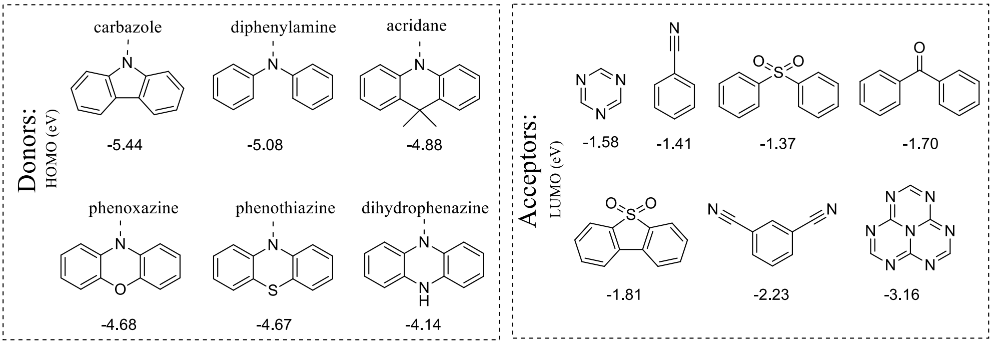

Fig. 2.3. Chemical structures of widely used donor and acceptor fragments along with the corresponding HOMO and LUMO energies

So far, several design strategies have been applied to reduce the ΔE_{S-T} value to enable an efficient TADF process, which include:

1) Introduction of twisting conformations [17];
2) Steric hindrance and physical separation between the donor and the acceptor unit [18];
3) Introduction of fragments with multiple resonance effects [19].

2.3.2. Nitrile-based TADF emitters

A benzonitrile fragment has been widely used as the acceptor unit due to its strong electron-withdrawing ability. In early 2012, Adachi *et al.*[17] reported a series of dicyanobenzene-based TADF emitters with multiple carbazole donors (Fig. 2.4). Synthesized compounds were found to be an excellent example of the introduction of steric hindrance resulting in sufficient separation between the molecular orbitals (HOMO-LUMO). The HOMO-LUMO separation was ensured by the twist of carbazole units in respect to the benzonitrile plane. It was shown that cyano-groups suppress both non-radiative deactivation and geometry changes at the excited states of those materials, which results in the enhancement of PL efficiencies. The series of compounds presented by the authors exhibited a wide range of emission colors of toluene solutions and high PLQY values ranging from sky blue for 2CzPN (473 nm, 47% PLQY) to orange for 4CzTPN-Ph (577 nm, 26% PLQY), which depends on the number and the position of carbazole units attached to dicyanobenzene. The authors achieved the EQE value of up to 19% and utilized 4CzIPN as an emitting material doped in the CBP host. The highest EQE values for 4CzIPN among the series can be attributed to its negligible ΔE_{S-T} of 0.08 eV and a high PLQY of 94%. Nevertheless, blue and orange OLED devices reached comparable maximum EQE values of 8% and 11%. In this fashion, Kim *et al.* in 2014 reached the maximum EQE of 29% for a green device with 4CzIPN as the emitter by the optimization of the host system[20]. The authors mixed hole-transport 1,3-bis(N -carbazolyl)benzene (mCP) and electron-transport type 3,3″,5,5″-tetra(pyridine-3-yl)-1,1′:3′1″-terphenyl (BmPyPb) host materials, which ensured the deep HOMO, high singlet energy, and thus the efficient energy transfer along with reduced exciton quenching. The main disadvantage of mixed host systems is the possible exciplex formation between the hole- and electron-type host materials. Later the following year, Lee *et al.* reported an optimized device structure using a new single molecule bipolar host material 3-(3-(carbazole-9-yl)phenyl) pyrido[3′,2′:4,5]furo[2,3-b]pyridine (3CzPFP)[21] by doping 1% of the 4CzIPN emitter. The main achievement of using the bipolar 3CzPFP host was a high maximum EQE of 31%. Comparing the device performance with the one previously reported by Adachi *et al.*[17], the authors used the same 4CzIPN dopant but 3CzPFP as the host material. This allowed to enhance the quantum efficiency with the reduced doping concentration from 5% to 1%. Such an investigation displayed that, despite highly efficient TADF materials, the proper choice of the host materials for TADF devices is essential. Nevertheless, the small singlet-triplet energy splitting of the dicyanobenzene type compounds was achieved by the incorporation of a strong acceptor with the lower lying singlet state. These points make it difficult to design particularly blue TADF emitters with the phthalonitrile fragment.

In this manner, in 2016, Cho *et al.* reported a similar family of benzonitrile compounds with multiple carbazole substituents[22]. 5CzBN emitter bearing only one cyano-group with lower electron-withdrawing ability in respect to above-mentioned 4CzIPN showed bluer fluorescence (464 nm, 70% PLQY) as well as a moderate ΔE_{S-T} value of 0.22 eV (Fig. 2.4).

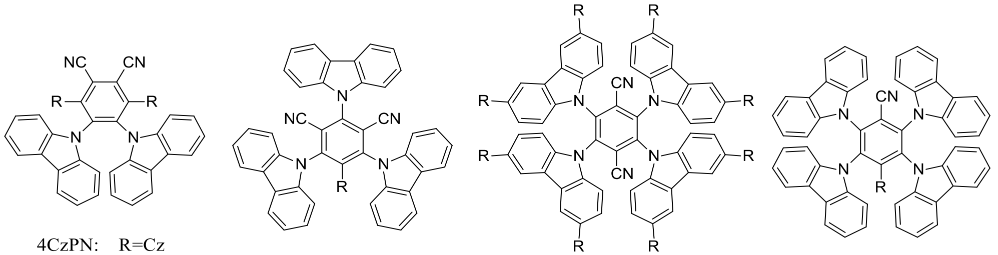

4CzPN: R=Cz
2CzPN: R=H

4CzIPN: R=Cz

4CzTPN: R=H
4CzTPN-Me: R=Me
4CzTPN-Ph: R=Ph

5CzBN: R=Cz
4CzBN: R=H

Fig. 2.4. Cyano-containing TADF materials

Interestingly, the authors fabricated devices by employing both vacuum evaporation and solution coating techniques while using a doped 5CzBN emitter and achieved a maximum EQE of 19.7% (80% lifetime of 100 h at 500 cd m^{-2}) and a high EQE of 18.7%, respectively. Therefore, its counterpart with fewer carbazole units 4CzBN exhibited deep blue (442 nm)[23] TADF emission and a PLQY of 49%, which is related to the slightly higher ΔE_{S-T} of 0.30 eV.

2.3.3. Triazine-based TADF emitters

Nitrogen-containing six-membered heterocycles, such as pyridine[24], pyrimidine[25, 26] and triazine[27, 28], also found wide application in the design of TADF emitters due to the high stability and electron-deficient nature. 1, 3, 5-triazine or s-triazine is the most popular among the class of triazines used for the construction of TADF emitters[29, 30].

In the pursuit of new and effective TADF emitters, a lot of approaches have been carried out to decrease the singlet-triplet differences while maintaining high PLQY values of the emitters. Thus, Adachi *et al.*[31] revealed the strategy, according to which, large delocalization of HOMO and LUMO in the compounds with the charge-transfer nature can significantly enhance the rate of radiative decay by inducing large oscillator strength while lowering the $\Delta E_{S\text{-}T}$ value. The authors reported compounds comprised of the triazine core as the electron-accepting part and indolocarbazole (1CzT) and carbazole (2CzT) as the electron-donating units (Fig. 2.5). Compounds 1CzT and 2CzT possessing similar $\Delta E_{S\text{-}T}$ estimated for toluene solutions of ca. 0.10 eV.

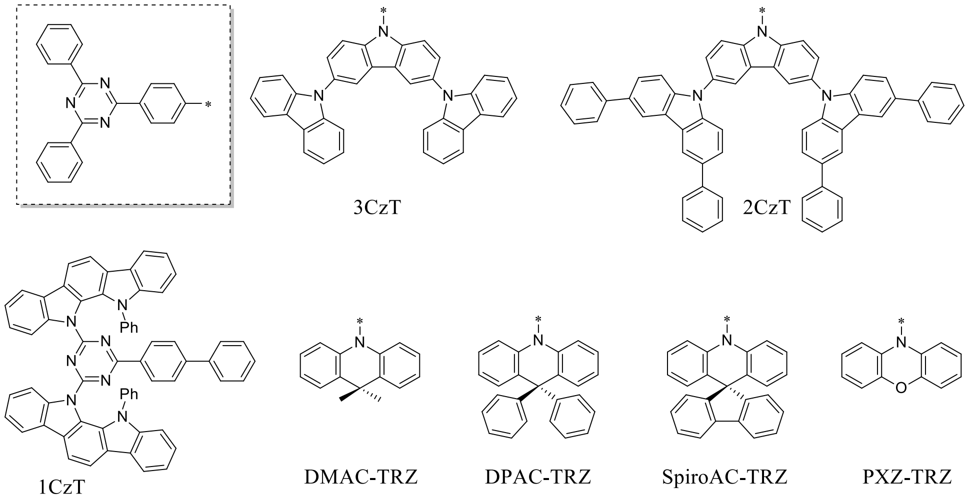

Fig. 2.5. Triazine-based TADF compounds

Nevertheless, 1CzT and 2CzT highly differ in PL efficiencies with the PLQY values of 10% and 74%, respectively. The authors explain the difference by the different degree of delocalization of HOMO confirmed by theoretical DFT calculations[31]. Interestingly, compound 3CzT with considerably higher singlet triplet energy splitting of 0.28 eV, in respect to 1CzT and 2CzT, still possessed high PL efficiency of 57%, which was also attributed to the high HOMO delocalization all over the tricarbazolyl fragment. Consequently, green (1CzT) and blue (2CzT and 3CzT) OLEDs devices based on (6 wt %) of 1CzT, 2CzT and 3CzT as guests doped in DPEPO host exhibited EQE of 7.7%, 21% and 17% at 10^{-2} mA cm^{-2}, respectively.

Based on the trends regarding the TADF compounds, a lot of explanations and strategies have been developed to increase the PLQY and facilitate the ISC process. In this manner, Dias *et al.* suggested a strategy for DF enhancement[32]. The authors showed that the DF efficiency can be enhanced by lone-pair orbitals on heteroatoms, such as nitrogen and sulfur[32]. The authors proved that the $^3n\pi^*$ triplet state has a fundamental role within the photophysics of delayed emission that can mediate the ISC process.

A lot of scientific groups studied the influence of *ortho-*, *meta- and para-*substitutions of the donor and the acceptor. It was shown that *ortho-* and *meta-*orientation is preferable for the efficient TADF process[33, 34].

Considerable attention has been paid to the influence and improvement of different donors for the efficient TADF process. Thus, in 2012, Adachi *et al.*[35] reported a new TADF emitter PXT-TRZ which exhibited green fluorescence with its emission maxima located at 560 nm and 540 nm for the neat film and doped in 4,4'-bis(N-carbazolyl)-1,1'- biphenyl (CBP) host film, respectively (Table 2.2). Compound PXT-TRZ possessed high PLQY values of 66% and 43% of neat and doped in CBP film. The efficiency of the fabricated device based on 6% of PXT-TRZ emitter doped in CBP host reached the value of 12%[35].

Table 2.2. Characteristics of discussed triazine-based TADF emitters

Compound	$\lambda_{PL,\ film}$ *nm*	$\lambda_{PL,\ doped}$ *nm*	*PLQY* $_{doped}$, *%*	$\Delta E_{S\text{-}T}$, *meV*	τ_1 *ns*	τ_2 *µs*	λ_{EL} *nm*	EQE_{max} [c], *%*
1CzT	466	492 [a]	10	100	12	120	506	7.7
2CzT	457	480 [a]	74	90	6.3	-	487	21
3CzT	458	475 [a]	57	280	6.0	-	478	17
PXZ-TRZ	560	540 [b]	66	19	20	1.1	529	12
DMAC-TRZ	500	495 [b]	90 [b]	62 [b]	20	1.9	495	20 [d]/27 [b]
DPAC-TRZ	478	478 [b]	82 [b]	133 [b]	15	2.9	490	26 [b]
SpiroAC-TRZ	480	480 [b]	100 [b]	72 [b]	17	2.1	495	37 [b]

[a] 6 wt % (emitter) in DPEPO host; [b] 12 wt % (emitter) in mCPCN; [c] maximum EQE at 100 cd m^{-2} [d] non-doped device

Alternatively, in 2015, Wu and co-workers[36] obtained a blue TADF emitter by modification of PXT-TRZ with weaker electron-donating 9,9-dimethyl-9, 10-dihydroacridine (DMAC) (Fig. 2.5). Synthesized DMAC-TRZ exhibited higher thermal stability and a higher glass transition temperature of 91 °C in respect to PXT-TRZ. Surprisingly, compared with PXT-TRZ, DMAC-TRZ showed a high PLQY value of 90% and 83% of both neat and doped in high triplet-energy bipolar host 9-(3-(9 H-carbazol-9-yl)phenyl)-9 H -carbazole-3-carbonitrile (mCPCN) films. The authors explained the high PLQY of the solid film of DMAC-TRZ by the presence of methyl groups on the steric sp^3 carbon of the DMAC unit which suppressed the concentration quenching and led to a high PLQY in the neat film. Hence, this encouraged the authors to fabricate both a doped and a non-doped device based on a DMAC-TRZ emitter which exhibited an EQE of 27% and 20%. Motivated by these results, the following year, the same group of Wu *et al.*[37] synthesized an acridine-based new compound DPAC-TRZ and SpiroAC-TRZ, where the methyl groups on the carbon atom (9-position) of the acridane moiety were replaced with bulky and rigid phenyl and 2,2′-biphenyl (spirobiphenyl) groups, respectively (Fig. 2.5). Noticeably, both DPAC-TRZ and SpiroAC-TRZ displayed blue-shifted emission of the solid films (478 nm, 480 nm) if compared to their counterpart DMAC-TRZ (495 nm). The authors claimed the occurrence of the bathochromic shift in fluorescence spectra by the stronger electron-accepting capability of the aryl substitution, which could inductively reduce the electron-donating nature of the acridine donor. Nevertheless, all the three compounds displayed the TADF nature with negligible

$\Delta E_{S\text{-}T}$ of 0.072, 0.133 and 0.062 eV for DMAC-TRZ, DPAC-TRZ, and SpiroAC-TRZ, respectively. Therefore, the PLQY values of 6% of the emitters (DMAC-TRZ, DPAC-TRZ, and SpiroAC-TRZ) doped in a mCPCN host were found to be 90%, 82% and 100%, which appears to correlate with the conformation/bending angles of the acridine moiety[37]. The highest PLQY of spiro- spirobiphenyl-substituted compounds was explained by the presence of a rigid spiroacridine donor which, presumably, restricts torsional/vibrational freedom. The series of OLEDs were fabricated by using 12% of the discussed compounds as emitting layers doped in an mCPCN host. Consequently, the best device based on the SpiroAC-TRZ compound displayed sky blue electroluminescence and an EQE of 36.7% (94 cd A^{-1}, 98.4 lm W^{-1})[37].

To conclude, the requirements for TADF emitters for organic devices are as follows:

1) Negligible $\Delta E_{S\text{-}T}$ value for efficient rISC process from T_1 to S_1 level;
2) Decoupled HOMO and LUMO;
3) Strong charge transfer nature of the excited state;
4) High solid state photoluminescence efficiency;
5) Molecular rigidity and twisted conformation;
6) Thermal and electrochemical stability.

2.4. Bimolecular donor:acceptor systems for the construction of efficient OLEDs

2.4.1. Exciplex formation

Upon electrical excitation, several types of excited states can be formed: intramolecular excited states, or bimolecular species (excimers, exciplexes, electromers and electroplexes)[38]. The resonance interactions between the molecular exciton and the neighboring neutral molecules comprised of identical molecular species can cause the formation of bimolecular excited state (M) which is termed *excimer* (excited state dimer). For the excimer, the excited and non-excited species are identical. Still, when the two species are different, the bimolecular excited state is called the *bimolecular excited complex*, or *exciplex*, and, in turn, the species are called the *donor* and the *acceptor* (Fig. 2.6). Exciplex formation is facilitated by the presence of an electron donor (D) and an electron acceptor (A) in the blend with well-defined HOMO and LUMO levels. During the exciplex formation, partial charge-transfer from the donor (D) molecule to the acceptor (A) molecule occurs. The formation of the bimolecular excited complex is facilitated in the excited state, while being extinguished in the ground state. Therefore, exciplexes can form in mixed blends of D and A molecules (bulk exciplex) as well as on the interface of two thin layers (interfacial exciplex) of the electronic devices.

An exciplex system can be formed between two molecules when the electron transfer is allowed with well-defined ionization potentials and electron affinities of D and A molecules. An important requirement for exciplex formation is that the acceptor should possess a higher electron affinity and ionization potential value than the electron-donating molecule ($EA_{acceptor} > EA_{donor}$, $IP_{acceptor} > IP_{donor}$)[42].

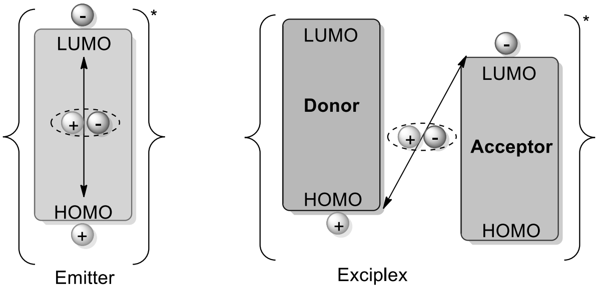

Fig. 2.6. Schematic representation of excitons formation in intramolecular and intermolecular donor-acceptor systems (adapted from literature [42])

Under excitation of the mixed blends, the D or A molecule gets excited and yields the excited species nominated as D* and A* (Fig. 2.7)[39]. Consequently, the molecule undergoes complex formation with an A or D molecule in the ground state through Columbic interaction forces (D*+A, D+A*). The following electron transfer from D to A occurs and results in the formation of intermolecular charge transfer excited state $(D^+A^-)^*$ (Fig. 2.7).

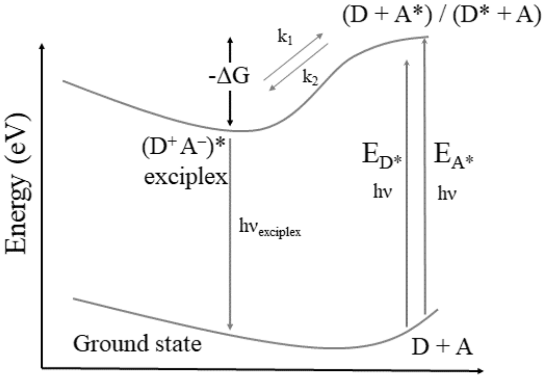

Fig. 2.7. Overall energy diagram of the formation of the exciplex system (adapted from the literature [42])

The energy of the exciplex ($E_{exciplex}$) blend is related to the properties of electron-donating and electron-accepting constituting molecules[40, 42]. Empirically, $E_{exciplex}$ is linearly correlated with the ionization potential (IP_{donor}) of the donor and the electron affinity of the acceptor ($EA_{acceptor}$):

$$E_{exciplex} = IP_{donor} - EA_{acceptor} + K \tag{1}$$

$$E_{exciplex} = E_{ox,donor} - E_{red,acceptor} + K \tag{2}$$

IP_{donor} and $EA_{acceptor}$ values, which correlate with the oxidation potential and electron affinity, can be estimated by electrochemical tools and can be replaced as the oxidation potential of the donor and the reduction potential of the acceptor (Equation 2). Meanwhile, K is defined as the Coulomb attraction energy at the equilibrium distance. Usually, Coulomb constant K for the solid or non-polar samples is minimal and can be ignored.

For the prediction of the formation of a long-lived exciplex, the driving force, or Gibbs energy ($-\Delta G$), is an important parameter which can be defined from the modified Rehm-Weller equation:

$$-\Delta G = E_{exciton} - E_{exciplex} \tag{3}$$

$$-\Delta G = E_{exciton} - (E_{ox,donor} - E_{red,acceptor} + K) \tag{4}$$

where $E_{exciton}$ is the exciton energy of the donor or the acceptor that can be determined as the difference between IP_{donor} and EA_{donor} or $IP_{acceptor}$ and $EA_{acceptor}$. It was found that the preferred for the exciplex formation $-\Delta G$ value should usually exceed the value of 0.45 eV[40].

2.4.2. Requirements for exciplex-forming donor and acceptor materials

Not a long time ago, exciplex formation was considered to be a destructive process for OLEDs performance which decreased device efficiency and damaged the color purity[41]. Nevertheless, along with TADF molecules, exciplex systems found wide application as effective emitters in the field of OLEDs. Nowadays, exciplex systems are being widely utilized as TADF emitters[49], hosts for fluorescent, phosphorescent, and TADF dopants[42]. In respect to small D-A molecules, exciplex systems afford easier screening of donor and acceptor moieties. Thus photophysical properties can be modified by simple adjustment of the donor or acceptor molecules with preferable HOMO or LUMO energies, respectively. Moreover, electrons and holes are distributed on two separate donor and acceptor molecules, respectively. This results in a small spatial HOMO-LUMO overlap and thus in small exchange energy. The proper choice of suitable donor and acceptor molecules is a vital factor to achieve efficient exciplex based devices which rely on the following criteria:

1) High hole-transporting properties of the electron-donor molecule and the high electron mobilities of the acceptor;
2) Appreciable difference between the donor's HOMO level and the LUMO of the acceptor molecule;
3) High triplet energies of the constituting donor and acceptor molecules in respect to the triplet level of the D:A exciplex for efficient exciton confinement;
4) A sufficient amount of charge carriers for the accumulation at the exciplex interface.

Most of the known accepting molecules for exciplex systems consist of oxadiazole, arylboron, triazine, N-heterocycles, and diphenylphosphine oxides fragments.

2.4.3. Exciplex systems as emitting layers of OLEDs

The extensive use of exciplex systems as efficient emitting systems started with the innovative work of Adachi *et al.* in 2012[43]. This team demonstrated the approach of realizing exciplex emission to enhance device efficiency through the rISC process.

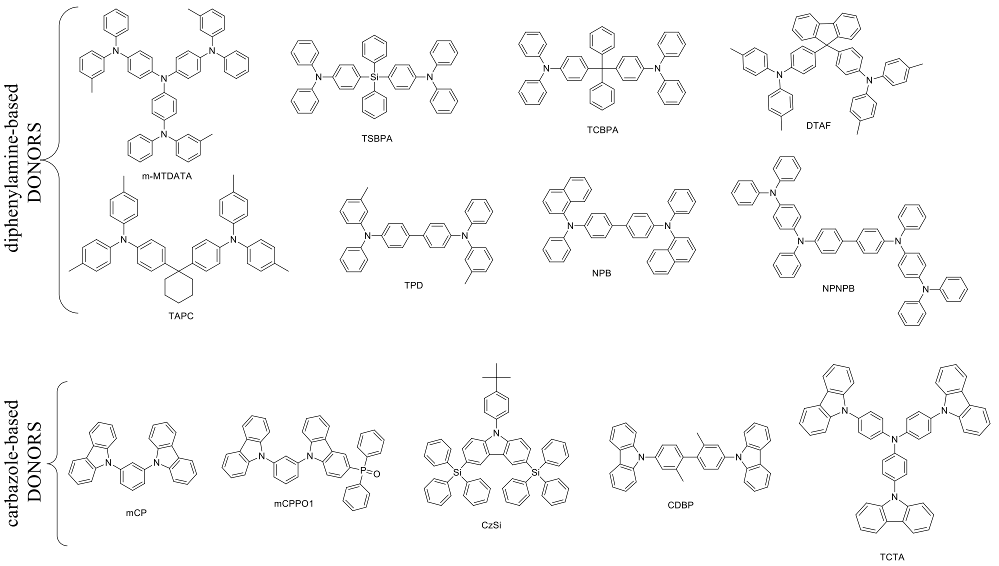

Fig. 2.8. Chemical structure of electron-donors

By comparing different exciplex blends, such as 4,4′,4″-tris[3-methylphenyl(phenyl)amino]triphenylamine and 2-(biphenyl-4-yl)-5-(4-*tert*-butylphenyl)-1,3,4-oxadiazole (m-MTDATA: *t*-Bu-PBD), and m-MTDATA: tris-[3-(3-pyridyl)mesityl]borane (3TPYMB), the authors demonstrated that the PLQY of exciplex systems highly affect the efficiency of the devices. m-MTDATA:*t*-Bu-PBD blend showed a PLQY of 20%, while m-MTDATA: 3TPYMB showed a value of 26%. The structures of exciplex forming electron-donating and electron-withdrawing materials are depicted in Fig. 2.8 and Fig. 2.10**.** However, the m-MTDATA: 3TPYMB system displayed a remarkably higher delayed component of the blend film than that of the m-MTDATA: *t*-Bu-PBD blend. The authors achieved the remarkable for that time EQE of 5.4% for an exciplex system and overcame the fluorescent limit of EQE of 5% by implementing an efficient rISC process.

A significant contribution to the investigation of exciplex systems was done by the group of Prof. A. Monkman. In 2014 and 2016, the authors presented an interesting strategy for designing and explaining the underlying mechanism of the TADF process in small molecules and exciplex blends[44, 45]. Moreover, the design strategy suggested by the authors could lead to a reduction in time and cost of the synthesis of emitting systems and the fabrication of efficient OLEDs. The authors presented and studied three D:A blends (*m*-MTDATA:TPBi, TPD:TPBi, and TPD:OXD-7). It was shown that the efficient rISC process, and thus the TADF mechanism, dominates for systems with an energetically close excited singlet charge transfer state (^{1}CT) and locally excited triplet states (^{3}LE) of the donor or the acceptor to diminish the thermal activation barrier, while TTA was observed for a system with a larger exchange energy ($E_{S\text{-}T}$) between ^{1}CT and ^{3}LE (Fig. 2.9). Therefore, the authors presented systems with mixed TADF and TTA processes. In this manner, by analysis of the ^{3}LE and ^{1}CT excited states, it was revealed that the *m*-MTDATA:TPBi exciplex showed negligible energy splitting between ^{1}CT and ^{3}LE of the donor and the acceptor molecules of $\Delta E_{1CT - 3LE(m\text{-MTDATA})} = (–0.01 \pm 0.03)$ eV and $\Delta E_{1CT - 3LE(TPBI)} = (–0.02 \pm 0.03)$ eV, which is preferable for the TADF process ①, ② (Fig. 2.9). Meanwhile, the TPD:TPBi blend displays the values of $\Delta E_{1CT - 3LE(TPD)} = (0.61 \pm 0.03)$ eV and $\Delta E_{1CT - 3LE(TPBI)} = (0.39 \pm 0.03)$ eV where the triplets are too far from the ^{1}CT state for up-conversion and thus TTA dominates ③, ④ (Fig. 2.9).

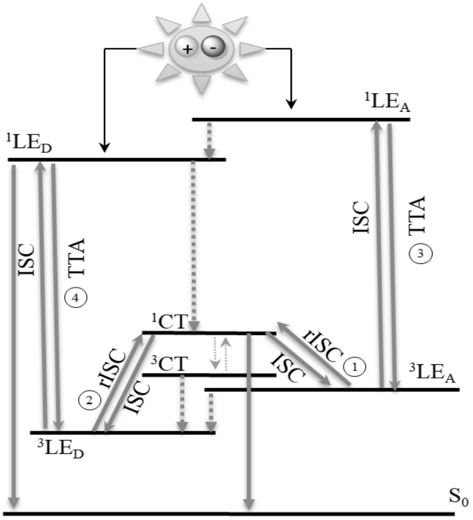

Fig. 2.9. Schematic energy diagram displaying decay pathways for the investigated exciplex blends (adapted from the literature[45])

The third TPD:OXD-7 system shows $\Delta E_{1CT - 3LE(TPD)} = (0.51 \pm 0.03)$ eV and $\Delta E_{1CT - 3LE(OXD\text{-}7)} = (0.23 \pm 0.03)$ eV, which is assigned to the mixed TTA and TADF processes of delayed fluorescence and shown as process ①, ④ on the energy diagram (Fig. 2.9). All the statements were supported with the measurements of the integrated area as a function of the laser excitation dose collected in the delayed region, which confirmed TADF, TTA, or the mixed nature of delayed fluorescence[45].

Judicious selection of electron-donating and electron-accepting materials allows achieving remarkable efficiency with the desired electroluminescence. Significant results have been achieved in the development of efficient blue, green, yellow, and orange exciplex-based OLEDs. Significant efforts have been made for the development of electron-deficient molecules with the desired HOMO-LUMO level and high charge mobilities. Thus the highly electron-accepting triazine core has been widely used and modified to develop new electron-transporting materials (ETL).

In 2013, Wong *et al.*[46] developed an efficient yellow (544 nm) exciplex system from the interface of a bilayer device based on the C_3-symetrical hole-transporting TCTA as the donor and electron-transporting 3P-T2T compounds as the acceptor part. The EQE of 7.7% with CE and PE of 22.5 Cd A^{-1} and 23.6 lm W^{-1}, respectively, with the electroluminescence peak at 544 nm, and CIE coordinates of 0.40, 0.55 was achieved for the bilayer-type exciplex OLED while employing TCTA:3P-T2T as the emitting system. According to the authors, one of the reasons of the high efficiency of the exciplex-based device is the higher triplet state energy of TCTA and 3P-T2T of ca. 2.85 eV, which endowed the efficient shuttle back of triplet excitons to emissive S_1. Not less reasonable is the high and balanced charge mobilities of TCTA and 3P-T2T as well as the large band-edge offsets (ca. 0.8 eV) at the TCTA/3P-T2T interface, which afforded holes and electrons to pass the TCTA and 3P-T2T layer and accumulate at the D-A interface[46].

The following year, the same group of Wong *et al.* presented the bilayer interface approach where two exciplexes, blue and orange, were combined for achieving white light electroluminescence[47]. The authors designed a new electron-accepting material with the electron-transporting features 2,4,6-Tris[3-(diphenylphosphinyl)phenyl]-1,3,5-triazine (PO-T2T) comprised of the triazine core with a higher LUMO energy of -2.83 eV than the above mentioned 3P-T2T compound with a LUMO energy of -2.98 eV (Fig. 2.10). With the aim of reducing the LUMO energy but still retaining the high triplet energy, three diphenylphosphine oxide fragments as the electron-withdrawing groups were introduced into the *meta*-positions of phenyl rings connected to the triazine manifold. The synthesized material was characterized by excellent thermal stability (T_d = 460 °C). The electron-transporting PO-T2T material showed weak violet emission of DCM solution peaking at 405 nm. PO-T2T exhibited a high energy of triplet levels (2.99 eV) and a HOMO of 6.83 eV as well as a low-lying LUMO of 2.83 eV preferable for electron-transporting and electron-accepting materials. The proper selection of donors with different HOMO levels allowed the authors to achieve efficient exciplex emissions from blue to red. The blue device based on the PO-T2T:1,3- bis(N-carbazolyl)benzene (mCP) exciplex system showed the maximum brightness of 24600 cd m^{-2} at 1040 mA cm^{-2} (11 V) with the CIE coordinates of (0.17, 0.23). The EQE, the current (CE) and power efficiencies (PE) of the blue device were found to be 8.0%, 15.5 cd A^{-1}, and 18.4 lm W^{-1}, respectively. The green electroluminescence was realized by a combination of PO-T2T and tri(N-carbazolyl)triphenylamine (TCTA), yellow – with 9,9-di[4-(di-*p*-tolyl)aminophenyl]fluorine (DTAF), orange – with 1,1-bis[(di-4-tolylamino)phenyl]cyclohexane (TAPC), and red – with *N*,*N* 9-diphenyl-*N*,*N* 9-di-[4-(*N*,*N* diphenyl-amino)phenyl]benzidine (NPNPB)[47]. In the paper[47], the authors for the first time demonstrated the strategy for fabrication of a tandem, TADF, all-exciplex-based white light organic light-emitting diode (WOLED) showing superb performance with the configuration of ITO/PEDOT:PSS (30 nm)/TAPC (20 nm)/mCP (15 nm)/ mCP:PO-T2T (1:1, 20 nm)/PO-T2T (45 nm)/Liq (1 nm)/Al (1 nm)/ MoO_3 (5 nm)/DTAF (20 nm)/DTAF:PO-T2T (1:1, 20 nm)/PO-T2T (50 nm)/Liq (0.5 nm)/Al (100 nm). The electroluminescence of the white device is the combination of blue (mCP:PO-T2T) and yellow (DTAF:PO-T2T) exciplex emission spectra which cover almost all the visible spectra. The fabricated WOLED demonstrated a turn-on voltage of 4.0 V, an L_{max} of 50300 cd m^2 at 24 V, and a maximum EQE of 11.6%. Inspired by these results, in 2015, Lee *et al.* reported the investigation of a blue exciplex system of the above mentioned PO-T2T acceptor in the CDBP:PO-T2T system with the PL peak of the exciplex emission at 476 nm[48].

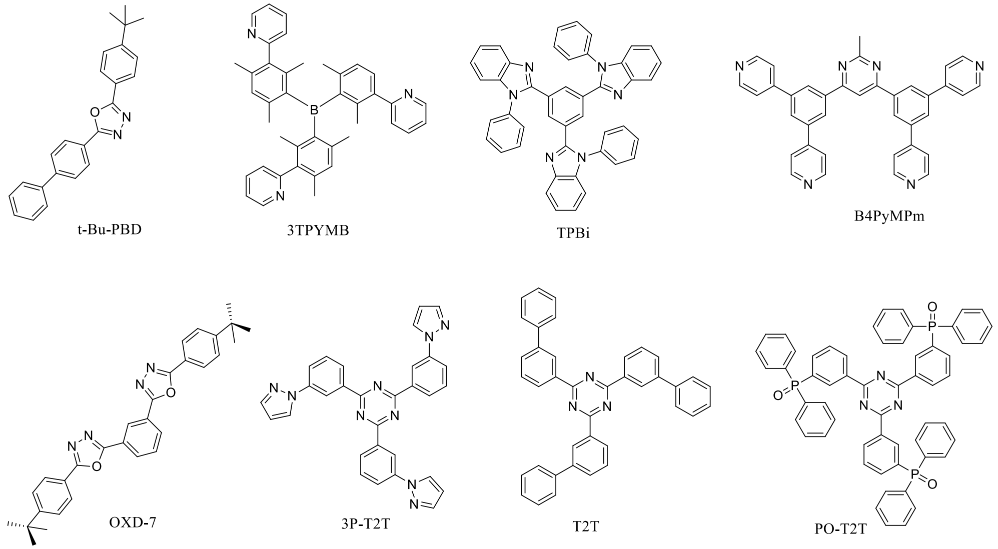
t-Bu-PBD
3TPYMB
TPBi
B4PyMPm
OXD-7
3P-T2T
T2T
PO-T2T

Fig. 2.10. Chemical structure of electron-acceptors

Interestingly, blue, green, red and white exciplex-based OLEDs were constructed based on the CDBP:PO-T2T system. Comprehensive analysis of the results published at the paper and the results previously obtained for similar devices was conducted[48]. The authors presented a blue device where the CDBP:PO-T2T system was used as the emitting layer, then, 4,4′-Cyclohexylidenebis[N , N -bis(4-methylphenyl)-aniline] (TAPC) and PO-T2T were used as the hole- and electron-transporting layer, respectively. The utilization of TAPC and PO-T2T which possess high hole- (TAPC) and electron- (PO-T2T) mobilities allowed the authors to fabricate a device with a ‘barrier-free’ architecture. Blue OLED showed a low turn-on voltage of 2.5 V, maximum efficiencies of 26.6 cd A^{-1} for CE, 27.8 lm W^{-1} for PE, and an EQE of 13.0%. The authors successfully employed the CDBP:PO-T2T exciplex system as the host for green and red iridium complexes[48]. Both green and red devices were characterized with low turn-on voltages and an EQE of 28.6% and 28.0%, respectively. Significant attention was paid to the fabrication of a single-EML hybrid white organic light emitting diode based on a combination of green and red phosphors doped in blue CDBP:PO-T2T. The hybrid WOLED demonstrated maximum efficiencies of 67.0 cd A^{-1}, 84.1 lm W^{-1} for CE, PE and EQE of 25.5%[40].

Recently, Data *et al.* presented exciplex-based devices which demonstrated an EQE value of 20%[49]. The authors studied steady-state and time-resolved photophysics and evaluated the energy levels of eight non-doped exciplex mixtures of different donors with a PO-T2T acceptor and achieved from blue to orange exciplex emission. The authors pointed out three pairs of exciplexes for describing TADF mechanisms with the rISC process occurring between the locally excited triplet state (^{3}LE) of the donor or the acceptor and the charge transfer singlet state (^{1}CT). What concerns the first case, when the ^{3}LE state of the donor or the acceptor lies below the ^{1}CT state, a significant energy barrier can be observed, which can hinder the rISC process. For the second case, observed for the mCP:PO-T2T and mCPPO1:PO-T2T exciplex systems, the energy of ^{3}LE is aligned with the ^{1}CT state, which was favorable for the efficient TADF process[50]. In the third case, where the rISC process was supposed to be weak, the energy levels were located in the way that ^{3}LE was visibly above the ^{1}CT state, which was the case of TSBPA:PO-T2T and TCBPA:PO-T2T blends. Interestingly, the authors reported that even despite the high ^{3}LE state level in respect to the ^{1}CT state by 0.2 and 0.32 eV in the third case, TSBPA:PO-T2T and TCBPA:PO-T2T showed an efficient rISC process (Fig. 2.11).

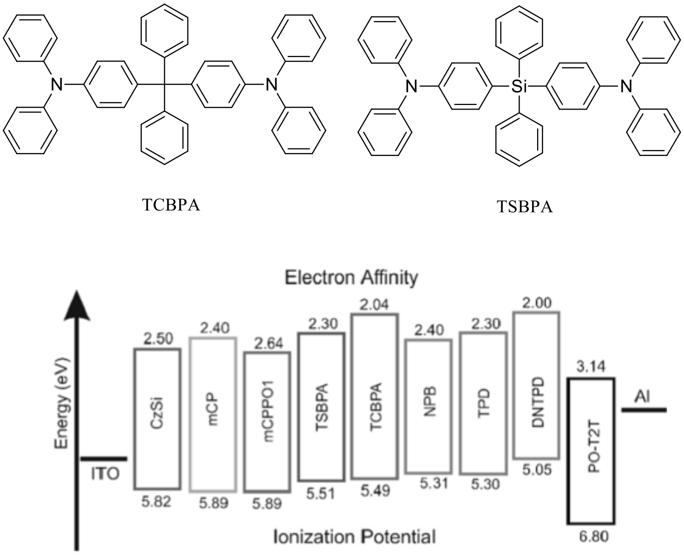

Fig. 2.11. The chemical structure of the donors and a diagram of the energy levels of the investigated donors and the acceptor (adapted from literature[49])

As the transitions between ^{3}CT and ^{1}CT are forbidden due to symmetry, the authors explained the high efficiency by the occurrence of hyperfine coupling between ^{3}CT and ^{1}CT which may provide fast spin exchange to promote ISC and rISC processes. The highest efficiency, reaching the value over the theoretical limit, was achieved for the green PO-T2T:4,4′-(diphenylsilanediyl)bis(*N*,*N* diphenylaniline) (TSBPA) system with the electroluminescence peak at 528 nm. According to the authors, one of the reasons of the high efficiency of the green TSBPA:PO-T2T device is the up to 100% quantum yield of the exciplex system, the high hole mobility, the high energy of the triplet level (2.9 eV) of TSBPA, as well as the small exchange energy of the exciplex system[49]. The green TADF OLED based on the TSBPA:PO-T2T exciplex system showed a record high CE of 60.9 (cd A^{-1}), a PE of 71 (lm W^{-1}), and an EQE of 20%. A fascinating approach of using bipolar compounds with intramolecular TADF features as the donor or acceptor molecules in exciplex systems was offered by Jankus *et al.*in 2014[51]. In this context, the authors demonstrated a D-A-D t-Cbs-SO molecule based on carbazole and dibenzothiophene S,S-dioxide fragments. It was found that t-Cbs-SO is able to emit not only via intramolecular CT, but also behave as an electron-accepting molecule and form an efficient exciplex system with the host TAPC molecule (Fig. 2.12). The authors studied the photophysics of the host: guest system with different concentrations of the t-Cbs-SO guest (5%, 30%, 38%, 40%, 55% by weight). It was discussed that emission processes highly depend on the concentration ratio of the guest molecule and the time after excitation, either the ICT state of the t-Cbs-SO dopant, or the exciplex state between the dopant and the TAPC host dominate the emission[51]. Thus, for the exciplex formation, a high dopant concentration (at least 30% t-Cbs-SO :TAPC) was preferred. The most efficient exciplex system of 30% of t-Cbs-SO exhibited yellow emission at 540 nm and a PLQY of 53%. The authors achieved EQE >10% for the 30% t-Cbs-SO:TAPC based device due to better injection and balanced charge transport. The t-Cbz-SO:TAPC device showed a maximum PE of 26.7 lm W^{-1} and CE of 32.3 cd A^{-1} at 100 cd m^{-2}, while, at high luminance of 1000 cd m^{-2}, the maximum PE and CE reached the values of 14.8 lm W^{-1} and 22.5 cd A^{-1}[43].

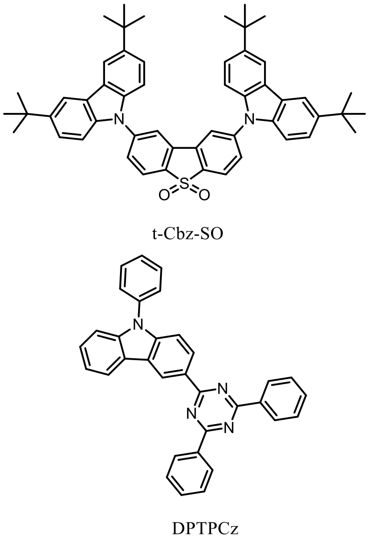

Fig. 2.12. Chemical structures of bipolar exciplex-forming compounds

In the subsequent year, three green exciplex emitters were developed by Zhang *et al.* In 2015, based on TAPC, TCTA and NPB as donors in pair with the bipolar D-A type compound 3-(4,6-diphenyl-1,3,5- triazin-2-yl)-9-phenyl-9*H*-carbazole (DPTPCz) (Fig. 2.12)[40]. The emission spectra of the exciplexes with peaks at 503, 502 and 491 nm for TAPC:DPTPCz, TCTA:DPTPCz, NPB:DPTPCz, respectively were significantly red-shifted in respect to the spectra of the constituting molecules (Table 2.3). The TAPC:DPTPCz blend exhibited the best characteristics among the exciplexes with a high PLQY of 68% and a small ΔE_{ST} of 0.047 eV, which enabled the efficient rISC process[40]. More profound studies on the photophysics of the investigated exciplexes revealed that 1) analysis of solution redox potentials of the donor and acceptor molecules can be used as a tool for the prediction of exciplex emission; 2) molecules with high triplet energies with regard to the exciplex energy are preferable for achieving exciplexes with high PLQY values.

Table 2.3. Summarized properties of the discussed bimolecular systems

Donor	*HOMO/LUMO eV*	*Acceptor*	*HOMO/LUMO eV*	$\lambda_{PL, exciplex}$, *nm*	*PLQY, %*	*EQE*$_{max}$*, %*	*Ref.*
m-MTDATA	–5.10/–2.00	***t*-Bu-PBD**	–6.10/–2.40	540	20	2	43
m-MTDATA	–5.10/–2.00	**3TPYMB**	–6.80/–3.30	~540	26	5.4	43
m-MTDATA	–5.10/–2.00	**TPBi**	–6.30/–2.80	~520	17	7	
TPD	–5.30/–2.20	**OXD-7**	–6.50/–2.80	~485	-	-	45
TPD	–5.10/–2.00	**TPBi**	–6.30/–2.80	~470	-	-	45
TCTA	–5.60/–2.30	**3P-T2T**	–6.40/–2.90	544		7.7	46
CDBP	–5.64/–2.13	**PO-T2T**	–6.83/–2.83	476	51	13	48
mCP	–6.10/–2.10	**PO-T2T**	–6.83/–2.83	472	-	8	47
TCTA	–5.62/–2.30	**PO-T2T**	–6.83/–2.83	552	-	6.2	47
DTAF	–5.31/–1.84	**PO-T2T**	–6.83/–2.83	572	-	5.7	47
TAPC	–5.30/–1.80	**PO-T2T**	–6.83/–2.83	586	-	3.7	47
NPNPB	–5.16/–2.20	**PO-T2T**	–6.83/–2.83	650	-	0.2	47
mCP	–5.89/–2.40	**PO-T2T**	–6.83/–2.83	480	-	16	49
mCPPO1	–5.89/–2.64	**PO-T2T**	–6.83/–2.83	480	-	6.5	49
TSBPA	–5.51/–2.30	**PO-T2T**	–6.83/–2.83	528	-	20	49
TCBPA	–5.49/–2.04	**PO-T2T**	–6.83/–2.83	542	-	12.8	49
TAPC	–5.30/–1.80	***t*-Cbz-SO(2d)**		540	53	14	51
TAPC	–5.30/–1.80	**DPTPCz**	–6.03/–3.08	503	68	15.4	40
TCTA	–5.60/–2.30	**DPTPCz**	–6.03/–3.08	502	55	11.9	40
NPB	–5.40/–2.81	**DPTPCz**	–6.03/–3.08	491	15	0.6	40
DMAC-DPS	–5.90/–2.90	**T2T**		480	-	4.44	52
DMAC-DPS	–5.90/–2.90	**B4PyMPm**		493	-	4.40	52
DMAC-DPS	–5.90/–2.90	**PO-T2T**	–6.83/–2.83	535	-	9.08	52
TPD	–5.30/–2.20	**DMAC-DPS**	–5.90	550	-	1.63	52
MAC	–5.64/	**PO-T2T**	–6.83/–2.83	514	8	17.8	54

In the same manner, Li *et al.*[52] in 2015 also reported the formation of exciplex systems between the bipolar TADF molecule DMAC-DPS and a set of different acceptors (T2T, B4PyMPm, PO-T2T) as well as between DMAC-DPS and the TPD donor. Exciplex blends of DMAC-DPS with the T2T, B4PyMPm and PO-T2T acceptor at 1:1 ratio exhibited fluorescence with peaks located at 480 nm, 493 nm, and 535 nm. A combination with the TPD electron-donor resulted in yellow emission with maxima at 550 nm. Among the devices based on exciplex systems, the DMAC-

DPS:PO-T2T exciplex exhibited the highest exciplex performance with a maximum EQE of 9.1%, luminescence of 35.000 cd m^{-2}, and CE of 30 cd A^{-1}. DMAC-DPS was utilized not only as the TADF dopant, but also as exciplex forming materials in other publications as well (Table 2.3)[53].

Inspired by the previous result, in 2016, Zheng *et al.*[54] reported a blue TADF molecule 6-(9,9-dimethylacridin-10(9*H*)-yl)-3-methyl-1H-isochromen-1-one (MAC) (Fig. 2.12) which behaved as a donor and formed excited complexes with a PO-T2T acceptor at a 7(MAC):3(PO-T2T) ratio with an emission peak at 514 nm, and a $\Delta E_{S\text{-}T}$ value of 0.014 eV. Thereby, by adjustment of the weight ratio of the donor and the acceptor molecules, the authors achieved high device performances of MAC:PO-T2T (7:3) devices with the EQE, CE and PE values of 16%, 46 cd A^{-1} and 38 lm W^{-1} at 100 cd m^{-2} (Table 2.3).

2.5. Improvement of solid state luminescence in the framework of aggregation induced emission phenomenon

Solid state emission intensity is one of the most important parameters influencing the efficiency of organic devices. Nevertheless, a lot of planar or close-to-planar semiconducting materials experience intense intermolecular π–π stacking interactions of adjoining luminophores in the solid state and concentrated solutions which result in the emission quenching of the luminophores and are called the aggregation-caused quenching effect[55]. The general phenomenon of fluorescence diminution with an increase of the solution concentration of aromatic systems was first discovered for the pyrene molecule by Förster and Kasper[56]. Thus the investigations of the photophysical parameters of organic compounds, such as emission intensity, fluorescence lifetimes, and decay rates, are usually performed in highly dilute non-polar solutions so that to avoid the interactions between the chromophoric species. In the area of organic light-emitting diodes, such an issue led researchers to the use of an organic emitter only in the doped layer of an organic device, which afforded to avoid the ACQ effect and to increase the device efficiency[57]. To simplify the manufacturing process and the production costs of OLED fabrication, chemists attempted to adapt the aggregation processes so that they could serve constructively and effectively in the solid matter. The concept of aggregation-induced emission (AIE) was developed by the group of Tang *et al.* in 2001[58]. It was found that, unlike conventional organic systems, non-emissive in solution hexaphenylsilole (HPS) compounds were induced to emit in the solid state by aggregate formation. Looking closer to the HPS structure, the six phenyl rings are connected to the silole core and dynamically rotate against the silole stator. When dissolved in the THF solvent, the dynamic rotation of the phenyl rings causes the decrease in the emission intensity. Meanwhile, its emission is significantly boosted in water: THF medium when f_w reaches the values of 80 *vol*% and higher as a result of the aggregation of HPS molecules[59]. The AIE-effect can be activated by simple structural modifications of the target compounds. Thus, the implementation of rotating, bulky, propeller-shape or non-symmetrical groups to the molecular architecture enables the AIE-effect. A lot of effort has been made to understand the driving mechanisms of the AIE phenomenon.

Earlier studies revealed that the AIE phenomenon can be associated with the neighboring mechanisms, such as conformational planarization[60], J-aggregate formation[64], restriction of the twisted intramolecular charge transfer[62], E-Z isomerization[61], along with the excited-state intramolecular proton transfer (ESIPT), or a combination of these[61]. Nevertheless, one of the main underlying mechanisms of aggregation emission enhancement is the restriction of the molecular motion (RIM) of the molecular fragments. The main types of molecule motion are rotations and vibrations. Molecules possessing the RIM-mechanism due to the presence of flexible rotor-carrying units undergo dynamic intramolecular rotations which result in non-radiative pathways in a dilute solution. However, upon aggregation, owing to the physical constraint, the intramolecular rotations are highly restricted, which blocks the non-radiative pathway and enables the radiative channel. Typical AIEgens are depicted in Fig. 2.13. The RIM mechanism can be enabled by a restriction of intramolecular rotations (RIR) and a restriction of intramolecular vibrations (RIV).

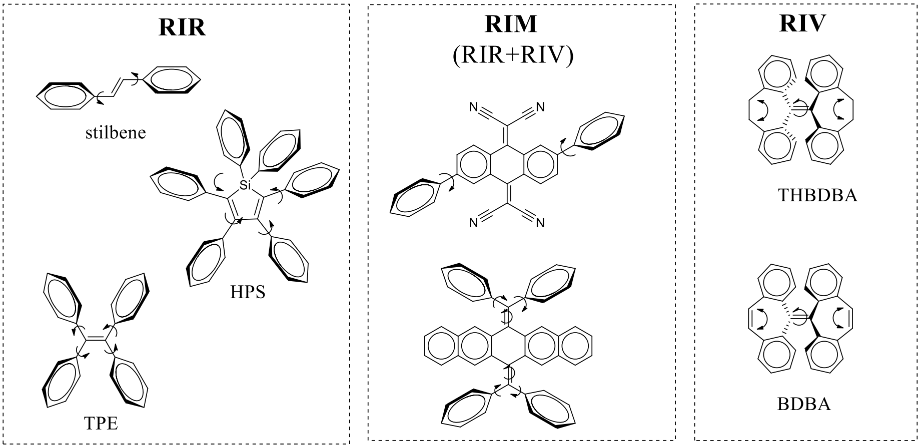

Fig. 2.13. Molecular structure of AIE compounds with different driving mechanisms

An excellent example of an AIE luminogen (AIEgen) possessing the RIR process is the aforementioned HPS molecule (Fig. 2.13) where the six phenyl rings attached to the silole core make it conformationally flexible. The face-to-face packing of highly twisted conformations caused by the steric repulsion between the rotatable peripheries and the adjacent phenyl groups is not possible. Due to the presence of RIR, in the solid state, molecules experience very weak π–π stacking interaction. In the solid state, the dynamic rotations of the phenyl rings which took place in the solution are highly suppressed by physical constraint, which opens a radiative channel for the excitons to decay. In turn, one of the most widely used AIE units is the stilbene analogue – tetraphenylethylene (TPE) – which possesses a splendid AIE effect (Fig. 2.13). Four phenyl rings rotate freely against the ethylene rotor endowing the relaxation channel for the excited state to decay. Most AIE luminophores possessing the RIR mechanism include a stilbene moiety in their structure. During the recent years, a lot of effort has been made to modify stilbene analogues for achieving high solid state emission intensity[61]. One of the examples of AIE-active molecules is the THBDBA and BDBA reported by Tang *et al.*[62] in 2014. The molecules THBDBA and BDBA do not bear any rotating groups and do not perform the RIR process (Fig. 2.13). Nevertheless, these molecules still show the AIE effect with an increased efficiency in the solid state (PLQY of 23% (THBDBA) and 30% (BDBA)) in respect to solution (PLQY<0.1). THBDBA and BDBA are the TPE based molecules covalently-linked by ethyl or ethenyl bridges thus adopting a ‘boat’, V-shaped, or mixed conformations. The presence of a distorted seven-membered central ring reduces the conjugation of the π-system. By quantum, molecular mechanics, and photophysical investigations, the authors suggested that the underlying mechanism for the AIE activation is the rotation of intramolecular vibrations (RIV). A molecule can adopt both the ‘chair’ and ‘boat’ conformations which can be stabilized by the neighboring interactions. The authors claim a decrease of fluorescence intensity in the solvated state by conformational motions, which can result in decay of excited states. AIE activation occurs by restriction of these vibrational motions endowing the radiative decay channel.

A combination of the RIR and RIV processes enable the RIM mechanism of the AIE effect. So far, combining most of the cases gives an overall picture that the RIM processes mechanistically dominate for all the AIE systems. It is noteworthy that the RIM processes can overlap with other mechanisms of luminescence enhancement, such as J-aggregate formation (JAF), twisted intramolecular charge transfer (TICT), and excited-state intramolecular proton transfer (ESIPT) (Fig. 2.14). When focussing on the cases where J-aggregation cooperates with the AIE effect, it is worth denoting the concept of aggregate formation and molecular packing[63].

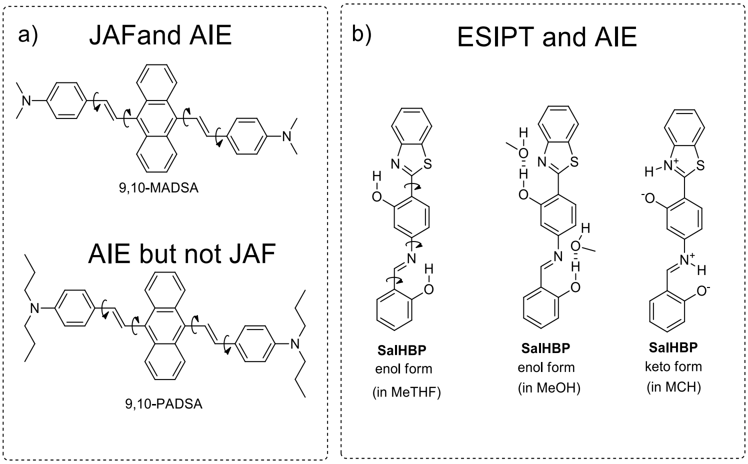

Fig. 2.14. Luminogens possessing AIE, JAF+AIE, ESIPT+AIE

Due to the different assemblies of the molecules, one can form either H- or J-aggregates, depending on the relative alignment of the transition dipole moments on the adjacent molecules. H- or J-aggregates are defined as the aggregates formed through the π–π interaction of the strongly coupled chromophoric fragments. The resulting molecule self-assembly can highly influence the energies of the excited states and thus amend the optical absorption and the photoluminescence spectra. The variety of organic luminogens does form J-aggregates, and, simultaneously, displays

AIE activity. With this aim, Yang *et al.* synthesized two Donor-π-Donor 9,10-distyrylanthracene derivatives 9,10-MADSA and 9,10-PADSA which exhibited crystallization-enhanced emission (CEE) properties (Fig. 2.14)[64]. It is notable that the photophysics of both compounds in the solution and aqueous media was found to be similar – thereby non-fluorescent in the solution and highly fluorescent in aqueous suspensions. Meanwhile, the crystalline state properties highly differ. The crystals of 9,10-MADSA exhibited emission peaking at 586 nm and a PLQY of 60%, while the counterpart 9,10-PADSA showed blue-shifted emission at 553 nm (PLQY=29%). The authors explained the origin of the different crystal emission by different molecular packing modes in the crystal with J-aggregate formation for 9,10-MADSA and H-aggregates for 9,10-PADSA[64].

Electronically excited state intramolecular proton transfer is defined as the intramolecular redistribution of electronic charge due to photon absorption facilitated by H-bonding within the molecule[65]. It was found that ESIPT can take a significant role in the molecule AIE behavior while rigidifying molecular structures and thus activate the RIR process[66, 67].

An example of an AIE-active ESIPT compound is N-salicylidene-3-hydroxy-4-(benzo[d]thiazol-2-yl) phenylamine SalHBP as reported in 2007 by Li *et al.*[68] Interestingly, the authors investigated the influence of the media on the H-bond formation. The emission behavior in a different surrounding was found to be different as SalHBP displayed low-intensity dual fluorescence in aprotic media (MeTHF) with peaks at 416 nm and 538 nm, which corresponds to the emission of enol and keto tautomer forms of SalHBP. Due to the possible conformational changes, single bond rotors can induce molecular motions and thus lead to fluorescence quenching. However, when dispersed in protonic methanol solvent, molecule SalHBP displayed much more intense dual emission, but the peak of the enol form at 416 nm significantly dominated in the PL spectrum. Such a behavior was assigned to the intermolecular H-bonding of the luminogen and the molecules of the solvent which partially caused the restriction of the molecular motion. In an apolar solvent, such as MCH, only one weak peak at 538 nm was observed. SalHBP undergoes a full ESIPT process facilitated by H-bonding within the molecule, and the enol form completely changes to the keto form. The authors presented the influence of the temperature and pressure on the photophysical change of fluorescence intensity of SalHBP and claimed that the RIM and ESIPT process was the main mechanism of fluorescence enhancement[68].

The main causes of emission quenching of the previously described AIE-active compounds are the torsional and vibrational motions which consume the exciton energy by nonradiative decay of their excited state in the solution. On the other hand, when dispersed in an organic solvent, the emission of D-A molecules is assigned to the transition from the so-called charge-transfer state[69]. The emission properties of D-A compounds strongly depend on the intramolecular twisting of Donor and Acceptor units. In this manner, boron dipyrromethene (BODIPY) derivatives reported by Pena-Cabrera *et al.* were found to possess both TICT and AIE characteristics[70]. The authors investigated the photophysical behavior of BODIPY- and triphenylamine-based compounds in solutions of different polarities (Fig. 2.15).

The investigated BODYPY derivatives 1 and 2 displayed a red shift in the PL spectra with an increase of the solvent polarity starting from green fluorescence (534 nm; 532 nm) of the non-polar hexane solution up to the red emission of highly polar THF solutions (663 nm, 688 nm). Meantime, the PLQY values decreased from 17% (1) and 18% (2) for non-polar hexane media up to 6% (1) and 1% (2) for THF solutions (Fig. 2.15). Significant emphasis was given to the evaluation of the AIE nature of compounds 1 and 2 (Fig. 2.15). Under photoexcitation, when dispersed in the THF solvent, compounds 1 and 2 emitted red light. It was found that, with the addition of a small amount of water to the THF solutions of 1 and 2, the emission was quenched and bathochromically shifted. Nonetheless, when the water content was reaching 70% and beyond, the emission was activated again. The authors explain such a behavior by the two competing mechanisms: twisted intramolecular charge-transfer and aggregation-induced emission processes.

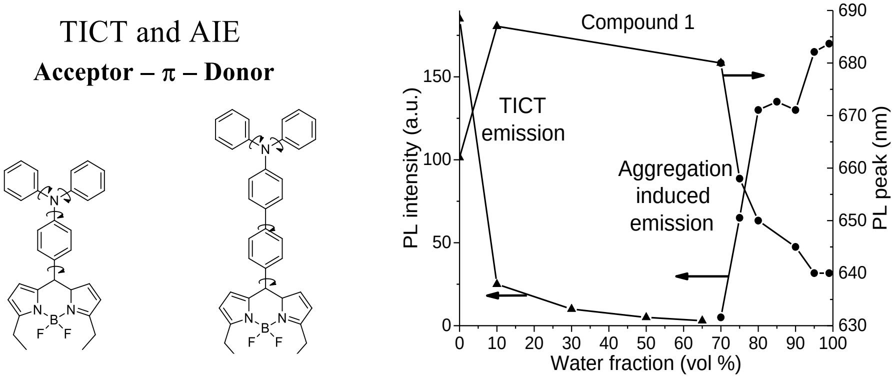

Fig. 2.15. Structures of AIE+TICT molecules along with photoluminescence intensity *vs.* water fraction of THF/H_2O mixtures

It is worth noting that the emission of molecules with an addition of a small amount of water to the mixtures is decreasing and red-shifted, whereas the fluorescence of a mixture with a water content of ~70% and beyond is increasing and blue-shifting. Apparently, the red shift and the decrease in the emission intensity is due to the transition from the TICT state which is sensitive to the surrounding polarity. Meanwhile, when a significant amount of water is added, due to the physical restraints of intramolecular rotations, the emission is revitalized. Therefore, the authors assign the blue shift to the less polar media inside the aggregates with respect to the outside environment of the molecules in the polar THF solvent. The same behavior was observed for a similar molecule with inserted biphenyl 2. A similar emission behavior was also observed for a variety of other AIE active D-A molecules[71, 72, 73].

2.6. Mechanochromic multifunctional materials

Organic semiconducting molecules have recently become a new highly topical field of scholarly investigation. Not less important is the nature of molecular assemblies and the interaction between molecules. A lot of attention has been drawn to the molecular response of the organic luminescent materials to the external stimuli (mechanical force, temperature, vapor, electric field, etc.). To the best of our knowledge, the first of a turn-off type mechanoresponsive material 4-*tert*-butyl-1-(4′-dimethyl amino benzylidene amino) pyridinium perchlorate (BDPP) which changed its emission from yellow-green up to orange by heating (185 °C) or by simple squeezing was reported in 1993 by Gawinecki *et al*.[74]. After the prior research on the pressure response of the AIE-active hexaphenylsilole reported by Tang *et al.*[75] In 2008, a high number of fluorescent materials that could switch their emission color by applying external forces have been synthesized. Ever since, mechanochromic luminescent (MCL) materials have found wide application as mechano-sensors, informational displays, and security features. It is still a challenge to fully elucidate the mechanisms of the emission color change of molecular assemblies caused by external forces. Nevertheless, several approaches were highlighted in the literature which partially explained the MCL behavior of molecular assemblies. Among them, the planarization of molecular structures, transformations between electronic states, conformational twisting, shear-sliding of molecular ‘planes’, etc., were suggested as the main driving force(s) of mechanoresponsive materials which can tune photophysical properties, such as the fluorescence color, quantum yield, and emission lifetime of organic luminophores. Taking this into account, one should understand and keep in mind the significant influence of molecular self-association or aggregation at the solid state on the optical properties of MCL materials. Thus, according to the exciton theory, the organic π-conjugated molecule is viewed as a dipole, and due to the interaction between the transition dipoles, the excitonic state of the aggregate splits into two levels. In turn, molecules can stack up or align in the parallel way thus forming H-dimers or align in the head-to-tail way and thus form J-dimers (Fig. 2.16).

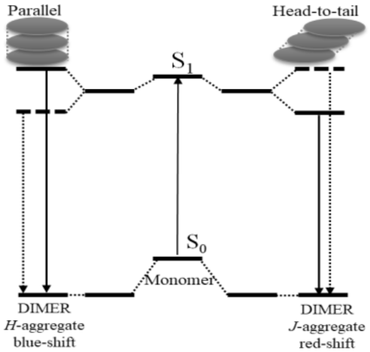

Fig. 2.16. Schematic representation of the formation of J- and H- aggregates based on the molecular exciton theory (adapted from the literature[75])

From the photophysical point of view, J-aggregates exhibited a narrow bathochromically shifted absorption band with respect to monomer absorption along with strong fluorescence. Meanwhile, the absorption bands of the H-aggregates shifted to the shorter wavelength and exhibited low fluorescence.

In 2016, Ma *et al.*[76] obtained a mechanically responsive and AIE-active cyano distyrylbenzene molecule (CN-DSB) which was found to form two crystalline phases:

the original blue emission (B-phase) with λ_{max}=445 nm, and the final green emission (G-phase) after being ground with λ_{max}=503 nm (Fig. 2.17). Therefore, the application of heating or pressure to the B-phase crystal resulted in re-assembled mixture phases or in a disordered state. Through single-crystal X-ray diffraction analysis, the authors examined the difference between the molecular configurations and molecular packings of the B- crystals and G- type crystals. It was shown that the configuration of the stable B-phase is highly twistable, while the G-phase adopts a more planar configuration leading to a substantial π–π overlap. Upon external stimuli, when the applied pressure reaches the critical value of 0.75 GPa, the transitions from the B- to the G-phase occur due to the planarization of the molecular structure and thus the switch of its emission color takes place. Moreover, the molecule solid exhibited restoration to the initial stable B- phase upon returning to the ambient pressure.

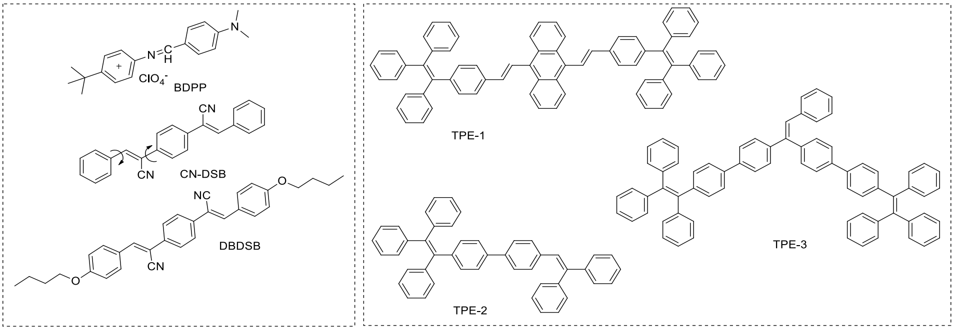

Fig. 2.17. Molecular structures of MCL compounds

Altering the approach of the formation of highly fluorescent ‘molecular sheets’ was offered by Park *et al.* in 2009 (Fig. 2.17)[77]. The authors reported a piezofluorochromic D-A-D distyrylbenzene molecule DBDSB whose fluorescence color could change between the two colors upon application of pressure triggered by the two-directional shear-sliding capability of molecular sheets maintained by multiple C-H···N and C-H···O hydrogen bonds. In turn, by using the structural, photophysical and theoretical tools, the authors revealed that, upon application of external stresses, such as heat, pressure and solvent vapor, DBDSB could switch between the metastable green-emitting G-phase and the thermodynamically stable blue-emitting B-phase independently of the arrangements of the local dipoles.

To the contrary, the structural relationship between the AIE phenomena and the MCL nature of compounds was investigated by Xu *et al.* (2011)[78]. Unlike the DBDSB molecule whose MCL nature was explained by the sheer-sliding of the molecular sheets formed by C-H···N and C-H···O hydrogen bonds, the mechanism of piezofluorochromic activity of the TPE-1 molecule based on twisted tetraphenylethylene and divinyl anthracene was explained by the highly twisted conformation in the initial state and the partial planarizarization and slip deformation of the molecular assembly upon external pressure (Fig. 2.17). Thus the authors explain the change in PL profiles from 506 nm to 574 nm after grinding by destruction of the crystalline packing with further planarization of the molecular conformation.

Therefore, TPE-1 demonstrated reversibility in both the absorption and emission spectra after several grinding-annealing cycles.

Similarly, the analogous molecule TPE-2 also demonstrated the AIE and MCL phenomenon[79]. Interestingly, their counterpart molecule TPE-3 also features AIE activity but exhibits no MCL nature. The authors explain such a behavior by the difference in morphologies of the initial states of compounds as TPE-3 is an amorphous solid, while TPE-2 adopts the crystalline state confirmed by PXRD analysis[79].

Significant interest has been paid to the area of multifunctional materials. In turn, compounds exhibiting MCL behavior along with the delayed fluorescence feature are of great demand. According to this trend, the phenothiazine unit as a strong electron-donating fragment has been widely used for the design of efficient TADF and MCL emitters. Despite the electron-donating capabilities, phenothiazine due to its bowl-shaped structure is capable to form several thermodynamically (*meta*-) stable states through the adoption of either parallel quasi-axial or perpendicular quasi-equatorial conformations of N-substituted phenothiazines (Fig. 2.18).

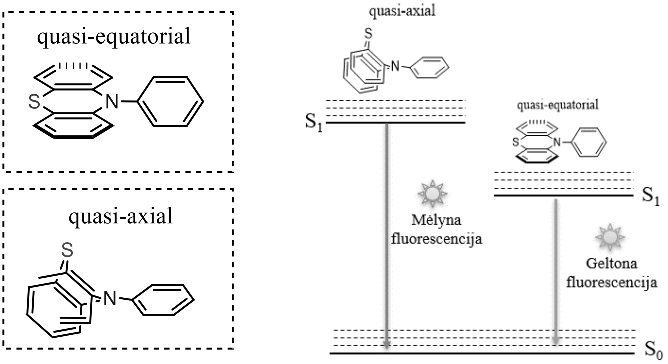

Fig. 2.18. Conformations of phenothiazine and a schematic energy diagram of conformers

According to the previous studies, the parallel quasi-axial phenothiazine conformer exhibited a significantly higher energy gap and higher energy of the first excited singlet state than its perpendicular analogue (Fig. 2.18). It was found that the transitions between quasi-axial and quasi-equatorial conformers can be realized by applying mechanical forces to the solid sample[80]. Keeping this in mind, emitters which exhibit dual emission from different states or switch between conformers, specifically, blue and orange, are of great interest. In this manner, in 2015, Zhang *et al.*[80] reported a single-molecular white-emitting asymmetrical compound OPC comprised of carbazolyl- and phenothiazinyl-based benzophenone fragments demonstrating aggregation-induced emission-delayed fluorescence and MCL properties (Fig. 2.18). Similarly, the following year, the same group reported a novel dual-emissive SCP compound consisting of a diphenylsulfone acceptor and phenyl-carbazole and phenothiazine donors[81]. As well as OPC, SCP showed mechanoresponsive behavior along with TADF characteristics. Interestingly, the OPC molecule exhibited dual emission with peaks at 456 and 554 nm. The fluorescence lifetime of the blue peak was found to be short and in the range of nanoseconds. Meanwhile, the yellow emission peak exhibited prompt and delayed components. In turn, a similar SCP molecule displayed prompt fluorescence at 415 nm (τ_p=3 ns) and delayed fluorescence at 545 nm (τ_p=6 ns, τ_{DF}=51μs) (Fig. 2.19)[80]. As mechanical force was applied for both OPC and SCP, the intensity of the blue component significantly decreased while the yellow component's delayed emission intensity remained unchanged. Under deeper analysis of the photophysical properties as well as molecule packing modes, the authors explained the tuneable emission of OPC by the switching between the two CT emissions of different conformers (quasi-axial, quasi-equatorial). Thus the blue component (456 nm) was ascribed to the crystalline state of the quasi-axial phenothiazine conformer of OPC, while the yellow emission corresponds to the amorphous state of the quasi-equatorial conformer. Meanwhile, the gradual emission change of SCP was ascribed to the change in the local conformations of the molecule along with the planarization of the phenylcarbazolyl unit under the gradual grinding process. In the same vein, in 2018, Li *et al.*[82] presented a FCO-CzS molecule based on a 4-fluoro-benzophenone fragment as the electron-withdrawing unit and phenothiazine as the electron-donating fragment (Fig. 2.19).

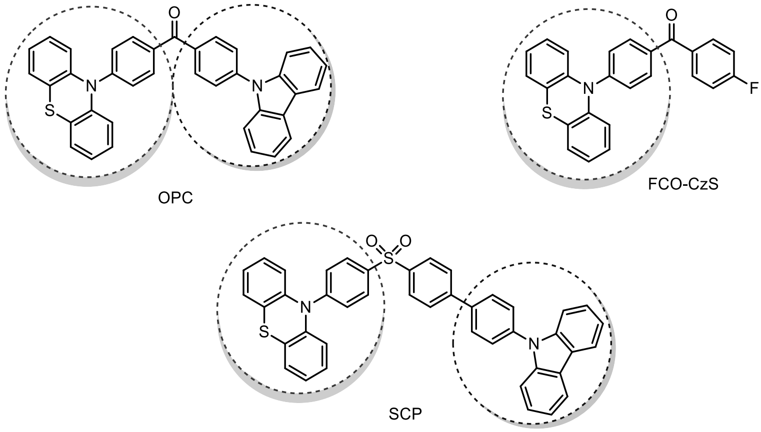

Fig. 2.19. Molecular structures of phenothiazine-based TADF-MCL materials

Similarly to the above mentioned compounds OPC and SCP, FCO-CzS showed mechanoluminescent emission from blue (449 nm) to white after slight grinding and yellow (544 nm) upon heavy grinding. Therefore, the authors ascribed the emission change to the transformation between molecular phenothiazine conformations from quasi-axial to almost orthogonal quasi-equatorial. Interestingly, the authors demonstrated that the introduction of the fluorine atom to the benzophenone fragment enhanced the intermolecular interactions by the formation of C-H···F bonds and restricted the nonradiative transition, which promoted the fluorescence efficiency[82]. A new insight into conformational changes was offered by Takeda *et al.* [83] in 2013 who reported new dibenzo[*a,j*]phenazine- and phenothiazine-based TADF-active multi-color-changing MCL compounds (Fig. 2.20 (a)). Thus the authors showed that both phenothiazine units could adopt either stable quasi-axial (ax) or quasi-equatorial (eq) conformer forms with the following set of possible conformers: quasi-axial/quasi-axial (ax-ax), quasi-equatorial/quasi-axial (eq-ax), and quasi-equatorial/quasi-equatorial (eq-eq) which exhibited a different emission color (Fig. 2.20 (b)). The synthesized material demonstrated distinct three-color variations in response to a variety of external stimuli, such as recrystallization, grinding, solvent exposure, and heating. Comparative analysis of the relationship between the emission color of different states and conformational arrangement was carried out. Thus the authors demonstrated that the red fluorescence from the solid 1_R is attributed to the emission of a highly twisted eq-eq conformer. Therefore, the slightly blue-shifted orange emission of 1_O should be coming from the weaker ICT excited state, which is the feature of the eq-ax conformer, as confirmed by single X-ray analysis. Consequently, the authors explained the highest energy emission of the 1_Y powder as the radiative process from the ^{1}LE state accompanying the ax-ax conformer (Fig. 2.20). Moreover, profound investigation of the TADF nature of 1 and 2 doped in the Zeonex matrix and the CBP host was performed. It was suggested that the two-phenothiazine fragment of 1 and 2 adopted electronically decoupled quasi-equatorial/quasi-equatorial (eq-eq) conformations which were perpendicular to the acceptor core.

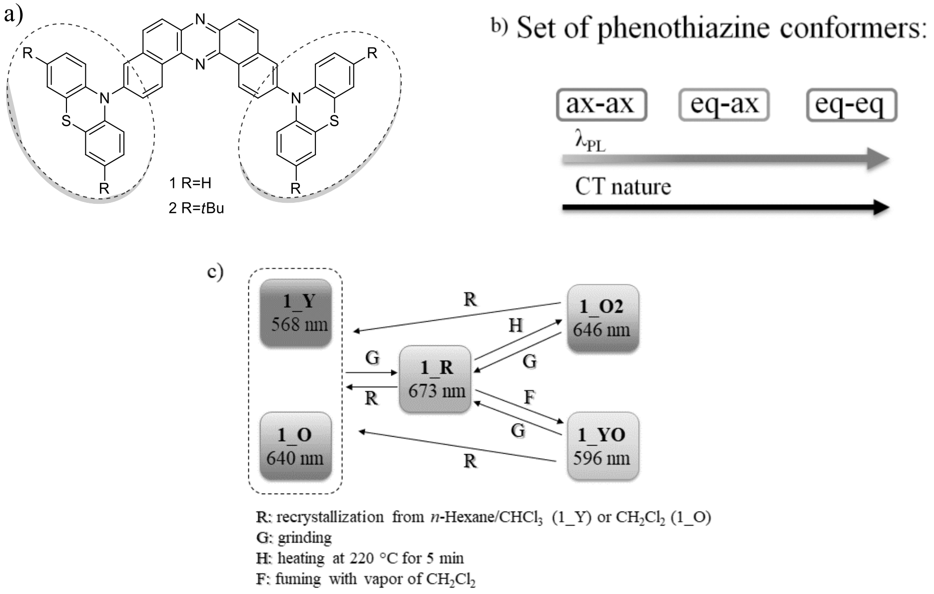

Fig. 2.20. a) The molecular structure of multifunctional materials; b) Possible conformer arrangements of phenothiazine fragments; c) Schematic MCL relationship and corresponding to the emission peaks

This led to low $\Delta E_{S\text{-}T}$ values for 1 and 2 of 0.08 and 0.13 eV, respectively, as well as long fluorescence lifetimes with prompt and delayed components. Hence, the best fabricated OLED device using 1 as the emitting layer with the structure ITO/NPB (40 nm)/10 wt% 1 in CBP (30 nm)/TPBi (50 nm)/LiF (1 nm)/Al (100 nm) showed orange electroluminescence with the peak at 613 nm, the maximum efficiency of 19.6 cd/A, and an EQE of 16.8%

2.7. Conclusions of the literature review

Despite the booming progress of the OLEDs technology during the recent years, OLEDs still struggle due to limited lifetimes and low color purity. Nevertheless, the efficiency of the best known TADF devices is in the range of 25–30%. OLEDs fabricated by vacuum deposition technique guarantee better efficiency and higher purity, while solution-processed devices are suitable for the low-cost, large area displays. In spite of the relatively short lifetimes, low color purity and high cost, OLEDs still offer flat, thin, bright and flexible displays. One way to increase the device efficiency is the utilization of new electrochemically and thermally stable donor-acceptor type emitting materials characterized with high radiative decay constants and delayed fluorescence properties. The concept of delayed fluorescence allows the harvesting of 75% of non-radiative triplet excitons by up-conversion to the radiative singlet state. Accurate chemical modification of molecular structures affords to activate efficient rISC and facilitate the TADF process. Donor-acceptor architectures with a twisted structure, steric hindrance between the donor and the acceptor, or multiple resonance effects are preferable to achieve negligible singlet-triplet energy splitting, and, consequently, relatively long photoluminescence lifetimes. Nevertheless, it is still a challenge to obtain bipolar materials, especially deep-blue emitting ones, with small singlet-triplet energy splitting and a high solid state PLQY. Most organic donor-acceptor materials suffer from the aggregation quenching effects, which results in a low PLQY and require the usage of host materials. Multifunctional compounds exhibiting bipolar charge transport, high solid state luminescence efficiency as well as aggregation induced emission enhancement or mechanoluminescent behavior are of great importance as they enable to fabricate non-doped OLEDs of the simplified structure. Solid-state luminescence efficiency can be improved by the implementation of rotatable units which activate aggregation induced emission enhancement. The manipulation of the modes of molecular packing or conformational arrangements can also affect the emission color or luminescence intensity. Mechanoresponsive materials are dependent on the molecular arrangements as well as on intermolecular interactions. Consequently, the hardest obstacle in obtaining multifunctional delayed fluorescence materials with the desirable emission color is the proper choice of electron-donating and electron-accepting fragments. As discussed in our literature review, bimolecular donor-acceptor exciplex systems allow much easier screening of the donor and acceptor fragments. Thus, the proper adjustment of electron-donating and electron-accepting moieties allows the altering of photophysical properties and the influencing of the OLED performances. However, exciplex systems suffer from lower luminescence efficiencies and device efficiency with respect to the monomolecular donor-acceptor materials. Efficient exciplex systems require a sophisticated design of electron-donating and electron-accepting molecules with high triplet energies, high charge-mobilities, and the appropriate IP and EA.

3. EXPERIMENTAL SECTION

3.1. Instrumentation

^{1}H, ^{13}C and ^{19}F NMR spectra were recorded in deuterated chloroform ($CDCl_3$) by using a *Bruker Avance III 400* spectrometer at 400 MHz (^{1}H), 100 MHz (^{13}C) and 375 MHz (^{19}F)) frequency at room temperature. Chemical shifts (δ) are reported in ppm referenced to tetramethylsilane or the internal solvent signal.

The IR spectra in the range of 400–4000 inverse centimeters (cm^{-1}) were recorded on a *Perkin Elmer Spectrum BX II FT-IR* System. The spectra of solid compounds were performed for KBr 1pellets. The FT-IR spectra were analyzed as a function of transparency (T) expressed in percent against the wavenumber (ν) expressed in cm^{-1}.

The mass spectra were measured by employing the electrospray ionization mass spectrometry (ESI-MS) method on an *Esquire-LC 00084* mass spectrometer.

Elemental analysis was done with an *Exeter Analytical CE-440 Elemental Analyzer*.

Differential scanning calorimetry (DSC) measurements were recorded by using *PerkinElmer DSC 8500* equipment at heating and cooling rates of 10 °C/min in the nitrogen atmosphere.

Thermogravimetric experiments (TGA) were conducted by using a *PerkinElmer TGA 4000* apparatus at a heating rate of 20 °C/min in the nitrogen atmosphere. The melting points were measured with a *MEL-TEMP* (Electrothermal) melting point apparatus.

The UV-vis spectra of dilute solutions and solid samples were recorded on a *PerkinElmer Lambda 35* spectrometer. The fluorescence spectra, fluorescence quantum yields (PLQY), and fluorescence decay curves of both solutions and solid films were recorded with a *FLS980* fluorescence spectrometer. An *Edinburgh Instruments FLS980* spectrometer and a *PicoQuant LDH-DC-375* laser (wavelength 374 nm) as the excitation source were used for recording photoluminescence (PL) decay curves and PL intensity dependencies on the laser flux of the samples at room temperature. The instrument response function (IR) for time-resolved fluorescence measurements was obtained by recording the temporal profile of the excitation light. For the measurements of scattered light, a dilute solution of colloidal silica (*Ludox, Aldrich, Inc.*) was used. An integrated sphere (inner diameter of 120 mm) spherical cavity calibrated with two analytical standards: quinine sulfate in 0.1 M H_2SO_4 and rhodamine 6G in ethanol was used for the measurements of fluorescence quantum yields.

Cyclic voltammetry (CV) measurements were performed by using a micro-*Autolab III* (*Metrohm Autolab*) potentiostat-galvanostat equipped with the standard three electrode configuration. A three-electrode cell equipped with a glassy carbon working electrode, an Ag/Ag (0.01 M in anhydrous DMF or DCM or THF) reference electrode, and a Pt wire counter electrode was employed. The measurements were conducted in anhydrous DMF/DCM/THF with 0.1 M tetrabutylammonium hexafluorophosphate ($Bu_4N(PF)_6$) as the supporting electrolyte under the nitrogen atmosphere at a scan rate of 0.1 V/s. The measurements were calibrated by using a ferrocene/ferrocenium (Fc) system as an internal standard.

The photoelectron emission spectra for previously vacuum-deposited layers were recorded as reported previously[84]. The samples for photoelectron emission measurements were vacuum-deposited by using fluorine-doped tin oxide-coated glass slides as substrates. The photoelectron emission spectra were recorded in an air exploiting setup which included an *ASBN-D130-CM* deep-UV deuterium light source, a *CM110* 1/8m monochromator, and a *6517B Keithley* electrometer.

The charge-transporting properties of vacuum deposited films were estimated by employing the time-of-flight (TOF) technique while using an *EKSPLA NL300* laser (excitation wavelength of 355 nm), *6517B* electrometer (*Keithley*), and a *TDS 3032C* oscilloscope (*Tektronix*). By taking transit times (ttr) from the photocurrent transients at the applied voltage (U) and the thicknesses of the layers (d) measured by the charge extraction by the linearly increasing voltage (CELIV), the technique assuming the dielectric constant $\varepsilon = 3$ for the studied compounds, $\mu = d^2/(U \times ttr)$ were utilized to calculate charge mobilities.

The theoretical calculations were performed by using the *Gaussian 09* quantum chemical package[85]. The geometry optimization of the ground state of the compounds was done with the density functional (DFT) method with *B3LYP* functional along with the *6-31G* (d, p) basis set in vacuum. The absorption spectra of the molecules were calculated by means of the time dependent density functional theory technique (TDDFT) for 20 excited states.

Lippert-Mataga equation

The Lippert-Mataga model describes the Stokes shift in terms of the changes in the dipole moment which occurs upon excitation in the solvents of various dielectric constant (*ε*) or refractive index (*n*)[86] :

$$\Delta\nu = \frac{2\Delta f}{4\pi\varepsilon_0\hbar c a^3}(\mu_e - \mu_g)^2 + b,$$

where the orientation polarizability of the solvent is defined as follows:

$$\Delta f = \frac{\varepsilon - 1}{2\varepsilon + 1} - \frac{n^2 - 1}{2n^2 + 1}$$

$\hbar$ stands for the Planck constant, *c* is the light velocity in vacuum, a stands for the Onsager radius, ε_0 is the permittivity of vacuum. Each solvent has its own values of $\mathcal{E}$, the dielectric constant, and *n*, the refractive index. The linear fit of the dependence of the Stokes shift value on Δf has slopes at 14 and 14.6 thousand cm^{-1} for pCzPPQ and mCzPPQ, respectively. These values correlate with the dipole moments of the emissive excited μ_e and ground μ_g states of the compounds. The slope value is proportional to $(\mu_e\text{-}\mu_g)^2$.

Indium tin oxide substrates were patterned and cleaned for the fabrication of OLEDs by using layer-by-layer thermal deposition. Current density-voltage and brightness-voltage characteristics were simultaneously recorded by using a source meter *Keithley 2400* and a certified photodiode *PH100-Si-HA-D0* together with *PC-Based Power* and *Energy Monitor 11S-LINK* (developed by *STANDA*). An *Aventes AvaSpec-2048XL* spectrometer was employed to take the electroluminescence (EL) spectra of the devices at different voltages. By using brightness, current density, and the EL spectra, the current, power and external quantum efficiencies were calculated. *Commission Internationale de l'Eclairage* (CIE 1931) chromaticity coordinates (x, y) and the color rendering index (CRI) were obtained by using the EL spectra and the software of an *FLS980* spectrometer.

3.2. Materials

The starting materials, i.e., 9*H*-carbazole, 10*H*-phenothiazine 2,3,4,5,6-pentafluorostyrene, sodium *tert*-butoxide, azobisisobutyronitrile (AIBN), 1-(4-bromophenyl)-1,2,2-triphenylethylene, 2-bromo-1,1,2-triphenylethylene, palladium acetate(II), *tetrakis*-triphenylphosphine palladium ($Pd(PPh_3)_4$), tri(*o*-tolyl)-phosphine, *o*-aminobenzophenone, 3-iodoacetophenone, 4-iodoacetophenone, ethyl bromide, glacial acetic and sulfuric acids, copper (Cu), potassium iodide (KI), potassium iodate (KIO_3), sodium hydroxide (NaOH), potassium carbonate (K_2CO_3), anhydrous sodium sulfate (Na_2SO_4), potassium hydroxide (KOH), copper cyanide (CuCN), 18-crown-6, and 1,2-dichlorobenzene were purchased from *Sigma-Aldrich* and used as received. The starting materials used for the synthesis of compounds described in Chapter 4 are reported in the corresponding work.

The organic solvents, i.e., toluene, chloroform ($CHCl_3$), ethyl acetate, methanol (MeOH), acetone, acetonitrile (MeCN), tetrahydrofuran (THF), dichloromethane (DCM), o-dichlorobenzene (*o*-DCB), dimethyl sulfoxide (DMSO) and *N,N*-dimethylformamide (DMF) (*Sigma-Aldrich*) were dried and distilled according to the previously reported procedures[87].

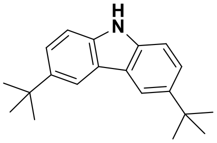

3,6-di-*tert*-butylcarbazole $C_{20}H_{25}N$ (M_w=279.42 g/mol) was synthesized by the Friedel-Crafts reaction according to the known procedure[88] as a white solid (yield 70%)

General procedure for monomer synthesis:

Sodium *tert*-butoxide (1.2 eq) was added to the DMSO or DMF solution of NH-heterocyclic compound (1 eq) and stirred for 5 min at room temperature for the salt formation. The mixture was added dropwise to the solution of 2,3,4,5,6-pentafluorostyrene (1.5 eq) in DMSO or DMF. The reaction mixture was stirred for 10 h at ambient temperature. Then the reaction mixture was poured into water and extracted with ethyl acetate. The organic phase was collected, dried over anhydrous Na_2SO_4, and concentrated under reduced pressure. The crude product was purified by column chromatography on silica gel by using hexane and dichloromethane in a volume ratio of 5:1 as the eluent mixture of solvents. The product was recrystallized from the eluent mixture of solvents.

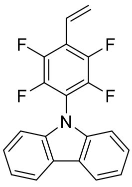

9-(2,3,5,6-tetrafluoro-4-vinylphenyl)-9*H*-carbazole (M1) was prepared from carbazole (0.4 g, 2.4 mmol), sodium *tert*-butoxide (0.28 g, 2.8 mmol), 2,3,4,5,6-pentafluorostyrene (0.7 g, 3.6 mmol) and DMSO (12 mL) by using the general procedure and was isolated in 57% yield as white crystals. mp: 104–106 °C. ^{1}H NMR (400 MHz, CDCl$_3$): δ 8.16 (d, J = 7.7 Hz, 2H), 7.52 – 7.43 (m, 2H), 7.37 (t, J = 7.5 Hz, 2H), 7.20 (d, J = 8.2 Hz, 2H), 6.84 (dd, J = 18.0, 11.9 Hz, 1H), 6.28 (d, J = 18.0 Hz, 1H), 5.86 (d, J = 11.9 Hz, 1H). ^{13}C NMR (101 MHz, CDCl$_3$): δ 139.98, 126.47, 124.72, 124.08, 122.06, 121.14, 120.53, 109.88. ^{19}F NMR (376 MHz, CDCl$_3$): δ -142.57 (td, J = 13.2, 4.3 Hz, 2F), -144.16 to -144.46 (m, 2F). *m/z*: cal. for $C_{20}H_{11}F_4N$ 342.3 [M+ H], found 342.6; FT-IR. ν_{max} in cm^{-1} (KBr): 2363, 2155, 1625, 1513, 1477, 1407, 1322, 1311, 1271, 1228, 1155, 973, 963, 955, 810, 743, 720.

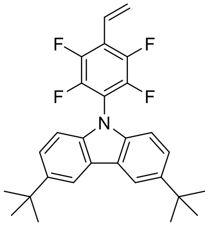

3,6-Di-*tert*-butyl-9-(2,3,5,6-tetrafluoro-4-vinylphenyl)-9*H*-carbazole (M2) was prepared from 3,6-di-*tert*-butylcarbazole (0.45 g, 1.6 mmol), sodium *tert*-butoxide (0.19 g, 1.9 mmol), 2,3,4,5,6-pentafluorostyrene (0.47 g, 1.9 mmol) and dry DMF (11 mL) by using the general procedure, and was isolated in 54% yield as white crystals. mp: 219–222 °C. ^{1}H NMR (400 MHz, CDCl$_3$): δ 8.14 (d, J = 1.8 Hz, 2H), 7.50 (dd, J = 8.6, 1.9 Hz, 2H), 7.09 (d, J = 8.6 Hz, 2H), 6.82 (dd, J = 18.0, 11.9 Hz, 1H), 6.26 (d, J = 18.0 Hz, 1H), 5.84 (d, J = 11.9 Hz, 1H), 1.47 (s, 18H). ^{13}C NMR (101 MHz, CDCl$_3$): δ 144.04, 138.35, 124.41, 124.04, 124.02, 122.15, 116.52, 109.31, 34.79, 31.96. ^{19}F NMR (376 MHz, CDCl$_3$): δ -142.85 (td, J = 12.8, 3.8 Hz, 2F), -144.41 (td, J = 12.8, 3.7 Hz, 2F). *m/z*: cal. for $C_{28}H_{27}F_4N$ 453.51 [M+ H], found 453.48. FT-IR. ν_{max} in cm^{-1} (KBr): 2955, 2901, 2865, 1886, 1653, 1631, 1620, 1515, 1488, 1408, 1363, 1295, 1261, 1237, 1167, 1033, 971, 875, 811.

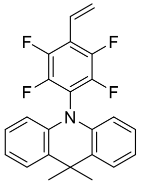

9,9-dimethyl-10-(2,3,5,6-tetrafluoro-4-vinylphenyl)-9,10-dihydroacridine (M3) was prepared from 9,9-Dimethyl-9,10-dihydroacridine (0.4 g, 1.9 mmol), sodium *tert*-butoxide (0.22 g, 2.8 mmol), 2,3,4,5,6-pentafluorostyrene (0.56 g, 2.2 mmol) in DMF (10 mL) by using the general procedure, and was isolated in 47% yield as a white crystals. mp: 133–135 °C. ^{1}H NMR (400 MHz, CDCl$_3$): δ 7.42 (dd, J = 7.6, 1.6 Hz, 2H), 7.05 – 6.91 (m, 4H), 6.74 (dd, J = 18.0, 11.9 Hz, 1H), 6.28 (dd, J = 7.9, 1.4 Hz, 2H), 6.18 (d, J = 18.0 Hz, 1H), 5.77 (d, J = 11.9 Hz, 1H), 1.61 (s, 6H). ^{13}C NMR (101 MHz, CDCl$_3$): δ 138.72, 131.31, 126.91, 125.48, 124.75, 122.15, 112.96, 36.14, 30.57. ^{19}F NMR (376 MHz, CDCl$_3$): δ -142.25 to -142.52 (m, 2F), -144.91 (dd, J = 21.7, 11.4 Hz, 2F). *m/z*: cal. for $C_{23}H_{17}F_4N$ 383.38 [M+ H], found 384.13. FT-IR. ν_{max} in cm^{-1} (KBr): 3037, 2984, 2910, 1936, 1699, 1629, 1592, 1504, 1476, 1450, 1331, 1271, 1248, 1140, 1044, 967, 939, 799, 747.

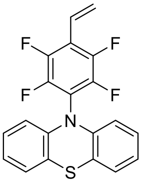

10-(2,3,5,6-tetrafluoro-4-vinylphenyl)-10*H*-phenothiazine (M4) was prepared from phenothiazine (0.45 g. 2.2 mmol), sodium *tert*-butoxide (0.26 g, 2.7 mmol), 2,3,4,5,6-pentafluorostyrene (0.66 g, 3.4 mmol) and dry DMF (15 mL) by using the general procedure, and was isolated in 44% yield as yellow crystals. mp: 119–123 °C. ^{1}H NMR (400 MHz, CDCl$_3$): δ 7.00 (dd, J = 7.4, 1.7 Hz, 2H), 6.86

(dtd, J = 21.3, 7.4, 1.5 Hz, 4H), 6.71 (dd, J = 18.0, 11.9 Hz, 1H), 6.19 (dd, J = 18.0, 9.9 Hz, 3H), 5.76 (d, J = 11.9 Hz, 1H). ^{13}C NMR (101 MHz, $CDCl_3$): δ 141.73, 127.35, 127.16, 125.02, 123.81, 122.03, 121.86, 115.25. ^{19}F NMR (376 MHz, $CDCl_3$): δ -142.03 (td, J = 13.7, 4.4 Hz, 2F), -144.17 (td, J = 13.6, 4.4 Hz, 2F). *m/z*: cal. for $C_{20}H_{11}F_4NS$ 373.37 [M+ H], found 373.32. FT-IR. ν_{max} in cm^{-1} (KBr): 3014; 2947; 1888; 1590, 1574, 1487, 1464, 1308, 1239, 966, 939, 844, 744, 715.

General procedure for polymer synthesis

The synthesized monomer (M1–M4) (0.1 g) was dissolved in 0.5 mL of dry THF under nitrogen atmosphere. Then, the mixture was heated to 60 °C, azobisisobutyronitrile (AIBN) (0.01 g) was added, and the mixture was stirred for additional 6 h. When the polymerization was completed, the product was precipitated in 20 mL of stirred cold methanol. The polymer was reprecipitated three times in excess of methanol. Then, the polymer was filtered, washed with methanol, and dried under vacuum.

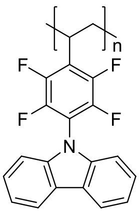

Poly(9-(2,3,5,6-tetrafluoro-4-vinylphenyl)-9*H*-carbazole) (P1) was synthesized according to the general procedure (white powder) in 89% of yield (89 mg).

^{1}H NMR (400 MHz, $CDCl_3$) δ 7.95 – 7.71 (m, 2H), 7.07 – 6.54 (m, J = 6.7 Hz, 6H), 3.02 – 2.84 (m, 1H), 2.58 – 2.29 (m, 2H). FT-IR. ν_{max} in cm^{-1} (KBr): 2360, 2341, 1738, 1514, 1477, 1448, 1332, 1266, 1224, 1155, 963, 907, 804, 742, 719.

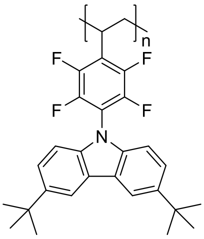

Poly[3,6-di-*tert*-butyl-9-(2,3,5,6-tetrafluoro-4-vinylphenyl)-9*H*-carbazole] (P2) was synthesized according to the general procedure and isolated as a white powder in 81% of yield (81 mg). ^{1}H NMR (400 MHz, $CDCl_3$) δ 7.98 (s, 1H), 7.81 (s, 1H), 7.15 – 6.11 (m, 4H), 3.58 – 3.07 (m, 1H), 2.75 – 2.22 (m, 2H), 1.24 (s, 18H). FT-IR. ν_{max} in cm^{-1} (KBr): 2962, 2905, 2865, 1651, 1515, 1489, 1457, 1364, 1322, 1296, 1265, 1232, 1162, 970, 875, 810, 704.

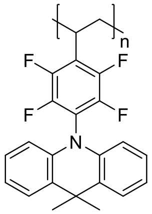

Poly[9,9-dimethyl-10-(2,3,5,6-tetrafluoro-4-vinylphenyl)-9,10-dihydroacridine] (P3) was synthesized according to the general procedure. The polymer was isolated as an off-white powder in 74% of yield (74 mg). ^{1}H NMR (400 MHz, $CDCl_3$) δ 7.37 (m, 2H), 7.12 – 6.34 (m, 4H), 6.17 (m, 2H), 3.33 – 3.02 (m, 1H), 2.72 – 2.16 (m, 2H), 1.52 (s, 6H). FT-IR. ν_{max} in cm^{-1} (KBr): 3072, 3087, 2971, 2865, 1638, 1596, 1487, 1453, 1331, 1270, 1238, 1164, 1048, 974, 957, 794, 744.

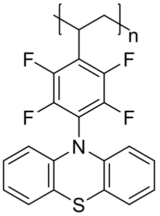

Poly[10-(2,3,5,6-tetrafluoro-4-vinylphenyl)-10*H*-phenothiazine] (P4) was synthesized according to the general procedure and isolated in 63% of yield (63 mg) as a yellow powder. ^{1}H NMR (400 MHz, $CDCl_3$) δ 7.16 – 6.46 (m, 6H), 6.43 – 5.70 (m, 2H), 3.28 – 2.82 (m, 1H), 2.71 – 2.21 (m, 2H). FT-IR. ν_{max} in cm^{-1} (KBr): 3068, 2953, 2879, 1931,1677, 1647, 1592, 1488, 1465, 1443, 1309, 1233, 1127, 1046, 955, 796, 742.

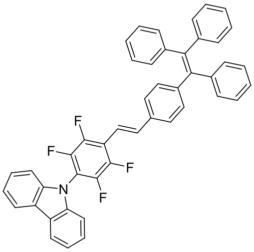

9-(2,3,5,6-Tetrafluoro-4-(4-(1,2,2-triphenylvinyl) styryl)phenyl)-9*H*-carbazole (C4FS1) was synthesized with a procedure similar to that reported previously[84]. 1-(4-Bromophenyl)-1,2,2-triphenylethylene (0.27 g, 0.65 mmol) and 9-(2, 3, 5, 6-tetrafluoro-4-vinyl-phenyl)-9*H*-carbazole (0.2 g, 0.59 mmol) were dissolved in 9 mL of dry DMF under argon atmosphere. Then, Pd(OAc)$_2$ (0.003 g, 0.012 mmol), P(*o*-tolyl)$_3$ (0,004 g, 0.012 mmol) and triethylamine (7 mL) were added. The solution was stirred at 110°C f or 12 h. The reaction mixture was filtered through Celite. The filtrate was extracted with EtOAc/water, washed with saturated brine solution, dried over Na_2SO_4, and concentrated under reduced pressure. The crude product was purified by column chromatography on silica gel by using hexane and dichloromethane as eluent mixture of solvents at a volume ratio of 10:1. After recrystallization from the eluent mixture of solvents, pale yellow crystals were obtained (0.23 g, 58%). mp: 219–221 °C (DSC) ^{1}H NMR (400 MHz, $CDCl_3$) δ 8.15 (d, J = 7.7 Hz, 2H, Ar), 7.53 (d, J = 16.8 Hz, 1H, CH), 7.49 – 7.43 (m, 2H, Ar), 7.38 – 7.32 (m, 4H, Ar), 7.22 – 7.02 (m, 20H, Ar, CH). ^{13}C NMR (101 MHz, $CDCl_3$) δ 145.04, 143.54, 143.45, 141.74, 140.27, 140.00, 137.99, 134.41, 131.94, 131.75, 131.36, 127.86, 127.79, 127.68, 126.71, 126.63, 126.60, 126.50, 126.43, 124.03, 121.08, 120.48, 118.49, 117.20, 112.85, 109.90. Elemental analysis cal. for $C_{46}H_{29}F_4N$: C, 82.25; H, 4.35; F, 11.31; N, 2.09. Found (%): C, 82.16; H, 4.41; F, 11.28; N, 2.15.

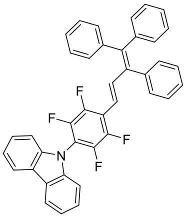

9-(2,3,5,6-tetrafluoro-4-(3,4,4-triphenylbuta-1,3-dien-1-yl)phenyl)-9*H*-carbazole (C4FS2) was prepared by a similar procedure to that of C4FS1. 2-Bromo-1,1,2-triphenylethylene (0.26 g, 0.77 mmol), 9-(2, 3, 5, 6-tetrafluoro-4-vinyl-phenyl)-9*H*-carbazole (0.24g, 0.7mmol), Pd(OAc)$_2$ (0,003g, 0.014mmol), P(*o*-tolyl)$_3$ (0,004 g, 0.014 mmol), triethylamine (9 mL) were stirred in dry DMF under argon at 120°C for 14 h. The mixture was filtered through Celite and extracted with ethyl acetate, and the organic phase was washed with water and brine. The solution was dried over Na_2SO_4, and the solvent was removed. The crude product was purified by column chromatography by using hexane/dichloromethane (10:1) as an eluent. Bright yellow crystals (0.26 g, 62%) were obtained after recrystallization from hexane. mp: 146 – 148 °C (DSC). ^{1}H NMR (400 MHz, $CDCl_3$) δ 8.13 (d, J = 7.7 Hz, 2H, Ar), 7.69 (d, J = 16.4 Hz, 1H, CH), 7.48 – 7.23 (m, 14H, Ar), 7.13 (d, J = 8.1 Hz, 2H, Ar), 7.10 – 7.05 (m, 3H, Ar), 6.97 – 6.93 (m, 2H, Ar), 6.36 (d, J = 16.4 Hz, 1H, CH). ^{13}C NMR (101 MHz, $CDCl_3$) δ 146.77, 145.92, 145.07, 144.22, 143.42, 142.28, 141.76, 140.52, 140.00, 139.23, 138.72, 131.43, 131.11, 131.05, 128.22, 128.10, 128.02, 127.45, 127.18, 126.84, 126.38, 123.97, 121.00, 120.45, 117.92, 117.00, 113.86, 109.85. MS *m/z*: cal. for $C_{40}H_{25}F_4N$ 596.63 [M+ H], found 596.79; cal. for C40H25F4N 618.63 [M+ Na], found 618.42. Elemental analysis cal. for $C_{40}H_{25}F_4N$: C, 80.66; H, 4.23; F, 12.76; N, 2.35. Found (%): C, 80.59; H, 4.33; F, 12.70; N, 2.38.

General procedure of acid-catalysed Friedlander synthesis

The compounds were synthesized similarly to the previously reported procedure [34]. To the solution of *o*-aminobenzophenone (2 mmol) and iodoacetophenone (2 mmol) in glacial acetic acid (15 ml), sulphuric acid (5 ml) was added and refluxed for 12 hours. Upon completion of the reaction, the mixture was poured into ice water with concentrated ammonium hydroxide. The aqueous mixture was extracted with ethyl acetate, concentrated and dried over anhydrous Na_2SO_4. The product was purified by column chromatography by using the eluent mixture of hexane and acetone at a volume ratio of 5:1 and crystalized from methanol.

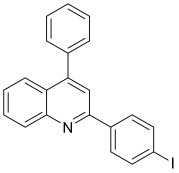

2-(4-Iodophenyl)-4-phenylquinoline (pIPPQ) was prepared by using the general procedure and was isolated in 77% yield (0.62 g) as a yellowish powder. ^{1}H NMR (400 MHz, $CDCl_3$) δ 8.14 (d, J = 8.4 Hz, 1H), 8.01 (d, J = 8.5 Hz, 2H), 7.82 (d, J = 8.2 Hz, 1H), 7.70 (s, 1H), 7.66 (t, J = 7.2 Hz, 1H), 7.57 (d, J = 8.5 Hz, 2H), 7.49 – 7.43 (m, 5H), 7.43 – 7.38 (m, 1H) ppm. ^{13}C NMR (101 MHz, $CDCl_3$) δ 155.58, 149.45, 148.80, 138.51, 138.27, 131.99, 130.12, 129.73, 129.56, 129.13, 128.66, 128.53, 126.59, 125.88, 125.72, 123.98, 118.86 ppm. ESI-MS (*m/z*): calculated for $C_{21}H_{14}IN$ 408.25 (M^++H), found 408.12.

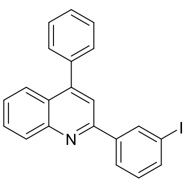

2-(3-Iodophenyl)-4-phenylquinoline (mIPPQ) was prepared by using the general procedure and was isolated in 70% yield (0.56 g) as a yellow powder. ^{1}H NMR (400 MHz, $CDCl_3$) δ 8.48 (s, 1H), 8.32 (d, J = 8.3 Hz, 1H), 8.12 (d, J = 7.8 Hz, 1H), 7.87 (d, J = 8.4 Hz, 1H), 7.76 – 7.68 (m, 3H), 7.52 – 7.43 (m, 6H), 7.23 – 7.17 (t, J = 7.8 Hz, 1H) ppm. ^{13}C NMR (101 MHz, $CDCl_3$) δ 155.01, 149.69, 148.57, 141.50, 138.31, 138.15, 136.58, 130.50, 130.05, 129.87, 129.57, 128.69, 128.61, 126.82, 126.79, 125.95, 125.74, 119.08, 94.93 ppm. ESI-MS (*m/z*): calculated for $C_{21}H_{14}IN$ 408.25 (M^++H), found 408.19.

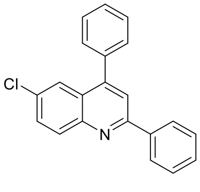

6-chloro-2,4-diphenylquinoline was prepared by using the general procedure from 2-amino-5-chlorobenzophenone (0.5 g, 2.2 mmol) and acetophenone (0.31 g, 2.6 mmol) and was isolated in 62% yield (0.42 g) as a yellow powder. ^{1}H NMR (400 MHz, $CDCl_3$) δ 8.11 (t, *J* = 8.2 Hz, 3H), 7.79 (d, *J* = 1.9 Hz, 1H), 7.76 (s, 1H), 7.59 (dd, *J* = 9.0, 2.0 Hz, 1H), 7.52 – 7.36 (m, 8H). ^{13}C NMR (101 MHz, $CDCl_3$) δ 157.04, 148.66, 147.06, 139.02, 137.71, 132.31, 131.61, 130.57, 129.71, 129.46, 128.95, 128.86, 128.78, 127.61, 126.52, 124.53, 120.10. ESI-MS (*m/z*): calculated for $C_{21}H_{14}ClN$ 315.80 (M^++H), found 315.72.

General procedure of the Ullmann reaction:

A mixture of pIPPQ or mIPPQ (0.3 g, 0.7 mmol), carbazole (0.15 g, 0.8 mmol), K_2CO_3 (0.31 g, 2 mmol), Cu (0.005 g, 0.07 mmol) and 18-crown-6 (0.002 g, 0.007 mmol) in 1,2-dichlorobenzene (9 mL) was heated at 170 °C under argon atmosphere overnight. After cooling to room temperature, the reaction mixture was filtered through Celite. The solvent was removed under reduced pressure, and the product was purified by column chromatography on silica gel by using the eluent mixture of hexane and ethyl acetate with the volume ratio of 10:1. Recrystallization from isopropanol/DMF mixture provided pure products

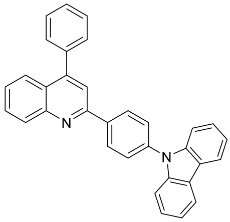

9-(4-(4-Phenylquinolin-2-yl)phenyl)-9*H*-carbazole (pCzPPQ) was obtained according to the general procedure and was isolated in 48% yield (0.32 g) as white crystals. mp: 152 – 154 °C. ^{1}H NMR (400 MHz, $CDCl_3$) δ 8.36 (d, J = 8.3 Hz, 2H), 8.21 (d, J = 8.4 Hz, 1H), 8.08 (d, J = 7.7 Hz, 2H), 7.87 (d, J = 8.4 Hz, 1H), 7.84 (s, 1H), 7.73 – 7.63 (m, 3H), 7.56 – 7.40 (m, 8H), 7.36 (t, J = 7.6 Hz, 2H), 7.23 (t, J = 7.4 Hz, 2H) ppm. ^{13}C NMR (101 MHz, $CDCl_3$) δ 156.00, 149.52, 148.92, 140.75, 138.78, 138.71, 138.34, 130.19, 129.78, 129.61, 129.15, 128.70, 128.56, 127.31, 126.61, 126.07, 125.90, 125.77, 123.57, 120.38, 120.13, 119.26, 109.89 ppm. Elemental analysis cal. for $C_{33}H_{22}N_2$: C, 88.76; H, 4.97; N, 6.27. Found (%): C, 88.02; H, 4.33; N, 6.15. ESI-MS (*m/z*): calculated for $C_{33}H_{22}N_2$ 447.54 (M^{+}+H), found 447.51.

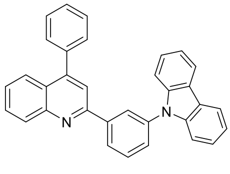

9-(3-(4-Phenylquinolin-2-yl)phenyl)-9*H*-carbazole (mCzPPQ) was obtained according to the general procedure and was isolated in 53% yield (0.36 g) as a white powder. mp: 140 – 142 °C. ^{1}H NMR (400 MHz, $CDCl_3$) δ 8.35 (s, 1H), 8.24 (d, J = 7.8 Hz, 1H), 8.14 (d, J = 8.5 Hz, 1H), 8.09 (d, J = 7.7 Hz, 2H), 7.84 (d, J = 8.4 Hz, 1H), 7.76 (s, 1H), 7.72 – 7.63 (m, 2H), 7.59 (d, J = 7.9 Hz, 1H), 7.50 – 7.38 (m, 8H), 7.34 (t, J = 7.6 Hz, 2H), 7.22 (t, J = 7.4 Hz, 2H) ppm. ^{13}C NMR (101 MHz, $CDCl_3$) δ 155.76, 149.57, 148.85, 141.78, 140.99, 138.35, 138.22, 130.40, 130.24, 129.75, 129.57, 128.66, 128.53, 128.04, 126.69, 126.45, 126.02, 125.98, 125.73, 123.44, 120.35, 120.02, 119.98, 119.18, 109.88 ppm. Elemental analysis cal. for $C_{33}H_{22}N_2$: C, 88.76; H, 4.97; N, 6.27. Found (%): C, 88.11; H, 4.42; N, 6.25. ESI-MS (*m/z*): calculated for $C_{33}H_{22}N_2$ 447.54 (M^{+}+H), found 447.34.

General procedure of the Buchwald-Hartwig reaction:

A mixture of quinoline halide (1.58 mmol), di-*tert*-butyl 9*H* phenothiazine (1.90 mmol), tris(dibenzylideneacetone) dipalladium (0) ($Pd_2(dba)_3$) (0.047 mmol), 2-dicyclohexylphosphino-2′,4′,6′-triisopropylbiphenyl (XPhos) (0.047 mmol) and sodium *tert*-butoxide (3.96 mmol) in toluene (12 ml) was stirred at 105 °C under inert atmosphere for 12 h. The mixture was extracted with DCM/water, washed with a saturated brine solution, dried over Na_2SO_4 and concentrated under reduced pressure. The crude product was purified by column chromatography on silica gel by using Hex:DCM as an eluent mixture at a volume ratio of 5:1. Recrystallization from isopropanol afforded the target products.

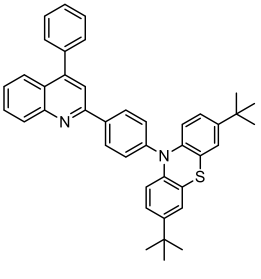

3,7-Di-*tert*-butyl-10-(4-(4-phenylquinolin-2-yl)phenyl) - 10*H*-phenothiazine (pPZPQ) was prepared by using the general procedure for the Buchwald-Hartwig reaction and was isolated in 67% yield (0.49 g) as yellow crystals. mp: 243 – 245 °C. ^{1}H NMR (400 MHz, $CDCl_3$) δ 8.16 (d, J = 8.4 Hz, 1H), 8.12 (d, *J* = 7.2 Hz, 2H), 7.99 (d, J = 8.5 Hz, 2H), 7.80 (d, J = 8.1 Hz, 1H), 7.73 (dd, *J* = 7.2, 2.2 Hz, 2H), 7.70 (s, 1H), 7.62 (t, J = 7.2 Hz, 1H), 7.57 (d, J = 8.3 Hz, 2H), 7.47 – 7.43 (m, 5H), 7.42 – 7.38 (m, 1H), 6.94 (s, 2H), 1.13 (s, 18H). ^{13}C NMR (101 MHz, $CDCl_3$) δ 146.22, 143.06, 140.70, 139.56, 139.50, 139.40, 137.82, 135.74, 132.57, 131.45, 129.57, 129.41, 129.24, 128.96, 128.91, 128.61, 127.53, 127.29, 124.19, 121.76, 120.59, 118.60, 115.55, 33.09, 30.24. ESI-MS (*m/z*): calculated for $C_{41}H_{38}N_2S$ 591.82 (M^++H), found 591.32.

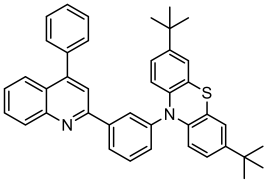

3,7-Di-*tert*-butyl-10-(3-(4-phenylquinolin-2-yl)phenyl)-10*H*-phenothiazine (mPZPQ) was prepared by using the general procedure for the Buchwald-Hartwig reaction and was isolated in 59% yield (0.43 g) as yellow crystals. mp: 226 – 228 °C. ^{1}H NMR (400 MHz, $CDCl_3$) δ 8.37 (s, 1H), 8.34 (d, J = 8.2 Hz, 1H), 8.15 (d, *J* = 7.2 Hz, 2H), 8.10 (d, J = 7.8 Hz, 1H), 7.85 (d, J = 8.4 Hz, 1H), 7.75 – 7.66 (m, 3H), 7.60 (dd, *J* = 7.2, 2.2 Hz, 2H) 7.55 – 7.45 (m, 6H), 7.20 – 7.12 (t, J = 7.8 Hz, 1H), 6.92 (s, 2H), 1.17 (s, 18H). ppm. ^{13}C NMR (101 MHz, $CDCl_3$) δ 159.21, 152.63, 150.32, 149.91, 147.32, 145.33, 144.92, 140.99, 139.66, 137.72, 137.15, 136.18, 131.26, 130.55, 129.92, 129.46, 128.79, 127.56, 126.80, 126.74, 126.03, 125.71, 122.18, 120.17, 94.93, 34.13, 31.35. ESI-MS (*m/z*): calculated for $C_{41}H_{38}N_2S$ 591.82 (M^++H), found 591.32.

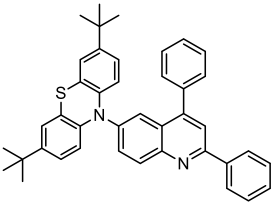

3,7-Di-*tert*-butyl-10-(2,4-diphenylquinolin-6-yl)-10*H*-phenothiazine (PZPQ) was prepared by using the general procedure for the Buchwald-Hartwig reaction and was isolated in 54% yield (0.51 g) as a yellow powder. mp: 242 – 244 °C. ^{1}H NMR (400 MHz, $CDCl_3$) δ 8.34 (d, *J* = 8.9 Hz, 1H), 8.15 (d, *J* = 7.2 Hz, 2H), 7.83 – 7.77 (m, 2H), 7.63 (dd, *J* = 8.9, 2.2 Hz, 1H), 7.51 – 7.36 (m, 8H), 7.03 (d, *J* = 2.1 Hz, 2H), 6.81 (dd, *J* = 8.5, 1.8 Hz, 2H), 6.19 (d, *J* = 8.6 Hz, 2H), 1.16 (s, 18H). ^{13}C NMR (101 MHz, $CDCl_3$) δ 149.25, 145.96, 141.70, 139.59, 139.54, 139.43, 137.84, 137.79, 132.47, 131.48, 129.58, 129.51, 129.04, 128.96, 128.83, 128.62, 127.63, 127.29, 124.09, 123.76, 120.99, 119.80, 116.65, 34.09, 31.24. ESI-MS (*m/z*): calculated for $C_{41}H_{38}N_2S$ 591.82 (M^++H), found 591.29.

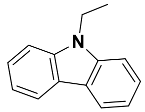

9-Ethyl-9*H*-carbazole was synthesized according to the previously reported procedure[89].

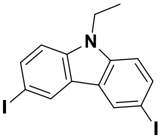

9-Ethyl-3,6-diiodo-9*H*-carbazole was obtained similarly to the known procedure[90].

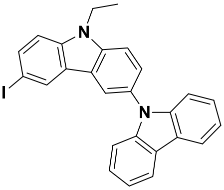

9-Ethyl-6-iodo-9*H*-3,9'-bicarbazole (2CzI) was prepared from 9-ethyl-3,6-diiodo-9*H*-carbazole (2.25 g, 5.02 mmol), 9*H* carbazole (0.7 g, 4.19 mmol), Cu (0.08 g, 1.26 mmol), 18-crown-6 (0.01 g, 0.042 mmol), K_2CO_3 (1.16 g, 8.37 mmol) in *o*-DCB by using the general procedure for Ullmann coupling and was isolated in 71% yield (1.44 g) as a white powder. ^{1}H NMR

(400 MHz, $CDCl_3$) δ 8.41 (d, *J* = 1.0 Hz, 1H), 8.22 (dd, *J* = 4.8, 2.9 Hz, 3H), 7.80 (dt, *J* = 8.6, 1.9 Hz, 1H), 7.66 (dd, *J* = 8.6, 1.9 Hz, 1H), 7.63 – 7.60 (m, 1H), 7.47 – 7.39 (m, 4H), 7.36 – 7.28 (m, 3H), 4.46 (q, *J* = 7.2 Hz, 2H), 1.54 (t, *J* = 7.2 Hz, 3H). ^{13}C NMR (101 MHz, $CDCl_3$) δ 141.84, 139.73, 139.02, 134.57, 129.59, 129.41, 125.96, 125.90, 125.08, 123.14, 122.59, 120.31, 119.74, 119.67, 110.89, 109.77, 109.71, 81.65, 37.98, 13.90. ESI-MS (*m/z*): calculated for $C_{26}H_{19}IN_2$ 486.35 (M^+), found 486.54.

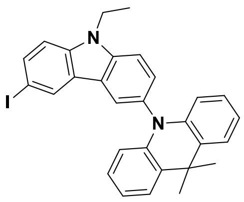

10-(9-Ethyl-6-iodo-9*H*-carbazol-3-yl)-9,9-dimethyl-9,10-dihydroacridine (ACzI) was prepared from 9-ethyl-3,6-diiodo-9*H*-carbazole (1.54 g, 3.44 mmol), 9,9-dimethyl-9,10-dihydroacridine (0.6 g, 2.87 mmol), Cu (0.06 g, 0.86 mmol), 18-crown-6 (0.01 g, 0.029 mmol), K_2CO_3 (0.79 g, 5.73 mmol) in *o*-DCB by using the general procedure for Ullmann coupling and was isolated in 52% yield (0.95 g) as a white powder. ^1H NMR (400 MHz, $CDCl_3$) δ 8.39 (d, *J* = 1.6 Hz, 1H) , 8.06 (d, *J* = 1.9 Hz, 1H), 7.79 (dd, *J* = 8.6, 1.6 Hz, 1H), 7.67 (d, *J* = 8.6 Hz, 1H), 7.55 – 7.49 (m, 2H), 7.47 – 7.44 (m, 1H), 7.30 (d, *J* = 8.7 Hz, 1H), 7.02 – 6.93 (m, 4H), 6.37 – 6.23 (m, 2H), 4.48 (q, *J* = 7.2 Hz, 2H), 1.78 (s, 6H), 1.56 (t, *J* = 7.2 Hz, 3H). ^{13}C NMR (101 MHz, $CDCl_3$) δ 141.64, 139.62, 139.21, 134.45, 132.80, 129.99, 129.63, 129.24, 126.33, 125.20, 125.18, 123.47, 123.37, 120.40, 114.26, 110.86, 110.75, 81.63, 37.98, 36.04, 31.44, 13.93. ESI-MS (*m/z*): calculated for $C_{29}H_{25}IN_2$ 528.43 (M^+), found 528.19.

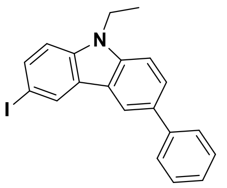

9-Ethyl-3-iodo-6-phenyl-9*H*-carbazole (PhCzI) was obtained by the Suzuki coupling reaction. A Schlenk flask was charged with phenylboronic acid acid (0.5 g, 4.1 mmol), 9-ethyl-3,6-diiodo-9*H*-carbazole (2.20 g, 4.92 mmol), tetrakis(triphenylphosphine)palladium(0) $Pd(PPh_3)_4$ (0.14 g, 0.12 mmol) and an aqueous 2M K_2CO_3 solution (6.15 ml) containing toluene (10 ml). The resulting solution was kept at inert atmosphere at 90 °C for 12 hours and then cooled down to room temperature. The crude product was extracted with water/DCM, and the organic phase was dried over Na_2SO_4. The solvent was removed, and the residue was purified by column chromatography by using hexane/ DCM (6/1) as an eluent. The target product was obtained in the 59% yield (0.96 g) as an oil-like product. ^1H NMR (400 MHz, $CDCl_3$) δ 8.42 (d, *J* = 1.0 Hz, 1H), 8.34 (d, *J* = 1.2 Hz, 1H), 7.92 (dd, *J* = 8.3, 1.6 Hz, 1H), 7.73 – 7.64 (m, 3H), 7.55 – 7.37 (m, 4H), 7.32 (t, *J* = 7.4 Hz, 1H), 4.41 (q, *J* = 7.2 Hz, 2H), 1.38 (t, *J* = 7.1 Hz, 3H). ^{13}C NMR (101 MHz, $CDCl_3$) δ 141.77, 140.45, 137.35, 133.12, 128.91, 127.22, 126.55, 126.50, 125.67, 124.87, 122.57, 120.54, 120.27, 108.54, 106.62, 102.35, 39.41, 13.76. ESI-MS (*m/z*): calculated for $C_{20}H_{16}IN$ 397.25 (M^+), found 397.43.

General procedure of the Rosenmund-von Braun cyanation:

Corresponding aryl halide (1 eq.) and copper (I) cyanide CuCN (3 eq.) in DMF were charged in a flask and mixed for 20 hours at 130 °C. After the completion of the reaction, the product was poured in water with ammonia and stirred for 1 hour. The mixture was extracted with water/DCM. The organic layer was dried with anhydrous Na_2SO_4 and concentrated under reduced pressure. The crude product was purified by column chromatography by using hexane/dichloromethane (2:1) as an eluent and crystalized from isopropanol.

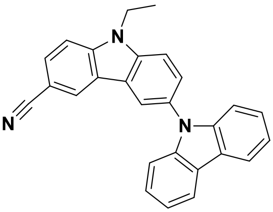

9-Ethyl-9*H*-[3,9'-bicarbazole]-6-carbonitrile (2CzCN) was obtained from 2CzI (0.5 g, 1.00 mmol) and CuCN (0.28 g, 3.08 mmol) in DMF (12 ml) by using the general procedure and isolated in 52% yield (0.21 g). mp: 217 – 219 °C. ^{1}H NMR (400 MHz, $CDCl_3$) δ 8.29 (d, *J* = 1.0 Hz, 1H), 8.18 (d, *J* = 1.6 Hz, 1H), 8.10 (d, *J* = 7.7 Hz, 2H), 7.67 (dd, *J* = 8.6, 1.4 Hz, 1H), 7.61 (dd, *J* = 8.6, 1.8 Hz, 1H), 7.57 (d, *J* = 8.6 Hz, 1H), 7.44 (d, *J* = 8.6 Hz, 1H), 7.36 – 7.30 (m, 2H), 7.27 (d, *J* = 8.0 Hz, 2H), 7.25 – 7.19 (m, 2H), 4.41 (q, *J* = 7.2 Hz, 2H), 1.47 (t, *J* = 7.2 Hz, 3H). ^{13}C NMR (101 MHz, $CDCl_3$) δ 142.26, 141.73, 139.60, 130.45, 129.59, 126.77, 125.99, 125.70, 123.24, 123.08, 122.77, 120.39, 120.33, 119.98, 119.86, 110.31, 109.64, 109.59, 102.15, 38.26, 13.95. ESI-MS (*m/z*): calculated for $C_{27}H_{19}N_3$ 385.16 (M^+), found 385.68.

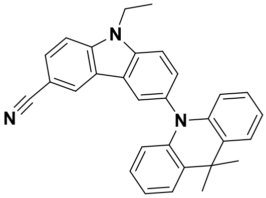

6-(9,9-dimethylacridin-10(9*H*)-yl)-9-Ethyl-9*H*-carbazole-3-carbonitrile (ACzCN) was obtained from ACzI (0.6 g, 1.14 mmol) and CuCN (0.31 g, 3.41 mmol) in DMF (13 ml) by using the general procedure and isolated in 46% yield (0.22 g). mp: 252 – 254 °C. ^{1}H NMR (400 MHz, $CDCl_3$) δ 8.27 (d, *J* = 1.0 Hz, 1H), 8.02 (d, *J* = 1.8 Hz, 1H), 7.68 (dd, *J* = 8.6, 1.5 Hz, 1H), 7.62 (d, *J* = 8.6 Hz, 1H), 7.47 – 7.38 (m, 4H), 6.88 – 6.82 (m, 4H), 6.29 – 6.09 (m, 2H), 4.41 (q, *J* = 7.2 Hz, 2H), 1.67 (s, 6H), 1.49 (t, *J* = 7.2 Hz, 4H). ^{13}C NMR (101 MHz, $CDCl_3$) δ 142.17, 141.48, 139.83, 133.83, 130.21, 130.06, 129.49, 126.34, 125.69, 125.32, 123.96, 123.72, 122.86, 120.55, 120.35, 114.13, 111.33, 109.54, 102.12, 38.26, 36.04, 31.45, 13.96. ESI-MS (*m/z*): calculated for $C_{30}H_{25}N_3$ 427.54 (M^+), found 427.42.

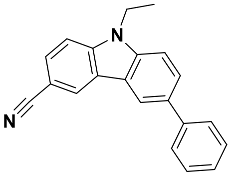

9-Ethyl-6-phenyl-9*H*-carbazole-3-carbonitrile (PhCzCN) was obtained from PhCzI (0.65 g, 1.64 mmol) and CuCN (0.44 g, 4.91 mmol) in DMF (14 ml) by using the general procedure and isolated in 60% yield (0.29 g). mp: 128 – 130 °C. ^{1}H NMR (400 MHz, $CDCl_3$) δ 8.35 (d, *J* = 0.9 Hz, 1H), 8.22 (d, *J* = 1.3 Hz, 1H), 7.72 (dd, *J* = 8.5, 1.6 Hz, 1H), 7.65 – 7.60 (m, 3H), 7.46 – 7.35 (m, 4H), 7.29 (t, *J* = 7.4 Hz, 1H), 4.33 (q, *J* = 7.2 Hz, 2H), 1.40 (t, *J* = 7.2 Hz, 3H). ^{13}C NMR (101 MHz, $CDCl_3$) δ 142.03, 141.46, 139.96, 134.03, 129.12, 128.92, 127.34, 126.91, 126.72, 125.40, 123.26, 122.57, 120.61, 119.28, 109.39, 109.27, 101.66, 38.05, 13.86. ESI-MS (*m/z*): calculated for $C_{21}H_{16}N_2$ 296.37 (M^+), found 296.93.

4. Results and Discussion

4.1. Tetrafluorostyrene-based donor-acceptor monomers and polymers

4.1.1. Synthetic routes

Investigation of new tetrafluorostyrene-based monomers and polymers was previously published by the author of this thesis[91]. The synthesis and structures of the target monomers and polymers are shown in Scheme 4.1. Tetrafluorostyrene-based monomers were synthesized by nucleophilic substitution of a fluorine atom by NH-heterocycle in moderate yields. Radical polymerization of vinyl monomers was performed by using AIBN as the initiator.

The molecule structures of the monomers were confirmed by ^{1}H and ^{13}C, ^{19}F NMR, mass and IR spectroscopy. The structures of the polymers were verified by analysis of ^{1}H NMR and IR spectra.

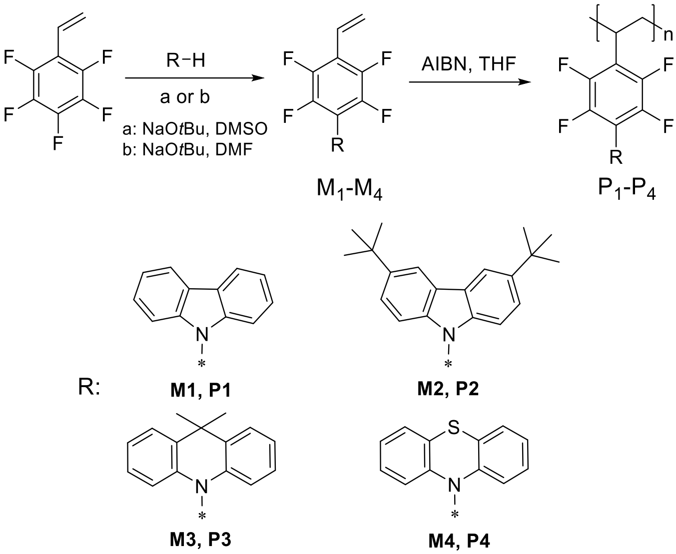

Scheme 4.1. Synthetic route towards monomers and polymers M1–M4, P1–P4

4.1.2. SEC analysis of polymers

Fluorostyrene-based monomers underwent self- and initiated free radical polymerization. Number average molecular weights of the polymers and their polydispersity indices (PDI) were estimated by size exclusion chromatography (SEC). The data is collected in Table 4.1. The monomers and polymers were found to be soluble in organic solvents, such as toluene, tetrahydrofuran (THF), dichloromethane (DCM), and dimethylformamide (DMF). The number-average molecular weights (M_n) of the polymers obtained in the reactions initiated with AIBN ranged from 8560 up to 113590 in dependence on the nature of chromophores in the structures of monomers. The polymer with carbazole fragment P1 showed the highest M_n and weight-average molecular weight (M_w) of 113590 and 201670, respectively (Table

4.1). The higher molecular weight of the carbazolyl-containing polymer can be attributed to the decreased steric hindrance of the pendant chromophore and/or less intensive chain transfer and chain termination reactions. The PDI of the synthesized polymers ranged from 1.2 to 1.8.

Table 4.1. Molecular weights of polymers

Polymer	M_n	M_w	PDI
P1	113590	201670	1.8
P2	14140	17000	1.2
P3	11390	13400	1.2
P4	8560	11430	1.3

M_n is number-average molecular weight; **M_w** is weight-average molecular weight; **PDI** is polydispersity index

The highest PDI was observed for P1 with the highest molecular weight. This observation can apparently be explained by the higher rate of chain transfer reactions in the synthesis of P1. In addition, since the C-3 and C-6 positions of the carbazole moiety are very active, some side reactions including step-growth polymerization could occur and affect the PDI of the polymer[92].

4.1.3. Computational calculations

Theoretical calculations of the structures of the monomers were carried out with *Gaussian 16* program. The geometries were optimized in the electronic ground state by using the basic density functional (DFT) method with the 6–31 G** basis set in vacuum conditions. It was found that the lowest unoccupied molecular orbital (LUMO) for monomers M1–M4 is mainly localized on the tetrafluorostyrene fragment due to the presence of the accepting fluorine atoms, which resulted in the similar electron affinity values of 2.33–2.44 eV for the series of monomers (Table 4.2). According to the calculations, the torsion angles between the donating units and the tetrafluorostyrene acceptor range from 61° to 88°, with the lowest value for carbazole-based M2, and the highest one for phenothiazine-based monomer M4. For compounds M1, M2 containing a carbazolyl group, the lower torsion angle of 61° and 62° between the donor and the tetrafluorostyrene acceptor resulted in a higher overlap between the HOMO and LUMO orbitals. HOMO is delocalized not only on the electron-donating carbazole moiety but also on the styrene unit. However, for M3 and M4 which contain strong phenothiazine and 9,9-dimethyl acridan donor moieties, the torsion angles of 85° and 88° resulted in considerable HOMO-LUMO separation.

A replacement of the donating fragment from the carbazole moiety to the acridan or phenothiazine units increases the twisting angle between the donor and acceptor units, which leads to the decrease of the energy gap value. Fig. 4.1 shows the optimized molecular configurations along with the frontier orbitals of the investigated compounds. The highly twisted molecular structures of M3 and M4 determine spatially separated HOMO-LUMO frontier orbital distributions with the highest molecular orbitals (HOMO) centred on phenothiazine and acridan units. The overlap between HOMO and LUMO is one of the factors influencing the singlet-triplet energy splitting ($\Delta E_{S\text{-}T}$). Phenothiazine containing compound M4 with the lowest extent of the HOMO-LUMO overlap demonstrated the lowest value of experimentally obtained $\Delta E_{S\text{-}T}$, while compound M2 containing a weaker di-*tert*-butyl-carbazole donor possessed the highest $\Delta E_{S\text{-}T}$ (Table 4.4).

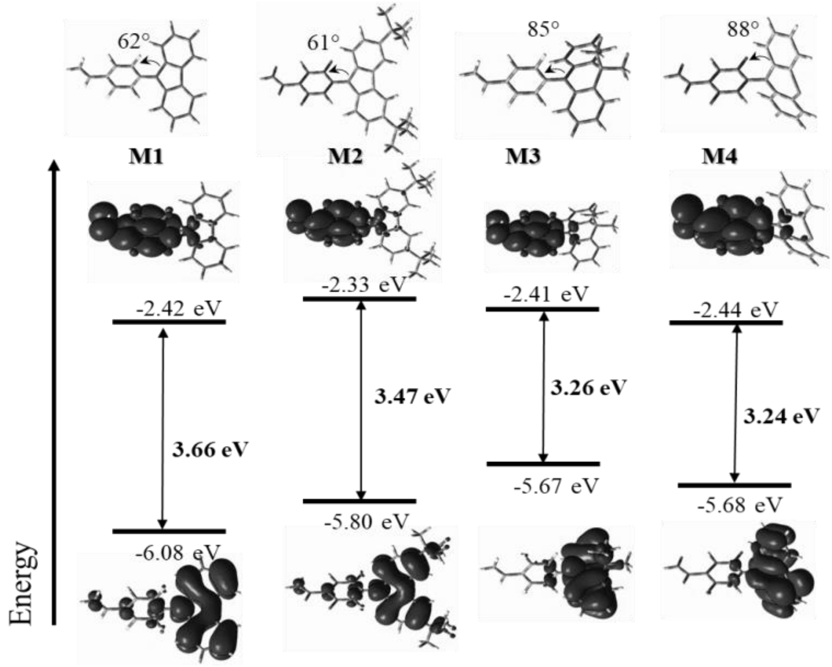

Fig. 4.1. Optimized geometries, frontier orbitals and HOMO-LUMO gaps of M1–M4

The theoretically calculated HOMO-LUMO values are in good agreement with the data obtained from CV measurements (Table 4.2). The trend of the energy band gaps obtained from DFT calculations is also consistent with the CV data and the increase in the line of M4 < M3 < M2 < M1 with the values of 3.36 eV < 3.42 eV < 3.43 eV < 3.54 eV.

4.1.4. Electrochemical properties

Cyclic voltammetry (CV) measurements were performed for the synthesized monomers and polymers. For compounds M2 and M4 containing 3,6-di-*tert*-butyl carbazole and phenothiazine fragments, reversible oxidation waves were observed. In the meantime, compound M1 with the active C-3 and C-6 position of the carbazole moiety was characterized with irreversible oxidation processes due to the formation of carbazole radical cations[93]. All the studied monomers and polymers demonstrated irreversible reduction waves with reduction potentials (E_{red}) varying from -2.30 – -2.37 V for the monomers and -2.39 – -2.54 V for the polymers (Table 4.2). The ionization potential (IP_{CV}) and electron affinities were determined by using the formula $IP_{CV} = |e|\ (4.8 + E_{ox})$ and $EA_{CV} = |e|\ (4.8 + E_{red})$. It should be noted that, for the DCM solution of polymers (P1–P4), no reduction signals at the negative potential range were detected; therefore, the reduction processes for the polymeric compounds were recorded in the THF solvent due to the more accessible potential window of the THF/ 0.1M Bu_4NPF_6 electrolyte system (Fig. 4.2). Among the monomers and polymers, the highest oxidation potentials of 1.01 V and 1.13 V were observed for M1 and P1 containing a carbazole donor moiety. A slightly lower Eox value observed for M1 in comparison with that of P1 can be explained by the prolonged conjugation of the monomer containing an unsaturated vinyl group. The lower oxidation potentials, and, therefore, IP_{CV} recorded for M3 and M4 in respect to carbazole based monomers M1 and M2 are conceivably due to the presence of the stronger electron-donating effect of 9,9-dimethylacridan and phenothiazine fragments, respectively. Among the studied monomers (M1–M4), the lowest IP_{CV} value of 5.32 eV was observed for M4 containing a phenothiazine unit. The same trend was observed for the corresponding polymers.

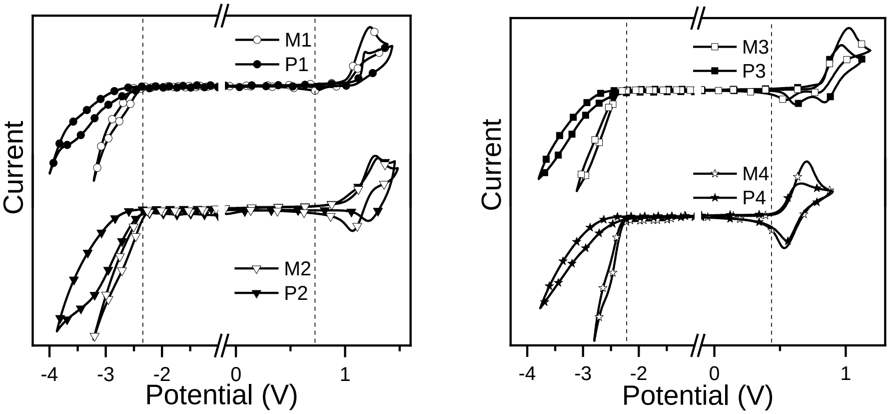

Fig. 4.2. Cyclic voltammograms of monomers (M1–M4) for CH_2Cl_2 solution and polymers (P1–P4) (oxidation process recorded for DCM and reduction part recorded for THF solutions) with 0.1M Bu_4NPF_6 electrolyte system

P4 with a phenothiazine unit demonstrated the lowest IP_{CV} value of 5.30 eV, while the highest IP_{CV} was observed for carbazole containing P1 (Table 4.2). Energy gaps (E^{elc}_g) estimated by CV measurements were calculated as the difference between IP_{CV} and EA_{CV} and ranged from 2.84 to 3.40 eV for monomers and from 2.89 to 3.60 eV for polymers. As expected, the highest E^{elc}_g values were observed for the carbazolyl-containing monomer and polymer (M1 and P1) and were found to be 3.40 eV and 3.60 eV, respectively. Phenothiazine containing compounds M4 and P4 were characterized with the lowest energy gaps of 2.84 eV and 2.89 eV, respectively. The E^{elc}_g values increased in the lines M4 < M3 < M2 < M1 and P4 < P3 < P2 < P1, which is in agreement with the increment of electron-donating abilities of the linked donor units. The band-gap values of the polymers were found to be close to those of the corresponding monomers. The optical band gap values observed for monomers and polymers were in good agreement with the band gaps obtained from CV measurements (Table 4.2).

Table 4.2. Electrochemical and optical characteristics of compounds M1–M4 and P1–P4

Compounds	E_{ox} V	E_{red} V	IP_{CV}, eV	E_{HOMO}, eV	EA_{CV}, eV	E_{LUMO}, eV	E^{elc}_{g}, eV	$E^{opt}_{g,\mathrm{film}}$, eV	E^{theor}_{g}, eV
M1	1.01	-2.32	5.81	-6.08	2.41	-2.42	3.40	3.57	3.66
P1	1.13	-2.49	5.93	-	2.31	-	3.60	3.62	-
M2	1.07	-2.30	5.87	-5.80	2.50	-2.33	3.37	3.43	3.47
P2	0.97	-2.42	5.77	-	2.38	-	3.39	3.47	-
M3	0.81	-2.37	5.61	-5.67	2.43	-2.41	3.18	3.31	3.26
P3	0.80	-2.54	5.60	-	2.26	-	3.34	3.42	-
M4	0.52	-2.32	5.32	-5.68	2.48	-2.44	2.84	2.99	3.24
P4	0.50	-2.39	5.30	-	2.41	-	2.89	3.24	-

E_{ox}/E_{red} is the onset of the first oxidation/reduction wave; IP_{CV} is the ionization potential determined by formula $IP_{CV} = |e|\ (4.8 + E_{ox})$; EA_{CV} is the electron affinity calculated by formula $EA_{CV} = |e|\ (4.8 + E_{red})$; E^{elc}_{g} is the electrochemical band gap determined by formula $E^{elc}_{g} = IP_{CV} - EA_{CV}$; $E^{opt}_{g,\, film} = 1240/\lambda_{abs,\, onset,\, film}$; E_{HOMO}, E_{LUMO} are the theoretically calculated HOMO and LUMO energies for model compounds M1–M4;. E^{theor}_{g} is the theoretically calculated energy band gap obtained by using the B3LYP/6-31G** basis set.

4.1.5. Thermal properties

The thermal and morphological stability of materials and their layers is an important issue in organic optoelectronics. The thermal properties of perfluorostyrene based monomers (M1–M4) and of the corresponding polymers (P1–P4) were studied by TGA and DSC (Fig. 4.3, Fig. 4.4).

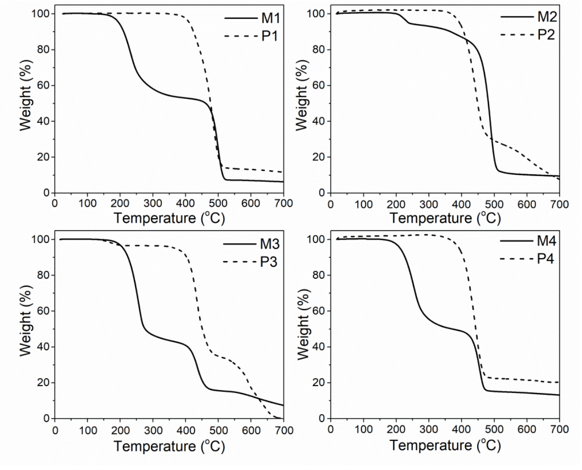

Fig. 4.3. TGA profiles of the investigated monomers (solid lines) and the corresponding polymers (dashed lines)

The monomers demonstrated moderate thermal stability with 5% weight loss at temperatures ranging from 194 to 237 °C. The thermal stability of the polymers was found to be considerably higher. Their 5% weight loss temperatures were in the range of 366–411 °C (Table 4.3). For all the studied monomers, two peaks were observed on the TGA curves which correspond to the two processes which occur during the heating of the samples. In the first step, the weight loss is attributed to the sublimation processes of the monomers confirmed by a comparison of the IR spectra of the sublimed substance and the monomeric compounds. In the second step, the decomposition of the corresponding polymeric compound occurs, formed after thermal self-polymerization of vinyl-containing monomers occurs (Fig. 4.3). The higher 5% weight loss temperature of M2 relative to those of the other studied tetrafluorostyrene compounds can be explained by the higher molecular weight of M2. The increased molecular weight of the polymers and the absence of sublimation resulted in higher thermal stability and considerably higher 5% weight loss temperatures (T_d) of the polymers relative to those of the corresponding monomers (Table 4.3).

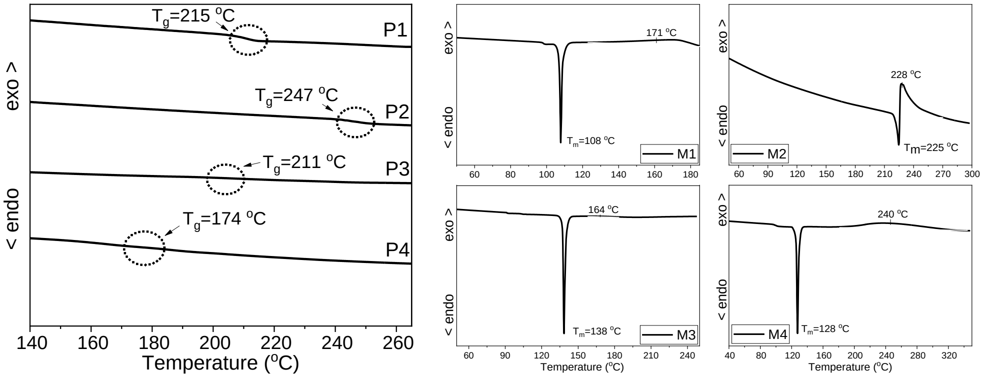

Fig. 4.4. DSC curves of monomers M1–M4 and polymers P1–P4

Surprisingly, carbazole containing monomer M1 exhibited the lowest T_d value of 194 °C among the monomers, while its polymer P1 demonstrated the highest T_d value of 411 °C. This discrepancy can be explained by the different processes causing the initial weight losses. In the case of M1, it is sublimation, while in the case of P1, it is thermal degradation. Polymers P1–P4 were obtained as amorphous substances, thus only glass transitions were observed during DSC heating scans.

Table 4.3. Thermal characteristics of monomers and polymers

Monomer/Polymer	T_g^a	T_m^a	T_d^b
M1 / P1	-/ 215	108 / -	194 / 411
M2 / P2	-/ 247	225 / -	237 / 392
M3 / P3	-/ 211	138 / -	210 / 366
M4 / P4	-/ 174	128 / -	213 / 387

T_g is the glass transition temperature, scan rate 10 °C/min, nitrogen atmosphere; T_m is the melting temperature; T_d is the 5% weight loss temperature, scan rate 20 °C/min, nitrogen atmosphere; ^{a} Estimated by DSC. ^{b} Estimated by TGA.

The highest glass transition temperature (T_g) of 247 °C was recorded for polymer P2, presumably due to the presence of bulky *tert*-butyl groups which restrict the rotational freedom of the monomeric fragments in the polymer chain[94]. Monomers M1–M4 were obtained after the synthesis and purification as crystalline materials; they revealed endothermic melting peaks during the first heating scans in the range of 108–225 °C. Cooling of the melts did not result in the formation of molecular glasses. Among the monomers, compound M2 showed the highest melting temperature of 225 °C, which can be assigned to the highest molecular weight of the monomer and to the strong intermolecular interaction of *tert*-butyl groups.

4.1.6. Photophysical properties

Incorporation of fragments with a different electron-donating ability in the *para*-position of the tetrafluorostyrene and polytetrafluorostyrene structures allows tuning the energy band-gap of the compounds and thus altering their photophysical properties. The shapes of the UV-vis spectra of the toluene solutions and the solid films of monomers M1–M4 were found to be similar to those of the corresponding polymers (P1–P4) with a negligible blue shift of the absorption spectra of the polymers (Fig. 4.6 (a, b)). Normalized UV-vis and fluorescence spectra of toluene solutions and solid films of the monomers and polymers are depicted in Fig. 4.6 and Fig. 4.7, and the data is collected in Table 4.4. The UV-vis spectra of the solid films of M1–M4 and P1–P4 were found to be almost identical to those of the corresponding toluene solutions (Fig. 4.6). For a better comparison and understanding of electronic transitions, the spectra of the solutions and films of separate carbazole (Cz), di-*tert*-butyl carbazole (*t*-BuCz), 9,9-dimethyl acridine (Acr) and phenothiazine donors along with the spectrum of the pentafluorostyrene (PFS) acceptor were recorded and are depicted in Fig. 4.5.

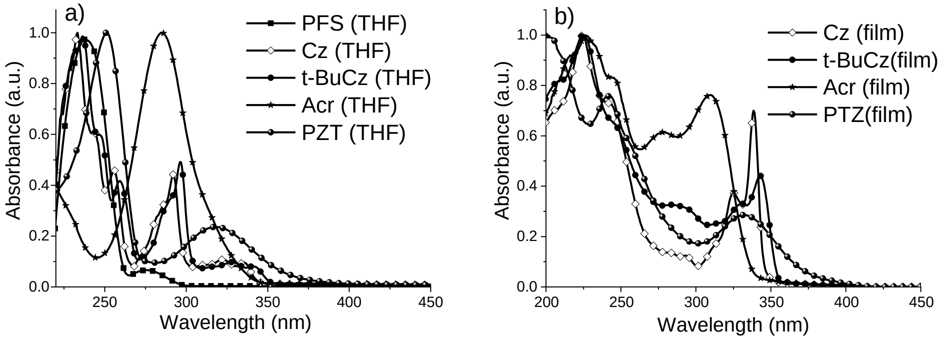

Fig. 4.5. Absorption spectra of (a) THF solutions and (b) solid films of separate molecules: Pentafluorostyrene (PFS), carbazole (Cz), di-*tert*-butyl carbazole (*t*-BuCz), 9,9-dimethyl acridane (Acr), phenothiazine (PTZ)

The UV-vis spectra of electron-accepting fluorostyrene display two main absorption bands with the peaks at 237 and 276 nm which correspond to the π–π* transitions of the conjugated perfluorinated styrene fragment. In the UV-vis spectra of the monomers and polymers, the absorption bands of the PFS fragment were not observed because of the overlapping with the spectra of the donating units. In the meantime, the shape of the spectra of carbazolyl-containing compounds M1, M2, P1, and P2 resemble the spectra of carbazole and di-*tert*-butyl carbazole. In these spectra, pronounced high intensity absorption bands around 226–292 nm and 320–330 nm correspond to the *π–π** and *n–π** electronic transitions of the locally excited carbazole moiety[95]. The absorption spectra of M2 and P2 are bathochromically shifted with respect to those of M1 and P1 due to the presence of electron-donating *tert*-butyl groups in the 3,6-positions of the carbazole moiety of M2 and P2. The absorption spectra of M3, P3 and M4, P4 were found to be similar to the spectra of acridan and phenothiazine, respectively (Fig. 4.5, Fig. 4.6). Compounds containing the acridan donor moiety (M3 and P3) showed absorption peaks at around 245 and 273 nm, which can be attributed to the allowed π–π* and *n*–π* transitions within the acridan moiety. The presence of the phenothiazine fragment is responsible for the appearance of the peaks at ca. 316 and 248 nm which dominate in the UV-vis spectra of M4 and P4.

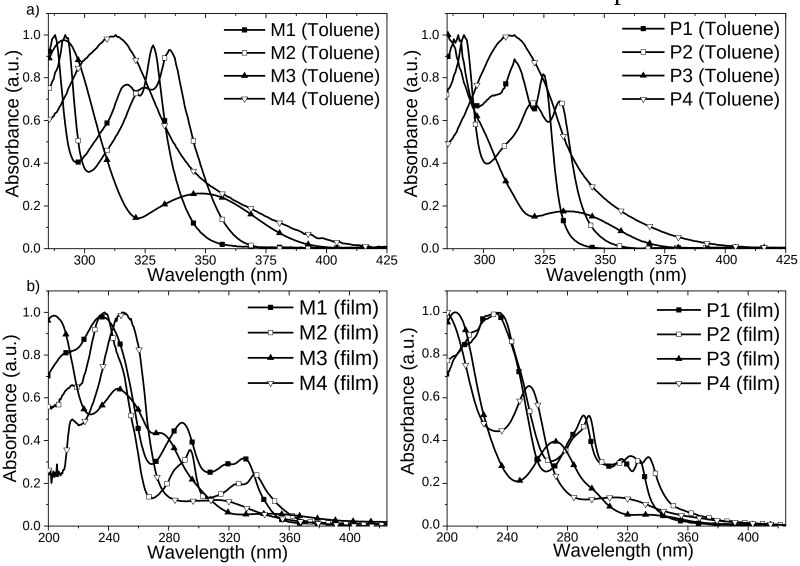

Fig. 4.6. Normalized UV-vis spectra of (a) toluene solutions and (b) solid films of monomers M1–M4 and polymers P1–P4

Presumably, the donor strength is the main factor controlling the emission wavelength of the studied compounds. The donor strength of the substituents decreases in the following order: phenothiazine > 9,9-dimethyl acridan > di-*tert*-butyl carbazole > carbazole. Phenothiazine is of the strongest electron-donating nature among the substituents due to the presence of the electronegative linking sulphur atom. With a lone pair of electrons, sulphur is able to donate electrons via resonance effects into the π-conjugated system, which results in the enhancement of the electron density of the overall donating fragment[96, 97.] 9,9-Dimethyl acridan contains an sp^3-hybridized less electronegative carbon atom as an alkyl linker between the adjacent phenyl rings. The carbon linker ‘breaks’ the central ring conjugation. Thus the presence of the less electronegative carbon linkage results in the weaker electron-donating nature of 9,9-dimethyl acridan relative to that of phenothiazine. Carbazole, with its central pyrrole ring with stable aromatic system, resists to provide simple electron transfer from the donor to the acceptor[98]. The higher electron ability of di-*tert*-butyl carbazole with respect to that of the non-substituted carbazole is caused by the inductive effects of alkyl substituents at 3- and 6- positions, which enriches the carbazole fragment with additional electron density[99].

The PL spectra of the solutions in a relatively polar toluene solvent and those of solid films of monomeric and polymeric compounds are presented in Fig. 4.7. The red shifts of the fluorescence spectra of the solutions of the monomers were observed in the following sequence: M1 < M2 < M3 < M4 (Fig. 4.7 (a)). This observation is consistent with the increasing strength of the donor substituents in the line: carbazole < 3,6-di-*tert*-butyl carbazole < 9,9 dimethyl-acridan < phenothiazine[100]. The same trends were observed for the fluorescence spectra of the solid films of the monomeric compounds (Fig. 4.7 (b)). The fluorescence spectra of the toluene solutions of the polymers follow a similar trend. The spectra exhibited bathochromic shifts in the following line: P1=P2 < P3 < P4 (Fig. 4.7 (a)). The toluene solutions of carbazole based monomers M1 and M2 emitted light in the violet-blue region with the emission maxima at 438 nm and 464 nm, respectively while the solutions of the corresponding polymers P1, P2 show blue emission with the same peak at 445 nm.

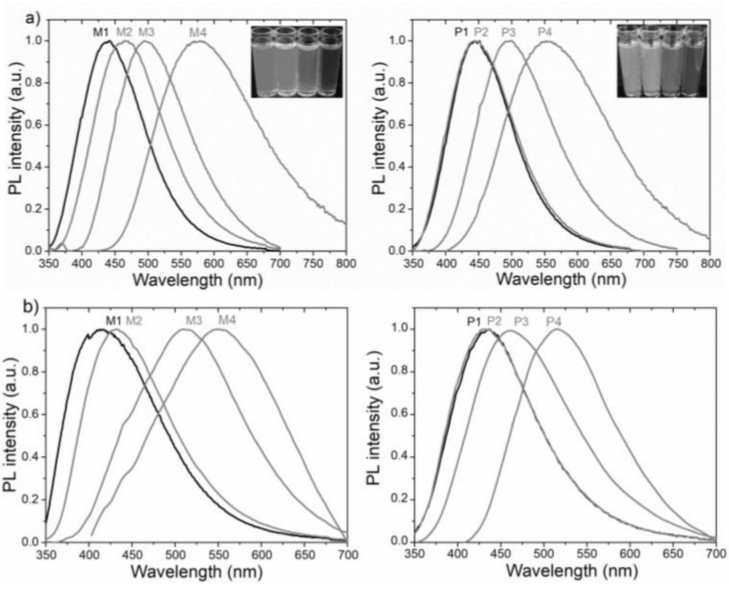

Fig. 4.7. Photoluminescence profiles of toluene solutions (10^{-5} M) (a) and solid films (b) of monomers and polymers (λ_{exc}=330 nm)

The toluene solutions of compounds containing stronger donors (9,9-dimethyl acridan and phenothiazine) display the most red-shifted emission with the emission maxima located at 497 and 577 nm for M3 and M4, respectively (Table 4.4). Carbazole-based P1 emitted blue light in the polar THF solution and in the solid state with the intensity maxima at 449 nm and 456 nm, respectively. The solutions and films of polymer P4 containing the strongest phenothiazine donor demonstrated yellow-to-green fluorescence peaking at 596 nm and 512 nm, respectively. Interestingly, the fluorescence of solid-state samples of all the monomers and polymers of the series was found to be blue-shifted with respect to their toluene solutions. Such an observation can probably be assigned to the lower dielectric constants of materials M1–M4 and P1–P4 than that of the toluene solvent. Moreover, the hypsochromic shift of the solid state emission of compounds can be attributed to the aggregation process in the solid state, which can lead not only to an increase of the emission intensity but also to a blue shift of the PL spectra[101]. The fluorescence spectra of the solutions and solid samples of monomer M2 containing a 3, 6-substituted carbazole fragment were found to be red-shifted by 20–26 nm with respect to the corresponding spectra of carbazolyl-containing monomer M1. This observation may be explained by the presence of the additional electron-donating *tert*-butyl groups attached to the carbazole moiety in the structure of M2. However, for the fluorescence spectrum of the toluene solution of polymeric compound P2, no shift was observed in comparison to the spectrum of the solution of P1.

Table 4.4. Photophysical data for monomers and polymers

Compound	$\lambda_{abs, film}$, nm	$\lambda_{PL, THF}$, nm	$\lambda_{PL,Tol}$, nm	$\lambda_{PL, film}$, nm	$\eta_{PL, THF}$, %	$PLQY_{, film}$, %	E_S, eV	E_T, eV	$\Delta E_{S\text{-}T}$
M1	347	456	438	414	9	20	3.43	ND	-
P1	343	449	445	435	11	7	3.33	2.97	0.36
M2	362	472	464	434	10	22	3.19	2.91	0.28
P2	357	448	445	435	11	9	3.21	3.01	0.20
M3	375	513	497	512	4	6	3.18	2.97	0.21
P3	367	494	495	459	2	2	3.13	2.88	0.25
M4	414	600	577	551	2	2	2.96	2.76	0.20
P4	383	596	552	512	1	1	2.93	2.70	0.23

λ_{abs} is the onset of the lowest energy absorption band; λ_{PL} is the emission maxima; η_{PL} is the photoluminescence quantum yield; $E_{S,}$ E_T are the energies of the first excited singlet and triplet states estimated from the onset of the fluorescence and phosphorescence spectra of the films at 77 K, respectively (λ_{exc}=330). The phosphorescence spectra were recorded after delay of 10 ms after excitation. E_S , E_T are the energies of the first excited singlet and triplet states (estimated from the onset of the spectra) (ND – not detected); $\Delta E_{S\text{-}T}$ is singlet-triplet energy splitting.

The toluene solutions and solid samples of carbazole-based polymers P1 and P2 showed identical blue emission spectra with peaks at 445 and 435 nm, respectively. This observation suggests that, due to the stiffness of the polymer chain and the monomer restriction in the polymer chain, electron-rich *tert*-butyl groups do not contribute to the overall intramolecular charge transfer (ICT) of polymer P2. For the compounds bearing stronger donors (M3, P3, M4, P4), the enhancement of the electron-donating nature of N-heterocycles linked to the tetrafluorobenzene fragment resulted in better electron delocalization and enhanced ICT[102]. The presence of a stronger electron-donating part leads to the bathochromic shift in the emission spectra and the decrement of the oscillator strength of the molecules[103]. Interestingly, the PL spectra of the THF solutions of polymers (P1–P4) were blue-shifted with respect to the spectra of monomeric compounds (Fig. 4.10, Table 4.4). This observation may apparently be assigned to a stronger solvatochromic effect of the monomeric compounds described below (Fig. 4.10) as well as to a higher rigidity of the monomeric blocks in the polymer chain, and, therefore, to the weaker intermolecular motions across the polymer chains. Usually, polymeric compounds possess lower photoluminescence quantum yields (PLQY) in the solid state relative to the corresponding monomers due to the intramolecular concentration self-quenching[104]. Among the four studied monomers, *tert*-butyl carbazolyl based monomer M2 was characterized by the highest PLQY value of 22% in the solid state. The PLQY of its THF solution was found to be 10%. The corresponding polymer P2 showed the highest solid-state PLQY among the polymers with the value of 9%. Meanwhile, the PLQY of the THF solutions of 11% were found to be the same for the similar carbazole based polymeric compounds P2 and P1. Monomers and polymers containing strong donors phenothiazine (M4, P4) and acridan (M3, P3) showed a lower PLQY of 1–4%. Lower PL quantum efficiencies of these compounds can be interpreted in terms of the stronger intramolecular interactions caused by the presence of stronger donors and thus higher special separation between HOMO and LUMO localized on the donor and acceptor moieties, respectively (Fig. 4.1). Surprisingly, PL quantum efficiencies of the solid samples of monomers M1, M2, M3 are almost two times higher than those of THF solutions. This observation can be assigned to the aggregation induced emission enhancement (AIEE) occurring in the solid state of monomeric compounds. This effect was not observed for monomer M4. Apparently, the molecules of M4 in the solid state experience partial emission quenching caused by the π–π interaction between the adjacent chromophores.

The tendency of PLQY enhancement in the solid state was not observed for the corresponding polymeric compounds. This observation can be assigned to the aggregation induced emission enhancement occurring in the solid state of monomeric compounds. We attribute the absence of the AIEE effect in the solid samples of polymeric compounds (P1–P4) to the short distances between monomer units in the polymer chains and thus to the enhanced π–π interactions. The fluorescence decay curves of the THF solutions and solid samples revealed mono- and bi-exponential decay profiles, respectively (Fig. 4.8, Table 4.5).

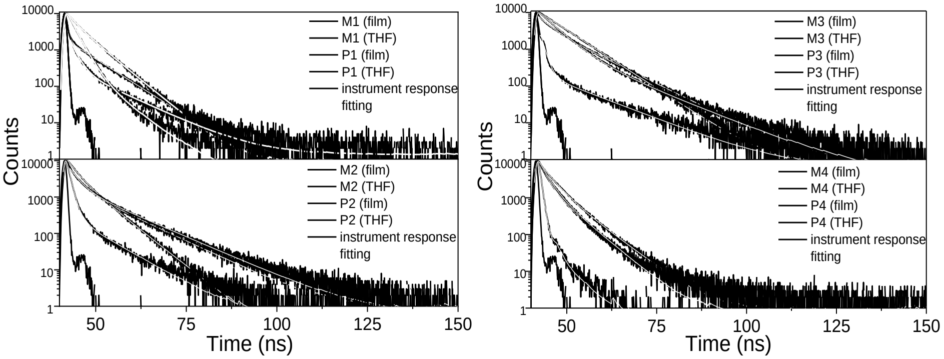

Fig. 4.8. PL decay curves of THF solutions and films of M1–M4 and P1–P4 (λ_{exc}=330 nm)

Double exponential fits required for the representation of the PL decay curves of the films of monomers and polymers can be explained by the intermolecular interaction in the solid state. The average fluorescence lifetimes of the studied compounds are in the range of nanoseconds thus justifying the fluorescent nature of the emission. The photoluminescence decay curves for the solutions of monomers (M1–M4) reveal shorter fluorescence lifetimes than the ones for the solutions of the corresponding polymers. This observation can apparently be explained by the intramolecular interaction of chromophores in polymers.

Table 4.5. Photoluminescence lifetimes recorded for THF solutions and solid films

Compounds	**τ_1 [a], ns**	**χ^2, [a]**	**τ_1/ τ_2 [b], ns**	**χ^2, [b]**
M1	5.1	1.038	0.5 (47%) / 6.9 (53%)	1.040
P1	5.7	1.243	1.7 (71%) / 9.4 (29%)	1.213
M2	5.5	1.006	2.3 (56%) / 9.3 (44%)	1.275
P2	6.9	1.400	0.9 (88%) / 7.5 (12%)	1.012
M3	7.0	1.025	3.1 (27%) /9.1 (73%)	1.207
P3	10.7	1.010	1.1 (65%) / 11.5 (35%)	1.143
M4	0.6	1.150	2.7 (52%) / 6.0 (48%)	1.057
P4	5.8	1.430	1.8 (60%) / 5.4 (40%)	1.190

τ_1/ τ_2 – photoluminescence decay curves of THF solutions and solid films of compounds with corresponding contribution percentages of times. [a] Estimated for 10^{-5} THF solution
[b] Measured for solid films of monomeric and polymeric compounds.

A comparison of the first singlet and triplet excited states energies of the studied monomers and polymers showed that the electron-donating group attached to the perfluorobenzene unit can significantly affect the E_S and E_T values (Fig. 4.9, Table 4.4). Compounds M1 and M2 bearing weaker electron donors such as carbazole and di-*tert*-butyl carbazole exhibited much higher E_S values of 3.43 eV (M1) and 3.19 eV (M2) than compound M4 containing a phenothiazine moiety (2.96 eV) (Table 4.4). S_1 energies of polymeric compounds were found to be slightly lower than or similar to those of the corresponding monomeric materials conceivably due to the interactions between the monomer units in polymer chains.

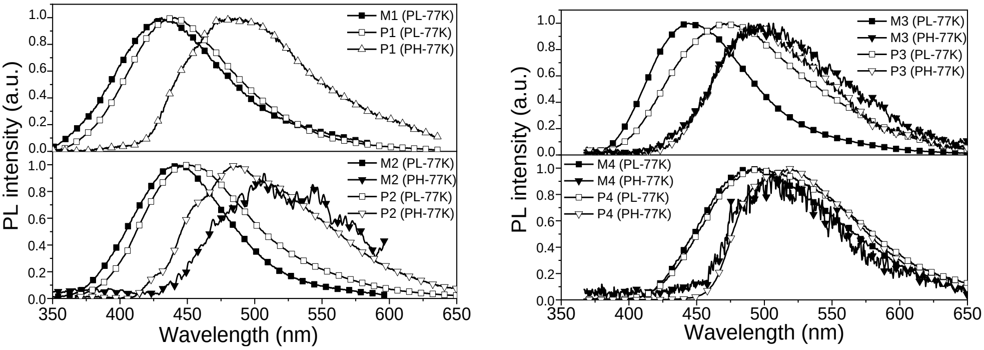

Fig. 4.9. Fluorescence and phosphorescence (10 ms delay after excitation) spectra of solid films of monomers M1–M4 and polymers P1–P4 (77 K, λ_{exc}=330 nm)

Similarly to S_1 level, the monomer-polymer pairs displayed close values of the first excited triplet state (T_1). In dependence of the nature of chromophores, S_1 energies decreased in the lines of M1 < M2 < M3 < M4 and P1 < P2 < P3 < P4. Consequently, for the series of polymers, the singlet-triplet energy splittings (ΔE_{S-T})

decreased following the same order with the highest value of 0.36 eV observed for P1 and the lowest value of 0.23 eV for P4 (Table 4.4). The corresponding monomeric compounds followed the same sequence. Di-*tert*-butyl carbazole based M2 possessed the highest $\Delta E_{S\text{-}T}$ value of 0.28 eV, and M4 showed the lowest value of 0.20 eV. To estimate the D-A character of monomeric and polymeric compounds, the UV-vis and PL spectra of the solutions in the solvents with different polarities were recorded (Fig. 4.10). All of the monomers exhibited positive solvatochromism, which resulted in bathochromic shifts of the PL spectra of the solutions with increasing polarities of the solvents. With the increasing solvent polarity from that of toluene to that of DMF (Fig. 4.10), a significant shift of the fluorescence spectra of monomers M1–M4 to the longer wavelength region was observed.

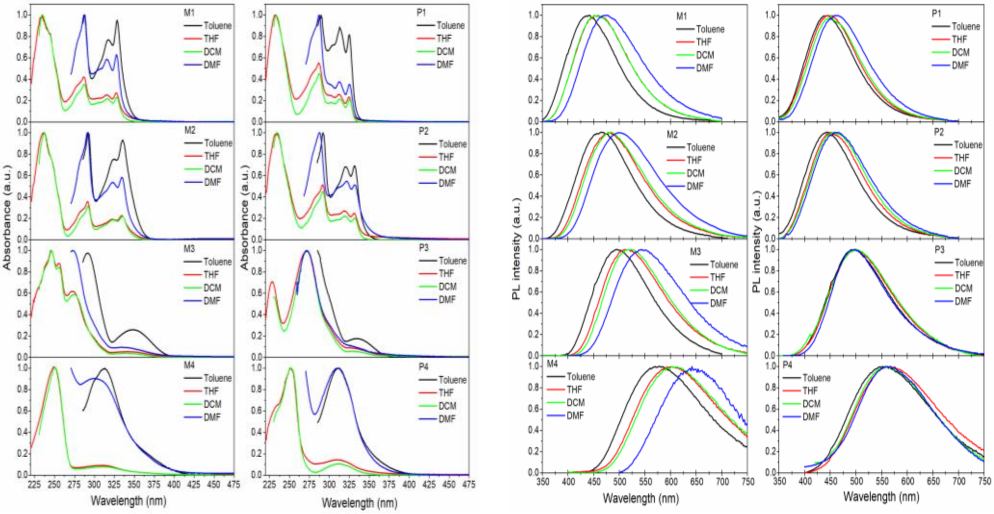

Fig. 4.10. UV-vis and photoluminescence spectra (λ_{exc}=330 nm) of monomers and the corresponding polymers in different solvents (10^{-5} M)

However, the PL spectra of the solutions of the polymers in different solvents were almost the same or showed only small red shifts with the increasing solvent polarity. Such a behavior of polymers (P1–P4) can apparently be assigned to the poor interaction of the solvents with fluorophores. The closer packing of monomeric units in the polymer chains apparently causes the restriction of monomeric building blocks and thus weaker positive solvatochromic properties with respect to those of monomers. The red shifts of the PL spectra of the solutions of the monomers in the solvents of different polarities are assigned to the ICT processes. They are commonly observed for compounds with the donor-acceptor architecture[100]. The shape of the fluorescence spectra of the solutions of monomers M1–M4 in DMF was found to be broader and less structured than those of the solutions in the less polar toluene, which is also a feature of the ICT character of molecules. The strongest solvatochromic effect was observed for M4. Its emission changed from yellow in toluene with the peak at 576 nm to red in the highly polar DMF with the emission maximum located at 647 nm. As it was expected, carbazole based monomer M1 showed a weaker solvatochromic effect. Its emission changed from violet in toluene (438 nm) to blue in DMF (473 nm). For the solutions of the other studied monomers in the solvents of increasing polarity, the fluorescence shifts were in agreement with the electron-donating nature of the substituents linked to tetrafluorostyrene moiety (Fig. 4.10) No solvatochromic effect was observed for the absorption spectra of the solutions of the compounds. The UV-vis absorption spectra of dilute solutions of monomeric and polymeric compounds in the solvents of different polarities are shown in Fig. 4.10. The negligible blue shift of the lowest-energy peak of UV-vis spectra of M1, M2, M4 and the M3–P3 pair with an increasing solvent polarity is conceivably due to the allowed *n*–π* electronic transition which is responsible for the hypsochromic shift which arises from the increased solvation of the lone pair of electrons of the heteroatom in the structure of the donor, which lowers the energy of the *n* orbital (Fig. 4.10)[105].

4.1.7. Aggregation induced emission enhancement of monomers

As mentioned above, the PLQY of the solid film of monomers was found to be significantly higher than the PLQY of solutions. This observation is attributed to aggregation induced emission enhancement (AIEE) (Fig. 4.11)[61].

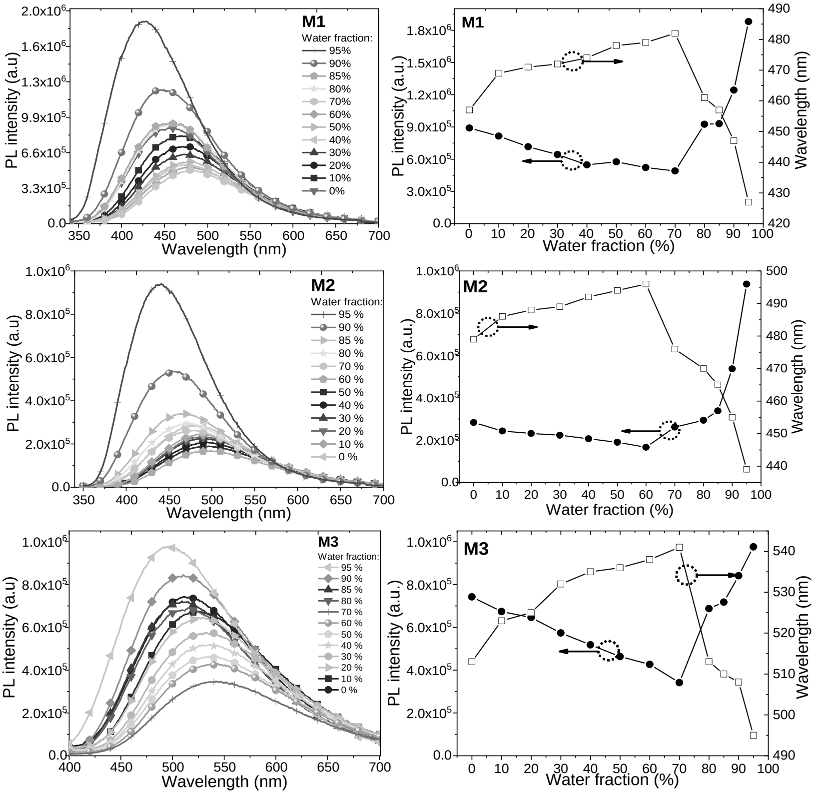

Fig. 4.11. (left) Fluorescence spectra of M1, M2 and M3 dispersed in THF:water mixtures with different water content and (right) fluorescence intensity/wavelength *versus* the water content of the solvent mixture

The monomers containing carbazole (M1), di-*tert*-butylcarbazole (M2) and acridan (M3) donor moieties demonstrated a low PLQY in solutions; however, it was considerably higher in the solid state. To estimate the extent of AIEE, photophysical investigation of the THF:water mixtures of M1–M3 were performed. Monomers M1, M2, M3 showed a similar behavior in the THF:water systems. As mentioned above, all the monomers contain environmentally sensitive fluorophores, which results in positive solvatochromic shifts of the PL spectra of solutions with an increase of the solvent polarity. With the addition of water, the overall polarity of the solutions increased, which resulted in the red-shifts of the PL spectra (Fig. 4.11). Along with the bathochromic shifts in the PL spectra, the fluorescence quenching of the mixtures was observed up to the water fraction of 50–70%. This observation is assigned to the ICT effect characteristic of M1–M3 (Fig. 4.11). For the water fraction from 0% up to 50–70%, depending on the monomer, the PL intensity decreased, and the emission maxima shifted toward the long-wavelength part of the spectrum. The strongest red-shift was observed for monomer M3 containing an acridan moiety as a result of the stronger electron-donating ability of the donor and thus the stronger ICT character of the entire molecule in comparison with carbazole- and di-*tert*-butylcarbazole-based compounds. When the water fraction reached 50–70%, the PL intensity dramatically increased, and a notable blue shift of the emission spectra was observed due to the predomination of aggregation of the molecules over the ICT process. To conclude, a series of monomers and the corresponding polymers comprised of the electron accepting tetrafluorobenzene core and a variety of electron-donating units were designed, synthesized and investigated. It was shown that the electrochemical, thermal and photophysical properties of the monomers strongly depend on the nature of the electron-donating fragment attached to the tetrafluorobenzene electron-withdrawing unit.

4.2. Tetrafluorophenylcarbazole and tri/tetraphenylethylene aggregation-induced emission enhancement luminogens

In the solid state, planar or disk-shape compounds often undergo strong intermolecular π–π stacking interactions[61]. The relaxation of excited states in the solid state is usually of nonradiative nature, which results in luminescence attenuation. Thus the application of solid organic emitters is rather restricted. Nevertheless, the aggregation-induced emission (AIE) or aggregation-induced emission enhancement (AIEE) phenomenon allows to totally overcome solid-state fluorescence quenching. Restriction of intramolecular motions[61] is considered as the main working mechanism of the AIE or AIEE phenomena which require non-planar conformational or vibrational rigidification of the molecular structures. The presence of the rotating systems, such as propeller-like rotors, in the molecular structures ‘turns on’ emission because π–π stacking interactions are suppressed in the solid samples of AIE-active materials. The attachment of AIE-active moieties to the backbone of the emissive molecules is a successful approach towards reducing aggregation-induced quenching and obtaining luminogens with a high photoluminescence quantum yield (PLQY) in the solid state. Such a strategy allows implementation of molecular aggregates in efficient nondoped organic light-emitting diodes (OLEDs) [106].

4.2.1. Synthesis

Compounds C4FS1 and C4FS2 were synthesized according to the synthetic route outlined in Scheme 4.2. The first step was the nucleophilic substitution reaction of a fluorine atom by the carbazole aromatic heterocycle with the further Heck coupling of the vinyl group with tri/tetraphenyl ethylene bromides as the final step. The chemical structures of the compounds were characterized by ^{1}H and ^{13}C NMR spectroscopies, mass spectrometry, and elemental analysis. The synthesized compounds showed good solubility in organic solvents, such as acetone, tetrahydrofuran (THF), toluene, and chloroform.

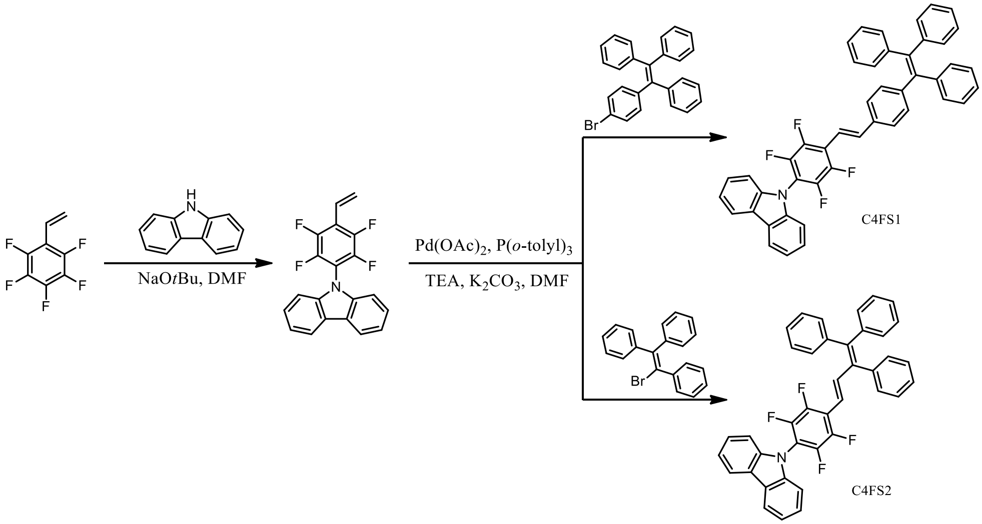

Scheme 4.2. Synthetic scheme of **C4FS1** and **C4FS2**

4.2.2. Theoretical insights

Theoretical geometry optimizations of the molecules in the electronic ground state as well as the distribution of electron density were performed with *Gaussian 09* program using the density functional (DFT) method with the 6–311G (d) basis set in vacuum.

The highest occupied molecular orbital (HOMO) was found to be located over the entire molecule for both molecules, whereas the lowest unoccupied molecular orbital (LUMO) is mainly located on electron accepting tetrafluorostyrene and partially on the multiphenyl ethylene scaffold as a result of the planar tetrafluorophenyl−C=C−tri/tetraphenylethylene manifold that can be noticed from the top and side view of the optimized structures (Fig. 4.12).

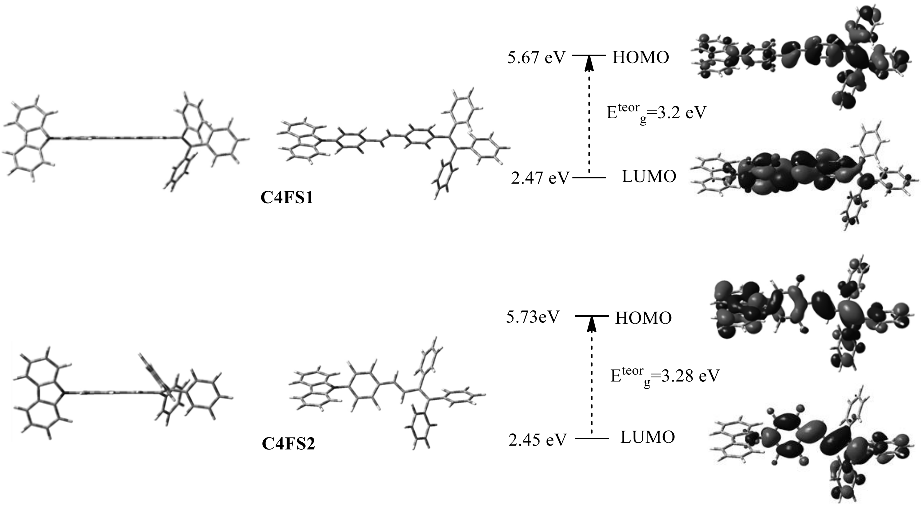

Fig. 4.12. Optimized geometries and HOMO / LUMO energy levels calculated by using B3LYP/6–311G basis set in Gaussian 09 program. E^{teor}_g (energy gap) = |LUMO-HOMO.|

4.2.3. Electrochemical, photoelectrical, and charge-transporting properties

Ionization potentials, electron affinities, and charge mobilities are the key parameters of organic electroactive materials used for the fabrication of optoelectronic devices. Cyclic voltammograms recorded for DMF solutions containing 0.1 M tetrabutylammonium hexafluorophosphate (Bu_4NPF_6) as the supporting electrolyte are presented in Fig. 4.13 (a). For compounds C4FS1 and C4FS2, the irreversible oxidation waves conceivable due to the active unsubstituted C-3- and C-6 positions of carbazolyl moieties were detected.

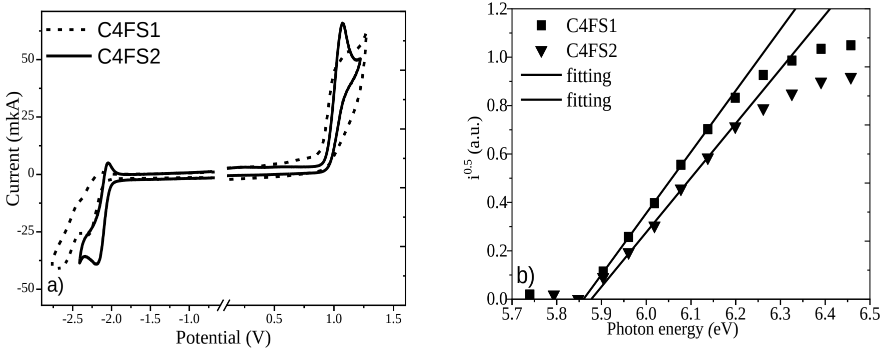

Fig. 4.13. a) Cyclic voltammograms of **C4FS1** and **C4FS2** recorded at a scan rate of 50 mV s^{-1}. b) Photoelectron emission spectra of the films of compounds **C4FS1** and C**4FS2**.

The oxidation peaks were observed at 1.01 and 1.08 V for C4FS1 and C4FS2, respectively. The oxidation potentials determined from the onset of the oxidation parts of the voltamperograms were found to be 0.83 and 0.95 V, respectively. Irreversible reduction peaks were detected at −2.29 V for C4FS1 and at −2.21 V for C4FS2. The reduction potentials for C4FS1 and C4FS2 as the onsets of the reduction parts were estimated to be −2.10 and −2.01 V, respectively. As C4FS1 and C4FS2 were designed for solid-state optoelectronic applications, the energy levels of the layers of C4FS1 and C4FS2 were important to evaluate. Solid-state ionization potentials IP_{PE} of the vacuum-deposited films determined from photoelectron photoemission spectra were found to be comparable, that is, 5.83 eV for C4FS1 and 5.87 eV for C4FS2 (Fig. 4.13 (b), Table 4.6). Finally, solid state electron affinities (EA_{PE}) of 3.01 and 2.98 eV for C4FS1 and C4FS2 were estimated by using the equation $EA = IP_{PE} - E_g$ and the optical band gap energies. EA_{PE} values were also found to be in good agreement with those obtained by electrochemical and theoretical techniques. To show the potential of C4FS1 and C4FS2 as organic semiconductors for optoelectronic applications, the charge-transporting properties of the vacuum-deposited layers of C4FS1 and C4FS2 were studied by the TOF technique. Both compounds showed bipolar charge transport. The TOF current transient curves for holes and electrons recorded at the different electric fields are shown in Fig. 4.14 (a).

Table 4.6. Electrochemical and photoelectrical properties of **C4FS1** and **C4FS2**

Compound	E_{ox} [a] V	E_{red} [a] V	IP_{PE} [b], eV	IP_{CV} [c], eV	EA_{CV} [c], eV	$E^{elc}_{g,}$ [d] eV	$E^{opt}_{g,\mathrm{film}}$, [e] eV
C4FS1	0.83	-2.10	5.83	5.63	2.71	2.93	2.81
C4FS2	0.95	-2.01	5.87	5.75	2.79	2.96	2.89

[a] Onset of the first oxidation/reduction potential. [b] Solid-state ionization potential, measured by photoelectron emission spectrometry. [c] Determined by formula IP_{CV}=|e|(4.8 + E_{ox}), EA_{CV} = |e|(4.8 + E_{red}). [d] Electrochemical band gap estimated by using approximation $E^{elc}_g = IP_{CV} - EA_{CV}$. [e] Optical band gap determined from the onset of the last absorption peak by using equation $E^{opt}_g = 1240/\lambda_{abs}^{film}$.

The compounds showed low-dispersity transport of holes and electrons. Electric field dependencies of charge mobilities of the layers of C4FS1 and C4FS2 are presented in Fig. 4.14 (b). Compound C4FS1 containing tetraphenyl ethylene moiety exhibited more efficient and more balanced charge transport than compound C4FS2 having triphenyl ethylene moiety.

C4FS1 showed slightly more efficient transport of electrons than that of holes, whereas C4FS2 showed the opposite phenomenon. Hole mobilities in the layer of C4FS2 exceeded electron mobilities. In the layer of C4FS1, hole drift mobility reached the value of 2.33×10^{-3} cm^2/V s at the electric field of 6.67×10^5 V cm^{-1}, whereas electron mobility was found to be 1.55×10^{-3} cm^2/V s. For the layer of C4FS2, hole mobility of 1.42×10^{-3} cm^2/V s and electron mobility of 5.78×10^{-4} cm^2/V s were recorded at the same electric field.

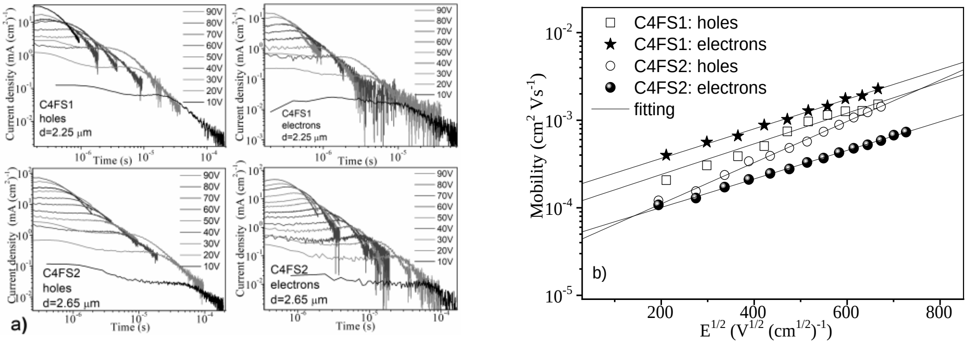

Fig. 4.14. a) Time-of-flight current transients for holes and electrons for the layers of C4FS1 and C4FS2. b) Electric field dependencies of hole and electron drift mobilities for the vacuum-deposited layers of compounds C4FS1 and C4FS2 recorded at room temperature.

4.2.4. Thermal properties

The behavior of C4FS1 and C4FS2 under heating was investigated by TGA and DSC under nitrogen atmosphere. The TGA and DSC curves of the compounds are shown in Fig. 4.15 (a, b). TGA revealed that compounds C4FS1 and C4FS2 exhibited high thermal stability, which is typical for carbazole-containing materials[107, 108].

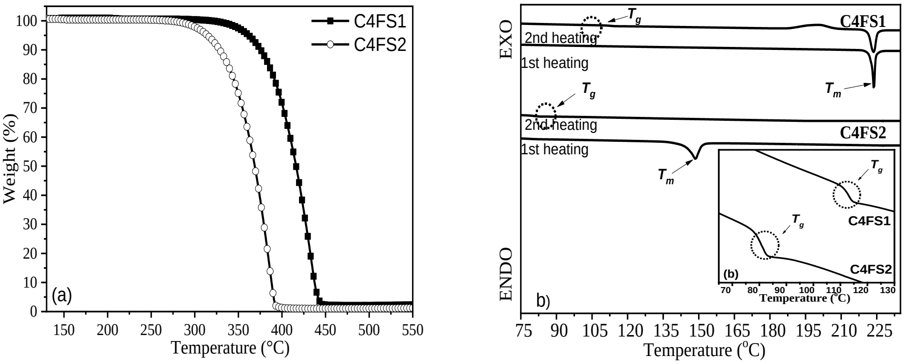

Fig. 4.15. TGA (a) and DSC (b) curves of **C4FS1** and **C4FS2**

The 5% weight loss temperatures (T_d) of the compounds were found to be 362 and 314 °C, respectively (Fig. 4.15 (a)). Very low carbonized residuals observed for C4FS1 and C4FS2 show that sublimation could be the main reason for the weight loss. The higher 5% weight loss temperature of C4FS1 can apparently be explained by its higher molecular weight, which predetermines stronger intermolecular interaction. C4FS1 and C4FS2 were obtained after the synthesis as crystalline substances. They showed endothermic melting signals in the first heating scans at 223 and 148 °C, respectively (Table 4.7). In the cooling scans, the samples did not show crystallization, whereas in the following second heating scans, they showed glass transitions at 112 and 80 °C, respectively. C4FS2 having one phenyl group less as compared to C4FS1, showed both a lower melting point and a lower glass-transition temperature. Despite the lower molar mass, the molecular glass of C4FS2 exhibited higher morphological stability relative to that of C4FS1. In the second DSC heating scan, C4FS2 showed only the glass-transition signal, whereas C4FS1 after the glass-transition signal showed crystallization and melting transitions.

Table 4.7. Thermal characteristics of **C4FS1** and **C4FS2**

Compounds	T_d [a], °C	T_g [b], °C	T_m [b], °C
C4FS1	362	112	223
C4FS2	314	80	148

T_D is 5% weight loss temperatures, scan rate 20 °C/min, nitrogen atmosphere. T_g is glass transition temperature, scan rate 10 °C/min, nitrogen atmosphere. T_m is the melting temperature. [a] Estimated from TGA. [b] Estimated from DSC.

4.2.5. Photophysical properties

The UV−vis absorption and fluorescence spectra of dilute solutions in toluene and those of solid films of compounds C4FS1 and C4FS2 are shown in Fig. 4.16. The photophysical data for the compounds is summarized in Table 4.8. The lowest energy absorption peaks of the dilute solutions of C4FS1 and C4FS2 were observed at 367 and 360 nm, respectively. Because of the similar chemical structure, the absorption spectra of the compounds are similar, but the lowest energy absorption band of the solution of C4FS1 is slightly red-shifted with respect to the corresponding band of C4FS2 owing to the prolonged molecular conjugation. For both compounds, the absorption spectra of the neat films are slightly red-shifted (by 9−10 nm) with respect to the spectra of the solutions, presumably due to the formation of aggregates and the occurrence of the intermolecular interactions in the solid state.

Table 4.8. Photophysical characteristics of **C4FS1** and **C4FS2**

Compounds	$\lambda^{Pl}_{max,tol,}$ [a] nm	$\lambda^{Pl}_{max,}$ [b] nm	Stokes shift [a/b], nm	PLQY, [a/b] %	τ_1 [b], ns
C4FS1	498	511	131/137	0.3/57	2.08 (χ^2=1.276)
C4FS2	445	502	85/135	0.1/28	2.16 (χ^2=1.141)

λ^{Pl}_{max} is wavelength of emission maximum; η_{PL} is photoluminescence quantum yield; τ_1 – photoluminescence lifetimes

[a] Dilute toluene solution (10^{-5}M). [b] Solid film.

Dilute toluene solutions of C4FS1 and C4FS2 exhibited fluorescence in the violet-blue range of the spectrum with the intensity peaks at 498 and 445 nm, respectively, whereas neat solid films showed emission intensity maxima at 511 and 502 nm, respectively. The emission band of the solution of C4FS1 showed a significant bathochromic shift of 53 nm in comparison to that of the solution of C4FS2, whereas, in the solid state, this shift is much smaller (9 nm). A considerably shorter Stokes shift observed for the solution of C4FS2 can apparently be explained by the shorter relaxation time in the excited state because of the presence of a less bulky and less rigid triphenylbutadienyl substituent. For more profound understanding of the photophysical processes, photoluminescence decay measurements for the solid samples were carried out. The fluorescence decay curves of both compounds C4FS1 and C4FS2 in the solid state revealed monoexponential decay profiles (Fig. 4.16 (c)). The fluorescence lifetimes of the solid samples of C4FS1 and C4FS2 were found to be of 2.08 and 2.16 ns (Table 4.8), respectively.

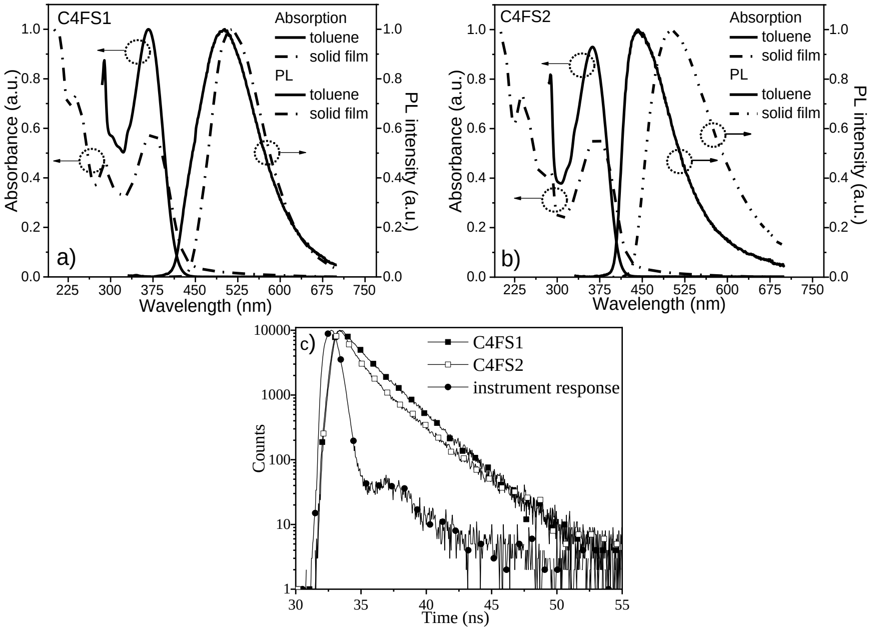

Fig. 4.16. Normalized UV-vis absorption and fluorescence spectra of 10^{-5} M toluene solution (solid lines) and thin films (dash and dot lines) of compounds **C4FS1** (a) and **C4FS2** (b); Fluorescence decay curves of solid films of **C4FS1** and **C4FS2** (c); (λ_{exc}=360 nm).

Both C4FS1 and C4FS2 were found to be soluble in typical organic solvents, yet insoluble in water. To study the AIEE properties of the compounds, the fluorescence spectra of the compounds dispersed in THF/water systems were estimated. The solution of C4FS1 and C4FS2 in THF showed very weak emission because of the intramolecular rotations and vibrations of the phenyl rotors against the ethylene stator. Nevertheless, with the addition of water, the formation of molecular aggregates resulting in the enhancement of fluorescence intensity was observed (Fig. 4.17 (a)). Fluorescence intensity started to grow dramatically when the content of water reached ca. 90% (Fig. 4.17). The bathochromic shift of the fluorescence maxima in the emission pattern, with the increment of the water fraction, can be explained by the gradual increase of the polarity of the media with the addition of polar water (Fig. 4.17). The twisted conformation of the incorporated multiphenyl ethylene unit linked to the carbazolyl tetrafluorostyrene moiety prevents photoluminescence quenching in the solid state. The PLQYs of toluene solutions of compounds C4FS1 and C4FS2 were estimated to be 0.3 and 0.1%, respectively, whereas those of the solid samples were found to be 57% and 28%, respectively. The lower PLQY of C4FS2 can be assigned to its less twisted conformation compared to that of C4FS1 and thus to a higher possibility of intermolecular interactions.

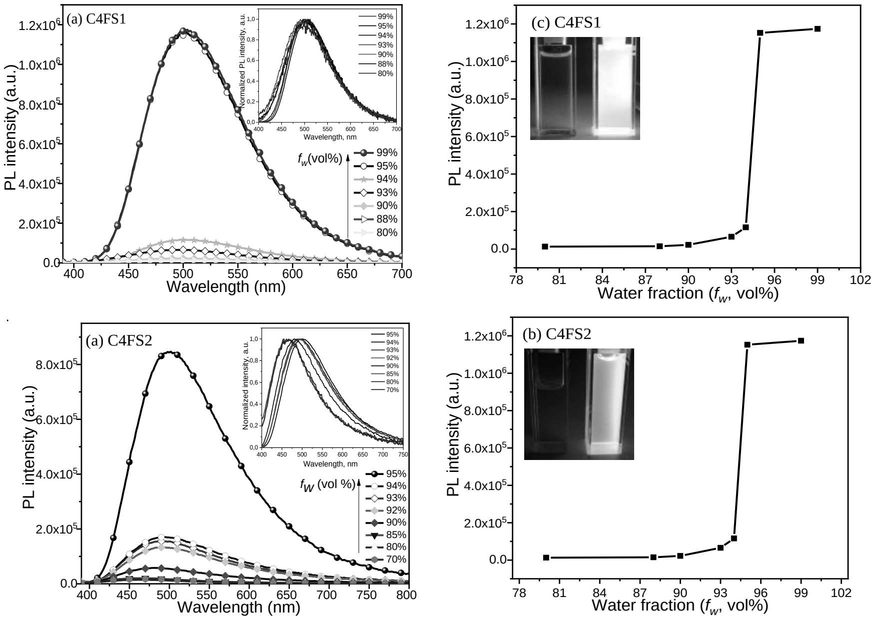

Fig. 4.17. PL spectra of C4FS1 (a) and C4FS2 (b) dispersed in THF:water mixtures with the different water content (f_w); photoluminescence intensity *versus* water fraction in THF:H_2O mixtures (b, c).

4.2.6. Performance in nondoped OLEDs

Nondoped solid films of C4FS1 or C4FS2 are characterized by high PLQY values, relatively high bipolar charge mobilities, and appropriate energy levels for hole and electron injection, all of which is required for OLED applications. To demonstrate the potential of C4FS1 or C4FS2 in OLED applications, nondoped light-emitting layers of the compounds were tested in OLEDs with the simple structures of ITO/MoO_3 (1 nm)/NPB (60 nm)/C4FS1 or C4FS2 (30 nm)/TPBi (60 nm)/LiF (0.5 nm)/Al (device A and device B, respectively). The equilibrium energy diagram of the devices is presented in Fig. 4.18. Low injection barriers for holes and electrons between the device interfaces were observed. The ionization potentials of 5.83 and 5.87 eV (the HOMO of solid samples) determined by photoelectron spectroscopy and estimated by using the optical band gap electron affinities of 3.02 and 2.98 eV (the LUMO of solid samples) for C4FS1 or C4FS2 were used to design the device structures. Good charge injection properties for devices A and B were expected when using hole and electron-transporting layers *N*,*N′*-di(1-naphthyl)-*N*,*N′*-diphenyl-(1,1′-biphenyl)-4,4′-diamine (NPB) and 2,2′,2″-(1,3,5-benzinetriyl)-tris(1-phenyl-1H-benzimidazole) (TPBi). Molybdenum trioxide (MoO_3) and lithium fluoride (LiF) vacuum-deposited films were utilized as the hole- and electron-injecting layers, respectively. The layers of ITO and aluminum (Al) played their usual roles of the anode and the cathode, respectively.

The intensity maxima of the EL spectra were observed at 496 and 499 nm, respectively, at different external voltages (Fig. 4.19 (a), Table 4.9). These maxima were slightly blue-shifted by 15 and 3 nm in comparison to the intensity maxima (511 and 502 nm) of the corresponding PL spectra of neat solid films C4FS1 and C4FS2, respectively (Fig. 4.16, Table 4.8). The slight differences between the PL and EL spectra of neat solid films C4FS1 and C4FS2 and devices A and B can apparently be explained by the different applied optical and electrical excitation sources, respectively.

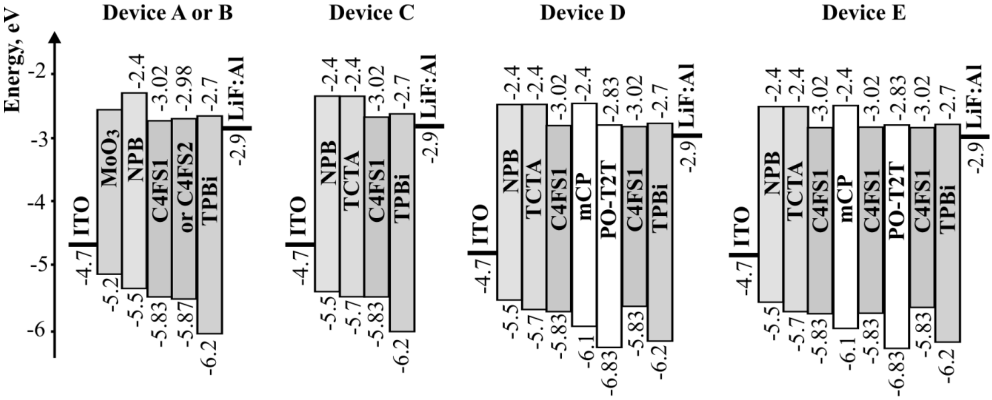

Fig. 4.18. Equilibrium energy diagrams for devices A–F. The values of I_P^{PE} and E_A^{PE}, estimated for solid films of **C4FS1** or **C4FS2**, were used for the device design.

For devices A and B, a very intensive EL was observed at high voltages while achieving the maximum brightness of 12500 and 3200 cd/m^2 at 7.5 V, respectively (Fig. 4.19 (b), Table 4.9). The EL of both devices A and B is characterized by green-blue light with the CIE coordinates of (0.185, 0.38) and (0.218, 0.367), respectively. Good charge injection properties and relatively low turn-on voltages of 3.8 V were observed for both devices A and B (Table 4.9). Because of the fluorescent nature of EL, rather low maximum external quantum efficiencies (EQE$_{max}$) of 1.08 and 0.34% were achieved for devices A and B, respectively. These values are lower than the theoretical maximum (5%) for fluorescent devices without out-coupling, mainly due to the relatively low PLQYs of C4FS1 or C4FS2 in the solid state as well as due to the lower than 100% charge recombination probability. Because of the higher PLQY of C4FS1 in the solid state and because of the higher efficiency of device A in comparison to C4FS2 and device B, C4FS1 was selected for the fabrication of the optimized devices. For device C featuring the structure of ITO/NPB (50 nm)/TCTA (15 nm)/C4FS1 (20 nm)/TPBi (65 nm)/LiF (0.5 nm)/Al (Fig. 4.18), a higher EQE$_{max}$ of 1.7% was achieved in comparison to device A based on the same emitter C4FS1 (Table 4.9).

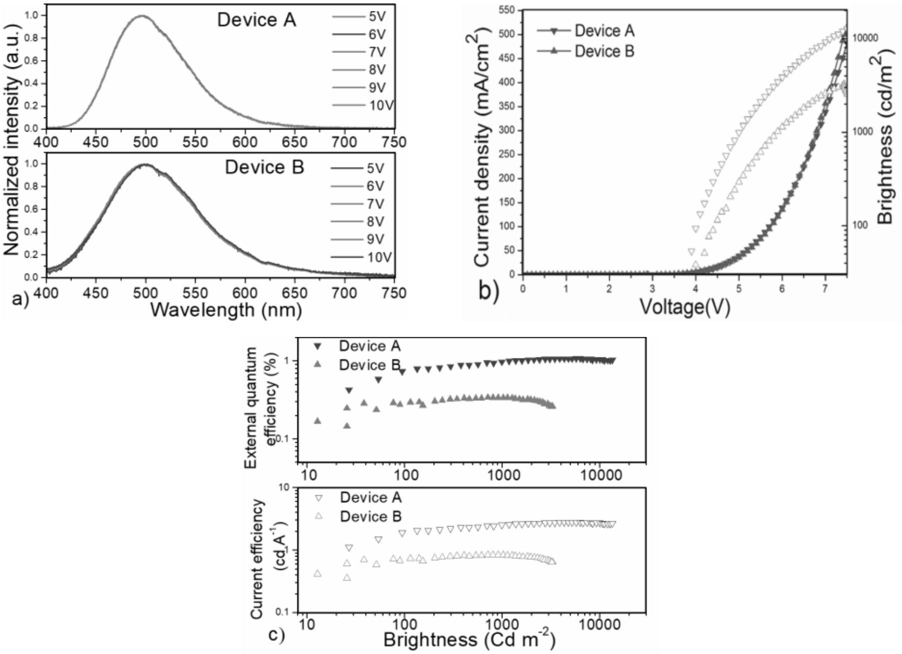

Fig. 4.19. (a) EL spectra of C4FS1- and C4FS2-based devices A and B recorded at different voltages; (b) current density and brightness *vs.* voltage; and (c) current and external quantum efficiencies *vs.* brightness for devices A and B

The higher efficiency of device C is apparently mainly related to the increase of the charge recombination probability. Despite such optimization, the EQE_{max} of device C is much lower than that of phosphorescent and TADF OLEDs. Indeed, because of the 25% limit of the exciton generation probability for fluorescent devices, OLEDs based on many efficient fluorescent emitters suffer from a low EQE.

Table 4.9. Characteristics of OLEDs

Device	Device structure	V_{on}, V	max. brightness, cd/m^2	CE_{max}	EQE_{max}, %	$λ_{EL}$, nm	CIE, (x, y)
A	ITO/MoO_3/NPB/C4FS1/TPBi/LiF/Al	3.8	12500	2.8	1.08	496	0.185, 0.38
B	ITO/MoO_3/NPB/C4FS2/TPBi/LiF/Al	3.8	3200	0.8	0.34	499	0.218, 0.367
C	ITO/NPB/TCTA/C4FS1/TPBi/LiF/Al	9.1	11800	4.5	1.7	496	0.202, 0.399
D	ITO/NPB/TCTA/C4FS1/mCP/PO-T2T/C4FS1/TPBi/LiF/Al	8.1	14100	6.2	2.2	496	0.194, 0.379
E	ITO/NPB/TCTA/C4FS1/mCP/C4FS1/PO-T2T/C4FS1/TPBi/LiF/Al	9.1	16300	7.3	2.6	498	0.205, 0.404

[a] CIE for EL spectrum recorded at 10 V

Therefore, the approach based on an interface exciplex-based host exhibiting TADF was used for the further increase of EQE of nondoped devices based on C4FS1. Taking into account the bipolar charge-transporting property of C4FS1, the light-emitting layer of device C was further modified by placing the layers 3-bis(9-carbazolyl)benzene (mCP) and 2, 4, 6-tris[3-(diphenylphosphinyl)phenyl]-1,3,5-triazine (PO-T2T) between the two layers of C4FS1 (Fig. 4.18, device D). We note that a solid-state mixture of PO-T2T and (mCP) is characterized by exciplex emission of the TADF nature[47]. As a result, device D with the structure ITO/NPB (50 nm)/TCTA (15 nm)/C4FS1 (10 nm)/mCP (5 nm)/PO-T2T (5 nm)/C4FS1 (10 nm)/ TPBi (65 nm)/LiF (0.5 nm)/Al was fabricated. Because of the HOMO and LUMO energy levels of mCP and PO-T2T (Fig. 4.18), the charge recombination zone in device D is predicted to be at the mCP/PO-T2T interface. As a result, both singlet and triplet excitons can be harvested at the mCP/PO-T2T interface in device D because of the TADF of the interface exciplex mCP/PO-T2T.

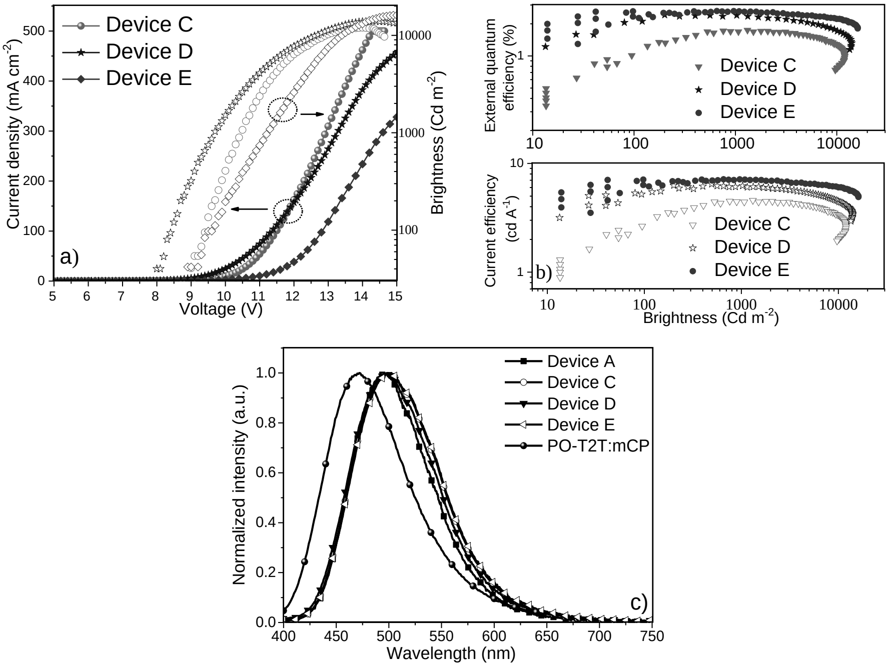

Fig. 4.20. a) Current density and brightness versus voltage; and b) Current and external quantum efficiencies versus brightness for C4FS1-based devices C, D, and E. c) PL spectrum of the solid mixture of mCP and PO-T2T, EL spectra of C4FS1-based devices C, D, and E recorded at 10 V

This consideration is supported by a higher EQE_{max} (2.4%) observed for device D in comparison to that of device C. Taking into account that exciplexes can be formed even in the presence of some distance between the donor and the acceptor layers, a 5 nm thick layer of emitter C4FS1 was placed in the region of the exciplex formation of device D. As a result, device E with the structure ITO/NPB (50 nm)/TCTA (15 nm)/C4FS1 (10 nm)/mCP (5 nm)/C4FS1 (5 nm)/PO-T2T (5 nm)/ C4FS1 (10 nm)/TPBi (65 nm)/LiF (0.5 nm)/Al was fabricated. The EQE_{max} of device E was found to be 2.6%, which is slightly higher than the value of device D (Fig. 4.20 (b)). The EL spectra of C4FS1-based devices C, D, and E were found to be very similar to that of C4FS1-based device A which showed emission of C4FS1 (Fig. 4.20 (c)). No influence of mCP/ PO-T2T interface exciplex emission on the EL spectra of the studied devices was observed. Blue spectral shifts in the EL of the exciplex based OLEDs with an increase of the external voltages were previously observed because of the electron-hole Coulomb attraction[109, 110]. The brightness of devices C, D, and E exceeded 10 000 cd/m^2 at high voltages (Fig. 4.20 (a), Table 4.9). Devices D and E are characterized by exciplex-enhanced efficiency demonstrating the potential of the proposed approach. We note that this approach towards efficiency enhancement of fluorescent nondoped OLEDs may be utilized for many other effective fluorescent emitters including those exhibiting the AIEE effect. The EQE$_{max}$ of exciplex-based device E was increased by more than 50% relative to that of device C.

To sum up, derivatives of 4-carbazolyl-substituted tetrafluorostyrene and tri/tetraphenyl ethylene were synthesized and characterized as materials exhibiting both AIE enhancement and bipolar charge-transporting properties. The difference in the molecular architecture of simply one phenyl ring can considerably change the properties of compounds. The solid sample of the compound having a tetraphenylethylene moiety is characterized by the two times higher PLQY of 57% than the layer of the compound containing a triphenylethylene moiety (27%). Nondoped OLEDs employing the synthesized compounds as emitters were fabricated; they exhibited green EL. Exciplex host-based OLEDs containing one or two emitting layers of a tetraphenylethenyl-containing emitter were fabricated and showed more than 50% higher EQE relative to that of the corresponding nondoped device. The best nondoped device-based tetraphenylethenyl-containing emitter showed a turn-on voltage of 9.1 V, the maximum brightness of 11800 cd/m^2, the maximum current efficiency of 4.5 cd/A, and an EQE of ca. 1.7%. The best modified device containing an exciplex-forming host showed a turn-on voltage of 9.1 V, the maximum brightness of 16 300 cd/m^2 (at V), the maximum current efficiency of 7.3 cd/A, and an EQE of ca. 2.6%.

4.3. Exciplex-forming quinoline and carbazole based materials

Bipolar conjugated compounds with the donor-acceptor architecture are of great interest due to their wide present and potential application in optoelectronic devices[111, 112]. Significant interest has been directed towards the development of white organic light emitting diodes (WOLEDs) as feasible low-cost, highly efficient alternatives for back-lights in flat panel displays [113, 114, 115, 116, 117]. The ideal electroluminescent spectrum of WOLED must cover the entire visible electromagnetic spectrum. To achieve this aim, various techniques have been applied including utilization of excimer-exciplex systems [118] and a combination of two (blue and orange) or three (red, blue and green) emission colors in a single emissive layer of an organic electroluminescent device[119]. The employment of exciplex-forming systems as emissive materials can also be a successful strategy for the fabrication of WOLEDs[120, 121, 122]. A careful and accurate choice of the appropriate electron-donating and electron-accepting molecules provides the opportunity to tune the emission of exciplexes for the generation of white light[123]. To simplify the structure of an exciplex-based WOLED, in this work, we propose a new approach to achieving white light by mixing two exciplex emissions with the structures of D−A/D and D−A/A. Warm-white electroluminescence is obtained by using a donor-acceptor (D−A) compound which forms an interface orange exciplex of the D−A/D structure and a blue exciplex of the D−A/A structure (Scheme 4.3). To design such D−A molecules capable of the formation of D−A/D and D−A/A exciplexes, quinoline, which is known for its electron-accepting properties as well as thermal stability, was used as the electron-accepting unit [124, 125, 126].

A carbazole moiety was used as the electron-donating unit taking into account that many carbazole-based derivatives were characterized by good hole-transporting abilities, high triplet levels, good thermal properties, and acceptable photochemical stability [127, 128].

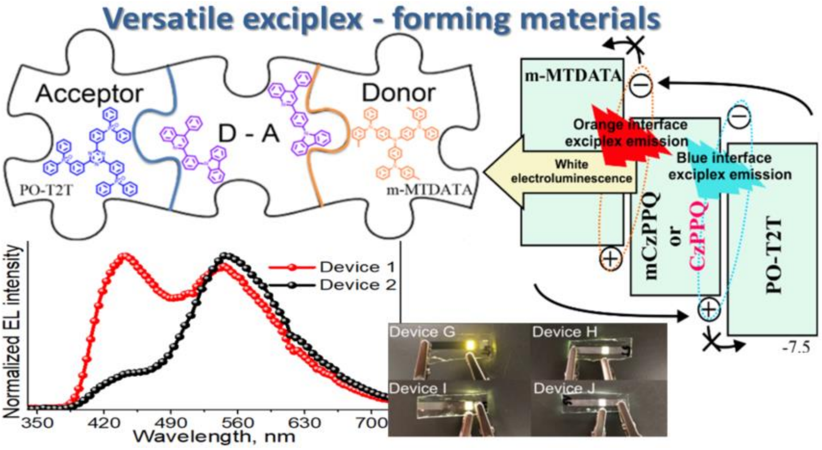

Scheme 4.3. Schematic representation of exciplex-forming properties of pCzPPQ and mCzPPQ

In this work, we propose a unique application of donor-acceptor compounds as versatile exciplex-forming materials which can form two different types of exciplexes D−A/D and A/D−A at the same time. The synthesized compounds were tested in simplified nondoped WOLEDs based on two blue and orange interface exciplexes which were formed between three nondoped layers (A/blue interface exciplex/D−A/orange interface exciplex/D).

4.3.1. Synthesis

Friedlander condensation of *o*-aminobenzophenone with the corresponding iodo- acetophenone afforded quinoline-based compounds in high yield. The target compounds were synthesized by the Ullmann-type cross-coupling reaction. The synthetic route for pCzPPQ and mCzPPQ is depicted in Scheme 4.4. The structures of compounds were confirmed by using ^{1}H NMR, ^{13}C NMR, and mass spectroscopy.

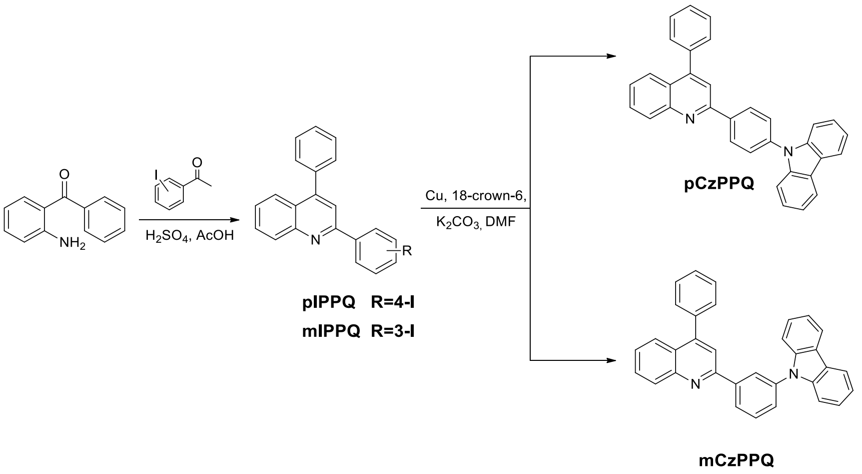

Scheme 4.4. Synthesis of pCzPPQ and mCzPPQ

4.3.2. Electrochemical and photoelectrical properties

To elucidate the electrochemical stability of the target molecules, cyclic voltammetry (CV) was used. CV experiments were performed for the DMF/tetrabutylammonium hexafluorophosphate system which promotes solubilization of compounds as well as a preferable potential window. The cyclic voltammograms of the synthesized quinoline derivatives are depicted in Fig. 4.21 (a).

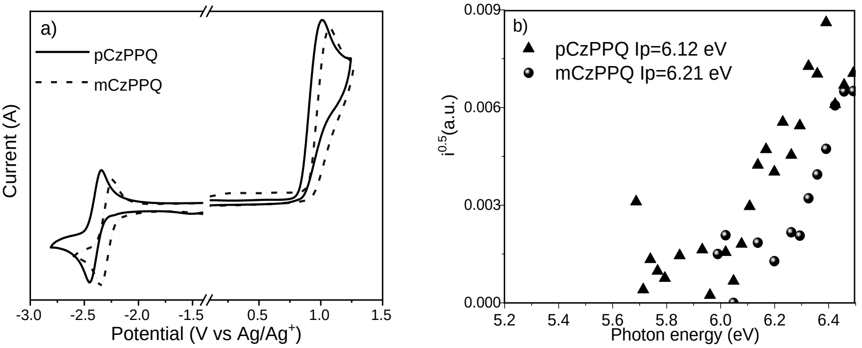

Fig. 4.21. a) Cyclic voltammograms and b) photoelectron emission spectra of **pCzPPQ** and **mCzPPQ**

Because of the similar molecular architecture, analogous shapes of CV curves were observed. For both compounds, a single irreversible oxidation peak was observed, apparently, due to the presence of a carbazolyl unit with C-3 and C-6 nonsubstituted positions. Irreversible oxidation waves were observed for pCzPPQ and mCzPPQ with the peaks of potential at +1.01 and +1.07 V, respectively. In the negative potential range, single reversible waves were observed at peak potentials of −2.45 and −2.35 V for pCzPPQ and mCzPPQ, respectively, presumably due to the formation of a stable radical anion of the quinoline moiety. Equations $IP_{CV} = |e|(4.8 + E_{ox})$ and $EA_{CV} = |e|(4.8 + E_{red})$ were used to evaluate the ionization potential (IP_{CV}) and electron affinity

(EA) from CV measurements. The ionization potential and electron affinity estimated from CV measurements were found to be 5.60 and 5.71 eV for *para*- and *meta*-isomers, respectively. The lower IP_{CV} value of 5.60 eV was determined for pCzPPQ, conceivably due to the higher degree of conjugation of the *para*-isomer then the *meta*-one[129]. The solid-state ionization potential values (IP_{PE}) were estimated by photoelectron emission spectroscopy measurements. IP_{PE} of the amorphous films was found to be slightly higher for mCzPPQ of 6.21 eV than for pCzPPQ with the value of 6.12 eV due to the influence of *meta*- substitution of the phenyl-bridge by the quinoline and carbazole units (Fig. 4.21 (b)). Nevertheless, the electrochemical band gap for both compounds is the same, with the value of 3.13 eV; then, the optical gaps are 3.12 eV for pCzPPQ and 3.37 eV for mCzPPQ. The trend observed by the electron photoemission method is in good agreement with the values observed by CV (Table 4.10). Both measurements revealed the slightly higher IP of the *meta*-isomer.

Table 4.10. Electrochemical and photoelectrical characteristics of quinoline derivatives

Compound	$E_{ox\ (onset)}$ [a] *V*	$E_{red\ (onset)}$ [a] *V*	IP_{CV} [b] *eV*	EA_{CV} [b] *eV*	IP_{PE} [c] *eV*	EA_{film} [d] *eV*	$E_{g,\ opt}$ [e] *eV*	$E_{g,\ CV}$ [f] *eV*
pCzPPQ	0.8	-2.33	5.60	2.47	6.12	3.00	3.12	3.13
mCzPPQ	0.91	-2.21	5.71	2.58	6.21	2.84	3.37	3.13

[a] Determined from CV measurements of dilute DMF solutions. [b] Estimated by using approximation $IP_{CV} = |e|(4.8 + E_{ox\ (onset)})$; $EA_{CV} = |e|(4.8 + E_{red\ (onset)})$. [c] Determined from photoelectron emission spectra. [d] Estimated by using equation $EA_{film} = IP_{PE} - E_{g,\ opt}$. [e] Optical band gap calculated by using equation $E^{opt}_{g} = 1240/\lambda_{abs}^{film}$. [f] Electrochemical band gap determined from equation $E_{g,\ CV} = IP_{CV} - EA_{CV}$.

4.3.3. Charge-transporting properties

The bipolar character of the molecules was verified by the time-of-flight (TOF) method. The transit times (t_{tr}) for both holes and electrons were well observed in the log-log plots, which indicated low-dispersity transport of both positive and negative charges (Fig 4.22 (a)). These results are in good agreement with the results of the charge drift mobility measurements of pCzPPQ by the space charge limited current (SCLC) method[130]. Fig 4.22 (b) shows electric field dependencies of hole and electron drift mobilities for the vacuum deposited layers of pCzPPQ and mCzPPQ. The mobilities of both holes and electrons substantially exceeded 10^{-4} cm^2 V^{-1} s^{-1} at electric fields higher than 10^5 V/cm. The charge mobilities observed for pCzPPQ are higher than the previously reported ones[130]. Since the SCLC method is highly sensitive to the structure of the studied samples[131] as well as to the thicknesses of the layers[132], the differences in the mobility values were obtained for compound pCzPPQ measuring by the SCLC and TOF methods[130]. Importantly, well-balanced hole and electron mobilities were obtained for pCzPPQ and mCzPPQ. This observation shows that they are promising hosts, hole- and electron-transporting materials for OLEDs. Similar well balanced hole/electron transport properties were previously shown for a compound consisting of single carbazole and quinoline units[130]. Slightly higher values of charge-drift mobilities observed for the *para*-isomer pCzPPQ relative to those of the *meta*- one mCzPPQ can apparently be explained by the more favorable packing of the linear molecules of pCzPPQ in the layer.

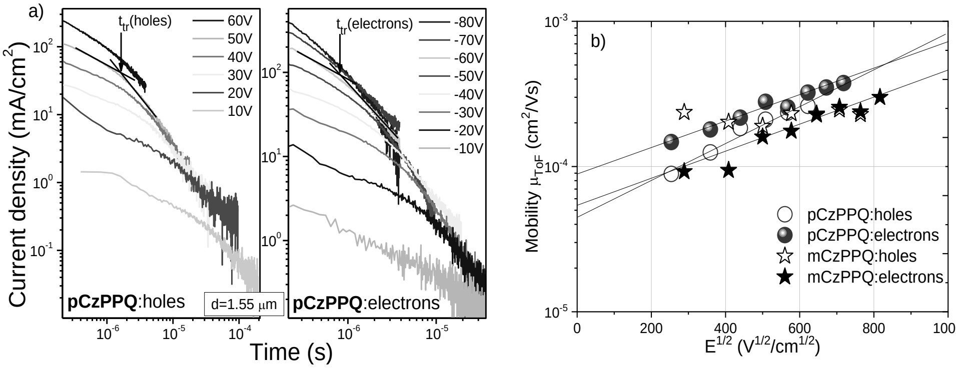

Fig 4.22. Photocurrent transients (a) for holes and electrons in film p**CzPPQ** and hole/electron drift mobility-electric field (E) dependencies (b) for **pCzPPQ** and **mCzPPQ** compounds

4.3.4. Thermal properties

TGA and DSC measurements in a wide range of temperatures were performed for the samples of mCzPPQ and pCzPPQ. The results are given in Fig. 4.23 and Table 4.11. Both compounds were found to be thermally stable. Their 5% weight loss temperatures (T_d) prominently exceeded 300 °C.

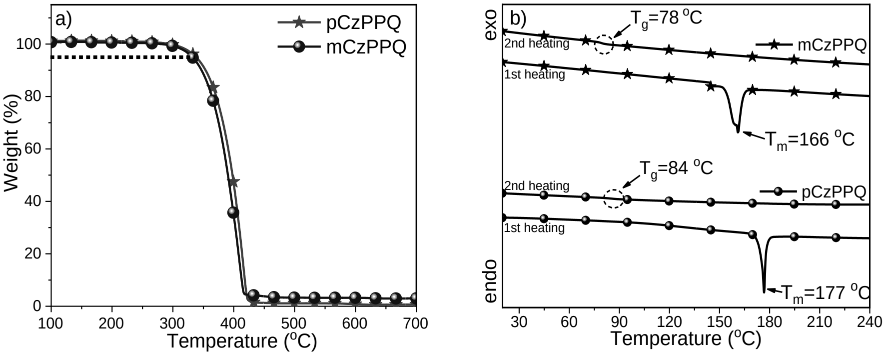

Fig. 4.23. (a) TGA and (b) DSC curves of **mCzPPQ** and **pCzPPQ**

The *para*-isomer exhibited slightly higher thermal stability with T_d of 339. Compounds mCzPPQ and pCzPPQ were obtained after synthesis as crystalline substances. They showed melting signals in the first DSC heating scans. Both compounds were found to be capable of glass formation. Their samples did not show any signals of crystallization in the following DSC heating scans. The glass transition temperature (T_g) of pCzPPQ was found to be by 6 °C higher than that of mCzPPQ. The *para*-isomer also showed a higher melting point of 177 °C (Table 4.11). These observations can apparently be explained by the more symmetrical molecular architecture of pCzPPQ, which resulted in stronger intermolecular interaction both in crystalline and in amorphous phases[133].

Table 4.11. Thermal characteristics of compounds

Compound	$T_g{}^a$, °C	$T_m{}^a$, °C	$T_d{}^b$, °C
pCzPPQ	84	177	339
mCzPPQ	78	166	332

^{a} Estimated from DSC; ^{b} Estimated from TGA;

T_g is glass transition temperature; T_m is melting point; T_d is the temperature of 5% weight loss

4.3.5. Photophysical properties

Since pCzPPQ and mCzPPQ consist of electron-accepting quinoline and electron-donating carbazole units linked through a phenyl spacer, they were found to be capable of forming two different types of exciplexes: D−A/D and D−A/A.

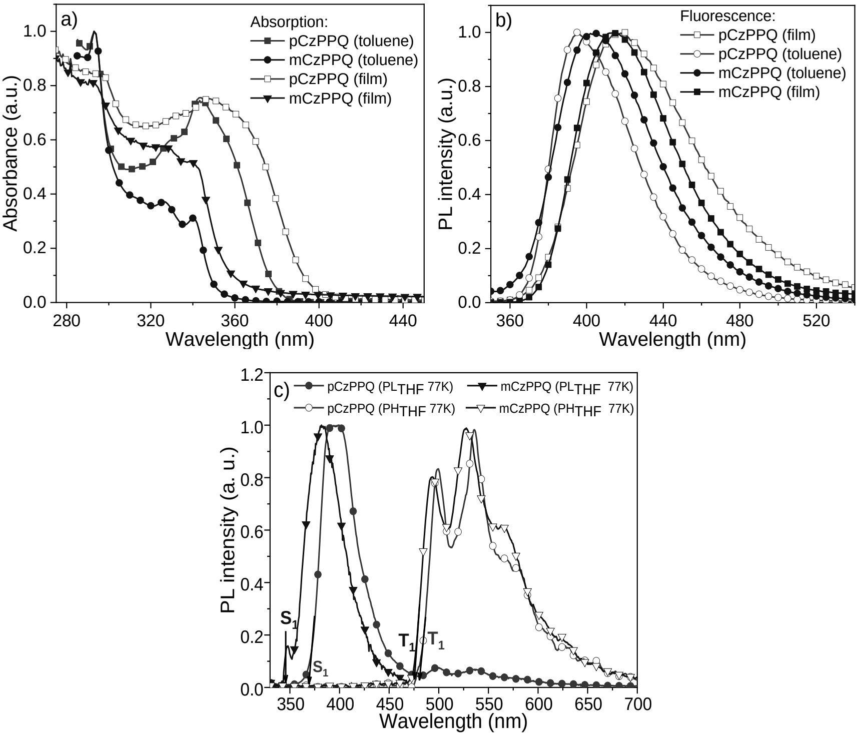

Fig. 4.24. (a) UV-vis and (b) PL spectra of 10^{-5} M toluene solutions and solid films of **pCzPPQ** and **mCzPPQ** (300 K, λ_{exc}=330 nm). (c) Photoluminescence and THF solutions of **pCzPPQ** and **mCzPPQ** (77 K, λ_{exc}=374 nm). Phosphorescence spectra were recorded after a delay of > 50 ms after excitation. First singlet (S_1) and triplet (T_1) energy levels (marked by arrows) were taken from the onsets of fluoresce and phosphorescence spectra of **pCzPPQ** and **mCzPPQ**.

For the formation of such two types of exciplexes with pCzPPQ and mCzPPQ, the appropriate commercially available acceptor and donor were selected. In previous studies, pCzPPQ was used as an efficient host for red PhOLEDs[130], but the exciplex-forming properties of these derivatives have not been reported yet. pCzPPQ and mCzPPQ exhibited similar photophysical properties. The absorption and PL spectra of the dilute solutions (10^{-5} M) in different solvents and of solid films of compounds pCzPPQ and mCzPPQ are shown in Fig. 4.24 (a) and Fig. 4.25. The wavelengths of the maxima of the low-energy absorption and PL bands are presented in Table 4.12.

Table 4.12. Photophysical data for pCzPPQ and mCzPPQ

Compound	$\lambda_{onset, tol}$ nm	$\lambda_{abs, film}$/ $\lambda_{onset, film}$ nm	$\lambda_{PL, tol}$ nm	$\lambda_{PL, film}$ nm	$PLQY_{tol}$, %	$PLQY_{film}$, %	$\tau_1 / \tau_2 (\chi^2)$ ns	E_T, eV	E_S, eV
pCzPPQ	343/380	343/398	395	415	69	22	2.1 / - (1.106)	2.57	3.35
mCzPPQ	340/351	340/368	403	413	11	10	9.1 / 22.9 (1.247)	2.61	3.57

λ_{abs} is the maximum of the low-energy absorption band; λ_{onset} is the onset of the last absorption band; λ_{PL} is the wavelength of the emission maximum of the toluene solution (10^{-5}M) or solid films of compounds; η_{tol}, η_{film} are photoluminescence the quantum yields of the toluene solution (10^{-5}M) and solid film; τ_1 / τ_2 are the photoluminescence lifetimes of neat films of compounds; To calculate the singlet (E_S) and triplet (E_T) energy levels of both isomers, empiric formulas E_S=1239/λ_S and E_S=1239/λ_T were used where λ_S and λ_T are the wavelengths taken from the onsets of fluorescence and phosphorescence spectra recorded at 77 K for compounds mCzPPQ and pCzPPQ, respectively.

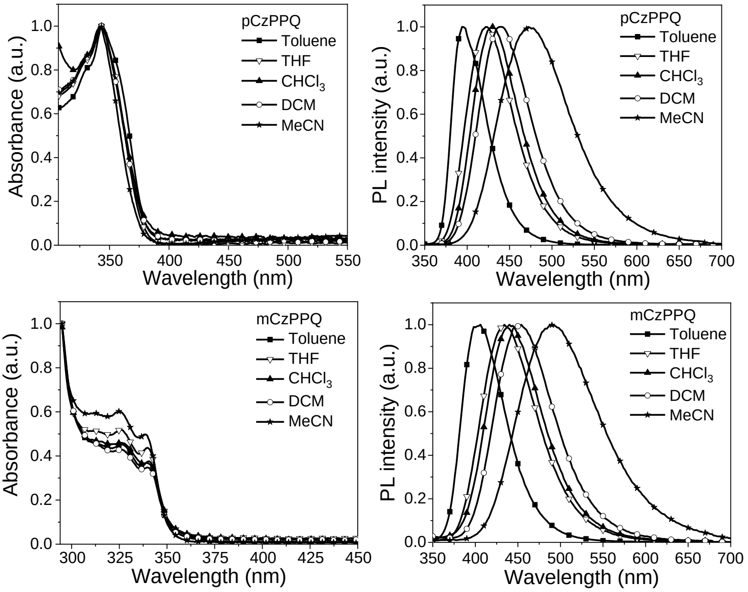

Fig. 4.25. Absorption and photoluminescence spectra of **pCzPPQ** and **mCzPPQ** in different solvents (10^{-5} M)

Low-energy absorption bands were observed at similar wavelengths (at ca. 343 and 340 nm in the case of pCzPPQ and mCzPPQ, respectively) for the solutions in the solvents of different polarities as well as for solid films. Meanwhile, the low-energy edges of the absorption spectra of the films of pCzPPQ and mCzPPQ were slightly red-shifted in comparison to those of the solutions (Table 4.12). The shifts of the edges of the absorption spectra of the films can presumably be explained by molecular interactions in the solid state. PL spectra undergo significant red shifts while going from the less polar toluene ($\varepsilon = 2.38$) to the highly polar acetonitrile ($\varepsilon = 37.5$). This observation shows that both molecules exhibit positive solvatochromism (Fig. 4.25). This behavior is attributed to the intramolecular charge transfer (ICT) character of emissions which is commonly observed for donor-acceptor compounds[134].

Different Stokes shifts of the solutions of pCzPPQ and mCzPPQ were observed due to ICT. The Lippert-Mataga equation was used to analyze Stokes shifts of the solutions of pCzPPQ and mCzPPQ in different solvents. The Stokes shifts (ν_{abs}-ν_{em}) versus orientation polarizability of solvents (Δf) dependencies were plotted and were linearly fitted (Fig. 4.26). The smaller slope of 13950 cm^{-1} was observed for pCzPPQ in comparison to that of 14644 cm^{-1} recorded for mCzPPQ thus indicating difference in dipole moments of the emissive excited states of these compounds (Fig. 4.26).

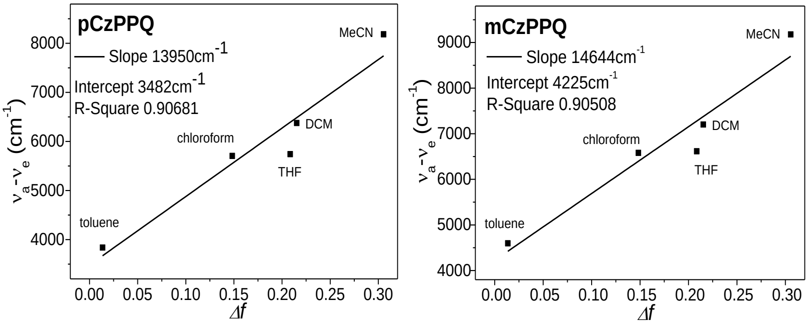

Fig. 4.26. Lippert-Mataga plot (Stokes shift (ν_a-ν_e) against orientation polarizability of solvent (Δf) of pCzPPQ and mCzPPQ

Because of the differences in the dipole moments of pCzPPQ and mCzPPQ, the solution of mCzPPQ in toluene demonstrated a considerably lower PLQY of 11% compared to 69% observed for the *para*-isomer (pCzPPQ). The same tendency was observed for the solid films of these compounds. The film of the *para*- isomer exhibits a higher PLQY value of 22% relative to that of the *meta*-isomer (10%) (Table 4.12). The lower photoluminescence quantum efficiency of mCzPPQ in the solution and in the solid state can be explained by a higher dipole moment of mCzPPQ in comparison to that of pCzPPQ. Additionally, it can be explained by confined electron delocalization through the *meta*- substitution of the phenyl spacer[129]. To obtain the first triplet energy levels of pCzPPQ and mCzPPQ, the PL spectra of the solutions of pCzPPQ and mCzPPQ in THF were recorded at the temperature of liquid nitrogen (Fig. 4.24 (b)). The values of the first singlet and triplet energy levels were taken from the onsets of the fluorescence and phosphorescence spectra, respectively (Table 4.12). *meta*-isomer mCzPPQ showed a marginally higher value of the lowest triplet excited state (E_T) of 2.61 eV in comparison with the *para*-isomer (pCzPPQ) with a triplet energy value of 2.57 eV (Fig. 4.24 (b)). The energies of the first excited singlet state (E_S) were estimated to be 3.35 and 3.57 eV for the THF solutions of pCzPPQ and mCzPPQ, respectively (Table 4.12). In addition, the red shift of ca. 40 nm of the room temperature fluorescence spectrum was observed in comparison to the PL spectrum recorded at a low temperature (77 K) for the THF solutions of pCzPPQ and mCzPPQ. Such a bathochromic shift can be explained by the stabilization of the excited state of the molecules by the polar solvent at room temperature while the same process does not occur at 77 K due to the solidification of the solvent (Fig. 4.24 (b))[135]. Exciplex formation between the synthesized molecules and the commercially available acceptors or donors was identified by the appearance of the bathochromically shifted emission bands of the blends as compared to the emission of separate donors and acceptor (Fig. 4.27). During the donor-acceptor intermolecular interaction in the excited state, an electron is transferred from the HOMO of an electron-donating molecule to the LUMO of an acceptor[136].

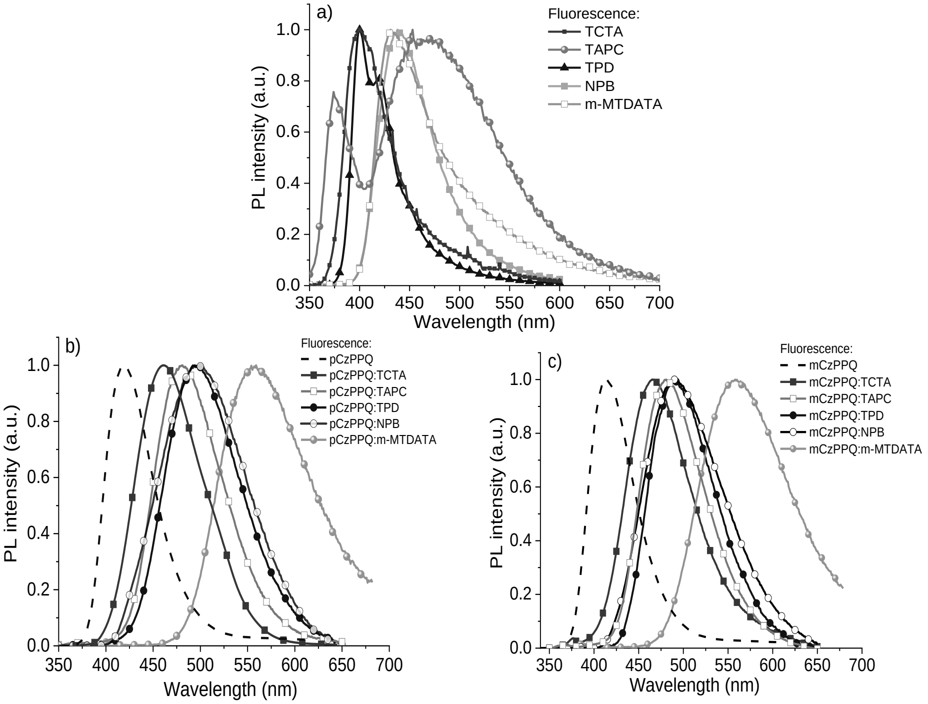

Fig. 4.27. Photoluminescence spectra of the films of electron-donors (a) and the molecular blends of **pCzPPQ** (b) and **mCzPPQ** (c) with different donors

Bipolar molecules pCzPPQ and mCzPPQ formed excited complexes and behaved as donors in pair with an acceptor or as acceptors in pair with a donor. Thus pCzPPQ and mCzPPQ form blue exciplexes with acceptor PO-T2T and yellow exciplex with donor m-MTDATA and blue exciplexes with other donors, such as TCTA, TPD, NPB, and TAPC. The photoluminescence spectra of the blends as well of the neat films of donors are presented in Fig. 4.27, and the data is collected in Table 4.13. All the equimolar blends, compared with individual donors and acceptor (pCzPPQ or mCzPPQ), demonstrated red-shifted broadband emission spectra, which can be assigned to the formation of exciplexes. pCzPPQ or mCzPPQ acted as donors in the blends with acceptor PO-T2T and showed orange exciplex fluorescence with the intensity maxima at 464 and 458 nm, respectively. With the aim to obtain white light emission, blue exciplex pairs of pCzPPQ/mCzPPQ with PO-T2T and pairs of pCzPPQ/mCzPPQ with m-MTDATA, which emit orange light, were selected for more profound investigation (Fig. 4.27).

Table 4.13. A photoluminescence maximum peaks of exciplex mixtures of **mCzPPQ/pCzPPQ** with PO-T2T acceptor and different donors

Exciplex blends (1:1)	$\lambda_{\mathrm{PL,\ film}}$[a], nm	Exciplex blends (1:1)	$\lambda_{\mathrm{PL,\ film}}$[a], nm
mCzPPQ (neat film)	413	pCzPPQ (neat film)	415
PO:T2T : mCzPPQ	458	PO:T2T : pCzPPQ	464
mCzPPQ : TCTA	465	pCzPPQ : TCTA	461
mCzPPQ : TAPC	480	pCzPPQ : TAPC	480
mCzPPQ : TPD	489	pCzPPQ : TPD	494
mCzPPQ : NPB	490	pCzPPQ : NPB	496
mCzPPQ : m-MTDATA	546	pCzPPQ : m-MTDATA	551

[a] Photoluminescence peaks of blends

The absorption and PL spectra of the solid samples of the separate molecules and exciplex emitters are presented in Fig. 4.28. The emission of exciplex forming molecular mixture mCzPPQ:PO-T2T with the intensity maximum observed at 458 nm was blue-shifted relative to that of the pair of pCzPPQ:PO-T2T with the emission peak at 464 nm. This observation can be explained by the slightly higher energy of HOMO for mCzPPQ (Table 4.10). A similar hypsochromic shift of 5 nm was observed for the PL emission of the mCzPPQ:m-MTDATA system compared to that of pCzPPQ:m-MTDATA, which can be assigned to the lower LUMO value of mCzPPQ. The UV-vis spectra of the studied exciplex-forming molecular mixtures and the corresponding acceptor and donors are depicted in Fig. 4.28 (a). The absorption spectra of the exciplex-forming systems pCzPPQ:PO-T2T and mCzPPQ:PO-T2T are very similar to the spectra of the constituting molecules pCzPPQ and mCzPPQ.

The shapes of the absorption spectra of the films of exciplex-forming mixtures of the compounds with the m-MTDATA donor resemble that of a pure m-MTDATA film. Thus the absorption spectra of the blends overlap with the absorption spectra of the donors and acceptors in use. Nonetheless, direct exciplex CT absorption of the ground state of the studied solid mixtures mCzPPQ/POT2T, pCzPPQ/PO-T2T, mCzPPQ/m-MTDATA and pCzPPQ/m-MTDATA was not clearly detected (Fig. 4.28 (a)). Apparently, a more sensitive method is required to record the intermolecular charge-transfer absorption of the studied exciplexes[137]. Fluorescence decays of the solid films of the compounds and degassed exciplex-forming blends are depicted in Fig. 4.28 (b). In addition, PL decays of mCzPPQ/POT2T, pCzPPQ/POT2T, mCzPPQ/m-MTDATA and pCzPPQ/m-MTDATA were observed in the microsecond range, which is much longer than the nanosecond range of fluorescence of the individual donor and acceptor (Fig. 4.28).

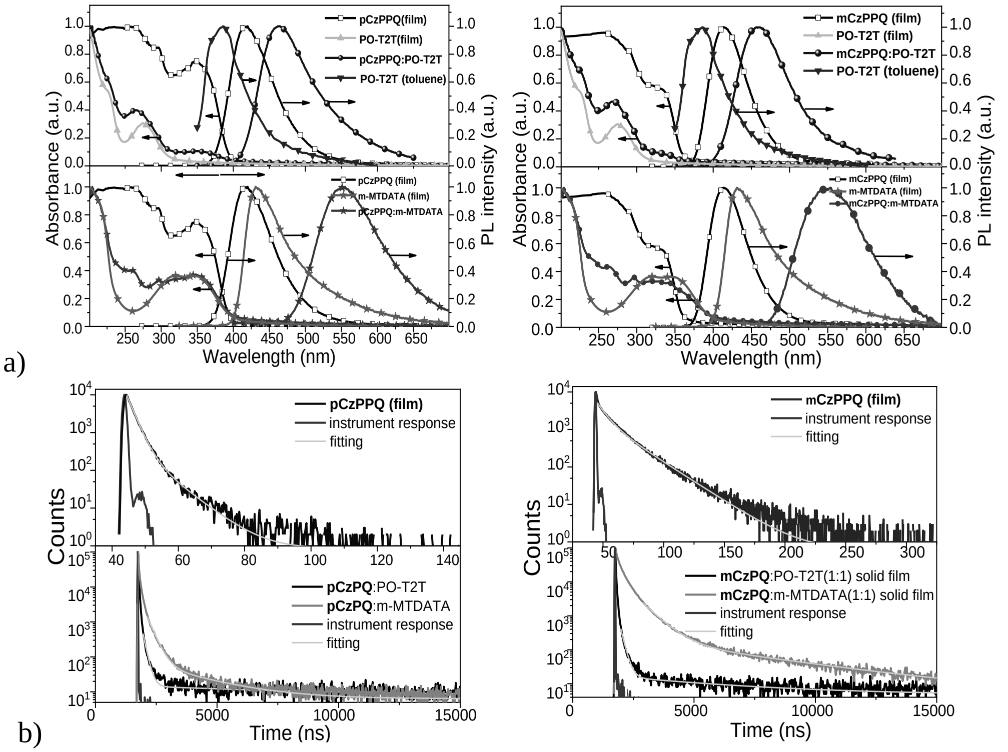

Fig. 4.28. UV-vis, PL spectra (a) and PL decay curves (b) of the thin films of individual compounds and molecular mixtures of **pCzPPQ** and **mCzPPQ** with PO-T2T and m-MTDATA

Measured under vacuum condition (at pressure <5 × 10^{-5} mBar), PL decay curves revealed the double exponential character of decays of the exciplex-forming systems with the components of prompt and delayed fluorescence. The nanosecond components of the decay curves refer to the prompt fluorescence, while the longer-lived components can be attributed to delayed fluorescence (Table 4.14).

Table 4.14. Photophysical data for selected exciplex-forming systems

Exciplex system	λ_{PL} [a], nm	PLQY [b], %	τ_1 [c], ns	τ_2, ns	χ^2
pCzPPQ:PO-T2T	464	6	130.1 (55%)	7963.2 (45%)	1.265
pCzPPQ:m-MTDATA	551	4	257.5 (76%)	2017.4 (24%)	1.299
mCzPPQ:PO-T2T	458	4	146.2 (56%)	4813.1 (44%)	1.368
mCzPPQ:m-MTDATA	546	3	612.0 (65%)	4290.2 (35%)	1.294

[a] Wavelengths of PL peaks of exciplex blends; [b] Photoluminescence quantum yield of exciplex blends; [c] PL lifetimes of exciplex blends

The exciplex forming mixtures of pCzPPQ and mCzPPQ with the PO-T2T acceptor showed slightly higher PLQY values of 6% and 4% if compared to the corresponding blends with the m-MTDATA donor with PLQY value reaching 4% for pCzPPQ:m-MTDATA and 3% for mCzPPQ:m-MTDATA. It should be noted that these PLQYs values were recorded under air conditions, and they are contributed mainly by the prompt fluorescence of exciplexes which are not sensitive to oxygen. Nevertheless, the obtained PLQY values display a higher exciplex emission efficiency of pCzPPQ-based solid mixtures. Apparently, the linear molecular structure of pCzPPQ is more appropriate for efficient exciplex emission than the v-shaped one of mCzPPQ.

4.3.6. Exciplex-based nondoped white OLEDs

Since mCzPPQ and pCzPPQ compounds were characterized by a sufficiently high T_g, well-balanced charge transport, appropriate HOMO/LUMO levels for hole/electron injection, and unique exciplex-forming properties, their nondoped layers were used in the design and fabrication of white OLEDs. Vacuum-deposited OLEDs comprised of the nondoped layers of mCzPPQ or pCzPPQ were fabricated in a multilayer architecture ITO/MoO_3(1 nm)/m-MTDATA(60 nm)/ mCzPPQ (or pCzPPQ) (x nm)/PO-T2T(10 nm)/ TPBi(40 nm)/LiF(0.5 nm)/Al. In these OLED structures, the layers of different thicknesses (x of 10, 20, and 30 nm) of mCzPPQ were deposited in devices A−C and of pCzPPQ in devices D−F, respectively (Table 4.15). The hole and electron injecting layers of molybdenum trioxide (MoO_3) and lithium fluoride (LiF), and the electron transporting layer of 2,2′,2″-(1,3,5-benzinetriyl)tris(1-phenyl-1-H- benzimidazole) (TPBi) were deposited in the studied devices. Therefore, efficient charge injection and transport from indium tin oxide (ITO) and aluminum (Al) electrodes to the three-layered interface exciplex based emitters m-MTDATA/mCzPPQ (or pCzPPQ)/PO-T2T were provided in the devices (Fig. 4.29).

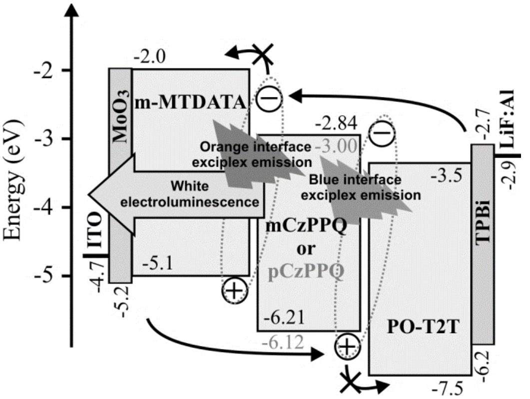

Fig. 4.29. Equilibrium energy diagram of the fabricated devices

The layers of mCzPPQ or pCzPPQ mainly played the role of double interface exciplex formation and spacers for the regulation of emission intensities of exciplexes. In the case of perfect alignment of emission intensities of orange m-MTDATA/ mCzPPQ (or pCzPPQ) and blue mCzPPQ (or pCzPPQ)/PO-T2T interface exciplexes, white electroluminescence was expected for the designed OLEDs. Indeed, both blue and orange bands were observed in the electroluminescence (EL) spectra of the fabricated devices A−F thus proving that the charge pairs recombined at mMTDATA/mCzPPQ (or pCzPPQ) and mCzPPQ (or pCzPPQ)/PO-T2T interfaces (Fig. 4.30 (a)). *Commission Internationale de l'Eclairage* (CIE 1976) chromaticity coordinates (u', v') of devices A−F corresponded to different white colors with the color rendering index (CRI) reaching 70 at an applied voltage of 8 V (Fig. 4.31, Table 4.15). The color temperature (T_C) of the electroluminescence of devices A−F was observed in the wide range from warm (T_C = 4200) to cold (T_C = 8500) white colors (Table 4.15). This observation can be explained by the different distribution of emission intensities of the blue and orange exciplexes of mCzPPQ- and pCzPPQ-based devices. As it is seen from parts *a* and *d* of Fig. 4.30, the EL spectra of the studied devices are highly sensitive to the distribution of charge pairs at mMTDATA/ mCzPPQ (or pCzPPQ) and mCzPPQ (or pCzPPQ)/POT2T interfaces. Commonly, a different distribution of charge pairs in device structures stems from different charge-injection and charge-transport characteristics. Since the same functional layers having the same HOMO/LUMO energy values were used for mCzPPQ-based and pCzPPQ-based devices, different charge-injection properties cannot be the reason for a large variation in the device emission responses.

On the other hand, different thicknesses of the functional layers (mCzPPQ (or pCzPPQ) and PO-T2T) resulted in different electric fields in the device. This leads to different charge mobilities in the functional layers of the devices at different electric fields. Thus different charge-transporting properties are the main reason for the large variation in the device emission responses.

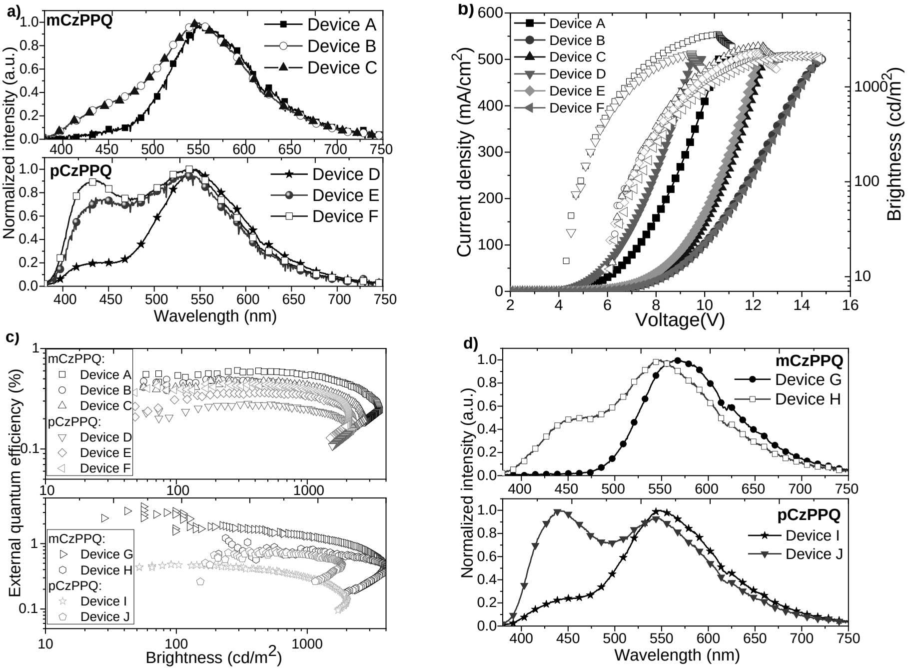

Fig. 4.30. EL spectra recorded at 8 V (a) and current density–voltage–brightness characteristics (b) for devices A–F; EL spectra recorded at 12 V (c) for devices G–J and EQE-brightness characteristics (d) of the devices

The distribution of the emission intensities of the blue and orange exciplexes can be controlled by changing the thicknesses of the layers of mCzPPQ (or pCzPPQ) (Fig. 4.30 (a)). The lowest turn-on voltages of 4.4 V at 10 cd/m^2 were observed for devices A and D with the thinnest layers of mCzPPQ (or pCzPPQ). Devices A and D showed a maximum brightness of 3600 and 2200 cd/m2 and maximum EQE of 0.6 and 0.27%, respectively (Fig. 4.30 (b, c), Table 4.15).

These parameters changed by increasing the thicknesses of the layers of mCzPPQ (or pCzPPQ) thicknesses in devices B, C and E, F, which led to the change of the charge recombination probability. Similar changes were observed for current and power efficiencies (Fig. 4.32, Table 4.15). The thicknesses of m-MTDATA, mCzPPQ (or pCzPPQ), PO-T2T and TPBi layers were further optimized in devices G−J featuring structures ITO/MoO_3(1 nm)/mMTDATA(50 nm)/ mCzPPQ (or pCzPPQ) (x nm)/PO-T2T(y nm)/ TPBi(55 nm)/LiF(0.5 nm)/Al (Table 4.15).

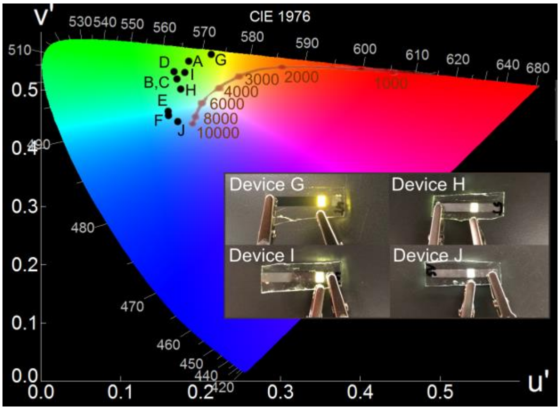

Fig. 4.31. Color coordinates of EL spectra at 8 and 12 V for non-doped warm-white OLEDs A–F and G–J, respectively. Insets: photos of devices G–J.

Before optimization, the charge recombination zone was mostly placed at mMTDATA/mCzPPQ (or pCzPPQ) interface resulting in intensive emission of the mMTDATA:mCzPPQ (or pCzPPQ) exciplex. This means that electrons reached the mMTDATA/ mCzPPQ (or pCzPPQ) interface much faster than holes reached the mCzPPQ (or pCzPPQ)/PO-T2T interface. To balance the recombination zones, the thicknesses of the TPBi and PO-T2T layers were increased while the thickness of the m-MTDATA layer was decreased in devices G−J. As a result, devices G−J were characterized by improved CRI values achieving 76 for EL spectrum of device J at an applied voltage of 12 V in comparison to those of other mCzPPQ- and pCzPPQ-based devices A−F (Table 4.15).

The best maximum EQE of 3.15% was obtained for device G. The output parameters of the fabricated devices were not impressive partly due to the low-lying triplet energy level of mCzPPQ and pCzPPQ. We hope that the next generation of versatile exciplex-forming materials will be characterized by high enough triplet energy levels which are vitally required for the high efficiency of exciplex-based OLEDs[138, 139].

Table 4.15. Summary of basic white OLED parameters

Device	**V_{on}, V**	**Max. brightness, cd/m^2**	**CE_{max}, cd/A**	**PE $_{max}$, lm/W**	**EQE_{max} %**	**CIE 1976 (u’, v’)**	**CRI**	**T_C**
A	4.4	3600	1.76	1.1	0.6	(0.19, 0.55)	57	4200
B	6.2	2100	1.35	0.7	0.5	(0.17, 0.52)	63	5200
C	6.2	2700	1.3	0.57	0.49	(0.17, 0.52)	63	5200
D	4.4	2200	0.84	0.46	0.27	(0.17, 0.53)	59	5100
E	6.1	2200	0.83	0.35	0.35	(0.16, 0.46)	70	7900
F	6.1	2100	1.02	0.43	0.42	(0.16, 0.46)	69	8500
G	6.0	3900	8.9	4.45	3.15	(0.21, 0.56)	52	3400
H	7.1	4100	2.75	1.13	1.06	(0.18, 0.5)	68	5400
I	8.7	2000	1.29	0.4	0.5	(0.18, 0.53)	63	4600
J	7.8	1800	1.64	0.47	0.75	(0.17, 0.45)	76	8300

[a] CIE, CRI and T_C of EL spectrum for devices A–F recorded at 8 V and for devices G–J recorded at 12 V

Interface exciplex-forming layers:
A: mMTDATA(60 nm)/**mCzPPQ** (10 nm)/PO-T2T(10 nm) **B**:mMTDATA(60 nm)/**mCzPPQ** (20 nm)/PO-T2T(10 nm)
C:mMTDATA(60 nm)/**mCzPPQ** (30 nm)/PO-T2T(10 nm) **D**:mMTDATA(60 nm)/ **pCzPPQ** (10 nm)/PO-T2T(10 nm)
E:mMTDATA(60 nm)/ **pCzPPQ** (20 nm)/PO-T2T(10nm) **F**:mMTDATA(60nm)/ **pCzPPQ** (30 nm)/PO-T2T(10 nm)
G:mMTDATA(50 nm)/**mCzPPQ** (10 nm)/PO-T2T(10 nm) **H**:mMTDATA(50 nm)/**mCzPPQ** (20 nm)/PO-T2T(20 nm)
I:mMTDATA(50 nm)/ **pCzPPQ** (10 nm)/PO-T2T(10 nm) **J:**mMTDATA(50 nm)/ **pCzPPQ** (20nm)/PO-T2T(20 nm)

Due to the relatively low triplet levels of compounds mCzPPQ and pCzPPQ (Table 4.12), lower efficiency of blue exciplex emission was obtained in the exciplex-forming systems mCzPPQ (or pCzPPQ)/PO-T2T relative to those of orange exciplex-forming systems mMTDATA/mCzPPQ (or pCzPPQ). Therefore, the highest EQE value was obtained in device G in EL spectrum, of which, the lowest contribution of blue exciplex emission was observed (Fig. 4.32 (a, d)). Because of the low contribution of blue exciplex emission, the lowest CRI of 52 was detected for device G. It can be assumed that the intensive yellow emission is partly due to the long-range exciplex between m-MTDATA and PO-T2T[140]. The very low contribution of the long-range exciplex was previously detected for the 10 nm-thick spacer layer[140]. In addition, the emission of exciplex m-MTDATA: PO-T2T (λ_{max} ~ 640 nm[141] is red-shifted in comparison to that of *m*-MTDATA:mCzPPQ (λ_{max} = 546 nm) or m-MTDATA:pCzPPQ (λ_{max} = 551 nm). However, an additional band (shoulder) was not detected for the EL spectra of devices A, D, G, and I in contrast to other devices with the thicker layers of the versatile exciplex-forming materials mCzPPQ or pCzPPQ (20 and 30 nm). Therefore, the long-range exciplex between m-MTDATA and PO-T2T most probably did not influence the EL of the devices.

On the other hand, nonradiative triplets of mCzPPQ/POT2T and pCzPPQ/POT2T can diffuse to another interface for light emission since the two emission zones are separated by thin spacers (mCzPPQ or pCzPPQ). It is most probably the case for devices A, D, G, and I with a thin layer (10 nm) of versatile exciplex-forming materials mCzPPQ or pCzPPQ since the diffusion length of the triplet can be longer than 10 nm[131]. Indeed, in the cases of the devices with thin layers of mCzPPQ or pCzPPQ, the intensity of yellow emission was higher. This observation can be explained by the diffusion of the nonradiative triplet of mCzPPQ/PO-T2T or pCzPPQ/PO-T2T to another interface mCzPPQ/m-MTDATA or pCzPPQ/m-MTDATA for light emission in devices A, D, G, and I. Thus, in this work, we demonstrate the approach for the design of white nondoped OLEDs based on the new type of dual exciplex forming materials. Further development of D−A molecules with improved dual exciplex-forming properties may lead to an increase of EQE of OLEDs fabricated by using this approach. Such D−A molecules have to be characterized at least by high triplet energies, bipolar charge transport, and to possess appropriate for hole and electron injection HOMO and LUMO levels.

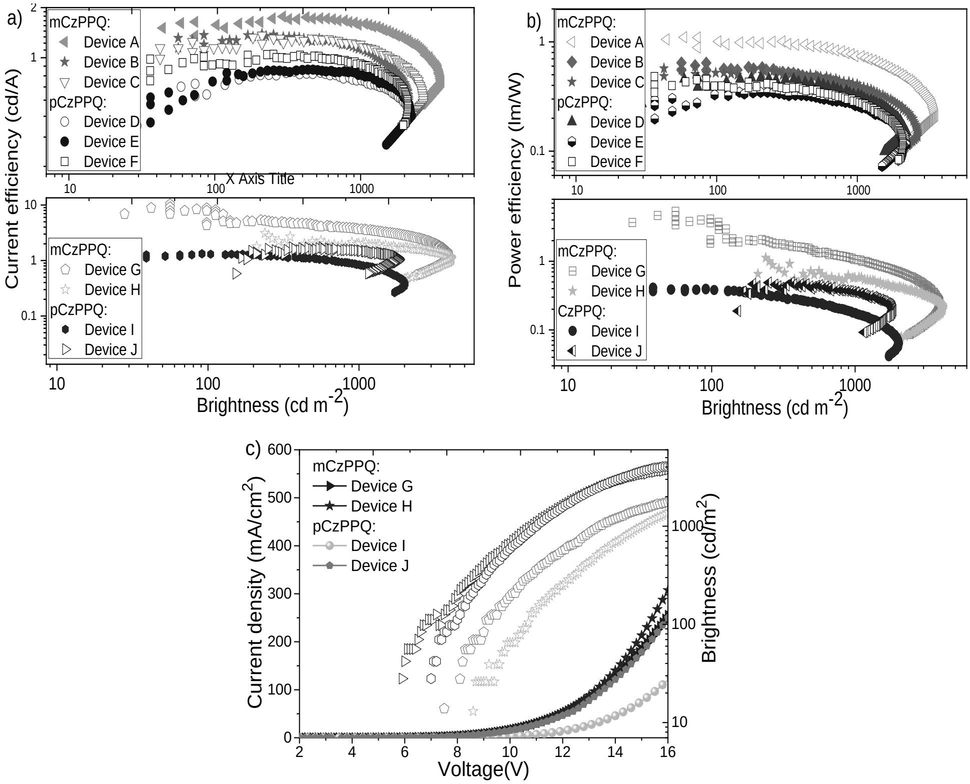

Fig. 4.32. Current-brightness (a) and power-brightness (b) characteristics for the studied devices and current density-voltage-brightness characteristics (c) for devices G–J

To conclude, we have synthesized and investigated two isomeric compounds bearing quinoline and carbazole units. The photophysical, electrochemical, thermal and charge-transporting properties of the synthesized compounds were examined. The investigated compounds exhibited high thermal and electrochemical stability as well as bipolar charge transport. The *para*-isomer showed higher photoluminescence quantum efficiency of the toluene solution of 67% and a slightly lower energy of the triplet level. The *meta*-isomer showed a slightly higher v ionization potential of 6.21 eV. The compounds were examined as exciplex forming compounds. They showed both electron-accepting and electron-donation nature in pair with the commercially available donors and acceptor. In pair with donor 4,4′,4″-tris[3-methylphenyl(phenyl)amino]- triphenylamine, they form orange exciplexes, while with acceptor 2,4,6-tris[3-(diphenylphosphinyl)phenyl]-1,3,5-triazine they form blue exciplexes with relatively long fluorescence lifetimes. Orange and blue exciplex systems were used for the preparation of the emitting layer of the white OLED. The highest maximum external quantum efficiency of 3.15% was observed for the best device. The best contribution of blue and orange exciplex emission in the electroluminescent spectra of the optimized device resulted in the high color rendering index of 76 and a color temperature of 8400 K.

4.4. Multifunctional quinoline-based materials

4.4.1. Synthesis

The strategy for the synthesis of target compounds is depicted in Scheme 4.5. Synthetic pathways towards target quinoline-based compounds pPZPQ and mPZPQ were similar to the previously discussed procedure (Chapter 4.3.1). The synthetic route includes first step acid-catalysed Friedlander cyclocondensation to yield a quinoline derivative. The second step Buchwald-Hartwig cross-coupling reaction of halide-containing quinoline derivative and di-*tert*-butyl-phenothiazine NH-donor afforded the final materials.

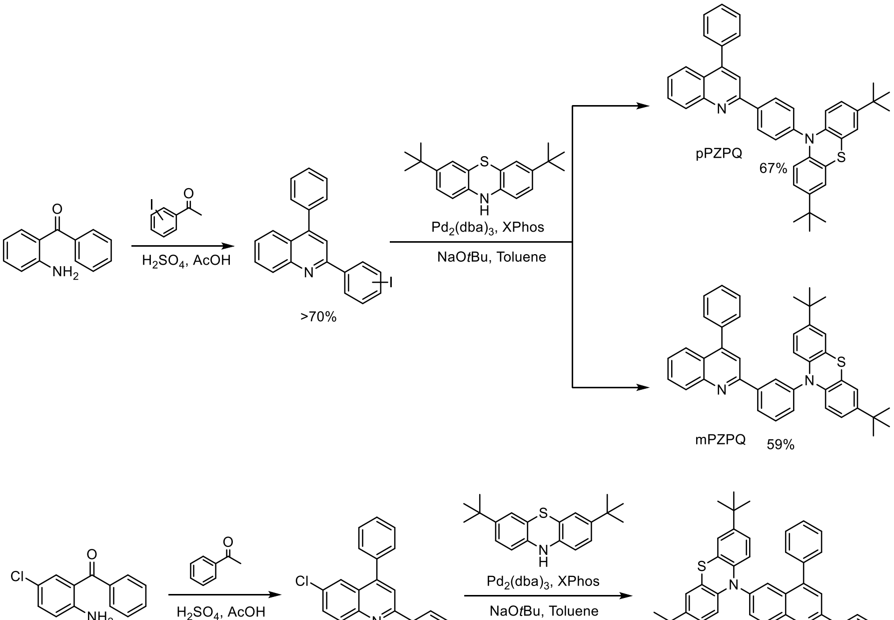

Scheme 4.5. Synthetic route toward compounds pPZPQ, mPZPQ and PZPQ

4.4.2. Thermal properties

The thermal properties of the synthesized materials were investigated by TGA and DSC methods under nitrogen atmosphere. The TGA and DSC curves are depicted in Fig 4.33. Consistent with the TGA results, the 5% weight loss temperature were found to be similar for all the quinoline-based materials along the series and varied in the range of 348–385 °C. The thermal properties of the target compounds are summarized in Table 4.16.

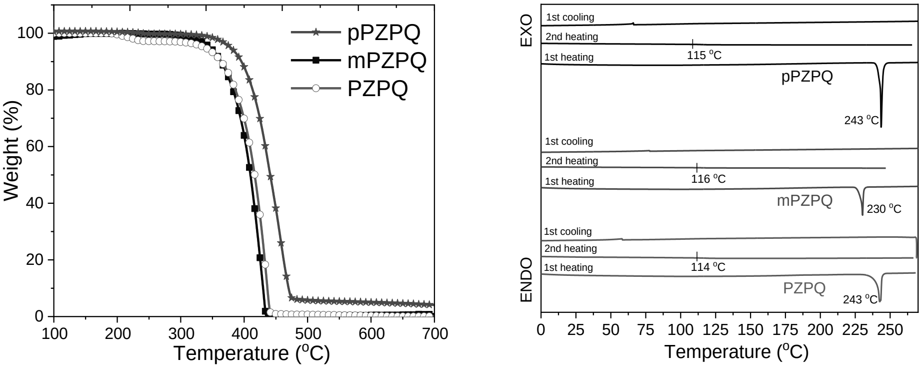

Fig 4.33. TGA and DSC curves of investigated compounds

The target compounds were obtained after the synthesis as crystalline substances. Therefore, compounds showed melting signals during the first scan of DSC measurement. The higher melting temperature of 244 °C for pPZPQ relative to the corresponding mPZPQ isomer with its T_d value of 230 °C can be attributed to the more symmetrical structure of pPZPQ, which leads to the tighter packing of pPZPQ molecules[142]. In addition, all the three compounds pPZPQ, mPZPQ and PZPQ were capable to form molecular glasses during the second heating scan. Due to the similar molecular architectures, the isomeric compounds possessed with comparable glass transition temperatures of ~115 °C.

Table 4.16. Thermal characteristics of pPZPQ, mPZPQ and PZPQ

Compounds	T_d,^{a} °C	T_g,^{b} °C	T_m,^{b} °C
pPZPQ	385	115	244
mPZPQ	360	116	230
PZPQ	348	114	243

Estimated from TGA ^{a} and DSC ^{b}

4.4.3. Electrochemical and photoelectrical properties

For the estimation of the electrochemical stability of target compounds, cyclic voltammetry measurements for the DMF/tetrabutylammonium hexafluorophosphate systems were performed. Therefore, CV measurements were also performed for the elucidation of the ionization potential (IP_{CV}) and electron affinities (EA_{CV}) values which are one of the crucial parameters of organic semiconducting materials. The CV curves of the compounds are depicted in Fig. 4.34, and the respective electrochemical data is collected in Table 4.17. Due to the presence of identical fragments in the structures of the target molecules, analogous shapes of CV curves were detected. As it can be seen from CV curves, three quinoline and phenothiazine-based compounds demonstrate both reversible oxidation and reduction processes during the first CV scan. The peak of the reversible oxidation process appeared at 0.45 V, 0.45 V and 0.38 V for pPZPQ, mPZPQ and PZPQ, respectively.

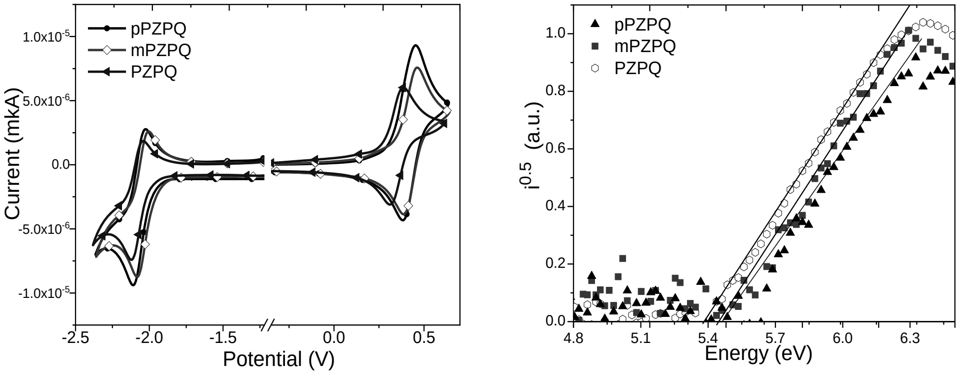

Fig. 4.34. (a) Cyclic voltammograms and (b) Photoelectron emission spectra of pPZPQ, mPZPQ and PZPQ

In the negative potential range, the peak of the reduction wave appeared at ~ -2.10 V for all three compounds. For more precise estimation of the electrochemical properties of the compounds, the IP_{CV} and EA_{CV} values were calculated by using the equation: $IP_{CV} = |e|(4.8 + E^{ox}_{onset})$; $EA_{CV} = |e|(4.8 + E^{red}_{onset})$. Thus, due to bearing the same electron-withdrawing quinoline fragment, each compound from the series possessed similar EA_{CV} values varying from 2.82 eV for PZPQ up to 2.85 eV for pPZPQ and mPZPQ.

Table 4.17. Electrochemical and photoelectrical properties of compounds

Compound	E^{ox}_{onset}[a], V	E^{red}_{onset}[a], V	IP_{CV}[b], eV	EA_{CV}[b], eV	IP_{theor}[c], eV	EA_{theor}[c], eV	IP_{PE}[d], eV
pPZPQ	0.31	-1.95	5.11	2.85	4.28	2.14	5.43
mPZPQ	0.35	-1.95	5.15	2.85	4.23	2.07	5.40
PZPQ	0.26	-1.98	5.06	2.82	4.28	2.07	5.33

[a] Estimated from CV data; [b] Estimated using the approximation $IP_{CV} = |e|(4.8 + E^{ox}_{onset})$; $EA_{CV} = |e|(4.8 + E^{red}_{onset})$. [c] Calculated by DFT B3LYP/6-31G (d, p) method in vacuum; [d] Estimated from photoelectron emission spectra

Therefore, despite the different substitution pattern between quinoline and 9-phenylphenothiazine or phenothiazine, the IP_{CV} values were found to be comparable and ranged from 5.06 eV to 5.15 eV. The lowest IP_{CV} value of 5.06 eV for PZPQ can be assigned to the direct D–A connection and thus the stronger interactions between the donor and acceptor units[143]. The IP_{PE} values obtained from the photoelectron emission spectra varied from 5.33 to 5.44 eV.

4.4.4. Theoretical studies

9-substituted phenothiazine derivatives can adopt two types of conformers: quasi-equatorial and the quasi-axial (Fig. 2.18). Theoretical calculations were carried out to get more profound insight into the conformational diversity. Keeping this in mind, the optimization of ground state geometries of quasi-axial (q-ax) and quasi-equatorial (q-eq) conformers of the investigated compounds was conducted by using B3LYP functional together with 6–31G (d, p) basis set in vacuum. To estimate the stability and thus the possibility of existence of double molecular conformations, the energies of the ground state of the conformers for pPZPQ, mPZPQ and PZPQ were calculated. Interestingly, for all the molecules, quasi-axial forms were found to be more stable than the quasi-equatorial conformers (ca 1.5 kcal/mol). Nevertheless, the energies of two conformers (q-ax and q-eq) differ slightly, which suggests the possibility of existence of both conformers (Table 4.18). Hence, minor energy differences of two conformers for each compound suggest that both conformers with different excited states can exist. The time dependent density functional theory method (TD-DFT)[144] with the 6–31G (d, p) basis set was employed in order to understand the nature of the excited states of quasi-axial and quasi-equatorial conformers of each compound (pPZPQ, mPZPQ, PZPQ). The ground state geometries were obtained by theoretical optimization of each conformer. The optimized geometries of the ground and excited states of the molecules with different phenothiazine conformers are depicted in Fig. 4.36. The dihedral angles between the phenothiazine unit and the electron-accepting fragment play a key role in the understanding of the conformational arrangement. The dihedral angles between the donor and acceptor units of the quasi-axial conformers of pPZPQ, mPZPQ and PZPQ bearing more planar configuration were calculated to be 8 °, 4 ° and 5 °, respectively.

Table 4.18. Ground state optimized geometries along with the corresponding energies

	pPZPQ q-ax	pPZPQ q-eq	mPZPQ q-ax	mPZPQ q-eq	PZPQ q-ax	PZPQ q-eq
Molecular Structure	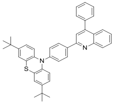	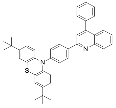	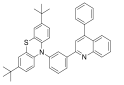	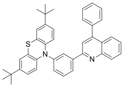	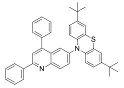	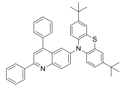
Optimized molecular conformer	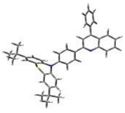	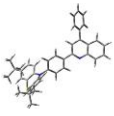	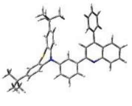	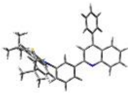	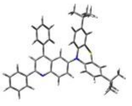	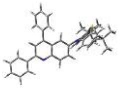
Energy, kcal/mol	1313405.63	1313406.07	1313404.19	1313406.31	1313404.94	1313405.97

In respect to the quasi-axial conformers, the near to orthogonal quasi-equatorial conformers of pPZPQ, mPZPQ and PZPQ showed dihedral angles of 81°, 81°, and 80° in the ground state (Fig. 4.36). To investigate the properties of electronic transition, theoretical UV-vis spectra were obtained with up to 40 excited states calculated for each conformer. For better visualization, experimental UV-vis spectra of the THF solutions were shown along with the theoretical absorption spectra of the compounds (Fig. 4.35). The experimental spectra are in good agreement with the theoretical transitions resembling the UV-vis bands of both q-ax and q-eq conformers, which indicates the presence of double molecular conformations. Nevertheless, as seen from the theoretical spectra of the quasi-equatorial conformers of pPZPQ, mPZPQ and PZPQ, additional transition with the pure CT nature can be observed in the regions of 450–500 nm, whereas it is negligible or hidden in the experimental spectra (Fig. 4.35).

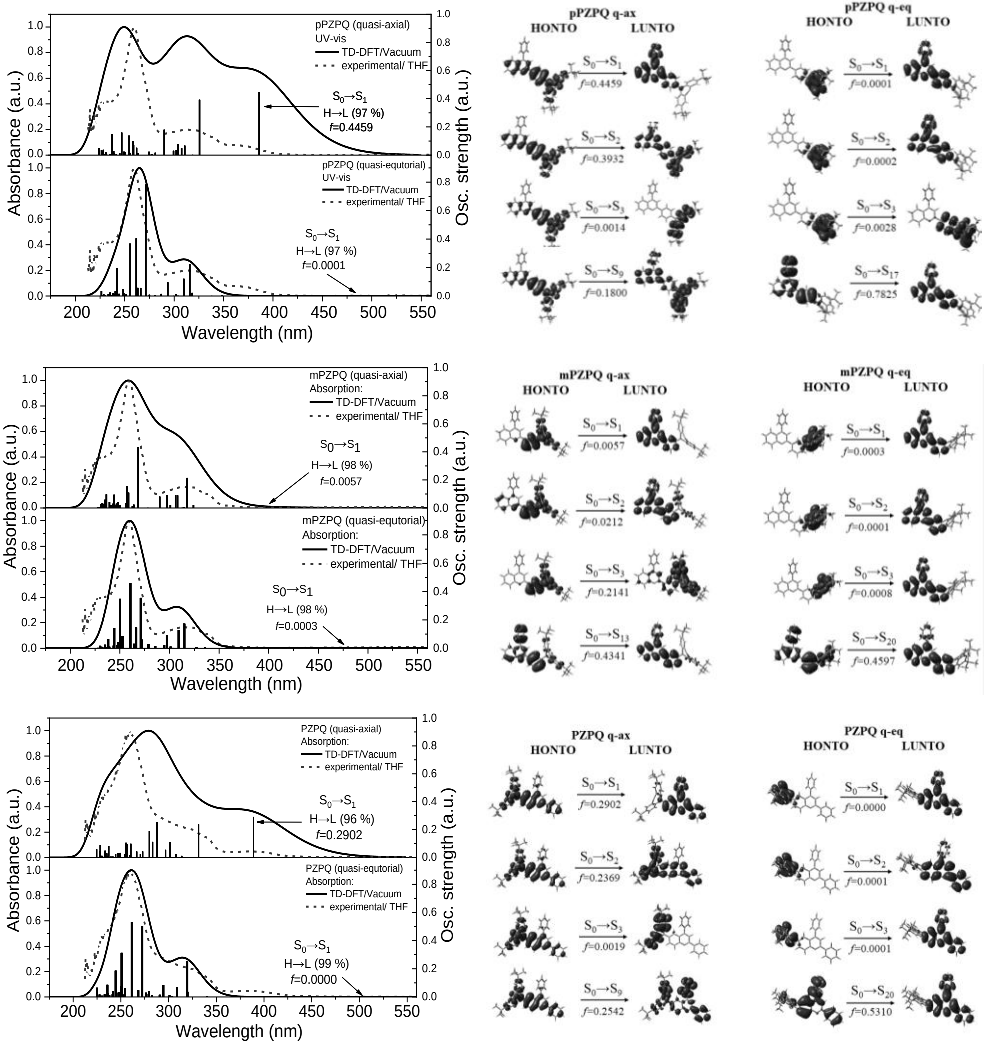

Fig. 4.35. Theoretical UV-vis spectra (left) along with the UV-vis for THF solutions and the nature of the energy transitions (right)

The examined $S_0 \rightarrow S_1$ transition of quasi-equatorial conformers possessed almost zero oscillator strength which is assigned to the perpendicular D–A geometries. Such a low intensity of the first electronic ($S_0 \rightarrow S_1$) transition is usually of the charge-transfer (CT) nature. If paying attention to the $S_0 \rightarrow S_1$ transition for q-ax conformers, the more planar inter-ring geometry leads to the well-resolved lowest energy band (LEB) with the oscillator strength varying from 0.4459 for pPZPQ up to

0.2902 for PZPQ. Interestingly, as it can be observed in Fig. 4.35, the quasi-equatorial conformers of the investigated compounds possess more intense absorption peaks with a higher oscillator strength with respect to the more planar q-ax conformer. This also suggests that the q-eq conformer would show a more intensive emission peak than the q-ax conformer. The nature of the transitions which correspond to $S_0 \rightarrow S_1$ transition as well as to other higher energy transitions with the corresponding oscillator strengths for all the conformers are shown in Fig. 4.35. Therefore, paying attention to the first electronic transition of the two conformers (q-ax and q-eq), the intensity of $S_0 \rightarrow S_1$ of the q-ax conformers of pPZPQ and PZPQ is much higher than the one of the q-eq conformer. This is due to the highly twisted structures of q-eq molecular conformers with respect to the q-ax ones. Thus, more twisted configurations of the q-eq conformers are responsible for the higher degree of HOMO-LUMO separation for the q-eq conformers in comparison with the lower HOMO-LUMO separation for the less twisted q-ax conformer. Interestingly, for the q-ax conformer of *meta*- isomer mPZPQ, the intensity of $S_0 \rightarrow S_1$ transition is almost negligible (f=0.0057) in comparison to the q-ax conformer of *para*- congener pPZPQ (f=0.4459). In order to understand the nature of the initial electronic transition, especially when the transitions originate from multiple excitations transition, calculation of NTO was carried out (Fig. 4. 35).

According to the analysis of natural transition orbitals (NTO), the $S_0 \rightarrow S_1$, $S_0 \rightarrow S_2$, $S_0 \rightarrow S_3$ transitions for q-eq conformers are of CT character, as discussed previously, and the holes are mainly localized on the di-*tert*-butyl phenothiazine unit. Meanwhile, electrons are injected into the phenyl-quinoline or simply quinoline electron-withdrawing unit. Additionally, the main contribution to the first vertical $S_0 \rightarrow S_{1,\,2}$ transitions of all the conformers is mainly due to the HOMO→LUMO and HOMO→LUMO+1 transitions.

Going further to the excited state geometry optimization, upon the vertical excitation of the molecules followed by geometry optimization, it adopts the most stable geometry. Thus, at the excited singlet state q-ax conformer of *para*- and *meta*-congeners, pPZPQ and mPZPQ adopt a more planar configuration with a dihedral angle between the phenothiazine and phenylquinoline plane of 1° (Fig. 4.36). Meanwhile, the q-eq conformers of pPZPQ and mPZPQ adopt the flat form of the phenothiazine unit with perpendicular geometry between phenothiazine and the phenylquinoline acceptor with a dihedral angle of 90 °. Interestingly, at the excited singlet state, the q-ax and q-eq conformers of PZPQ maintained identical perpendicular geometry between phenothiazine and the quinoline fragment. Analysis of the frontier orbitals and the excited states energies of the two phenothiazine conformers for each compound afforded to predict the photophysical diversities of the compounds. The MO profiles revealed that, at the singlet excited state q-ax conformers of pPZPQ, HOMO is delocalized throughout the whole phenyl-phenothiazine and quinoline system. Meanwhile, the HOMO of the q-ax conformer *meta*-substituted mPZPQ isomer spreads only over the phenyl-phenothiazine fragment. Such a distribution is, apparently, due to the higher level of π-conjugation for the *para*-isomer pPZPQ with respect to its *meta*- counterpart.

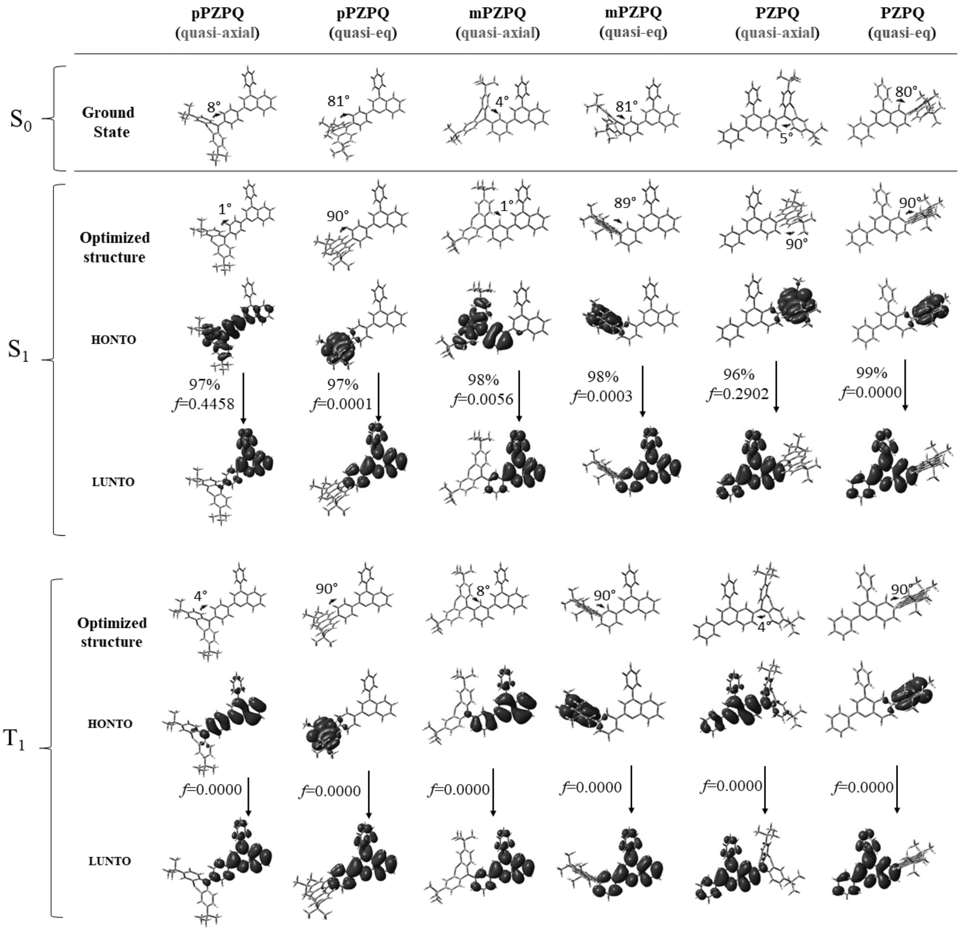

Fig. 4.36. Optimized geometries of pPZPQ, mPZPQ and PZPQ (B3LYP/6–31G(d, p) in the ground and excited state along with the molecular orbitals (MO) distribution at the first singlet and triplet excited states

Contrary to the q-ax PTZ conformers of pPZPQ and mPZPQ, the HOMO of the q-eq conformers is localized mainly on the phenothiazine fragment with a slight distribution at the phenyl linker, which is due to the perpendicular geometries between di-*tert*-butyl phenothiazine and the phenyl quinoline plane (Fig. 4.36). In line with their isomers, the HOMO of both q-ax and q-eq conformers of PZPQ at the excited state is primarily delocalized on the electron-donating di-*tert*-butyl phenothiazine fragment. Meantime, the LUMO of pPZPQ, mPZPQ and PZPQ is strictly localized over the phenylquinoline electron-withdrawing unit. The HOMO-LUMO energies of q-ax and q-eq conformers of the three molecules vary significantly (Table 4.19). To estimate the excited states energies of each conformer for pPZPQ, mPZPQ and PZPQ, calculations of the first three excited Singlet (S_{vert}) and Triplet (T_{vert}) states of each conformer were carried out. According to the calculations, the energy levels of S_{vert} of q-ax conformers are significantly higher and above 3 eV (Table 4.19). Meanwhile, the

S_{vert} values of the corresponding q-eq conformers were found to be lower by ca. 0.65 eV. Interestingly, the MO distribution also differed for the excited triplet states of the conformers. The triplet states for all the q-ax conformer of each compound were found to be of the local character where HONTO and LUNTO are mainly localized on the phenylquinoline fragment. Meanwhile, the first excited triplet states of the q-eq conformers of pPZPQ, mPZPQ and PZPQ were of the charge transfer character with a small HONTO-LUNTO overlap where HONTO is localized on electron-donating di-*tert*-butyl phenothiazine and LUNTO is localized on the electron-deficient phenylquinoline fragment.

Remarkably, all the conformers were characterized by similar T_{vert} energy ranging from 2.35 eV to 2.56 eV, which probably stems from the ^{3}LE state of the donor or the acceptor. Taking a deeper view at the energies of the excited state, one can notice that the theoretically calculated singlet-triplet energy splitting ($\Delta E_{\mathrm{Svert\text{-}Tvert}}$) varies significantly along the conformers. Hence, the $\Delta E_{\mathrm{Svert\text{-}Tvert}}$ values for q-ax conformers were found to be considerably higher (0.73–0.84 eV) in comparison with the corresponding q-eq conformer with the values of 0.01–0.02 eV. Such an observation gives a hint of the possible presence of the delay fluorescence of the q-eq conformers of pPZPQ, mPZPQ and PZPQ.

Table 4.19. Results of theoretical calculations for conformers

Compound	***pPZPQ (q-ax)***	***pPZPQ (q-eq)***	***mPZPQ (q-ax)***	***mPZPQ (q-eq)***	***PZPQ (q-ax)***	***PZPQ (q-eq)***
HOMO, eV	4.99	4.74	5.07	4.78	5.02	4.77
LUMO, eV	1.39	1.78	1.49	1.74	1.38	1.81
$E_{g,\ theor}$, eV	3.6	2.96	3.58	3.04	3.64	2.96
S_{vert}, eV	3.21	2.54	3.12	2.61	3.19	2.45
T_{vert}, eV	2.48	2.53	2.56	2.59	2.35	2.44
$\Delta E_{Svert\text{-}Tvert}$	0.73	0.01	0.56	0.02	0.84	0.01

HOMO/LUMO are the highest occupied/lowest unoccupied molecular orbitals calculated for the ground state of the molecules using B3LYP/6.31G (d, p); $E_{g,\ theor}$ is the theoretically calculated band gap; S_{vert}/ T_{vert} are the theoretically obtained vertical values of the first excited singlet and triplet states; $\Delta E_{Svert\text{-}Tvert}$ is the singlet-triplet energy splitting.

4.4.5. Photophysical properties

Compounds containing a phenothiazine unit have been found to show double molecular conformation with different excited state properties. Thus, two conformers can show double emission in their fluorescence spectra[80]. A similar situation was observed for the investigated compounds pPZPQ, mPZPQ and PZPQ. All the compounds showed dual emission in the solution and solid state fluorescence spectra with blue and red-shifted peaks (Fig. 4.37). Coupled with theoretical calculations, the high energy blue peak can be assigned to the emission of q-ax conformers, while the main red-shifted peak can be assigned to the emission from q-eq conformers. Notably, the intensity of the second yellow peaks from q-eq conformers is much more intensive than that of q-ax conformers.

Experimental evidence of the excited state being of CT character is the solvatochromism in the emission[145]. The UV-vis absorption and fluorescence spectra of the compounds in solvents of different polarities are depicted in Fig. 4.37. All the compounds exhibited the solvatochromic effect which causes a bathochromic shift of the PL spectra with the increasing solvent polarity from toluene ($\varepsilon=2.3$) going to tetrahydrofuran ($\varepsilon=7.6$) and the most polar dichloromethane ($\varepsilon=8.93$). Remarkably, both q-ax and q-eq conformers are sensitive to the enhancement of polarity of the media. Nevertheless, while the emission of the q-ax conformers of pPZPQ and mPZPQ shift slightly from toluene to DCM solutions, the red shift of the emission of q-eq conformers is significant (100–130 nm). It is noteworthy in the emission profile of *meta*-substituted mPZPQ that the emission intensity of the q-ax conformer is very weak in comparison with the q-eq conformer and can be observed only for a highly polar DCM solution (Fig. 4.37). By this observation, in collaboration with theoretical calculations, one can assume the stronger CT character of the q-eq conformer than that of the q-ax conformer.

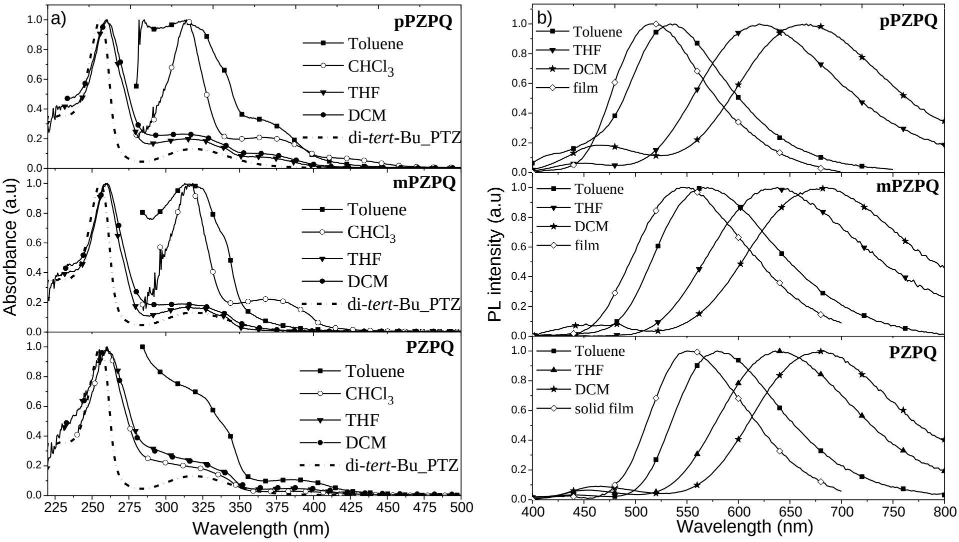

Fig. 4.37. (a) UV-vis absorption and (b) fluorescence spectra of solutions (10^{-5}) and solid state of compounds pPZPQ, mPZPQ and PZPQ

As discussed above, the experimental absorption spectra of the investigated compounds is the mix of absorption profiles of the two conformers (Fig. 4.35). Thus, for compounds pPZPQ and mPZPQ, LEB corresponds to the $S_0 \rightarrow S_1$ transition (H→L) of the q-ax conformer. Interestingly, that the theoretical spectrum of the q-ax and q-eq conformers of mPZPQ was similar. The LEB of mPZPQ corresponds to the $S_0 \rightarrow S_3$ transitions of the q-ax PTZ conformer, while the $S_0 \rightarrow S_{1,2}$ transition of the q-ax and q-eq conformers was found to be hidden. Therefore, the high energy absorption bands with peaks at 257 and 322 nm correspond to the π–π^* electronic transitions of the locally excited di-*tert*-butyl phenothiazine moiety (Fig. 4.37 (a)). Keeping an eye on the solid state properties, pPZPQ and PZPQ exhibited dual emission from the two conformers with peaks at (415nm, 515 nm) and (427nm, 552 nm), respectively. By contrast, *meta*-isomer mPZPQ showed only one visible peak in the solid state emission spectra with the maximum located at 547 nm (Fig. 4.37 (b)).

Table 4.20. Photophysical data of compounds

Compound	$\lambda_{toluene}$	λ_{film}	λ_{mCP}^{b}	$QY_{toluene}$	QY_{film}	QY_{mCP}^{b}	S_{exp}, eV	T_{exp}, eV
pPZPQ	417/536	415/515	571	5	2	15	3.21	2.59
mPZPQ	-/568	-/547	528	7	2	4	2.58	2.57
PZPQ	439/580	427/552	578	13	3	24	3.04	2.56

$\lambda_{toluene}$/ λ_{film}/λ_{mCP} are the PL peak of toluene solutions/solid films/10% of compound doped in mCP; $QY_{toluene}$/ QY_{film}/ QY_{mCP} are the quantum yields of toluene solutions/solid films/10% of compound doped in mCP; S_{exp}/ T_{exp} are the energies of the first excited singlet/triplet states calculated from the onset of photoluminescence and phosphorescence spectra (77 K)

The PLQY values of the toluene solution of compounds varied from 5% up to 13%. D-A molecules without the π-linker PZPQ exhibited the highest PLQY values of both the solution and the solid state of 13% and 3%. The photoluminescence and phosphorescence spectra were recorded at a low temperature (77 K) to understand the alignments of the singlet-triplet energy level of the compounds. As it can be seen from low temperature measurements (Fig. 4.38), two well-resolved peaks can be observed at the PL spectra of compounds pPZPQ and PZPQ.

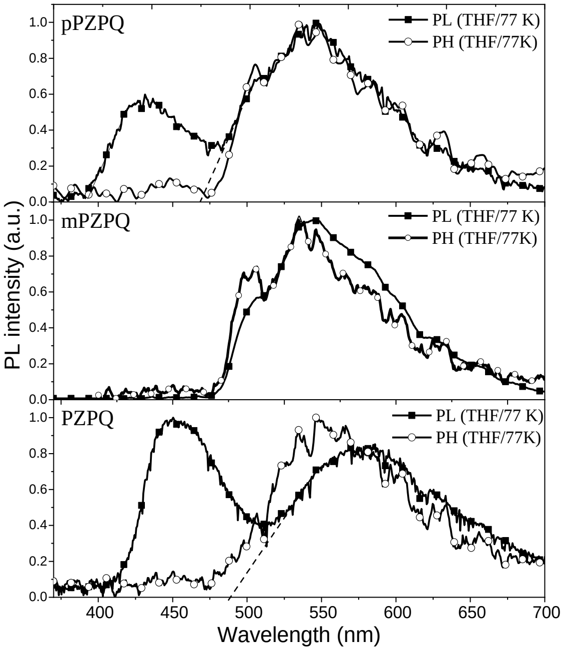

Fig. 4.38. PL and PH spectra recorded for THF solutions (10^{-5} M) at 77 K

However, only one peak was detected for mPZPQ. Supported by theoretical calculations, one can assume that, presumably, the first peak is assigned to the emission of the q-ax conformer, whereas the second red-shifted peak is assigned to the emission of the q-eq conformer. Similarly to the PL spectra (Fig. 4.38), the q-ax conformer of the *meta*-isomer mPZPQ emits with low intensity, thus the peak at the blue region was not detected. Due to our assumption, the energy level of the two conformers of each compound was estimated from the onset of each band of the spectra and calculated by using equation $S_{exp}=1240/\lambda_{onset}$. Accordingly, the energy of the singlet states of the q-ax conformers of pPZPQ and PZPQ were found to be 3.21 and 3.04, respectively. Due to the observation of the single emission peak at the emission spectra of mPZPQ, the onset of the band is attributed to the singlet state of the q-eq conformer. In strong agreement with the theoretical investigations (Table 4.19), the calculated negligible singlet-triplet energy splitting of ~0.02 eV is assigned to the $\Delta E_{Svert\text{-}Tvert}$ q-eq conformer, whereas q-ax conformers possess significant $\Delta E_{Svert\text{-}Tvert}$ values of 0.6–0.7 eV (Table 4.20). To understand the behavior of the crystalline state of materials and conformer arrangements, single crystal X-ray diffraction measurements were performed. The X-ray molecular structure of the investigated material is outlined in Fig. 4.39. Thus the molecular structure revealed the appearance of the quasi-equatorial conformers of the materials with the torsion angles between the donor and the acceptor parts for PPZPQ, MPZPQ and PZPQ of 85°, 84°, 76°, respectively.

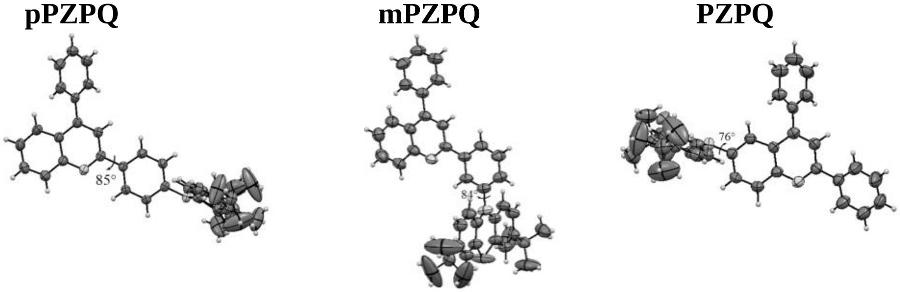

Fig. 4.39. Single crystal molecular structures of compounds obtained from X-ray analysis. The torsion angles between the donor and the acceptor are shown.

Interestingly, molecule PZPQ with the donor-acceptor architecture exhibited a slightly lower torsion angle than its isomers pPZPQ and mPZPQ with the inserted phenyl linker between the donor and the acceptor. The single crystal data is in agreement with a theoretically optimized structure for the quasi-equatorial conformers of compounds (Fig. 4.39).

The compound with direct D-A linking PZPQ exhibited potential delayed fluorescence properties. Thus the first step to the screen potential TADF emitter is to estimate the contribution of the triplet states to the overall emission of the compound. With this purpose, the PL spectra of aerated and nonaerated toluene solutions were recorded to verify the contribution of the triplet states to the total emission of PZPQ. Interestingly, 2.37-fold enhancement of the emission intensity of the second peak occurred after bubbling the toluene solution of PZPQ with N_2 (Fig. 4.40 (a)). Meanwhile, the intensity of the blue peak assigned to the emission of the q-ax conformer practically did not change (Fig. 4.40 (a, inserted)).

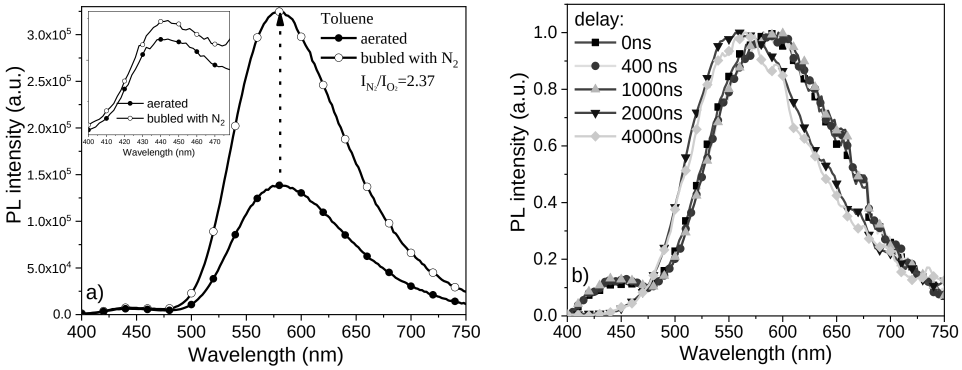

Fig. 4.40. (a) Steady-state PL spectra of aerated and non-aerated toluene solutions of PZPQ (b) PL spectra with a different delay time of 10% of PZPQ in the mCP host

Going further, in order to investigate the solid state properties, the PZPQ compound was doped in the host material. mCP was chosen as the host material due to its high triplet state energy and appreciable HOMO-LUMO energies for better charge injection. Intense DF fluorescence was observed for 10% of PZPQ doped in the mCP host by setting the delay of 1 µs, 2 µs and 4 µs (Fig. 4.40 (b)). Remarkably, with the delay of 2 µs, the first blue peak disappears, which also confirms the non-DF nature of the q-ax conformer of PZPQ. Finally, time-resolved measurements were carried out for each conformer in order to estimate whether both conformers possess DF. Notably, the fluorescence lifetime for the q-ax conformer with the emission peak localized at 440 nm was found to be in the range of nanoseconds (τ_1=0.68 ns, τ_2=23 ns) (Fig. 4.41, Table 4.21).

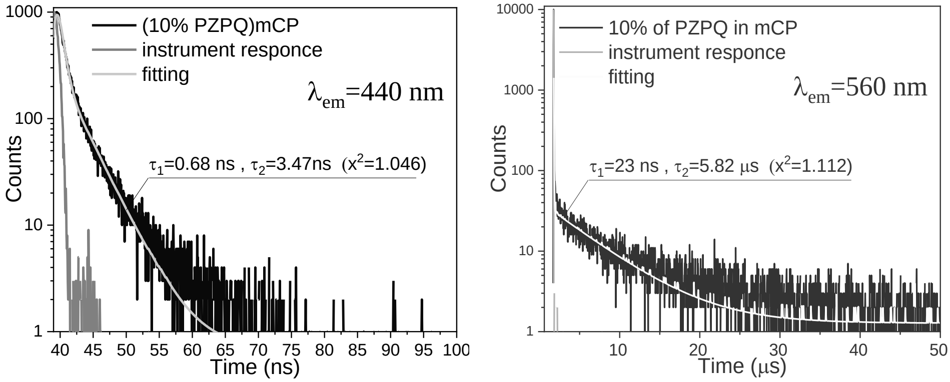

Fig. 4.41. Photoluminescence decay curves for conformers of PZPQ

Consequently, the q-ax conformer of PZPQ did not possess the DF properties, apparently due to the significant $\Delta E_{S\text{-}T}$ value, which decreases the possibility of up-conversion of the triplet excitons to the singlet state. Meanwhile, the PL decay curve of the q-eq conformer of PZPQ highly differed and revealed double exponential fit with short- and long-lived components. Thus, the short component of 3.47 ns was attributed to the prompt fluorescence, while the long-lived component of 5.8 µs was attributed to the delay component (Fig. 4.41, Table 4.21). The temperature dependence of DF is essential to understand the mechanism of DF. To estimate the type of DF, the decay kinetics as a function of temperature for PZPQ dispersed molecularly in the mCP host were studied (Fig. 4.41 (a)). As it can be seen from Fig. 4.42, the photoluminescence decay dynamics of PZPQ in the mCP host is dependent on the temperature.

Table 4.21. Photophysical data for conformers of PZPQ

Conformer*	***λ*** ***PL, max*, *nm***	***τ1, ns***	***τ2, ns***	χ^2
q-ax	440	0.68	3.47	1.046
q-eq	560	23	5822	1.112

*Measured for the solid film (10% PZPQ in mCP), $\lambda_{\text{PL, max}}$ is the PL maxima for each conformer; τ_1/ τ_2 is the fluorescence lifetimes measured for emission of the corresponding conformer

The decrease of the DF lifetime with the increase of the temperature can be observed, which is assigned to the facilitated rISC process. At low temperatures, phosphorescence can be observed which is much longer than DF lifetimes. It can be seen that the shapes and position of the PL spectra for the sample at different temperatures remain to be the same (Fig. 4.42 (inserted)). Nevertheless, a slight red shift was observed for the spectra recorded at 300 K.

Finally, to confirm the TADF origin of the PZPQ emitter and to exclude a possible TTA mechanism[145], the dependence of the delayed fluorescence intensity as a function of laser pulse energy was investigated. The PL intensity decreased with the decrease of the laser power (Fig. 4.42 (inserted)). Fig. 4.42 (b) revealed the power dependences of the emission integral with a slope of 0.998. Consequently, the linear singular dependence indicates that TADF the mechanism is responsible for DF[146].

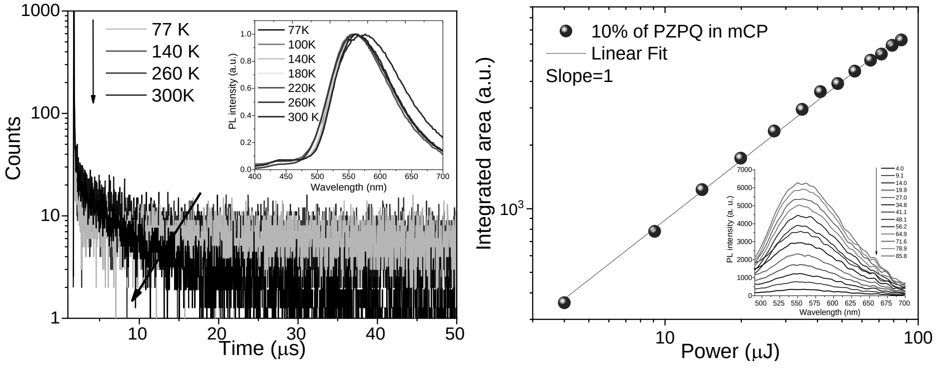

Fig. 4.42. PL decay curves of 10% of PZPQ in mCP at different temperatures (λ_{em} =560 nm) and power dependence of delayed fluorescence (RT)

4.4.6. Mechanoluminescence behavior

Mechanoluminescent materials exhibit reversible color change under external stimuli (grinding, fuming, and melting)[80]. The PL spectra of different states of compounds are presented in Fig. 4.43 and listed in Table 4.22. The initial as-prepared powder of pPZPQ, mPZPQ and PZPQ emitted blue and green light with emission peaks located at 478, 506 and 519 nm, respectively. Under mechanical grinding, a drastic red shift of the emission for ~30–60 nm toward the yellow region occurs for all the three compounds. Upon grinding, the most significant shift of 62 nm was observed for D-π-A compounds pPZPQ and mPZPQ, while the direct D-A molecule PZPQ shifted only for 30 nm from the initial to the ground form (Fig. 4.43). More pronounced MCL properties of pPZPQ and mPZPQ relatively to PZPQ can be assigned to the more rigid structure of PZPQ due to the absence of a phenyl linker between the donor and the acceptor moieties. As observed for the *meta*-isomer mPZPQ, emission change took place, apparently due to the transition between the crystalline and the amorphous states confirmed by powder X-ray diffraction (PXRD) measurements. The powder XRD patterns of the initial, ground, fumed with CH_2Cl_2 vapors and melted forms are presented in Fig. 4.44. Indeed, the initial and fumed forms of mPZPQ exhibited sharp and strong diffraction peaks which disappeared after grinding or melting. Under mechanical force (grinding), the greenish initial form with a peak at 506 nm converted to a broad and structureless yellow emission band with a single peak at 549 nm. The emission change indicated the phase transition from the stable initial phase to the meta-stable ground form. The ordered alignment of the molecules in the crystalline phases resulted in blue-shifted emission, while the amorphous state led to red-shifted emission. The phase transition causes the destruction or change in the intermolecular interactions and stacking modes of the molecules. It resulted in both a red shift and a broadening of the spectra.

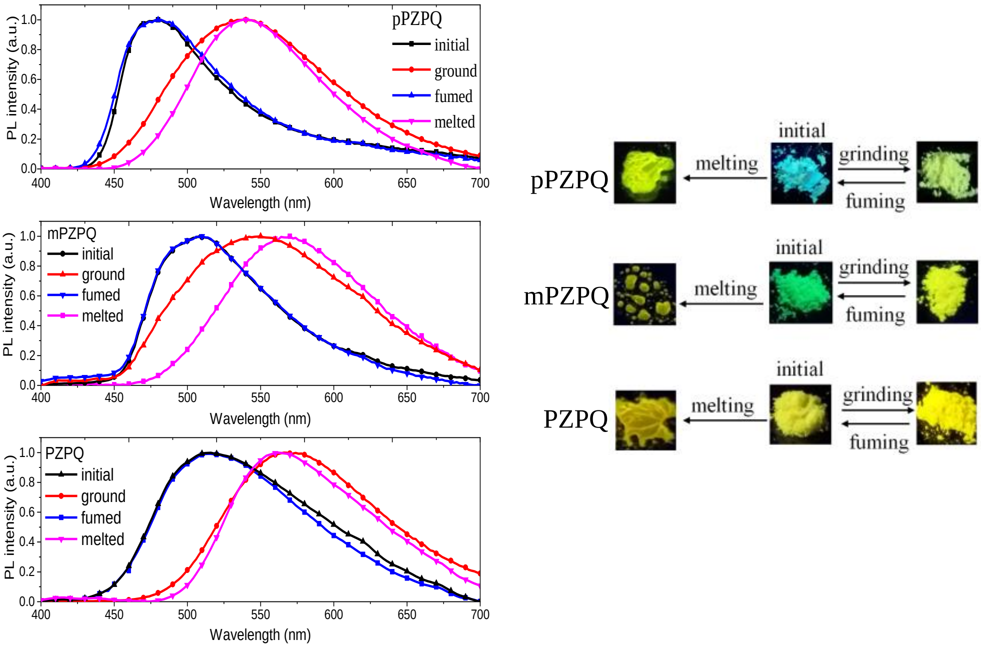

Fig. 4.43. (left) PL spectra and images (right) of different states of compounds (initial, ground, fumed with CH_2Cl_2 and melted) (λ_{exc}=330 nm). The images were taken under excitation light at 365 nm.

By treatment of ground powders with CH_2Cl_2 vapor, the luminescence color of the forms spontaneously recovers to the stable initial forms for all the three compounds due to the vapor-induced re-crystallization process. Consequently, the amorphous ground state changes to the crystalline state with luminescence switching between yellow-orange to blue-green.

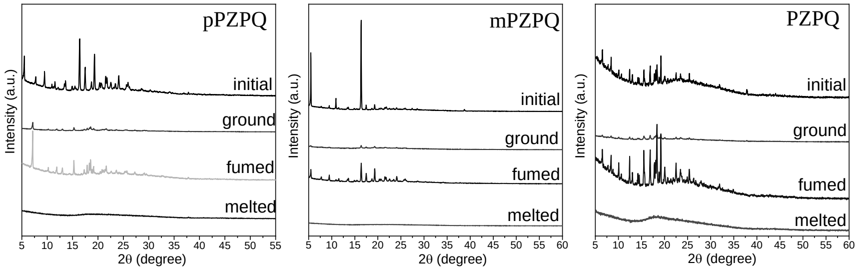

Fig. 4.44. PXRD pattern of compounds before/after grinding, melting and after fuming with CH_2Cl_2 vapors

Additionally, melting of the initial powders causes a significant red shift of the PL spectra as well. The color alteration between the initial form and the bathochromically shifted melted form takes place due to the phase transition from the crystalline to the amorphous state. Moreover, close packing of the molecules in the melted form induces π–π interactions and leads to emission changes. It is noteworthy that the spectra of the ground and melted forms were found to be wider relatively to the spectra of the initial powders. This observation can be assigned to the more localized weak nature of the emissive CT state of the initial powders than that of the ground and melted forms.

Table 4.22. PL emission peaks of different forms of compounds

State	pPZPQ	mPZPQ	PZPQ
initial	478	506	519
ground	538	549	569
fumed	478	506	518
melted	540	569	563

* photoluminescence peak (nm)

In order to get more profound insights in the MCP properties and electronic processes of the emissive species, PL decay dynamics of different forms of compounds pPZPQ, mPZPQ and PZPQ were studied (Fig. 4.45, Table 4.23). Similarly to their solid film, the initial forms of compounds pPZPQ and mPZPQ exhibited short fluorescence lifetimes. The PL decay curves of the initial stable states of pPZPQ and mPZPQ were well-fitted by monoexponential fit with the lifetimes of 2.2 and 10.4 ns, respectively. The initial and fumed forms experienced identical blue-green emission accompanied with the same PL dynamics in the range of nanoseconds, which confirms complete restoration of the meta-stable ground sample to the initial stable one. Meanwhile, similarly to its solid sample, the initial/fumed form of PZPQ possessed prompt (4.8 ns/8.2 ns) and delayed components (1.4 µs/1.2 µs).

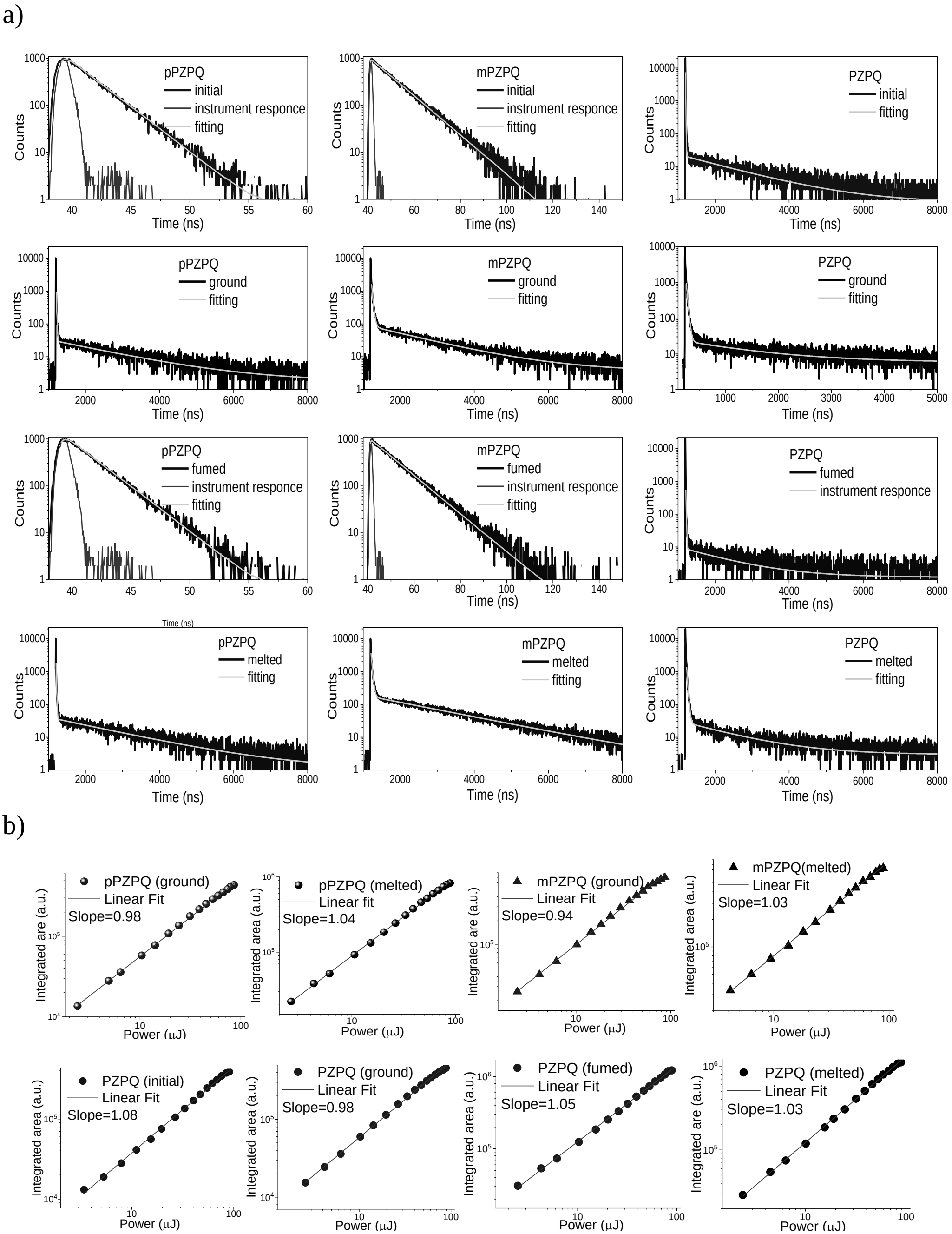

Fig. 4.45. (a) PL decay curves of different states of compounds pPZPQ, mPZPQ and PZPQ; (b) integrated DF area as a function of the excitation dose (λ_{exc}=330 nm) measured for the ground and melted forms of pPZPQ and mPZPQ and for the initial, ground, fumed and melted forms of PZPQ

Interestingly, along with the emission spectral red shift, delayed components were observed for pPZPQ and mPZPQ powders after the grinding and melting processes (Fig. 4.45). The ground and melted states of compounds experience distortion of the molecular packing and stronger π–π intermolecular interactions relative to the initial and fumed forms accompanied with significantly longer PL lifetimes[147]. To determine the mechanism of delayed emission, the dependence of the PL intensity of the different forms of compounds on the excitation laser fluence was recorded. The linear fit of DF intensity on the laser power and a slope of 1 revealed the monomolecular origin of the delayed components, which corresponds to the TADF nature of the emission (Fig. 4.45 (b)).

Table 4.23. PL decay dynamics of the states of pPZPQ, mPZPQ and PZPQ

pPZPQ	τ_1, ns	τ_2, ns	χ^2
Initial	2.2 (100%)	-	1.160
Ground	10.7 (23%)	1747.3 (77%)	1.150
Fumed	2.2 (100%)	-	1.081
Melted	9.3 (31%)	1747.7 (69%)	1.119

mPZPQ	τ_1, ns	τ_2, ns	χ^2
Initial	10.4 100%)	-	1.032
Ground	33.3 (33%)	1524.1 (67%)	1.300
Fumed	10.6 (100%)	-	1.074
Melted	30.3 (27%)	1946.1 (73%)	1.227

PZPQ	τ_1 , ns	τ_2 , ns	χ^2
Initial	4.8 (78%)	1402.5 (22%)	1.097
Ground	24.8 (54%)	1329.8 (46%)	1.231
Fumed	8.2 (55%)	1222.9 (54%)	1.006
Melted	26.4 (57%)	1317.5 (43%)	1.265

τ_1/τ_2 is the photoluminescence lifetime

Moreover, upon grinding and melting processes, apparently, relaxation of the dihedral angle between the donor and acceptor moieties appeared, which caused reduction of the energy difference between the first excited S_1 and ground S_0 states. It is noteworthy that the ground and melted forms of *para-* isomer pPZPQ showed identical delayed components of 1.7 µs, thus assuming similar molecular interaction in the two states. D-A molecule PZPQ demonstrated analogous behavior: the ground and melted forms of PZPQ possessed similar prompt and delayed components of 25–26 ns and 1.3 µs. Nevertheless, for its *meta*-substituted counterpart mPZPQ, the short component was found to be unchanged, while the delay time of the ground (1.5 µs) and melted (1.9 µs) forms varies. This is, apparently, due to the closer distance between the molecules in the melted from, thus stronger π–π interaction and prolonged PL lifetimes are observed.

4.5. Cyanocarbazolyl-based exciplex-forming materials

A new series of cyanocarbazolyl-based materials was designed and synthesized (Scheme 4.6). The synthesized materials were capable to behave as electron-donor and form exciplexes with commercially available electron-withdrawing material PO-T2T.

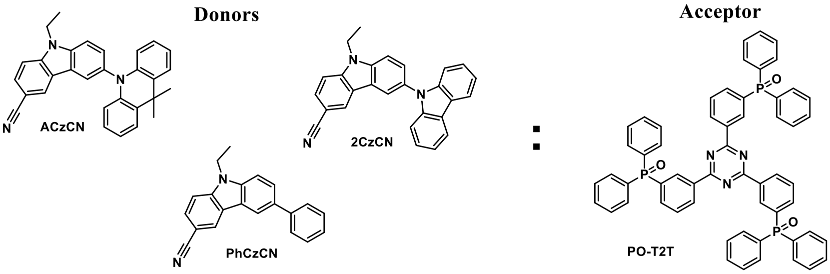

Scheme 4.6. Chemical structures of exciplex forming electron-donating materials (2CzCN, ACzCN, PhCzCN) and electron-accepting PO-T2T material

4.5.1. Synthesis

Exciplex-forming electron-donating materials 2CzCN and ACzCN were obtained by following the synthetic routes shown in Scheme 4.7.

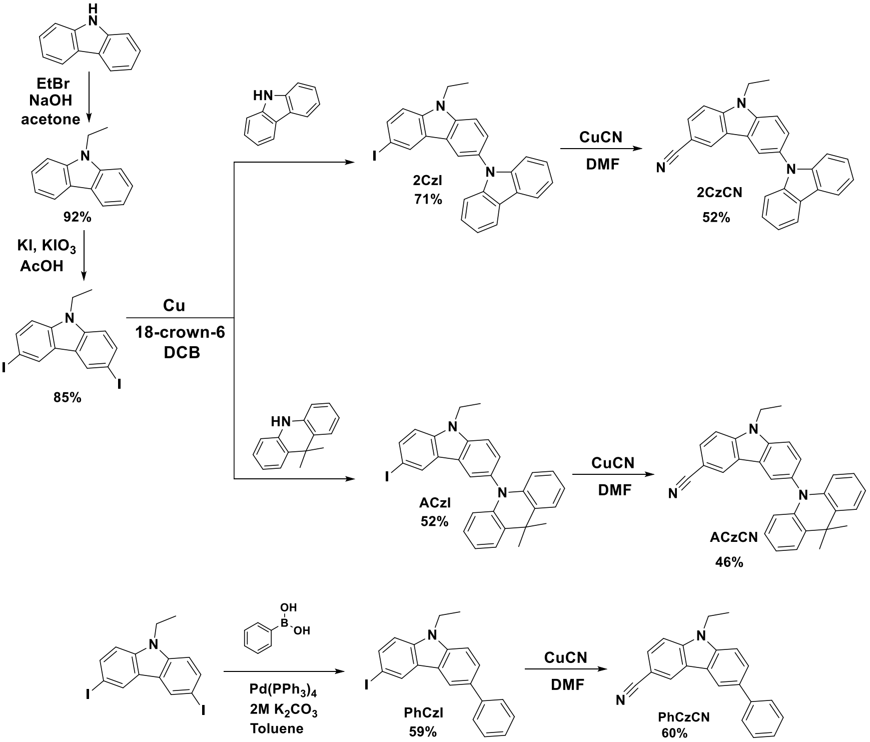

Scheme 4.7. Synthetic routes toward obtaining compounds 2CzCN, ACzCN, PhCzCN

Compound PhCzCN was synthesized according to the similar outlined four-step procedure. In the first step, the alkylation reaction of the 9*H*-carbazole compound afforded the 9-ethyl-carbazole compound[89]. Iodinated at 3- and 6- position carbazole heterocycle was obtained by the action of KI and KIO_3 in glacial acetic acid solution on alkylated carbazole according to the Tucker iodination reaction[90]. At the next step, the copper-catalyzed Ullmann coupling reaction of carbazole or acridane and 3,6-di-iodocarbazole afforded monosubstituted intermediate compounds 2CzI and ACzI. Meanwhile, the palladium-catalyzed Suzuki cross coupling reaction between phenyl boronic acid and the corresponding halides was used to obtain monosubstituted intermediate compound PhCzI. At the final step, the Rosenmund-von Braun reaction of the intermediate halides with an excess of copper (I) cyanide in a polar high-boiling DMF solvent afforded the target compounds in moderate yields.

4.5.2. Thermal properties

The thermal behavior of the target compounds was studied by TGA and DSC analysis. The thermal characteristics are listed in Table 4.24. The TGA and DSC curves are depicted in Fig. 4.46 (a, b). The TGA curves of the compounds highlight that the highest temperature of the 5% weight loss ($T_{d\text{-}5\%}$,) was observed for bi-carbazolyl-based compound 2CzCN. Its $T_{d\text{-}5\%}$ was found to exceed 350 °C.

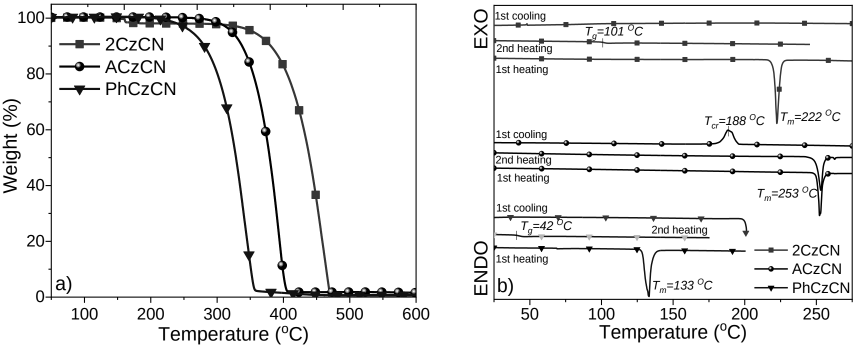

Fig. 4.46. (a) TGA and (b) DSC analysis of investigated compounds 2CzCN, ACzCN and PhCzCN

It should be noted that the weight losses of the compounds are caused by sublimation processes. The investigated compounds 2CzCN and PhCzCN were isolated as crystalline materials. During the first heating scan, 2CzCN and PhCzCN were capable to form glasses with T_g values of 101 °C and 42 °C. A higher T_g value for 2CzCN with respect to PhCzCN is conceivably due to the higher molecular weight of 2CzCN and thus stronger intermolecular interactions[148]. However, during the first and second heating-cooling cycles for the ACzCN sample, no glass transition temperature was recorded. Therefore, in the cooling cycle for ACzCN, a crystallization peak was observed (Fig. 4.46 (b)). Nevertheless, during the cooling processes of 2CzCN and PhCzCN, no crystallization peaks were recorded as both materials formed an amorphous phase after melting. All the compounds in the series exhibited endothermic melting signals during the first heating scans with melting temperatures reaching the value of 253 °C. The melting temperatures values of the compounds strongly depend on the size of the molecules. From this point, ACzCN featuring the highest molecular weight exhibited the highest T_m of 253 °C, meanwhile, the smallest PhCzCN showed the lowest T_m of 133 °C (Fig. 4.46 (b)).

Table 4.24. Thermal characteristics of cyanocarbazolyl-based compounds

Compound	T_g,[a] °C	T_m,[a] °C	T_{cr},[a] °C	$T_{d-5\%}$,[b] °C
2CzCN	101	222	-	362
ACzCN	-	253	188	325
PhCzCN	42	133	-	261

T_g is the glass transition temperature; T_m is the melting point; T_{cr} is the crystallization temperature; $T_{d-5\%}$ is the temperature of 5% weight loss; [a] Estimated from DSC; [b] Estimated from TGA.

4.5.3. Electrochemical and photoelectrical properties

The electrochemical behavior of the compounds was studied for 10^{-3} DMF solution of compounds with 0.1 M tetrabutylammonium hexafluorophosphate as the electrolyte by cyclic voltammetry (CV). All the compounds of the series exhibited irreversible oxidation and reduction processes (Fig. 4.47 (a)). The IP_{CV} and EA_{CV} values were calculated from the onset of oxidation and reduction waves following equation $IP_{CV} = |e|(4.8 + E^{ox}_{onset})$ and $EA_{CV} = |e|(4.8 + E^{red}_{onset})$. As expected, ACzCN exhibited the lowest IP_{CV} value of 5.33 eV among the compounds due to the extended π-conjugation and the stronger electron-donating ability of the acridan moiety in comparison with carbazole and phenyl side-substituents. Meanwhile, PhCzCN with its reduced conjugation strength displayed the highest IP_{CV} value of 5.70 eV. Due to the presence of identical electron-withdrawing cyano groups, all the three compounds were characterized by similar EA_{CV} of 2.21–2.22 eV. The ionization potential of the solid samples IP_{PE} was estimated from the onsets of the photoelectron emission spectra (PE) of the vacuum deposited layers of compounds (Fig. 4.47 (b)). The IP_{PE} values were found to be relatively high; they fall in the range of 5.80–6.13 eV.

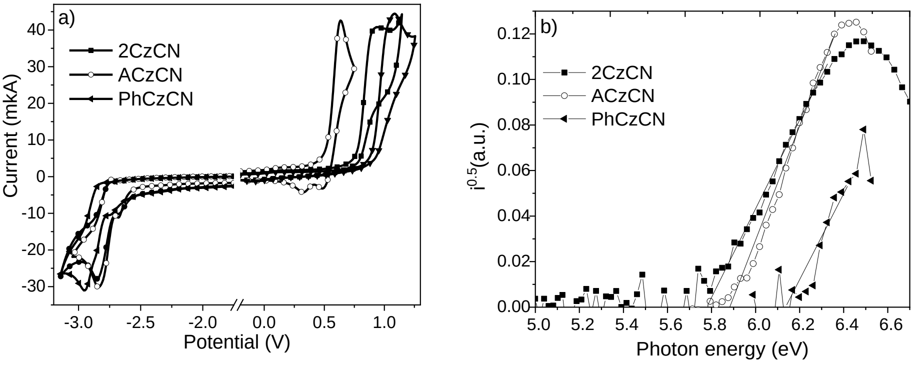

Fig. 4.47. (a) CV curve and (b) photoelectron emission spectra of compounds

The divergence of the IP values obtained from the CV and PE spectra, apparently, is due to the different environments of dilute DMF solutions and the solid samples of the target compounds. EA_{PE} were calculated by using the relationship $EA_{PE}=IP_{PE}-E_g$. The optical band gap was estimated by the following relationship: $E_g=1240/\lambda_{abs, onset}$, where $\lambda_{abs, onset}$ is the onset of the last absorption band. The data from the CV and PE measurements is listed in Table 4.25. To conclude, the substituent 6th position of the 3-cyanocarbazole fragment highly influences the energy levels of the compounds.

Table 4.25. Electrochemical and photoelectrical data for compounds 2CzCN, ACzCN, PhCzCN

Compound	***E^{ox} onset, V***	***E^{red} onset, V***	***IP_{CV}, eV***	***EA_{CV}, eV***	***$E_{g, CV}$, eV***	***IP_{PE}, eV***	***EA_{PE}, eV***	***$E_{g, opt}$ eV***
2CzCN	0.77	-2.58	5.58	2.22	3.36	5.80	2.42	3.38
ACzCN	0.53	-2.59	5.33	2.21	3.12	5.85	2.45	3.39
PhCzCN	0.90	-2.58	5.70	2.22	3.48	6.12	2.72	3.40

E^{ox}_{onset} / E^{red}_{onset} is the onset of the first oxidation/reduction waves; IP_{CV} , EA_{CV} is the ionization potential and electron affinity calculated by using relationships $IP_{CV} = |e|(4.8 + E^{ox}_{onset})$ and $EA_{CV} = |e|(4.8 + E^{red}_{onset})$; IP_{PE} is the ionization potential obtained from the photoelectron emission spectra; EA_{PE} was calculated by equation $EA_{PE}=IP_{PE}-E_g$; E_g is the optical band gap ($E_g=1240/\lambda_{abs, onset}$).

4.5.4. Charge-transporting properties

The hole- and electron- transporting properties of compounds 2CzCN and ACzCN were established by using the time-of-flight (TOF) method. The TOF transients of holes and electrons of a thin layer of 2CzCN and ACzCN are shown in Fig. 4.48. Nevertheless, it was not possible to prepare appropriate for the TOF measurements samples of PhCzCN, apparently, due to the low glass transition temperature of 42 °C and the small size of the molecule, which caused the fast crystallization of the molecule at the solid state (Table 4.24).

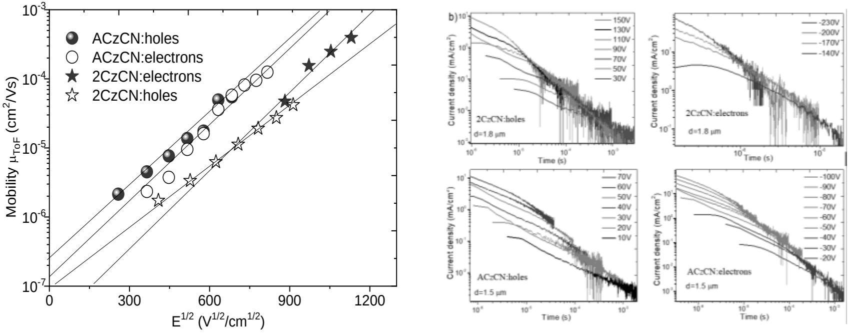

Fig. 4.48. (a) Hole- and electron- drift mobilities as a function of $E^{1/2}$ and (b) TOF current transients for holes and electrons for the deposited layers of 2CzCN and ACzCN

Still, compounds 2CzCN and ACzCN showed low-dispersity transport of holes and electrons. Therefore, acridane-based compound ACzCN exhibited more balanced charge-transport of holes and electrons than its congener 2CzCN. Nevertheless, 2CzCN showed more efficient transport of electrons than that of holes, whereas ACzCN exhibited balanced charge-transport. The deposited layer of 2CzCN exhibited relatively low hole drift mobility with a value of 5.41 × 10^{-5} cm^2/V s at the electric field of 6.81 × 10^5 V cm^{-1}, while the electron mobilities were found to be 5.20 × 10^{-5} cm^2/V. Meanwhile, the hole and electron mobilities for 2CzCN was found to be of 1.57 × 10^{-5} cm^2/V (at an electric field of 9.66 × 10^5 V cm^{-1}) and 1.78 × 10^{-5} cm^2/V (at an electric field of 7.79 × 10^5 V cm^{-1}).

4.5.5. Photophysical properties

The synthesized cyano-carbazolyl compounds are well soluble in common organic solvents, such as toluene, tetrahydrofuran, dichloromethane and chloroform. UV-vis along with the fluorescence spectra of individual compounds are depicted in Fig. 4.49. The UV-vis spectra of the neat films of the studied compounds resembled those of their dilute toluene solutions (10^{-5} M). The target compounds 2CzCN, PhCzCN and ACzCN emit light in the violet-deep blue region with the emission maxima peaks centered at 410 nm, 425 nm and 407 nm measured for the solid samples, respectively. Predictably, the position of the emission spectra depends on the conjugation length of the compounds. Accordingly, compound PhCzCN with the minor conjugation length of the phenyl substituent at the 3^d-position of cyano carbazole exhibited the most blue-shifted emission in both toluene solution and solid states (Table 4.26).

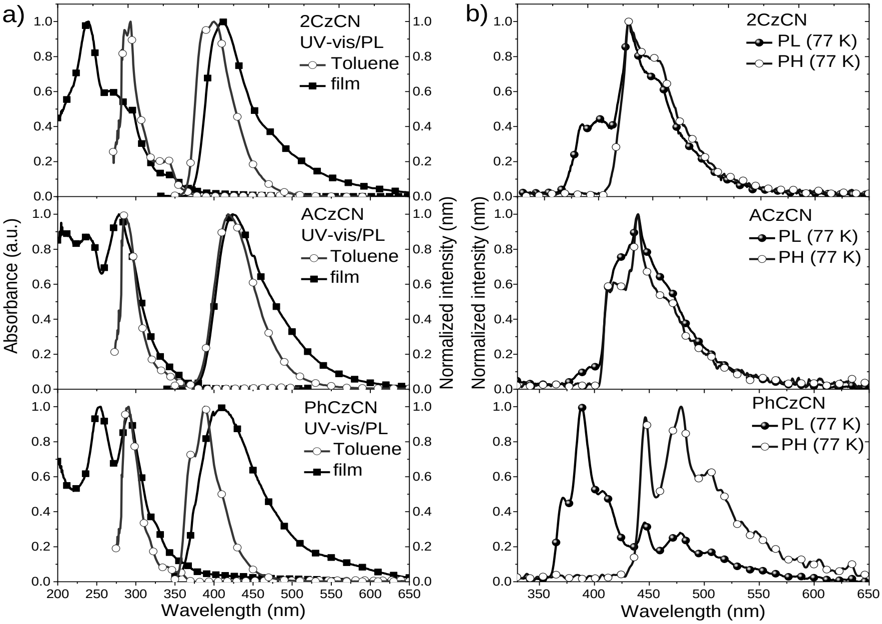

Fig. 4.49. (a) UV-vis and fluorescence spectra of dilute toluene solutions of compounds 2CzCN, ACzCN and PhCzCN along with photoluminescence (PL) and phosphorescence (PH) spectra (with a delay of 50 µs) recorded for THF solutions at 77 K

Therefore, compound ACzCN comprised of an acridane unit linked to the cyanocarbazolyl moiety showed the most red-shifted deep blue emission of toluene solutions and the film with maxima peaks located at 378 and 420 nm, respectively.

Interestingly, two materials 2CzCN and PhCzCN exhibited dual emission peaks of low polarity toluene solutions. Such a resolved vibronic shape of the PL is, apparently, due to the emission originating from the locally excited carbazole moiety[149, 150]. In order to evaluate the energies of the excited states of the compounds, the phosphorescence and luminescence spectra were recorded at 77 K (Fig. 4.49 (b)).

Table 4.26. Photophysical characteristics of compounds

Compound	$\lambda_{abs,\ onset}{}^{b}$, *nm*	$\lambda_{PL,\ max}{}^{a}$, *nm*	$\lambda_{PL,\ max}{}^{b}$, *nm*	*PLQY*^{b}, *%*	E_S, *eV*	E_T, *eV*	$\tau_1\ (\chi^2)^{a}$ *ns*	$\tau_1/\tau_2\ (\chi^2)^{b}$ *ns*
2CzCN	363	396	410	15	3.34	3.03	5.04 (1.001)	1.35/7.79 (1.069)
ACzCN	378	420	425	7	3.33	3.04	4.46 (1.246)	0.92/5.54 (1.057)
PhCzCN	373	372/385	407	11	3.45	2.90	8.50 (1.108)	0.80/8.96 (1.219)

^{a} Measured for dilute toluene solutions (10^{-5}) of compounds ^{b} Measured for solid films of compounds; $\lambda_{abs,\ onset}$ is the onset of the last absorption band; $\lambda_{PL,\ max}$ is the fluorescence maxima; E_S, E_T is the energy of the first excited singlet and triplet states estimated from the photoluminescence and phosphorescence measurements at 77 K (50 µ delay) and calculated by using equation $E_S=1240/\lambda_{onset,\ PL}$, $E_T=1240/\lambda_{onset,\ PH}$; τ_1/τ_2 are the PL lifetimes.

The values of the first excited singlet and triplet levels were determined from the onsets of the luminescence and phosphorescence spectra (Table 4.26). Cyano carbazolyl-based compounds exhibited high first excited singlet level energies, which explained their violet-blue fluorescence profiles (Fig. 4.49 (a)). All the compounds in the series displayed intense broad well-resolved phosphorescence spectra, which, apparently, is attributed to the local excitation of the triplet state of the carbazole fragment, similarly to the previously reported other carbazole-based materials[151, 152]. The compounds are characterized with a high energy of the triplet states varying from 2.90 eV for PhCzCN and moving up to 3.03–3.04 eV for 2CzCN and ACzCN.

The PL decay dynamics and the photoluminescence quantum yields (PLQY) of all the cyano carbazolyl containing compounds were estimated at room temperature (Fig. 4.50).

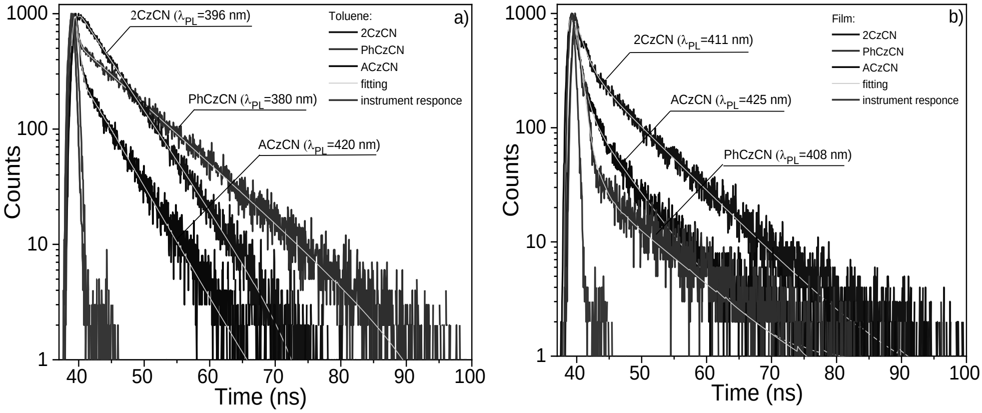

Fig. 4.50. PL decay of (a) toluene solutions and (b) neat films of 2CzCN, ACzCN and PhCzCN at the corresponding PL peaks

The PL decay curves of toluene solutions of the compounds were monoexponential, while the solid films of the compounds showed biexponential character (Table 4.26). Therefore, the fluorescence lifetimes of the solid samples of the compounds were found to be in the short range of nanoseconds (4–10 ns) thus conforming the pure fluorescent nature of the compounds. The PLQY values estimated for the neat films of the compounds ranged from 7% for acridan-containing ACzCN up to 15% for bi-carbazolyl based 2CzCN. The compound comprising the phenyl side-substituent demonstrated a PLQY of 11% (Table 4.26). Obviously, the lowest PLQY value for acridan-based 2CzCN can be assigned to the diminution of the conjugation between the cyano carbazolyl and acridan moieties. Synthesized bipolar cyanocarbazolyl-containing compounds were tested as electron-donating materials forming excited complexes with the electron-withdrawing commercially available 2,4,6-tris[3-(diphenylphosphinyl)phenyl]-1,3,5-triazine (PO-T2T) molecule. As discussed above, the electron-transporting PO-T2T acceptor was characterized with excellent thermal stability, a high triplet state energy and a high LUMO energy level preferable for exciplex-forming electron-acceptors. In this attempt, synthesized materials were mixed with the electron-accepting PO-T2T molecule in 1:1 molar ratio. Fig. 4.51 (a) presents the absorption spectra of the exciplex blends. Moreover, the absorption spectra of the individual donors (2CzCN, ACzCN and PhCzCN) and the acceptor (PO-T2T) molecules were added as well in Fig. 4.51 (a).

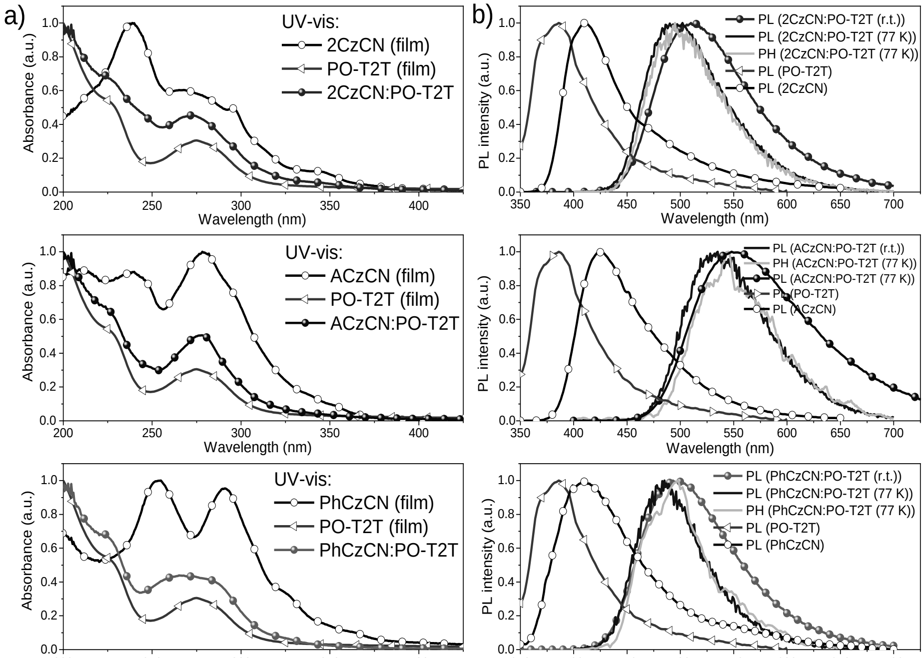

Fig. 4.51. The UV-vis and photoluminescence (PL) spectra (r.t.) along with the phosphorescence (PH) spectra (77 K, 10 µs delay) of exciplex systems and constituting molecules

Thus the shape and position of the absorption bands of the exciplex systems are a mix of the absorption spectra of individual donors and the PO-T2T acceptor. Therefore, the absorption bands assigned to the formation of CT complexes at the ground state were not recorded. Exciplex-forming blends displayed typically CT, broad, Gaussian-shaped emission (Fig. 4.51 (b)). It is noteworthy that the PL profiles of molecular exciplex mixtures are clearly red-shifted relatively to the spectra of individual molecules (Fig. 4.51 (b)). As mentioned above, the energy of the exciplex can be approximated as the difference between the HOMO of the donor and the LUMO energy of the accepting molecule. As reported previously, the PO-T2T acceptor is denoted by the electron affinity value of 3.14 eV. As examined from the photoelectron emission spectra, the investigated compounds 2CzCN, ACzCN and PhCzCN exhibited relatively high IP_{PE} values of 5.80, 5.85 and 6.13 eV, respectively. Thus PhCzCN with its highest IP_{PE} value of 6.13 eV displayed the most blue-shifted exciplex emission in pair with PO-T2T peaking at 494 nm. Accordingly, the exciplex blend of ACzCN with the PO-T2T acceptor showed yellow exciplex emission with its maxima at 552 nm. The exciplex blend of bicarbazolyl-based 2CzCN with PO-T2T showed green luminescence (509 nm).

In order to understand the mechanism of exciplex emissions, low-temperature (77 K) measurements were performed. In this manner, luminescence (PL) and phosphorescence (PH) measurements were carried out to estimate the energy of the excited states of bimolecular systems. The corresponding PL and PH profiles of all the exciplex systems are depicted in Fig. 4.51 (b). Unlike their constituting molecules, due to their intermolecular CT feature, exciplex systems exhibited well-broad, not structured, single-peaked fluorescence and phosphorescence spectra. The energies of the excited singlet and triplet states of the investigated solid molecular mixtures were calculated from the onsets of the PL and PH spectra recorded at low temperatures (Fig. 4.51 (b)). Thereby, the energies of the singlet states (E_S) of excited complexes were found to be in the range of 2.62–2.87 eV, while the energies of the triplet states (E_T) varied from 2.56 eV up to 2.86 eV. Predictably, 3-phenyl cyano carbazole PhCzCN and 3-carbazolyl cyano carbazole 2CzCN possessed the higher triplet state energy of 2.86 eV and 2.82 eV, respectively.

Table 4.27. Photophysical properties of exciplex-forming blends

Exciplex	***$\lambda_{PL,max}$* nm**	***PLQY* %**	***E_S* eV**	***E_T* eV**	***ΔE_{S-T}* eV**	***$\tau_1/\tau_2/\tau_3$ (χ^2)* ns**
2CzCN:PO-T2T	509	15	2.83	2.82	0.01	27.8 (13%)/901.5 (23%)/3044.7 (64%) (**1.272**)
ACzCN:PO-T2T	552	14	2.62	2.56	0.06	41.9 (9%)/1113.3 (44%)/2864.8 (47%) (**1.232**)
PhCzCN:PO-T2T	494	37	2.87	2.86	0.01	38.5 (6%)/4288.2 (94%)/- (**1.104**)

$\lambda_{PL,\ max}$ – the emission peak of the exciplex blends; PLQY was estimated by using the integrating sphere; E_S/ E_T – the energies of the first excited singlet and triplet states estimated from the luminescence and phosphorescence spectra; ΔE_{S-T} – singlet-triplet energy splitting; τ_1/τ_2 – PL lifetimes.

Meanwhile, their acridan-based congener displayed the lowest E_T of 2.56 eV, apparently, due to the presence of an acridan moiety with a low-lying locally excited triplet state. According to the previous studies, in order to achieve an efficient TADF exciplex system, the triplet states of the individual donors and acceptor must be higher than the triplet level of the exciplex D:A system[32]. Additionally, negligible ΔE_{S-T} is required for efficient TADF systems. Due to the localization of HOMO and LUMO on the separate donor and acceptor molecules, extremely small ΔE_{S-T} values of 0.01–0.06 eV were achieved for the solid mixtures of 2CzCN, PhCzCN and ACzCN with PO-T2T. This suggest the possible TADF nature in investigated exciplex systems (Fig. 4.51).

In order to screen the possible delayed fluorescence properties of exciplex mixtures, the PL dynamics of the blends of 2CzCN, ACzCN and PhCzCN with PO-T2T fluorescence decay curves at 300 K were recorded.

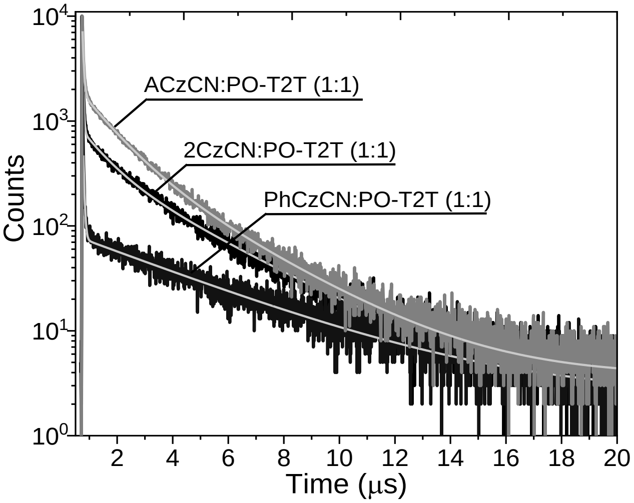

Fig. 4.52. PL decay curves of exciplex blends at 300 K (λ_{exc}=330 nm)

Unlike the individual molecules with their pure fluorescent nature, in pair with PO-T2T, exciplex systems exhibited short- and long-lived components. It is well known that the photophysics of exciplex-forming systems is much more complex than that of the individual compounds exhibiting the intramolecular CT nature[36]. As shown in Fig. 4.52., exciplex mixtures exhibited complex PL decay dynamics and could only be described by multi-exponential fittings. Thus, at room temperature, the exciplex systems of 2CzCN:PO-T2T and ACzCN:PO-T2T experienced tri-exponential decays. The fluorescence lifetime of PhCzCN:PO-T2T was characterized with bi-exponential decay. The first short-time components of 27–42 ns observed at nanosecond ranges are attributed to the prompt fluorescence, whereas the second and third ones in the μs range (1–4 μs) are attributed to the delayed fluorescence. The fluorescence lifetimes of the exciplexes are listed in Table 4.27. Complex multi-exponential decays can be explained by the different distribution of exciplexes in the molecular blends with different molecular geometries and arrangements.

In order to gain insight into the nature of delayed fluorescence, time-resolved emission spectra and PL decay measurements at different temperatures were recorded.

In this manner, Fig. 4.53 represents the normalized emission spectra of exciplexes with different delay times at room temperature (r.t.). The emission spectra do not shift by setting a different delay time of 800 ns, 1 µs, 2 µs, 4 µs and 8 µs, which means the presence of the energetically stable ^{1}CT state. Therefore, the exciplex system of PhCzCN with PO-T2T exhibited delay fluorescence only with a delay of 800 ns and 1 µs.

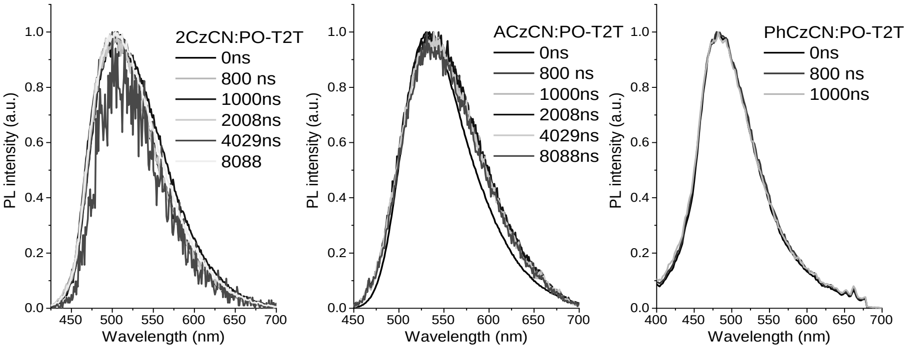

Fig. 4.53. PL spectra of exciplex solid mixtures with different delay times

In all the cases, clearly separated rapid decay of prompt fluorescence was recorded along with pronounced long-lived delayed fluorescence. The prompt fluorescence was not temperature dependent displaying the same intensity from 77 K up to 300 K. Meantime, the long-lived DF and PH components displayed strong temperature dependence (Fig. 4.54).

At low temperatures, the long-lived component is assigned to the intensive triplet emission – i.e., to the phosphorescence process. The decay curves were found to be similar over the temperature range of 77–140 K where the PH process dominates. Upon temperature increase, the long-lived component gradually decreases, and TADF markedly activates. DF fluorescence observed at higher temperatures (180–300 K) is related to TADF. This assumption was supported by the small singlet-triplet energy splitting of exciplex systems of ~0.01 eV (Table 4.27) and thus the rISC process was activated. Additionally, the PL spectra at different temperatures shown at inserts in Fig. 4.54 were slightly red-shifting or stayed unchangeable.

In order to determine the mechanism, which is responsible for DF, the intensity dependence of the DF as the function of laser pulse energy was plotted (Fig. 4.55). In this manner, by careful inspection of the DF spectra, the intensity of DF gradually decreases with a decrease of the excitation dose. (Fig. 4.55 (b)). For all the three exciplexes, the linear relationship with a slope close to 1 was observed. The linear relationship confirms the fact that the TADF process is responsible for the DF of the studied exciplexes rather than the TTA process[145].

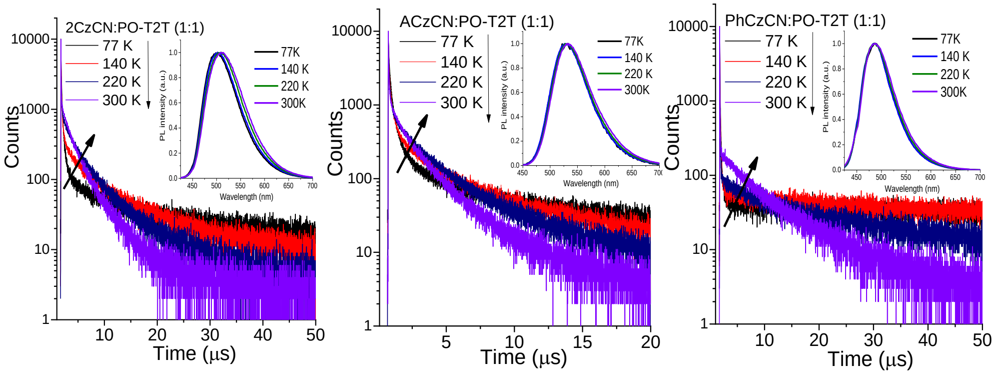

Fig. 4.54. PL decay curves of exciplex blends and inserted normalized PL at different temperatures

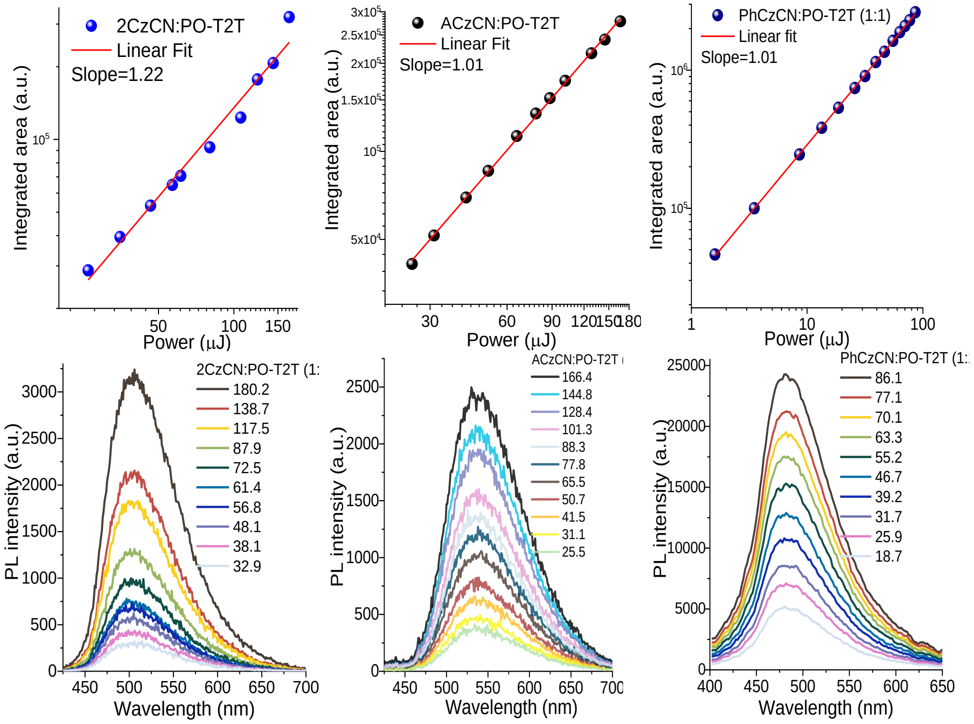

Fig. 4.55. Integrated DF area as a function of the excitation dose (λ_{exc}=330 nm) along with the corresponding PL spectra of 2CZCN/ACZCN/PHCZCN:PO-T2T systems recorded at room temperature

5. CONCLUSIONS

1. Four new monomers and polymers containing an electron-deficient tetrafluorobenzene moiety were prepared. It was established that the linked electron-donating fragment influenced the thermal, electrochemical and photophysical properties of the monomers and polymers. The polymerization of the vinyl monomers affected the thermal and photophysical properties of the materials.
    1.1. Free radical polymerization of the vinyl monomers afforded polymers with number average molecular weight in the range of 8500–114000. The size and the nature of the linked to tetrafluorobenzene electron-donating chromophore affected the polydispersity indices which ranged from 1.2 for di-*tert*-butyl carbazole and acridane-based polymers to 1.8 for the carbazole containing polymer.
    1.2. The energy gaps and, consequently, the emission color of the monomers and polymers ranging from violet to yellow can be effectively tuned by manipulation of the linked electron-donating fragments with different electron-donating capabilities.
    1.3. The stronger intramolecular interactions and the rigidified structure of the monomer building blocks in the polymer chain resulted in the higher thermal stability of the polymers with 5% weight loss temperatures being in the range of 366–411 °C with respect to those of the corresponding monomers (194–237 °C).
    1.4. The restricted rotational motions in the aggregated state resulted in aggregation induced emission enhancement of the monomers containing carbazole, di-*tert*-butyl carbazole and acridane moieties.
2. Derivatives of 4-carbazolyl-substituted tetrafluorostyrene and tri/tetraphenyl ethylene were synthesized and characterized as materials exhibiting both aggregation induced emission enhancement and bipolar charge-transporting properties.
    2.1. The solid state photoluminescence quantum yields were significantly increased by the implementation of multiphenylethylene rotors responsible for aggregation induced emission enhancement. The solid sample of the compound with more twisted configuration and prolonged π-conjugation demonstrated more than two times higher photoluminescence quantum yield (57%) than the layer of the compound having a triphenylethylene moiety (27%).
    2.2. Tri/tetraphenylethenyl-substituted derivatives demonstrated high thermal stability with 5% weight loss temperatures of 314 and 362 °C and high glass-transition temperatures of 80 and 112 °C.
    2.3. The best non-doped OLED based on the tetraphenylethenyl-containing emitter showed a turn-on voltage value of 9.1 V, maximum brightness of 11 800 cd/m^2, maximum current efficiency of 4.5 cd/A, and external quantum efficiency of ca. 1.7%. The best device containing an exciplex-forming host and a tetraphenylethenyl-containing emitter showed turn-on voltage of 9.1

V, maximum brightness of 16300 cd/m^2 (at V), maximum current efficiency of 7.3 cd/A, and external quantum efficiency of ca. 2.6%.

3. Two isomeric quinoline and 9-phenylcarbazole derivatives with different linking topologies were synthesized as versatile exciplex-forming materials.
    - 3.1. The substitution manipulation affected the thermal, electrochemical and photophysical properties of phenylquinoline-based compounds. The solutions and solid films of both synthesized compounds showed violet fluorescence with the emission intensity maxima at 395 nm and 415 nm. The compounds exhibited moderate triplet energies (2.57–2.64 eV) and high ionization potentials of 6.12 and 6.21 eV.
    - 3.2. The studied compounds showed bipolar charge-transport properties with hole- and electron mobilities exceeding 10^{-4} cm^2 V^{-1} s^{-1} at electric fields exceeding 10^5 V/cm.
    - 3.3. Owing to their bipolar nature, the studied compounds formed two kinds of exciplexes: blue-emitting exciplexes with acceptor 2,4,6-tris[3-(diphenylphosphinyl) phenyl]-1,3,5-triazine, and orange-emitting exciplexes with donor 4,4′,4″-tris[3-methylphenyl- (phenyl)amino]triphenylamine.
    - 3.4. White electroluminescence was achieved via the combination of two interface exciplex emissions in three-layered sandwich-type OLEDs. The best fabricated and optimized non-doped device emitted white electroluminescence with a color rendering index of 76, color temperature of 8400 K, and maximum external quantum efficiency of 3.15%.
4. Three new mechanochromic compounds comprised of quinoline and di-*tert*-butyl phenothiazine units with donor-acceptor and donor-π-acceptor architecture were synthesized, and their properties were studied.
    - 4.1. The extent of π-conjugation between the donor and the acceptor affect the thermal and photophysical properties of the compounds. The 5% weight loss temperatures of the compounds varied in the range of 348–385 °C. The more symmetrical structure of the *para*-isomer resulted in higher mass loss and melting temperatures relative to the *meta*-linked isomer.
    - 4.2. The conformational diversity of the phenothiazine (quasi-axial and quasi-equatorial) moiety resulted in dual emission of the solid samples, doped films and solutions. Supported by theoretical calculations, the observed blue-shifted peaks were assigned to the emission from quasi-axial conformers, while the red-shifted charge transfer peaks were assigned to the emission from the quasi-equatorial conformers.
    - 4.3. The quasi-equatorial conformer of the phenothiazine-based donor-acceptor compound without a phenyl linker exhibited thermally activated delayed fluorescence. The compound with direct linkage between the donor and the acceptor showed dual emission with peaks at 440 nm and 560 nm.
    - 4.4. The fluorescence change under external stimuli (grinding, fuming, and melting) developed due to the reversible switching between the crystalline and amorphous states. The ground and melted forms of donor-π-acceptor compounds showed biexponential fluorescence decays with longer lifetimes with respect to the initial and fumed forms.

5. Three new cyanocarbazolyl-based exciplex-forming compounds were obtained and characterized.
    5.1. Photophysical, electrochemical and thermal properties were modified by the manipulation of substituents in the C-3 position of the cyano carbazole moiety. The compounds demonstrated high thermal stability with 5% mass loss temperatures in the range of 261–362 °C. The compounds formed molecular glasses with glass transition temperatures reaching 101 °C.
    5.2. The compounds displayed bipolar charge-transporting properties. The acridan-based compound exhibited more balanced charge-transport of holes and electrons than its bicarbazolyl-based congener. The layer of the bicarbazolyl-based compound exhibited hole drift mobility of 5.41×10^{-5} cm^2/V s at an electric field of 6.81×10^5 V cm^{-1}, while its electron mobilities were found to be 5.20×10^{-5} cm^2/V.
    5.3. The materials exhibited violet-deep blue emission and a high energy of the triplet levels ranging from 2.90 eV up to 3.04 eV.
    5.4. The molecular mixtures of the compounds with 2,4,6-tris[3-(diphenylphosphinyl)phenyl]-1,3,5-triazine exhibited thermally activated delayed fluorescence. The exciplex emission color was tuned from sky-blue peaking at 494 nm to yellow peaking at 552 nm by the change of the electron-donating moieties.

6. REFERENCES

1. MEIGHEN, E. A. Genetics of bacterial bioluminescence. *Annual Review of Genetics* [interactive]. 1994, Vol. 28, 117–139. Access via doi: 10.1146/annurev.ge.28.120194.001001
2. EINSTEIN, A. Zur Elektrodynamik bewegter Körper. *Annals of Physics* [interactive]. 1905, Vol. 322 (10), 891–921. Access via doi: 10.1002/andp.19053221004
3. EINSTEIN, A. Über einen die Erzeugung und Verwandlung des Lichtes betreffenden heuristischen Gesichtspunkt. *Annals of Physics* [interactive]. 1905, Vol. 322 (6), 132–148. Access via doi: 10.1002/andp.19053220607
4. OSTROVERKHOVA, O. Organic optoelectronic materials: mechanisms and applications. *Chemical Reviews* [interactive]. 2016, Vol. 116 (22), 13279–13412. Access via doi: 10.1021/acs.chemrev.6b00127
5. MUCCINI, M. A bright future for organic field-effect transistors. *Nature Materials* [interactive]. 2006, Vol. 5, 605–613. Access via doi: 10.1038/nmat1699
6. LIU, Y., et al. All-organic thermally activated delayed fluorescence materials for organic light-emitting diodes. *Nature reviews* [interactive]. 2018, Vol. 3, 18020 (1–20). Access via doi: 10.1038/natrevmats.2018.20
7. TAO, Y., et al. Thermally activated delayed fluorescence materials towards the breakthrough of organoelectronics. *Advanced Materials* [interactive]. 2014, Vol. 26 (47), 7931–7958. Access via doi: 10.1002/adma.201402532
8. TANG, C. W. and VANSLYKE, S. A. Organic electroluminescent diodes. *Applied Physics Letters* [interactive]. 1987, Vol. 51, 913–915. Access via doi: 10.1063/1.98799@apl.2019.APLCLASS2019.issue-1
9. BURROUGHES, J. H., et al. Light-emitting diodes based on conjugated polymers. *Nature* [interactive]. 1990, Vol. 347, 539–541. Access via doi: 10.1038/347539a0
10. DUAN, L., et al. Solution processable small molecules for organic light-emitting diodes. *Journal of Materials Chemistry* [interactive]. 2010, Vol. 20, 6392–6407. Access via doi: 10.1039/b926348a
11. SHIBATA, M., et al. Advantages and disadvantages of vacuum-deposited and spin-coated amorphous organic semiconductor films for organic light-emitting diodes. *Journal of Materials Chemistry C* [interactive]. 2015, Vol. 3, 11178–11191. Access via doi: 10.1039/c5tc01911g
12. CHI, Y., and CHOU, P.-T. Phosphorescent dyes for organic light-emitting diodes. *Chemistry: A European Journal* [interactive]. 2007, Vol. 13 (2), 380–390. Access via doi: 10.1002/chem.200601272
13. ZHANG, Q.-C., et al. Luminescent oligonuclear metal complexes and the use in organic light-emitting diodes. *Coordination Chemistry Reviews* [interactive]. 2019, Vol. 378, 121–133. Access via doi: 10.1016/j.ccr.2018.01.017
14. KONDAKOV, D. Y., et al. Triplet annihilation exceeding spin statistical limit in highly efficient fluorescent organic light-emitting diodes. *Journal of Applied Physics* [interactive]. 2009, Vol. 106 (12), 124510. Access via doi: 10.1063/1.3273407

15. BOHNE, C., et al. Characterization of the triplet-triplet annihilation process of pyrene and several derivatives under laser excitation. *Journal of the American Chemical Society* [interactive]. 1990, Vol. 112 (11), 4226–4231. Access via doi: 10.1021/ja00167a018
16. PARKER, C. A. and HATCHARD, C. G. Triplet-singlet emission in fluid solutions. Phosphorescence of eosin. *Transactions of the Faraday Society* [interactive]. 1961, Vol. 57, 1894–1904. Access via doi: 10.1039/TF9615701894
17. UOYAMA, H., et al. Highly efficient organic light-emitting diodes from delayed fluorescence. *Nature* [interactive]. 2012, Vol. 492, 234–238. Access via doi: 10.1038/nature11687
18. MEHES, G., et al. Enhanced electroluminescence efficiency in a spiro-acridine derivative through thermally activated delayed fluorescence. *Angewandte Chemie International Edition* [interactive]. 2012, Vol. 51 (45), 11311 –11315. Access via doi: 10.1002/anie.201206289
19. HATAKEYAMA, T., et al. Ultrapure blue thermally activated delayed fluorescence molecules: efficient HOMO–LUMO separation by the multiple resonance effect. *Advanced Materials* [interactive]. 2016, Vol. 28 (14), 2777−2781. Access via doi: 10.1002/adma.201505491
20. KIM, B.-S., and LEE, J. Y. Engineering of mixed host for high external quantum efficiency above 25% in green thermally activated delayed fluorescence device. *Advanced Functional Materials* [interactive]. 2014, Vol. 24 (25), 3970−3977. Access via doi: 10.1002/adfm.201303730
21. LEE, D. R., et al. Above 30% external quantum efficiency in green delayed fluorescent organic light-emitting diodes. *ACS Applied Materials & Interfaces* [interactive]. 2015, Vol. 7 (18), 9625–9629. Access via doi: 10.1021/acsami.5b01220
22. CHO, Y. J., et al. Molecular engineering of high efficiency and long lifetime blue thermally activated delayed fluorescent emitters for vacuum and solution processed organic light-emitting diodes. *Advanced Optical Materials* [interactive]. 2016, Vol. 4 (5), 688−693. Access via doi: 10.1002/adom.201500634
23. ZHANG, D., et al. Sterically shielded blue thermally activated delayed fluorescence emitters with improved efficiency and stability. *Materials Horizons* [interactive]. 2016, Vol. 3, 145−151. Access via doi: 10.1039/C5MH00258C
24. LIU, W., et al. Novel carbazole-pyridine-carbonitrile derivative as excellent blue thermally activated delayed fluorescence emitter for highly efficient organic light-emitting devices. *ACS Applied Materials & Interfaces* [interactive]. 2015, Vol. 7 (34), 18930−18936. Access via doi: 10.1021/acsami.5b05648
25. PAN, K.-C., et al. Efficient and tunable thermally activated delayed fluorescence emitters having orientation-adjustable CN-substituted pyridine and pyrimidine acceptor units. *Advanced Functional Materials* [interactive]. 2016, Vol. 26. (42), 7560–7571. Access via doi: 10.1002/adfm.201602501
26 WU, K., et al. Optimizing optoelectronic properties of pyrimidine-based tadf emitters by changing the substituent for organic light-emitting diodes with external quantum efficiency close to 25 % and slow efficiency roll-off. *Chemistry: A European Journal* [interactive]. 2016, Vol. 22 (31), 10860–10866. Access via doi: 10.1002/chem.201601686

27. XIANG, Y., et al. Asymmetric-triazine-cored triads as thermally activated delayed fluorescence emitters for high-efficiency yellow OLEDs with slow efficiency roll-off. *Journal of Materials Chemistry C* [interactive]. 2016, Vol. 4, 9998–10004. Access via doi: 10.1039/C6TC02702D
28. CHA, J.-R., et al. Design of *ortho*-linkage carbazole-triazine structure for high-efficiency blue thermally activated delayed fluorescent emitters. *Dyes and Pigments* [interactive]. 2016, Vol. 134, 562–568. Access via doi: 10.1016/j.dyepig.2016.08.023
29. TANAKA, H., et al. Twisted intramolecular charge transfer state for long-wavelength thermally activated delayed fluorescence. *Chemistry of Materials* [interactive]. 2013, Vol. 25, (18) 3766–3771. Access via doi: 10.1021/cm402428a
30. ALBRECHT, K., et al. Thermally activated delayed fluorescence OLEDs with fully solution processed organic layers exhibiting nearly 10% external quantum efficiency. *Chemical Communications* [interactive]. 2017, Vol. 53, 2439–2442. Access via doi: 10.1039/C6CC09275F
31. HIRATA, S., et al. Highly efficient blue electroluminescence based on thermally activated delayed fluorescence. *Nature Materials* [interactive]. 2015, Vol. 14, 330–336. Access via doi: 10.1038/NMAT4154
32. DIAS, F. B., et al. Triplet harvesting with 100% efficiency by way of thermally activated delayed fluorescence in charge transfer OLED emitters. *Advanced Materials* [interactive]. 2013, Vol. 25 (27), 3707–3714. Access via doi: 10.1002/adma.201300753
33. MATULAITIS, T., et al. Impact of donor substitution pattern on the TADF properties in the carbazolyl-substituted triazine derivatives. *The Journal of Physical Chemistry C* [interactive]. 2017, Vol. 121 (42), 23618–23625. Access via doi: 10.1021/acs.jpcc.7b08034
34. LEE, D. R., et al. Ideal molecular design of blue thermally activated delayed fluorescent emitter for high efficiency, small singlet-triplet energy splitting, low efficiency roll-off, and long lifetime. *ACS Applied Materials Interfaces* [interactive]. 2016, Vol. 8 (35), 23190–23196. Access via doi: 10.1021/acsami.6b05877
35. TANAKA, H., et al. Efficient green thermally activated delayed fluorescence (TADF) from a phenoxazine–triphenyltriazine (PXZ–TRZ) derivative. *Chemical Communications* [interactive]. 2012, Vol. 48, 11392–11394. Access via doi: 10.1039/C2CC36237F
36. TSAI, W.-L., et al. A versatile thermally activated delayed fluorescence emitter for both highly efficient doped and non-doped organic light emitting devices. *Chemical Communications* [interactive]. 2015, Vol. 51, 13662–13665. Access via doi: 10.1039/C5CC05022G
37. LIN, T.-A., et al. Sky-blue organic light emitting diode with 37% external quantum efficiency using thermally activated delayed fluorescence from spiroacridine-triazine hybrid. *Advanced Materials* [interactive]. 2016, Vol. 28 (32), 6976–6983. Access via doi: 10.1002/adma.201601675
38. KALINOWSKI, J. Excimers and exciplexes in organic electroluminescence. *Materials Science-Poland* [interactive]. 2009, Vol. 27, 735–756. Access via: https://www.researchgate.net/profile/Rafik_Karaman/post/Is_there_any_reason_for_excimer_formation_like_geometry_etc_in_some_of_the_organic_molecules_where

_only_excimer_forms/attachment/59d624bc79197b80779830d2/AS:313935356465152@1451859429138/download/Excimers.pdf

39. FREDERICHS, B., and STAERK, H. Energy splitting between triplet and singlet exciplex states determined with E-type delayed fluorescence. *Chemical Physics Letters* [interactive]. 2008, Vol. 460, 116–118. Access via doi: 10.1016/j.cplett.2008.05.086

40. LIU, X.-K., et al. Prediction and design of efficient exciplex emitters for high-efficiency, thermally activated delayed-fluorescence organic light-emitting diodes. *Advanced Materials* [interactive]. 2015, Vol. 27, 2378–2383. Access via doi: 10.1002/adma.201405062

41. CHEN, B., et al. Improved color purity and efficiency of blue organic light-emitting diodes via suppression of exciplex formation. *Synthetic Metals* [interactive]. 2001, Vol. 118, 193–196. Access via doi: 10.1016/S0379-6779(00)00278-2

42. SARMA, M., and WONG, K.-T. Exciplex: An intermolecular charge-transfer approach for TADF. *ACS Applied Materials & Interfaces* [interactive]. 2018, Vol. 10 (23), 19279–19304. Access via doi: 10.1021/acsami.7b18318

43. GOUSHI, K., et al. Organic light-emitting diodes employing efficient reverse intersystem crossing for triplet-to-singlet state conversion. *Nature Photonics* [interactive]. 2012, Vol. 6, 253–258. Access via doi: 10.1038/nphoton.2012.31

44. GRAVES, D., et al. photophysical investigation of the thermally activated delayed emission from films of m-MTDATA:PBD exciplex. *Advanced Functional Materials* [interactive]. 2014, Vol. 24, 2343–2351. Access via doi: 10.1002/adfm.201303389

45. DOS SANTOS, P. L, et al. Investigation of the mechanisms giving rise to TADF in exciplex states. *The Journal of Physical Chemistry C* [interactive]. 2016, Vol. 120, 18259−18267. Access via doi: 10.1021/acs.jpcc.6b05198

46. HUNG, W.-Y., et. al. Highly efficient bilayer interface exciplex for yellow organic light- emitting diode. *ACS Applied Materials Interfaces* [interactive]. 2013, Vol. 5, 6826−6831. Access via doi: 10.1021/am402032z

47. HUNG, W.-Y., et al. The first tandem, all-exciplex-based WOLED. *Sci. Rep.* [interactive]. 2015, Vol. 4, 1−6. Access via doi: 10.1038/srep05161

48. LIU, X.-K., et al. Remanagement of singlet and triplet excitons in single-emissive-layer hybrid white organic light-emitting devices using thermally activated delayed fluorescent blue exciplex. *Advanced Materials* [interactive]. 2015, Vol. 27, 7079–7085. Access via doi: 10.1002/adma.201502897

49. CHAPRAN, M., et al. Realizing 20% external quantum efficiency in electroluminescence with efficient thermally activated delayed fluorescence from an exciplex. *ACS Applied Materials Interfaces* [interactive]. 2019, Vol. 11 (14), 13460–13471. Access via doi: https://doi.org/10.1021/acsami.8b18284

50. DIAS, F. B., et al. The role of local triplet excited states and d-a relative orientation in thermally activated delayed fluorescence: photophysics and devices. *Advanced Science* [interactive]. 2016, Vol. 3, 1600080. Access via doi: 10.1002/advs.201600080

51. JANKUS, V., et al. Highly efficient TADF OLEDs: how the emitter-host interaction controls both the excited state species and electrical properties of the devices to achieve near 100% triplet harvesting and high efficiency. *Advanced*

Functional Materials [interactive]. 2014, Vol. 24 (39), 6178–6186. Access via doi: 10.1002/adfm.201400948

52. ZHANG, T., et al. Efficient exciplex emission from intramolecular charge transfer material. *Organic Electronics* [interactive]. 2015, Vol. 25, 6–11. Access via doi: 10.1016/j.orgel.2015.06.017

53. JEON, S. K., et al. Highly efficient exciplex organic light-emitting diodes using thermally activated delayed fluorescent emitters as donor and acceptor materials. *Nanotechnology* [interactive]. 2016, Vol. 27, 224001. Access via doi: 10.1088/0957-4484/27/22/224001

54. LIU, W. Novel strategy to develop exciplex emitters for high-performance OLEDs by employing thermally activated delayed fluorescence materials. *Advanced Functional Materials* [interactive]. 2016, Vol. 26, 2002–2008. Access via doi: 10.1002/adfm.201505014

55. BÜNAU, G. V. J. B. Birks: Photophysics of Aromatic Molecules. Wiley-Interscience, London 1970. 704 Seiten. Preis: 210s. *Berichte der Bunsengesellschaft für physikalische Chemie* [interactive]. 1970. Vol. 74 (12), 1294–1295. Available via doi: 10.1002/bbpc.19700741223

56. FÖRSTER, T., and KASPER, K. Ein konzentrationsumschlag der fluoreszenz. *Zeitschrift für Physikalische Chemie* [interactive]. 1954, Vol. 1, 275−277. Access via doi: 10.1002/bbpc.19550591018

57. WEICHSEL, C., et al. Organic light-emitting diodes for lighting: High color quality by controlling energy transfer processes in host-guest-systems. *Journal of Applied Physics* [interactive]. 2012, Vol. 111, 033102 (1–7). Access via doi: 10.1063/1.3679549

58. LUO, J., et al. Aggregation-induced emission of 1-methyl-1,2,3,4,5-pentaphenylsilole. *Chemical Communications* [interactive]. 2001, Vol. 0, 1740−1741. Access via doi: 10.1039/B105159H

59. MEI, J., et. al. Aggregation-induced emission: together we shine, united we soar! *Chemical Reviews* [interactive]. 2015, Vol. 115 (21), 11718−11940. Access via doi: < 10.1021/acs.chemrev.5b00263

60. CHEN, G., et al. Conjugation-induced rigidity in twisting molecules: filling the gap between aggregation-caused quenching and aggregation-induced emission. *Advanced Materials* [interactive]. 2015, Vol. 27 (30), 4496–4501. Access via doi: 10.1002/adma.201501981

61. MEI, J., et al. Aggregation-induced emission: the whole is more brilliant than the parts. *Advanced Materials* [interactive]. 2014, Vol. 26, 5429–5479. Access via doi: 10.1002/adma.201401356

62. LEUNG, N. L. C., et al. Restriction of intramolecular motions: the general mechanism behind aggregation-induced emission. *Chemistry: A European Journal* [interactive]. 2014, Vol. 20 (47), 15349–15353. Access via doi: 10.1002/chem.201403811

63. LI, X., et al. Highly fluorescent lyotropic mesophases and organogels based on j-aggregates of core-twisted perylene bisimide dyes. *Chemistry – A European Journal* [interactive]. 2008, Vol. 14, 8074–8078. Access via doi: 10.1002/chem.200800915

64. WANG, Y., et al. Aqueous nanoaggregation-enhanced one- and two-photon fluorescence, crystalline j-aggregation-induced red shift, and amplified spontaneous emission of 9,10-Bis(p-dimethylaminostyryl) anthracene. *The Journal of Physical Chemistry C* [interactive]. 2012, Vol. 116, 15576−15583. Access via doi: 10.1021/jp3031094

65. DOUHAL, A., et al. Proton-transfer reaction dynamics. *Chemical Physics* [interactive]. 1996, Vol. 207 (2−3), 477−498. Access via doi: 10.1016/0301-0104(96)00067-5

66. GAO, M., et al. A Fluorescent light-up probe with 'AIE+ESIPT' characteristics for specific detection of lysosomal esterase. *Journal of Materials Chemistry B* [interactive]. 2014, Vol. 2, 3438−3442. Access via doi: 10.1039/C4TB00345D

67. TANG, W. X., et al. Salicylaldehyde azines as fluorophores of aggregation-induced emission enhancement characteristics. *The Journal of Organic Chemistry* [interactive]. 2009, Vol. 74, 2163–2166. Access via doi: 10.1021/jo802631m

68. LI, S., et al. Understanding the pressure-induced emission enhancement for triple fluorescent compound with excited-state intramolecular proton transfer. *The Journal of Physical Chemistry A* [interactive]. 2007, Vol. 111, 11793−11800. Access via doi: 10.1021/jp075301a

69. SASAKI, S., et al. Recent advances in twisted intramolecular charge transfer (tict) fluorescence and related phenomena in materials chemistry. *Journal of Materials Chemistry C* [interactive]. 2016, Vol. 4, 2731—2743. Access via doi: 10.1039/c5tc03933a

70. HU, R., et al. Twisted intramolecular charge transfer and aggregation-induced emission of bodipy derivatives. *The Journal of Physical Chemistry C* [interactive]. 2009, Vol. 113 (36), 15845–15853. Access via doi: 10.1021/jp902962h

71. YAN, Z. Q., et al. Study of aggregation induced emission of cyano-substituted oligo (p-phenylenevinylene) by femtosecond time resolved fluorescence. *Spectrochimica Acta Part A: Molecular and Biomolecular Spectroscopy* [interactive]. 2011, Vol. 78 (5), 1640–1645. Access via doi: < 10.1016/j.saa.2011.01.056

72. LI, J., et al. From dark TICT state to emissive quasi-TICT state: the aie mechanism of n-(3-(benzo[d]oxazol-2-yl)phenyl)-4-*tert*butylbenzamide. *The Journal of Physical Chemistry C* [interactive]. 2015, Vol. 119 (4), 2133−2141. Access via doi: 10.1021/jp5089433

73. GOMEZ-DURAN, C. F. A., et al. Effect of AIE substituents on the fluorescence of tetraphenylethene-containing BODIPY derivatives. *ACS Applied Materials Interfaces* [interactive]. 2015, Vol. 7 (28), 15168−15176. Access via doi: 10.1021/acsami.5b05033

74. GAWINECKI, R., et al. 4- *Tert*-butyl-1-(4'-dimethylamino-benzylideneamino)pyridinium perchlorate (BDPP): a novel fluorescent dye. *Dyes and Pigments* [interactive]. 1993, Vol. 23 (2), 73–78. Access via doi: 10.1016/0143-7208(93)80026-W

75. FAN, X., et al. Photoluminescence and electroluminescence of hexaphenylsilole are enhanced by pressurization in the solid state. *Chemical Communications* [interactive]. 2008, 2989–2991. Access via doi: 10.1039/B803539C

76. XU, Y., et al. Fluorescence mutation and structural evolution of a π-conjugated molecular crystal during phase transition. *Journal of Materials Chemistry C* [interactive]. 2016, Vol. 4, 1257–1262. Access via doi: 10.1039/C5TC03745J
77. YOON, S.-J., et al. Multistimuli two-color luminescence switching via different slip-stacking of highly fluorescent molecular sheets. *Journal of the American Chemical Society* [interactive]. 2010, Vol. 132 (39), 13675–13683. Access via doi: 10.1021/ja1044665
78. ZHANG, X., et al. Piezofluorochromism of an Aggregation-Induced Emission Compound Derived from Tetraphenylethylene. *Chemistry – An Asian Journal* [interactive]. 2011, Vol. 6 (3), 808–811. Access via doi: 10.1002/asia.201000802
79. XU, B., et al. Piezofluorochromic and aggregation-induced-emission compounds containing triphenylethylene and tetraphenylethylene moieties. *Chemistry – An Asian Journal* [interactive]. 2011, Vol. 6 (3), 1470–1478. Access via doi: 10.1002/asia.201000802
80. XIE, Z., et al. White-light emission strategy of a single organic compound with aggregation-induced emission and delayed fluorescence properties. *Angewandte Chemie International Edition* [interactive]. 2015, Vol. 54 (24), 7181–7184. Access via doi: 10.1002/anie.201502180
81. XU, B., et al. Achieving remarkable mechanochromism and white-light emission with thermally activated delayed fluorescence through the molecular heredity principle. *Chemical Science* [interactive]. 2016, Vol. 7, 2201–2206. Access via doi: 10.1039/C5SC04155D
82. YANG, J., et al. Molecular conformation-dependent mechanoluminescence: same mechanical stimulus but different emissive color over time. *Angewandte Chemie International Edition* [interactive]. 2018, Vol. 57 (43), 14174–14178. Access via doi: 10.1002/anie.201809463
83. OKAZAKI, M., et al. Thermally activated delayed fluorescent phenothiazine-dibenzo[a,j]phenazine-phenothiazine triads exhibiting tricolor-changing mechanochromic luminescence. *Chemical Science* [interactive]. 2017, Vol. 8, 2677–2686. Access via doi: 10.1039/C6SC04863C
84. KUKHTA, N. A., et al. Structure–property relationships of star-shaped blue-emitting charge-transporting 1,3,5-triphenylbenzene derivatives. *Dyes and Pigments* [interactive]. 2015, Vol. 117, 122–132. Access via doi: 10.1016/j.dyepig.2015.02.013
85. FRISCH, M. J. et al. Gaussian 09, Revision E.01, Gaussian, Inc., Wallingford CT, 2009. Access via: http://gaussian.com/citation/
86. PALSSON, L.-O. et al. Efficient intramolecular charge transfer in oligoyne-linked donor–π–acceptor molecules. *Chemistry: A European Journal* [interactive]. 2010, Vol. 16 (5), 1470–1479. Access via doi: 10.1002/chem.200902099
87. WILLIAMS, D. B. G., and LAWTON, M. Drying of organic solvents: quantitative evaluation of the efficiency of several desiccants. *The Journal of Organic Chemistry* [interactive]. 2010, Vol. 75 (24), 8351–8354. Access via doi: 10.1021/jo101589h
88. LIU, Y., et al. π-Conjugated aromatic enynes as a single-emitting component for white electroluminescence. *Journal of the American Chemical Society* [interactive] 2006, Vol. 128 (17) 5592–5593. Access via doi: 10.1021/ja058188f

89. MATULAITIS, T., et al. Synthesis and properties of bipolar derivatives of 1,3,5-triazine and carbazole. *Dyes and Pigments* [interactive]. 2016, Vol. 127, 45−58. Access via doi: 10.1016/j.dyepig.2015.11.001
90. TUCKER, S. H. LXXIV.-Iodination in the carbazole series. *Journal of the Chemical Society* [interactive]. 1926, Vol. 129, 546–553. Access via doi: 10.1039/JR9262900546
91. SYCH, G., et al. Structure-properties relationship of tetrafluorostyrene-based monomers and polymers containing different donor moieties. *Reactive and Functional Polymers* [interactive]. 2019, Vol. 143, 104323 (1–10). Access via doi: 10.1016/j.reactfunctpolym.2019.104323.
92. VASILENKO, I. V., et al. Simultaneous step-growth and chain-growth cationic polymerization of styrenic monomers bearing carbazolyl groups. *Polymer* [interactive]. 2017, Vol. 129, 83–91. Access via doi: 10.1016/j.polymer.2017.09.036
93. AMBROSE, J. F., and Nelson, R. F. Anodic oxidation pathways of carbazoles, Journal of The Electrochemical Society. 1968, Vol. 115, 1159–1164. Access via doi: 10.1149/1.2410929
94. BOWMER, T. N., et al. Effect of substituents on the thermal transitions and degradation behavior of poly[bis(R-phenoxy)phosphazenes]. *Macromolecules* [interactive]. 1991, Vol. 24 (17), 4827–4833. Access via doi: 10.1021/ma00017a016
95. GONG, M. S., et al. Synthesis and device properties of mCP analogues based on fused-ring carbazole moiety. *Organic Electronics* [interactive]. 2017, Vol. 42, 66–74. Access via doi: 10.1016/j.orgel.2016.12.027
96. YANG, L., et al. Theoretical study on electronic structure and optical properties of phenothiazine-containing conjugated oligomers and polymers. *The Journal of Organic Chemistry* [interactive]. 2005, Vol. 70 (15) 5987–5996. Access via doi: 10.1021/jo050665p
97. KONIDENA, R. K., et al. Phenothiazine decorated carbazoles: effect of substitution pattern on the optical and electroluminescent characteristics. *The Journal of Organic Chemistry* [interactive]. 2015, Vol. 80 (11), 5812–5823. Access via doi: 10.1021/acs.joc.5b00787
98. SATHIYAN, G., et al. Review of carbazole based conjugated molecules for highly efficient organic solar cell application. *Tetrahedron Letters* [interactive]. 2016, Vol. 57 (3), 243–252. Access via doi: 10.1016/j.tetlet.2015.12.057
99. KWON, O., et al. Aromatic amines: a comparison of electron-donor strengths. *The Journal of Physical Chemistry A* [interactive]. 2005, Vol. 109 (41), 9346–9352. Access via doi: 10.1021/jp054334s
100. IM, Y., et al. Molecular design strategy of organic thermally activated delayed fluorescence emitters. *Chemistry of Materials* [interactive]. 2017, Vol. 29 (5), 1946–1963. Access via doi: 10.1021/acs.chemmater.6b05324
101. SKUODIS, E., et al. Aggregation, thermal annealing, and hosting effects on performances of an acridan-based TADF emitter. *Organic Electronics* [interactive]. 2018, Vol. 63, 29–40. Access via doi: 10.1016/j.orgel.2018.09.002
102. GRABOWSKI, Z. R., and Rotkiewicz, K. Structural changes accompanying intramolecular electron transfer: focus on twisted intramolecular charge-transfer

states and structures. *Chemical Reviews* [interactive]. 2003, Vol. 103 (10), 3899–4031. Access via doi: 10.1021/cr940745l

103. Anindita DAS, A., and GHOSH S. Supramolecular assemblies by charge-transfer interactions between donor and acceptor chromophores. *Angewandte Chemie International Edition* [interactive]. 2014, Vol. 53 (8), 2038–2054. Access via doi: 10.1002/anie.201307756

104. Zhang, X., et al. Donor/acceptor vinyl monomers and their polymers: Synthesis, photochemical and photophysical behaviour. *Progress in Polymer Science* [interactive]. 2006, Vol. 31 (10), 893–948. Access via doi: 10.1016/j.progpolymsci.2006.08.009

105. MCCONNELL, H. Effect of polar solvents on the absorption frequency of n→π electronic transitions. *The Journal of Chemical Physics* [interactive]. 1952, Vol. 20 (4), 700–704. Access via doi: 10.1063/1.1700519

106. SYCH, G., et al. Exciplex-enhanced singlet emission efficiency of nondoped organic light emitting diodes based on derivatives of tetrafluorophenylcarbazole and tri/tetraphenylethylene exhibiting aggregation-induced emission enhancement. *The journal of physical chemistry C* [interactive]. 2018, Vol. 122 (26), 14827–14837. Access via doi: 10.1021/acs.jpcc.8b03895.

107. LI, J., et al. A High Tg carbazole-based hole-transporting material for organic light-emitting devices. *Chemistry of Materials* [interactive]. 2005, Vol. 17 (5), 1208–1212. Access via doi: 10.1021/cm034731k

108. TSAI, M.-H., et. al. 3-(9-Carbazolyl)carbazoles and 3,6-Di(9-carbazolyl)carbazoles as effective host materials for efficient blue organic electrophosphorescence. *Advanced Materials* [interactive]. 2007, Vol. 19 (6), 862–866. Access via doi: 10.1002/adma.200600822

109. ATTAR, H. A. and MONKMAN, A. P. Electric field induced blue shift and intensity enhancement in 2d exciplex organic light emitting diodes; controlling electron–hole separation. *Advanced Materials* [interactive]. 2016, Vol. 28 (36), 8014–8020. Access via doi: 10.1002/adma.201600965

110. DEKSNYS, T. et al. Synthesis and characterization of a carbazole-based bipolar exciplex-forming compound for efficient and color-tunable OLEDs. *New Journal of Chemistry* [interactive]. 2017, 41, 559−568. Access via doi: 10.1039/C6NJ02865A

111. VELDMAN, D., et al. The energy of charge-transfer states in electron donor–acceptor blends: insight into the energy losses in organic solar cells. *Advanced Functional Materials* [interactive]. 2009, Vol. 19 (12), 1939−1948. Access via doi: 10.1002/adfm.200900090

112. DUAN, L., et al. Strategies to design bipolar small molecules for OLEDs: donor-acceptor structure and non-donor-acceptor structure. *Advanced Materials* [interactive]. 2011, Vol. 23 (9), 1137−1144. Access via doi: 10.1002/adma.201003816

113. JIANG, J. X., et al. High-efficiency white-light-emitting devices from a single polymer by mixing singlet and triplet emission. *Advanced Materials* [interactive]. 2006, Vol. 18 (13), 1769−1773. Access via doi: 10.1002/adma.200502740

114. THOMPSON, J., et al. White light emission from blends of blue-emitting organic molecules: A general route to the white organic light-emitting diode? *Applied Physics Letters* [interactive]. 2001, 79, 560−562. Access via doi: 10.1063/1.1388875

115. ZHANG, Z., et al. High efficiency fluorescent white organic light-emitting diodes with red, green and blue separately monochromatic emission layers. *Organic Electronics* [interactive]. 2009, Vol. 10 (3), 491−495. Access via doi: 10.1016/j.orgel.2009.02.006

116. CHERPAK, V., et al. Efficient ‘warm-white’ OLEDs based on the phosphorescent bis-cyclometalated iridium(III) complex. *The Journal of Physical Chemistry C* [interactive]. 2014, Vol. 118 (21), 11271−11278. Access via doi: 10.1021/jp503437b

117. D’ANDRADE, B. W., and FORREST S. R. White organic light-emitting devices for solid-state lighting. *Advanced Materials* [interactive]. 2004, Vol. 16 (18), 1585–1595. Access via doi: 10.1002/adma.200400684

118. KALINOWSKI, J., et al. Mixing of excimer and exciplex emission: A new way to improve white light emitting organic electrophosphorescent diodes. *Advanced Materials* [interactive]. 2007, Vol. 19 (22), 4000−4005. Access via doi: 10.1002/adma.200700655

119. LI, G., and SHINAR, J. Combinatorial fabrication and studies of bright white organic light-emitting devices based on emission from rubrene-doped 4,4′-bis(2,2′-diphenylvinyl)-1,1′-biphenyl. *Applied Physics Letters* [interactive]. 2003, Vol. 83 (26), 5359−5361. Access via doi: 10.1063/1.1635658

120. MAZZEO, M., et al. Organic single-layer white light-emitting diodes by exciplex emission from spin-coated blends of blue-emitting molecules. *Applied Physics Letters* [interactive]. 2003, 82 (3), 334−336. Access via doi: 10.1063/1.1531217

121. GRYBAUSKAITE-KAMINSKIENE, G., et al. Contribution of TADF and Exciplex Emission for Efficient ‘Warm-White’ OLEDs. *Journal of Materials Chemistry C* [interactive]. 2018, Vol. 6 (6), 1543−1550. Access via doi: 10.1039/C7TC05392D

122. ZHAO, Y., et al. White light emission from an exciplex based on a phosphine oxide type electron transport compound in a bilayer device structure. *RSC Advances* [interactive]. 2013, Vol. 3 (44), 21453−21460. Access via doi: 10.1039/C3RA43017K

123. CEKAVICIUTE, M., et al. Arylfluorenyl-substituted metoxytriphenylamines as deep blue exciplex forming bipolar semiconductors for white and blue organic light emitting diodes. *Dyes and Pigments* [interactive]. 2017, Vol. 140, 187−202. Access via doi: 10.1016/j.dyepig.2017.01.023

124. SYCH, G., et al. Dual interface exciplex emission of quinoline and carbazole derivatives for simplified nondoped white OLEDs. *The journal of physical chemistry C* [interactive]. 2019, 123, 2386−2397. Access via doi: 10.1021/acs.jpcc.8b09908.

125. LIU, Y., et al. Synthesis and characterization of a bipolar light-emitting copolymer consisting of tetraphenyldiaminobiphenyl and bis-quinoline units. *Chemistry of Materials* [interactive]. 1999, Vol. 11 (1), 27−29. Access via doi: 10.1021/cm980628x

126. AGRAWAL, A. K., et al. Synthesis and processing of heterocyclic polymers as electronic, optoelectronic, and nonlinear optical materials. 2. New series of conjugated rigid-rod polyquinolines and polyanthrazolines. *Macromolecules* [interactive]. 1993, Vol. 26 (5) 895−905. Access via doi: 10.1021/ma00057a003
127. KUWABARA, Y., et al. Thermally stable multilared organic electroluminescent devices using novel starburst molecules, 4,4′ ,4″ -tri(N-carbazolyl) triphenylamine (TCTA) and 4,4′ ,4″ -tris(3-methylphenylphenylamino)- triphenylamine (m-MTDATA), as hole-transport materials. *Advanced Materials* [interactive]. 1994, Vol. 6 (9), 677−679. Access via doi: 10.1002/adma.19940060913
128. JIANG, W., et al. High-triplet-energy tri-carbazole derivatives as host materials for efficient solution-processed blue phosphorescent devices. *Journal of Materials Chemistry* [interactive]. 2011, Vol. 21 (13), 4918−4926. Access via doi: 10.1039/C0JM03365K
129. WANG, Z., et al. The effect of *meta*- coupling on colour purity, quantum yield, and exciton utilizing efficiency in deep-blue emitters from phenanthroimidazole isomers. *Physical Chemistry Chemical Physics* [interactive]. 2015, Vol. 17 (47), 31894−31901. Access via doi: 10.1039/C5CP05097A
130. CHEN, C. H., et al. Highly efficient orange and deep-red organic light emitting diodes with long operational lifetimes using carbazole-quinoline based bipolar host materials. *Journal of Materials Chemistry C* [interactive]. 2014, 2 (30), 6183−6191. Access via doi: 10.1039/C4TC00523F
131. KOTADIYA, N. B., et al. Universal strategy for ohmic hole injection into organic semiconductors with high ionization energies. *Nature Materials* [interactive]. 2018, Vol. 17 (4), 329−334. Access via doi: 10.1038/s41563-018-0043-3
132. BLAKESLEY, J. C., et al. Towards reliable charge-mobility benchmark measurements for organic semiconductors. *Organic Electronics* [interactive]. 2014, Vol. 15 (6), 1263−1272. Access via doi: 10.1016/j.orgel.2014.02.008
133. GAVEZZOTTI, A. Molecular symmetry, melting temperatures and melting enthalpies of substituted benzenes and naphthalenes. *Journal of the Chemical Society, Perkin Transactions 2* [interactive]. 1995, Vol. 20, 1399−1404. Access via doi: 10.1039/P29950001399
134. VIGANTE, B., et al. Synthesis of linear and V-shaped carbazolyl substituted pyridine-3,5-dicarbonitriles exhibiting efficient bipolar charge transport and E-type fluorescence. *Chemistry: A European Journal* [interactive]. 2018, Vol. 25 (13), 3325−3336. Access via doi: 10.1002/chem.201805323
135. RUDNICK, A. A., et al. The influence of torsion on excimer formation in bipolar host materials for blue phosphorescent OLEDs. *Journal of Chemical Physics* [interactive]. 2016, Vol. 144 (21), 214906 (1−6). Access via doi: 10.1063/1.4953102
136. JEON, S. K. et al. Key factors of exciplex emission: Exciton binding and intermolecular molecular orbital overlap. *Organic Electronics* [interactive]. 2018, Vol. 63, 283−288. Access via doi: 10.1016/j.orgel.2018.09.044
137. KIM, H.-B., and KIM, J.-J. A simple method to measure intermolecular charge-transfer absorption of organic films. *Organic Electronics* [interactive]. 2018, Vol. 62, 511−515. Access via doi: 10.1016/j.orgel.2018.06.022

138. GUZAUSKAS, M. Dual nature of exciplexes: exciplex forming properties of carbazole and fluorene hybrid trimmers. *Journal of Materials Chemistry C* [interactive]. 2019, Vol. 7, 25−32. Access via doi: 10.1039/C8TC04708A
139. CHAPRAN, M. High triplet-level phthalimide based acceptors for exciplexes with multicolor emission. *Dyes and Pigments* [interactive]. 2019, Vol. 162, 872−882. Access via doi: 10.1016/j.dyepig.2018.11.022
140. NAKANOTANI, H. Long-range coupling of electron-hole pairs in spatially separated organic donor-acceptor layers. *Science Advances* [interactive]. 2016, Vol. 2 (2), 1501470 (1–7). Access via doi: 10.1126/sciadv.1501470
141. LUHMAN, W. A., and HOLMES, R. J. Enhanced exciton diffusion in an organic photovoltaic cell by energy transfer using a phosphorescent sensitizer. *Applied Physics Letters* [interactive]. 2009, Vol. 94, 153304 (1–3). Access via doi: 10.1063/1.3120566
142. BROWN, R. J. C., and BROWN R. F. C. Melting point and molecular symmetry. *Journal of Chemical Education* [interactive]. 2000, Vol. 77 (6) 724–731. Access via doi: 10.1021/ed077p724
143. CAO, X., et al. Simple phenyl bridge between cyano and pyridine units to weaken the electron-withdrawing property for blue-shifted emission in efficient blue TADF OLEDs. *Organic Electronics* [interactive]. 2018, Vol. 57, 247–254. Access via doi: 10.1016/j.orgel.2018.03.027
144. GROSS, E. K. U., and KOHN, W. Local density-functional theory of frequency-dependent linear response. *Physical Review Letters* [interactive]. 1986, Vol. 57 (7), 923. Access via doi: 10.1103/PhysRevLett.57.923.2
145. DIAS, F. B. Photophysics of thermally activated delayed fluorescence molecules. *Methods and Applications in Fluorescence* [interactive]. 2017, Vol. 5, 012001 (1–25). Access via doi: 10.1088/2050-6120/aa537e
146. DIAS, F. B. Kinetics of thermal-assisted delayed fluorescence in blue organic emitters with large singlet–triplet energy gap. *Philosophical Transactions of the Royal Society* [interactive]. 2015, Vol. 373: 20140447 (1–11). Access via doi: 10.1098/rsta.2014.0447
147. YANG, J. et al. The influence of the molecular packing on the room temperature phosphorescence of purely organic luminogens. *Nature Communication* [interactive]. 2018, Vol. 9, 840 (1–10). Access via doi: 10.1038/s41467-018-03236-6
148. TOMKEVICIENE, A., et al. Thianthrene and acridan-substituted benzophenone or diphenylsulfone: Effect of triplet harvesting via TADF and phosphorescence on efficiency of all-organic OLEDs. *Organic Electronics* [interactive]. 2019, Vol. 70, 227–239. Access via doi: 10.1016/j.orgel.2019.04.025
149. GALIEVSKY, V. A. Ultrafast intramolecular charge transfer with n-(4-cyanophenyl)carbazole. Evidence for a LE precursor and dual LE + ICT fluorescence. *The Journal of Physical Chemistry A* [interactive]. 2010, Vol. 114 (48), 12622–12638. Access via doi: 10.1021/jp1070506
150. KUKHTA, N. A. Deep-blue high-efficiency TTA OLED using *para*- and *meta*-conjugated cyanotriphenylbenzene and carbazole derivatives as emitter and host. *The Journal of Physical Chemistry Letters* [interactive]. 2017, Vol. 8 (24), 6199–6205. Access via doi: 10.1021/acs.jpclett.7b02867

151. BRUNNER, K. Carbazole compounds as host materials for triplet emitters in organic light-emitting diodes: tuning the HOMO level without influencing the triplet energy in small molecules. *Journal of the American Chemical Society* [interactive]. 2004, Vol. 126 (19), 6035–6042. Access via doi: 10.1021/ja049883a

152. HOLMES, R. J., and FORREST, S. R. Blue organic electrophosphorescence using exothermic host-guest energy transfer. *Applied Physics Letters* [interactive]. 2003, Vol. 82 (15), 2422–2424. Access via doi: 10.1063/1.1568146

7. LIST OF SCIENTIFIC ARTICLES ON THE DISSERTATION TOPIC

1. Sych, Galyna; Simokaitiene, Jurate; Bezvikonnyi, Oleksandr; Tsiko, Uliana; Volyniuk, Dmytro; Gudeika, Dalius; Grazulevicius, Juozas Vidas. Exciplex-enhanced singlet emission efficiency of nondoped organic light emitting diodes based on derivatives of tetrafluorophenylcarbazole and tri/tetraphenylethylene exhibiting aggregation-induced emission enhancement // Journal of Physical Chemistry C. 2018, Vol. 122, p. 14827−14837.
2. Sych, Galyna; Volyniuk, Dmytro; Bezvikonnyi, Oleksandr; Lytvyn, Roman; Grazulevicius, Juozas Vidas. Dual interface exciplex emission of quinoline and carbazole derivatives for simplified nondoped white OLEDs // Journal of Physical Chemistry C. 2019, Vol. 123, 2386−2397.
3. Sych, Galyna; Simokaitiene, Jurate; Lygaitis, Ramunas; Jatautiene, Egle; Pashazadeh, Ramin; Buika, Gintaras; Grazulevicius, Juozas Vidas. Structure-properties relationship of tetrafluorostyrene-based monomers and polymers containing different donor moieties // Reactive and Functional Polymers. 2019, 104323.

8. LIST OF PRESENTATIONS AT INTERNATIONAL CONFERENCES

1. Sych, G.; Simokaitiene, J.; Grazulevicius, J. V. Quasiplanar-triphenylamine derivatives as precursors for the synthesis of electroactive materials // ICEPOM–10: Electronic processes in organic and inorganic materials / 23rd–27th May, 2016, Ternopil, Ukraine.
2. Sych, G.; Simokaitiene, J.; Lytvyn, R.; Volynyuk, D.; Bezvikonnyi, O.; Grazulevicius, J. V. Synthesis and properties of fluorostyrene-based monomers for optoelectronics // BPS-2016: Baltic Polymer Symposium-2016 / 21st–23rd September, 2016, Klaipeda, Lithuania.
3. Sych, G.; Simokaitiene, J.; Volynyuk, D.; Grazulevicius, J. V. Synthesis and characterisation of terafluoro- phenyl carbazole containing tetra(tri)-phenylethylene AIE luminogens' BPS-2017: Baltic Polymer Symposium-2017 20th–22nd September, 2017, Tallinn, Estonia.
4. Sych, G.; Simokaitiene, J.; Volynyuk, D.; Bezvikonnyi, O.; Kublickas, R. H., Grazulevicius, J. V. Investigation of fluorostyrene-based monomers and polymers for optoelectronics // Chemistry and Chemical Technology-2017, 28th April, 2017, Kaunas, Lithuania.
5. Sych, G.; Simokaitiene, J.; Volynyuk, D.; Bezvikonnyi, O.; Grazulevicius, J. V. Synthesis and characterization of fluorobenzene-containing bipolar monomers and polymers // XXII International Krutyn Summer School / 20th–27th May, 2017, Krutyn, Poland.
6. Sych, G.; Simokaitiene, J.; Volynyuk, D.; Grazulevicius, J. V. Bipolar donor-acceptor quinoline and carbazole based molecules for white exciplex-based OLEDs // WOREN: 5th Workshop on Organic Electronics and Nanophotonics / 11th–15th February, 2018, Wisla, Poland.
7. Sych, G.; Pashazadeh, R.; Volynyuk, D.; Grazulevicius, J. V. New mechanochromic quinoline based donor-acceptor and donor-π-acceptor solid emitters for optoelectronic application // fπ14: 14th International Symposium on Functional π-Electron Systems / 2nd–7th June, 2019, Berlin, Germany.

9. ACKNOWLEDGEMENTS

First of all, I would like to express my greatest appreciation to my supervisor, Prof. Habil. dr. Juozas Vidas Gražulevičius (Department of Polymer Chemistry and Technology, Kaunas University of Technology) for the kind support, new ideas, and valuable advices during my PhD studies.

Also, I would like to extend my deepest gratitude to my family and my dear friends for the encouragement, relentless support, and love.

I gratefully acknowledge our entire group of organic chemists and physicists, my lab mates, colleagues and co-workers for practical advices, helpful suggestions and friendly atmosphere during these four years.

SL344. 2020-01-30. 17,75 leidyb. apsk. l. Tiražas 12 egz.
Išleido Kauno technologijos universitetas, K. Donelaičio g. 73, 44249 Kaunas
Spausdino leidyklos „Technologija“ spaustuvė, Studentų g. 54, 51424 Kaunas